The Impact of Massive Stars on the Interstellar Medium

Dissertation
zur Erlangung des Doktorgrades
der Mathematisch-Naturwissenschaftlichen Fakultät
der Christian-Albrechts-Universität
zu Kiel

vorgelegt von
Tim Freyer

Kiel
2005

Referent: Prof. Dr. G. Hensler

Korreferent: Prof. Dr. R. F. Wimmer-Schweingruber

Tag der mündlichen Prüfung: 12. Juli 2005

Zum Druck genehmigt: Kiel, den 13. Juli 2005

gez. Prof. Dr. J. Grotemeyer

Dekan

Contents

List of Figures iii

List of Tables vii

Zusammenfassung ix

Abstract xi

1 Introduction 1

2 The Interstellar Medium 3
- 2.1 HII Regions . . . 3
- 2.2 Theory of Stellar Wind Bubbles . . . 4
- 2.3 Instabilities . . . 9
- 2.4 Observations of Stellar Wind Bubbles . . . 13
  - 2.4.1 Main-Sequence Bubbles . . . 13
  - 2.4.2 A Young Bubble in the Orion Molecular Cloud . . . 15
  - 2.4.3 The Eagle Nebula . . . 16
- 2.5 Observations of Wolf-Rayet Bubbles . . . 17
  - 2.5.1 NGC 6888 . . . 18
  - 2.5.2 S308 . . . 20
- 2.6 The Deposition of Energy in the ISM . . . 22
  - 2.6.1 Analytical Approximations for HII Regions . . . 22
  - 2.6.2 Analytical Approximations for Stellar Wind Bubbles . . . 30
- 2.7 The Energization of the ISM in the Solar Neighborhood . . . 31
- 2.8 Previous Numerical Simulations of Stellar Wind Bubbles . . . 33

3 Numerical Method 37
- 3.1 Hydrodynamics . . . 37
- 3.2 Radiative Transfer . . . 39
- 3.3 Dissociation and Ionization . . . 41
- 3.4 Heating Processes . . . 42
  - 3.4.1 Heating by Photoionization of Hydrogen . . . 42
  - 3.4.2 Heating by Photoejection of Electrons from Dust Grains by Lyα Photons . . . 43
- 3.5 Cooling Processes . . . 43

3.5.1 Cooling by Recombination of Hydrogen . . . 43
3.5.2 Cooling by Collisional Ionization of Hydrogen . . . 44
3.5.3 Cooling by Bremsstrahlung . . . 44
3.5.4 Cooling by Collisionally Excited Lyα Emission of Hydrogen . . . 44
3.5.5 Cooling by Forbidden Lines of Oxygen and Nitrogen . . . 44
3.5.6 Energy Exchange of Gas and Dust . . . 45
3.6 Discretization and Grid Arrangement . . . 45
3.7 Initial Conditions . . . 47
3.8 Boundary Conditions . . . 49
3.9 Geometry and Resolution . . . 51
3.10 Tests . . . 51
3.10.1 Conservation of Mass and Energy . . . 51
3.10.2 Resolution Studies . . . 54

4 Results and Discussion **57**
4.1 The 60 $M_\odot$ Case . . . 57
4.1.1 The Evolution of the Circumstellar Medium . . . 57
4.1.2 The Energy Balance in the Circumstellar Medium . . . 67
4.1.3 The Impact of Dust . . . 79
4.1.4 Direct Observational Implications . . . 81
4.2 The 35 $M_\odot$ Case . . . 84
4.2.1 The Evolution of the Circumstellar Medium . . . 84
4.2.2 The Energy Balance in the Circumstellar Medium . . . 96
4.2.3 Comparison with Observations . . . 103
4.3 Unconsidered Physics and Differing Parameters . . . 108

5 Summary and Conclusions **111**

References **117**

Acknowledgements **123**

List of Figures

2.1 The schematic structure of a stellar wind bubble. 5
2.2 The similarity variables for velocity, pressure, and density in the shell of the swept-up HII region for the adiabatic solution of phase 1 according to Weaver et al. (1977). 7
2.3 Principle of the thin-shell overstability. 10
2.4 Principle of the ionization front instability according to Giuliani (1979). 12
2.5 The mean rate of energy transfer from thermal energy in an HII region to kinetic energy of the accelerated shell, calculated according to Lasker (1967). 29
2.6 The mean efficiency of energy transfer from thermal energy in an HII region to kinetic energy of the accelerated shell, calculated according to Lasker (1967). 29

3.1 Example of the nested grid structure. 46
3.2 Initial conditions for the two-dimensional calculations after 1000 yr in the $60\,M_\odot$ case. 48
3.3 Initial conditions for the two-dimensional calculations after 700 yr in the $35\,M_\odot$ case. 48
3.4 Time-dependent stellar parameters used as boundary conditions for the calculation of the $60\,M_\odot$ case. 49
3.5 Time-dependent stellar parameters used as boundary conditions for the calculation of the $35\,M_\odot$ case. 50
3.6 Check of the total mass conservation. 52
3.7 Check of the radiative energy input. 52
3.8 Check of the total energy balance. 53
3.9 Resolution study for the $60\,M_\odot$ case. 55
3.10 Resolution study for the $35\,M_\odot$ case. 55

4.1 Circumstellar mass density and velocity field, temperature, and degree of hydrogen ionization for the $60\,M_\odot$ case at age 10^3 yr (high-resolution run). 61
4.2 Same as Fig. 4.1, but at age 2×10^4 yr. 61
4.3 Same as Fig. 4.2, but at age 4×10^4 yr. 62
4.4 Same as Fig. 4.2, but at age 0.1 Myr. 62
4.5 Same as Fig. 4.2, but at age 0.2 Myr. 63
4.6 Same as Fig. 4.2, but at age 0.5 Myr. 63
4.7 Same as Fig. 4.6, but at age 1 Myr. 64

4.8 Same as Fig. 4.7, but for the medium-resolution run. 64
4.9 Same as Fig. 4.8, but at age 3.30 Myr. 65
4.10 Same as Fig. 4.9, but at age 3.36 Myr. 65
4.11 Same as Fig. 4.9, but at age 3.38 Myr. 65
4.12 Same as Fig. 4.9, but at age 3.41 Myr. 66
4.13 Same as Fig. 4.9, but at age 3.50 Myr. 66
4.14 Same as Fig. 4.9, but at age 4.07 Myr. 66
4.15 Temporal evolution of kinetic, thermal, and ionization energy in the 60 $M_\odot$ case. 67
4.16 Ratio of energies in the 60 $M_\odot$ case with and without a stellar wind. . . 69
4.17 Change rate of the ionization energy in the 60 $M_\odot$ case without a stellar wind. 71
4.18 Change rate of the ionization energy in the 60 $M_\odot$ case. 71
4.19 Change rate of the thermal energy in the 60 $M_\odot$ case without a stellar wind. 72
4.20 Change rate of the thermal energy in the 60 $M_\odot$ case. 72
4.21 Change rate of the kinetic energy in the 60 $M_\odot$ case without a stellar wind. 73
4.22 Change rate of the kinetic energy in the 60 $M_\odot$ case. 73
4.23 Energy transfer efficiency in the 60 $M_\odot$ case without a stellar wind. . . . 74
4.24 Energy transfer efficiency in the 60 $M_\odot$ case. 75
4.25 Radius of the ionized volume in the 60 $M_\odot$ cases. 79
4.26 Energy loss due to cooling in the 60 $M_\odot$ case with dust. 80
4.27 Angle-averaged Hα intensity in the 60 $M_\odot$ case with and without a stellar wind. 82
4.28 Angle-averaged soft (0.5-3.0 keV) X-ray intensity in the 60 $M_\odot$ case. . . 83
4.29 Circumstellar mass density and velocity field, temperature, and degree of hydrogen ionization for the 35 $M_\odot$ case at age 700 yr (high-resolution run). 88
4.30 Same as Fig. 4.29, but at age 5×10^4 yr. 88
4.31 Same as Fig. 4.30, but at age 0.2 Myr. 89
4.32 Same as Fig. 4.30, but at age 0.3 Myr. 89
4.33 Same as Fig. 4.30, but at age 0.4 Myr. 90
4.34 Same as Fig. 4.30, but at age 0.6 Myr. 90
4.35 Same as Fig. 4.34, but at age 1.0 Myr. 91
4.36 Same as Fig. 4.35, but for the medium-resolution run. 91
4.37 Same as Fig. 4.36, but at age 2.0 Myr. 92
4.38 Same as Fig. 4.37, but at age 3.0 Myr. 92
4.39 Same as Fig. 4.37, but at age 4.0 Myr. 93
4.40 Same as Fig. 4.37, but at age 4.59 Myr. 93
4.41 Same as Fig. 4.37, but at age 4.78 Myr. 94
4.42 Same as Fig. 4.37, but at age 4.80 Myr. 94
4.43 Same as Fig. 4.37, but at age 4.82 Myr. 95
4.44 Same as Fig. 4.37, but at age 4.95 Myr. 95
4.45 Temporal evolution of kinetic, thermal, and ionization energy in the 35 $M_\odot$ case. 97
4.46 Ratio of energies in the 35 $M_\odot$ case with and without a stellar wind. . . 98
4.47 Energy transfer efficiency in the 35 $M_\odot$ case. 99

4.48 Energy transfer efficiency in the $35\,M_\odot$ case without a stellar wind. . . . 100
4.49 X-ray luminosity in the energy band $0.1 - 2.4$ keV in the $35\,M_\odot$ case. . . 104
4.50 Angle-averaged unabsorbed X-ray intensity in the energy band $0.1 -$ 2.4 keV in the $35\,M_\odot$ case. 106

List of Tables

2.1 Energy transfer rate and transfer efficiency for HII regions around stars with different initial masses according to the model of Lasker (1967). . . 28
2.2 Hydrodynamical models of SWBs/HII regions around single early-type stars. 34

4.1 The energy components at the end of the 60 $M_\odot$ simulations. 76
4.2 The energy transfer efficiencies at the end of the 60 $M_\odot$ simulations. . . 76
4.3 The energy components at the end of the 35 $M_\odot$ simulations. 101
4.4 The energy transfer efficiencies at the end of the 35 $M_\odot$ simulations. . . 101

Zusammenfassung

In dieser Arbeit stelle ich Ergebnisse von numerischen Simulationsrechnungen vor, mit denen ich den Einfluss massereicher Sterne auf ihr umgebendes interstellares Medium studiert habe. Dabei wird die Entwicklung des zirkumstellaren Gases für zwei Modellsterne untersucht, die sich in ihren Entwicklungswegen und Sternparametern unterscheiden: Der erste Stern hat eine Anfangsmasse von $60\,M_\odot$ und entwickelt sich von einem Hauptreihen-O-Stern über verschiedene Phasen als „Luminous Blue Variable“ und Wolf-Rayet-Stern bis er schließlich als Supernova vom Typ II explodiert. Mit einer Anfangsmasse von $35\,M_\odot$ entwickelt sich der zweite Modellstern von der Hauptreihe zum Roten Überriesen und von dort zum Wolf-Rayet-Stern, bis auch dieser als Supernova explodiert. Im $60\,M_\odot$-Fall zeigt sich, dass die Wechselwirkung der fotoionisierten HII-Region mit der Sternwindblase zur Ausbildung vielfältiger Strukturen wie Schalen, Wolken, Fingern und Speichen führt. Diese Ergebnisse zeigen, dass die komplexen morphologischen Strukturen, die in HII-Regionen angetroffen werden, durchaus auch noch während der Entwicklung der HII-Region entstehen können. Die Strukturbildung im zirkumstellaren Gas während der frühen Hauptreihenphase des $35\,M_\odot$-Sterns ist dabei deutlich weniger ausgeprägt aufgrund der geringeren Windleuchtkraft dieses Sterns. Da andererseits die Schalenform der HII-Region weitgehend erhalten bleibt, kommen Effekte, die auf dieser Symmetrie basieren, stärker zum Vorschein. Des Weiteren habe ich auch den Eintrag der vom Stern in Form von Lyman-Kontinuumsstrahlung und Wind abgegebenen Energie in das interstellare Medium untersucht. Am Ende der Lebensdauer des $60\,M_\odot$-Sterns wurden 0.37 % dieser Energie im zirkumstellaren Gas angesammelt. Von diesem Anteil lagen 35 % in Form von Bewegungsenergie vor, 40 % als thermische Energie und 25 % als Ionisationsenergie von Wasserstoff. Die entsprechenden Anteile im $35\,M_\odot$-Fall sind 10 %, 36 % und 54 %, wobei die Gesamteffizienz des Energieeintrags hier bei 1 % liegt. Das Zusammenschieben des langsamen Roten-Überriesen-Windes durch den schnellen Wolf-Rayet-Wind führt zur Ausbildung bemerkenswerter Beobachtungssignifikanzen, die mit vorliegenden Beobachtungsdaten der Wolf-Rayet-Blase S308 verglichen werden. Mein Modell reproduziert die richtige Größenordnung der Röntgenleuchtkraft, die Temperatur des strahlenden Plasmas sowie die Mitte-Rand-Aufhellung des Röntgen-Intensitätsprofils. Das ist insofern bemerkenswert, als die bislang veröffentlichten analytischen und numerischen Modelle von Wolf-Rayet-Blasen diese Beobachtungsgrößen noch nicht konsistent erklären konnten. Die wichtige Erkenntnis aus den Ergebnissen der Modellrechnung ist, dass nahezu die gesamte Röntgenstrahlung in dieser Phase aus der Schale des zusammengeschobenen Roten-Überriesen-Windes kommt. Damit bietet sich eine Lösung für das sogenannte „Problem des fehlenden Windes“ bei Wolf-Rayet-Blasen.

Abstract

In this thesis I present results of numerical simulations carried out with a two-dimensional radiation hydrodynamics code in order to study the impact of massive stars on their surrounding interstellar medium. The evolution of the circumstellar gas is examined for two model stars with different evolutionary tracks and stellar parameters: The first star has an inital mass of $60\,M_\odot$ and evolves from a main-sequence O star through luminous blue variable and Wolf-Rayet phases, until it ultimately explodes as a supernova of Type II. The second model star, initially having a mass of $35\,M_\odot$, is supposed to undergo the evolution from the main sequence to the red supergiant and finally the Wolf-Rayet phase, until it also explodes as a supernova. In the $60\,M_\odot$ case the interaction of the photoionized HII region with the stellar wind bubble forms a variety of interesting structures like shells, clouds, fingers, and spokes. These results demonstrate that complex structures found in HII regions are not necessarily relics from the time before the gas became ionized but may result from dynamical processes during the course of the HII region evolution. In the $35\,M_\odot$ case structure formation in the circumstellar gas during the early main-sequence evolution is much less pronounced because of the lower mechanical wind luminosity of the star. On the other hand, since the shell-like structure of the HII region is largely preserved, effects that rely on this symmetry become more important. I have also analyzed the transfer and deposit of the stellar wind and radiation energy into the circumstellar medium. At the end of the stellar lifetime 0.37 % of the energy released by the $60\,M_\odot$ star as Lyman continuum radiation and stellar wind has been transferred to the circumstellar gas. From this fraction 35 % is kinetic energy of bulk motion, 40 % is thermal energy, and the remaining 25 % is ionization energy of hydrogen. The respective values in the $35\,M_\odot$ case are 10 %, 36 %, and 54 %, for a total energy transfer efficiency of 1 %. The sweeping up of the slow red supergiant wind by the fast Wolf-Rayet wind in the $35\,M_\odot$ case produces remarkable morphological structures and emission signatures, which are compared with existing observations of the Wolf-Rayet bubble S308, whose central star has probably evolved in a manner very similar to the model star. My model reproduces the correct order of magnitude of observed X-ray luminosity, the temperature of the emitting plasma, and the limb brightening of the X-ray intensity profile. This is remarkable, because current analytical and numerical models of Wolf-Rayet bubbles fail to consistently explain these features. A key result is that almost the entire X-ray emission in this stage comes from the shell of red supergiant wind swept up by the shocked Wolf-Rayet wind rather than from the shocked Wolf-Rayet wind itself as hitherto assumed and modeled. This offers a possible solution to what is called the "missing wind problem" of Wolf-Rayet bubbles.

Chapter 1

Introduction

In addition to the stars, the interstellar medium (ISM), which consists of gas and dust, is the second important component of galaxies. There are a variety of interaction processes between these two components. The ISM loses thermal energy and cools by emission of electromagnetic radiation. If the cooling is efficient enough, it can lead to the formation of the coldest phase of the ISM, the molecular clouds, in whose gravitationally collapsing cores stars are newly formed. On the other hand, once the stars are born, they return energy and processed material back to the ISM by their radiation and their stellar winds.

Massive stars ($M_\star \gtrsim 10\,\mathrm{M}_\odot$) play an important role in the evolutionary history of galaxies. Although these stars are only short-lived, they are the primary source of metals and dominate the turbulent energy input into the ISM. The radiation field of a massive star first dissociates the ambient molecular gas and forms a so-called photodissociation region of neutral hydrogen. Subsequently, the Lyman continuum photons of the star ionize the HI gas and produce an HII region that expands into the neutral ambient medium. A fast stellar wind creates shocks that form a so-called stellar wind bubble (SWB) filled with hot plasma, which expands into the HII region. Finally, the star explodes as a supernova of Type II (SNII), creating a supernova remnant (SNR) that sweeps up the ambient medium. The SWBs and SNRs of neighboring stars can overlap and form a superbubble with a diameter of order 1 kpc.

This thesis pursues two major goals. The first one is to examine the combined influence of wind and ionizing radiation on the dynamical evolution of circumstellar matter around massive stars; i.e., we are particularly interested in the interaction processes between the photoionized HII region and the SWB that evolves into the ionized gas. The second goal is to improve our knowledge of the energy transfer efficiency between massive stars and the ISM: How and to what fraction is the energy of stellar radiation and the stellar wind converted into kinetic, thermal, and ionization energy of the ISM? How does the formation of the SWB influence the transfer of stellar radiation? To what extent does all this depend on the evolutionary state of the star?

To investigate these effects, I performed numerical two-dimensional radiation hydrodynamic simulations of the interaction between an isolated massive star and its surrounding ISM via stellar hydrogen-ionizing photons and a stellar wind. The calculations consider the hydrodynamical evolution of the circumstellar gas coupled with radiation transfer, time-dependent ionization of hydrogen, and a realistic description of cooling.

The stellar mass-loss rate, the terminal velocity of the wind, the effective temperature, and the luminosity of the star are specified as time-dependent boundary conditions. The evolution of the circumstellar material is examined starting from the main-sequence (MS) phase of the star until it explodes as a supernova. The SNR formation is not yet considered. In this thesis I present results of these calculations for two model stars with initial masses of $60\,M_\odot$ and $35\,M_\odot$, respectively, extending the work of García-Segura et al. (1996a, hereafter GML1) and García-Segura et al. (1996b, hereafter GLM2) to a more precise analysis of the energetic aspect during the whole evolution of the star.

The remainder of this thesis is structured as follows: Chapter 2 comprises a brief review of the theoretical concepts that have been developed over the past decades in order to understand the formation of HII regions and SWBs around massive stars, including a description of hydrodynamical instabilities that are important in the context of the SWB evolution. Furthermore, an overview is given about the most important results from observational studies of SWBs around massive stars for later comparison with my numerical results. I also show how analytical approximations can be derived for the estimation of the energy deposition in the ISM by HII regions and SWBs (also for comparison with the numerical results) and describe how these data are used for studies of the energization of the ISM in the solar neighborhood. This chapter is completed with a small survey that lists the characteristics of previously published numerical simulations of SWBs/HII regions.

Chapter 3 is entirely dedicated to the description of the physical equations and the numerical method used to solve the equations. The considered heating and cooling processes are explained in detail and the employed geometry is described along with the initial conditions and the set of stellar parameters used as time-dependent boundary conditions. The accuracy of the results is discussed at hand of several test calculations.

The results of my numerical model calculations are presented in chapter 4. The evolution of the circumstellar gas is described in detail and the morphological structures and emission signatures are discussed in the context of other numerical investigations and compared with recent observations. The results regarding the energy transfer into the ISM are presented and compared to the analytical approximations. To wind up this chapter, I discuss the changes of the results that are expected if the ambient medium is modified or if the stellar parameters differ from those used in the model calculations and outline the possible influence of physical processes that are not yet considered in the models.

Finally, I summarize my main results in chapter 5 and draw some conclusions from the work presented in this thesis.

Chapter 2

The Interstellar Medium

2.1 HII Regions

HII regions are observed in various sizes and shapes. Depending on their geometrical extent, they are labeled as ultracompact, compact, extended, or giant. The ultracompact (linear size $\lesssim 0.1\,\mathrm{pc}$) and partly also the compact (0.1–0.3 pc) HII regions are still deeply embedded in their birthplaces, mature molecular clouds, and as a result of dust obscuration generally only observable in the IR and radio wavelengths. On the other hand, extended HII regions with sizes up to several parsecs and giant HII regions that are composed of individual HII regions and have sizes of a few 100 pc are often easily discernible in the optical by their bright Balmer and forbidden metal lines. Large holes and shells make it obvious that the giant HII regions are powered by not only stellar radiation but also stellar winds and supernova explosions in the underlying OB star cluster (see, e.g., Yang et al. 1996).

Starting with the pioneering work of Strömgren (1939), the formation of these HII regions is thought to be fairly well understood at least for simple cases with constant stellar photon fluxes, simple circumstellar density profiles, and without the consideration of hydrodynamical instabilities. MS stars more massive than about $10\,\mathrm{M}_\odot$ with effective temperatures higher than 20000 K produce sufficient Lyman continuum photons to ionize and heat a considerable amount of circumstellar hydrogen. When such a star switches on its radiation, after a step of photodissociation, the surrounding gas becomes ionized starting from the surface of the star. The sharp transition between the photoionized and the neutral gas moves outward as a weak R-type ionization front, ionizes and heats the circumstellar gas but otherwise leaves it undisturbed. Assuming that the star is a point source at $r = 0$ in a pure hydrogen gas, the velocity of this ionization front can be calculated as (Spitzer 1978)

$$\dot{r}_\mathrm{i} = \min\left\{c, \frac{1}{4\pi n_\mathrm{H} r_\mathrm{i}^2}\left[S_\mathrm{u}(0) - \frac{4\pi}{3} r_\mathrm{i}^3 n_\mathrm{H}^2 \alpha_\mathrm{B}\right]\right\}, \tag{2.1}$$

where r_i is the radius of the ionization front, c is the speed of light, n_H is the hydrogen number density, $S_\mathrm{u}(r)$ is the number of Lyman continuum photons that pass through a sphere of radius r per unit time, and α_B is the coefficient for hydrogen recombinations

into levels 2 and higher. When the total rate of Lyman continuum photons emitted by the star just balances the total rate of recombinations in the ionized gas (except those directly into the ground state of H) the ionization front has attained an equilibrium state at the Strömgren radius

$$r_{\mathrm{S}} = \left(\frac{3 S_{\mathrm{u}}(0)}{4\pi n_{\mathrm{H}}^2 \alpha_{\mathrm{B}}} \right)^{\frac{1}{3}} . \tag{2.2}$$

When the ionization front approaches the Strömgren radius it slows down and evolves from weak R-type to strong-D and then weak D-type. This moment at time t_0 also characterizes the beginning of the expansion phase when a shock front forms ahead of the ionization front separated from it only by a geometrically thin shell of swept-up gas. The expansion of the heated gas lowers the density inside the HII region, which implies a lower recombination rate that allows excess photons to ionize additional gas. The radius of the ionization front can approximately be obtained by (Spitzer 1978)

$$r_{\mathrm{i}} = r_{\mathrm{S}} \left(1 + \frac{7 c_{\mathrm{s,II}} \, (t - t_0)}{4 r_{\mathrm{S}}} \right)^{\frac{4}{7}} , \tag{2.3}$$

with $c_{\mathrm{s,II}}$ being the isothermal sound speed of the ionized gas. In case that the ionizing source continues to supply photons for a sufficiently long time, the expansion will stall when pressure equilibrium between the rarefied warm gas in the HII region and the cold neutral surrounding gas is reached ($r_{\mathrm{i}} \approx 5\, r_{\mathrm{S}}$). If the ionizing source fades, the HII region enters the recombination phase. Although the evolution of the HII region in this phase strongly depends on the facts when and how the source runs out of ionizing photons, the global behavior will be dominated by a recession of the ionization front. The diluted gas recombines and cools. When the pressure of the former HII region drops below the pressure of the ambient medium, it will collapse (at least after the expanding gas has lost its momentum in outward direction) if no stellar wind or supernova explosion will give rise to additional acceleration. For detailed reviews on the evolution of HII regions we refer the reader to, e.g., Yorke (1986) and Franco et al. (1998).

2.2 Theory of Stellar Wind Bubbles

First considerations about the inner structure of SWBs go back to Pikel'ner (1968), Avedisova (1972), Dyson & de Vries (1972), and Dyson (1973), but the works of Castor et al. (1975) and Weaver et al. (1977) set a milestone in the approach of understanding SWBs. They presented a fairly complete picture of the structure and evolution of SWBs together with a set of equations that describes the evolution under the simplifying assumptions of a point source of a constant and spherically symmetric strong wind that interacts with a homogeneous ambient ISM. The global structure that arises from such a wind-ISM interaction is depicted in Figure 2.1 together with the expanding HII region into which the SWB evolves. It consists of a free-flowing supersonic wind that is heated to about $10^6 - 10^8$ K when it passes the inner reverse shock at r_{s1}. The pressure of this hot rarefied gas that normally fills most of the volume of the SWB is typically much higher than the pressure in the photoionized ambient medium. As a consequence, the

hot gas bubble expands into the HII region producing a forward shock at r_{s2} that sweeps up the gas from the HII region in a shell that is separated from the hot bubble interior by a contact discontinuity at r_c.

Three phases in the evolution of such a bubble can be distinguished. The first is the adiabatic phase that lasts until the shock speed v_{s2} drops below $200\,\mathrm{km\,s^{-1}}$ (Falle 1975), typically a few times 10 to a few times 10^3 yr, depending on the mechanical luminosity of the wind and the ambient density. The bubble is expanding so fast that radiative cooling does not play a significant role for the dynamical behavior. The second stage of evolution is characterized by strong cooling in the shell of swept-up material (between

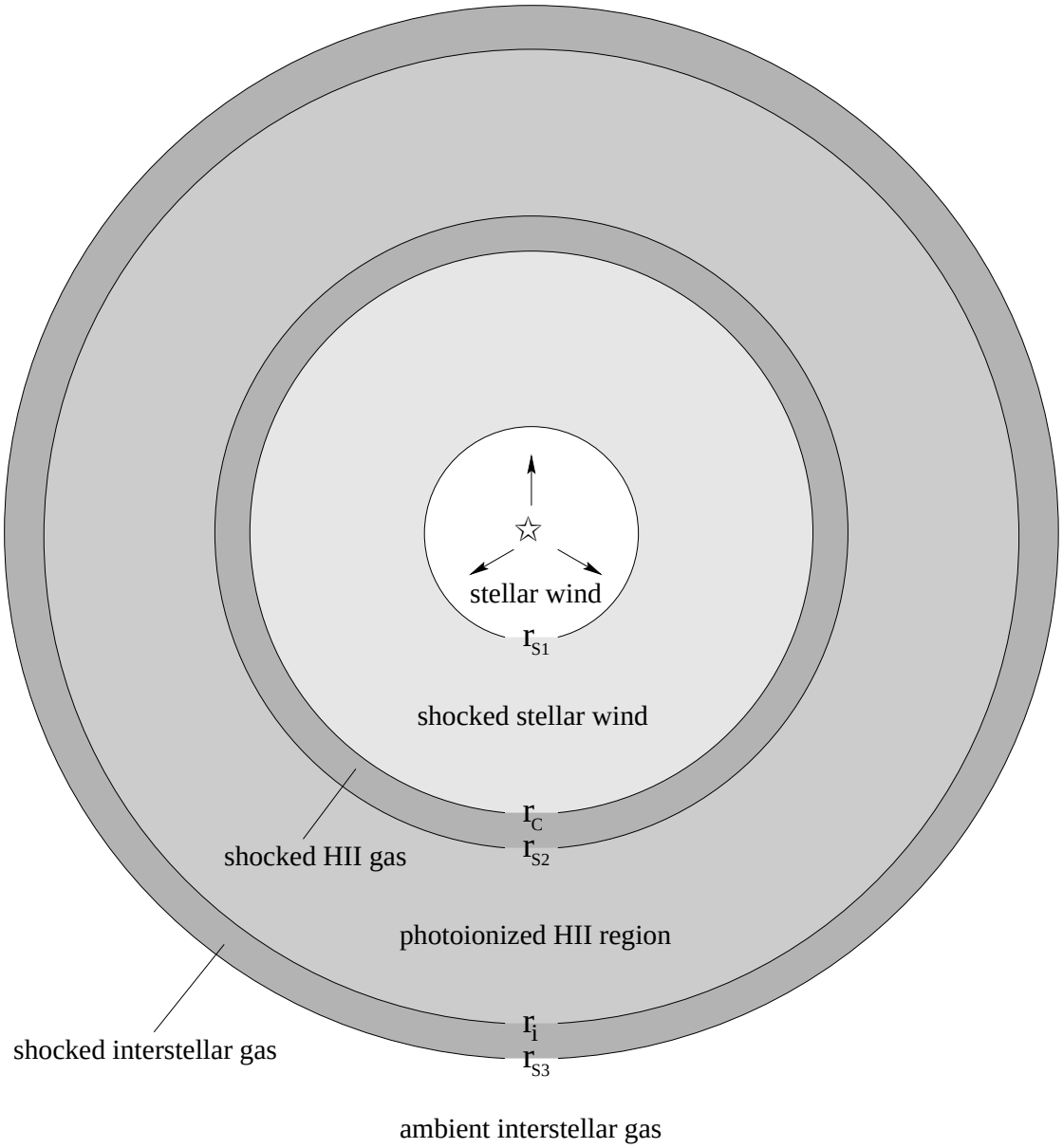

Figure 2.1: The schematic structure of an SWB: r_{s1} marks the position of the reverse shock, r_c the contact discontinuity, r_{s2} the forward shock of the stellar wind bubble, r_i the ionization front, and r_{s3} the forward shock of the HII region expansion.

r_c and r_{s2}), allowing it to be compressed into a geometrically thin ($r_c(t) = r_{s2}(t)$), dense shell, whereas for the hot bubble (between r_{s1} and r_c) cooling is still negligible. This phase lasts much longer than the first, so-called adiabatic phase. In the last phase cooling in the hot bubble also affects the evolution.

Under the assumptions made above, the evolution in the fully adiabatic first phase is determined by the density of the ambient medium (ρ_0) and the stellar wind luminosity $L_w = \frac{1}{2}\dot{M}_w v_w^2$, where $\dot{M}_w$ is the stellar mass-loss rate, and v_w the terminal velocity of the wind. Numerical integration of the equations of continuity, energy conservation, and motion for a spherically symmetric gas flow in the region of the swept-up HII gas between r_c and r_{s2} yields a self-similar solution for this region. Together with the additional assumption that the shocked stellar wind between r_{s1} and r_c is almost isobaric (the large sound speed connected with the high temperatures quickly smooths out pressure gradients) one can get a set of equations for the evolution of the stellar wind bubble in the fully adiabatic stage:

$$r_{s1}(t) = 0.74\,\dot{M}_w^{3/10}\,v_w^{1/10}\,\rho_0^{-3/10}\,t^{2/5}\ , \tag{2.4}$$

$$r_{s2}(t) = 0.88\,L_w^{1/5}\,\rho_0^{-1/5}\,t^{3/5}\ , \tag{2.5}$$

$$r_c(t) = 0.76\,L_w^{1/5}\,\rho_0^{-1/5}\,t^{3/5} = 0.86\,r_{s2}(t)\ . \tag{2.6}$$

The velocities of the fronts can simply be obtained as derivatives of the equations for the radii:

$$v_{s1}(t) = 0.30\,\dot{M}_w^{3/10}\,v_w^{1/10}\,\rho_0^{-3/10}\,t^{-3/5}\ , \tag{2.7}$$

$$v_{s2}(t) = 0.53\,L_w^{1/5}\,\rho_0^{-1/5}\,t^{-2/5}\ , \tag{2.8}$$

$$v_c(t) = 0.45\,L_w^{1/5}\,\rho_0^{-1/5}\,t^{-2/5} = 0.86\,v_{s2}(t)\ . \tag{2.9}$$

The free-flowing wind within r_{s1} is supposed to be pressureless with constant velocity and density proportional to r^{-2}. For the shocked stellar wind ($r_{s1} \le r \le r_c$), one gets

$$\rho(r,t) = \frac{0.628\,\dot{M}_w^{2/5}\,v_w^{-6/5}\,\rho_0^{3/5}\,t^{-4/5}}{\left(1-\frac{r^3}{r_c^3(t)}\right)^{8/33}} \tag{2.10}$$

$$= \frac{0.628\,\dot{M}_w^{2/5}\,v_w^{-6/5}\,\rho_0^{3/5}\,t^{-4/5}}{\left(1-2.3\,L_w^{-3/5}\,\rho_0^{3/5}\,r^3\,t^{-9/5}\right)^{8/33}}\ ,$$

$$v(r,t) = \frac{11}{25}r_c^3\,r^{-2}\,t^{-1} + \frac{4}{25}\,r\,t^{-1} \tag{2.11}$$

$$= 0.19\,L_w^{3/5}\,\rho_0^{-3/5}\,r^{-2}\,t^{4/5} + \frac{4}{25}\,r\,t^{-1}\ . \tag{2.12}$$

For the pressure in the range ($r_{s1} \ll r \le r_c$), there is

$$P(t) = 0.17\,L_w^{2/5}\,\rho_0^{3/5}\,t^{-4/5}\ , \tag{2.13}$$

which is less than 20% higher than the pressure directly behind the inner shock front obtained from the Rankine-Hugoniot jump conditions. This is not surprising, because the

approximation was used that the shocked stellar wind is almost isobaric. The numerical integration for the shell of swept-up gas between r_c and r_{s2} shows that velocity and pressure vary by less than 25% across the shell while the density strongly drops from r_{s2} to r_c (see Fig. 2.2).

The collapse of the region of swept-up gas between r_c and r_{s2} into a geometrically thin, dense shell due to radiative cooling marks the transition to the second phase of SWB evolution. Radiative cooling is still negligible for the hot bubble (between r_{s1} and r_c). This phase lasts much longer than the completely adiabatic first phase. Thermal conduction from the hot bubble interior to the collapsed shell becomes important and it modifies the structure of the bubble in this stage. Weaver et al. (1977) assume that an equilibrium between the conductive energy flux and a mechanical energy flux due to evaporation of shell mass in the reverse direction is established. Under the assumptions that the hot bubble between r_{s1} and $r_c = r_{s2}$ is isobaric and that the thermal energy contained within this region is much higher than the kinetic energy, Weaver et al. (1977)

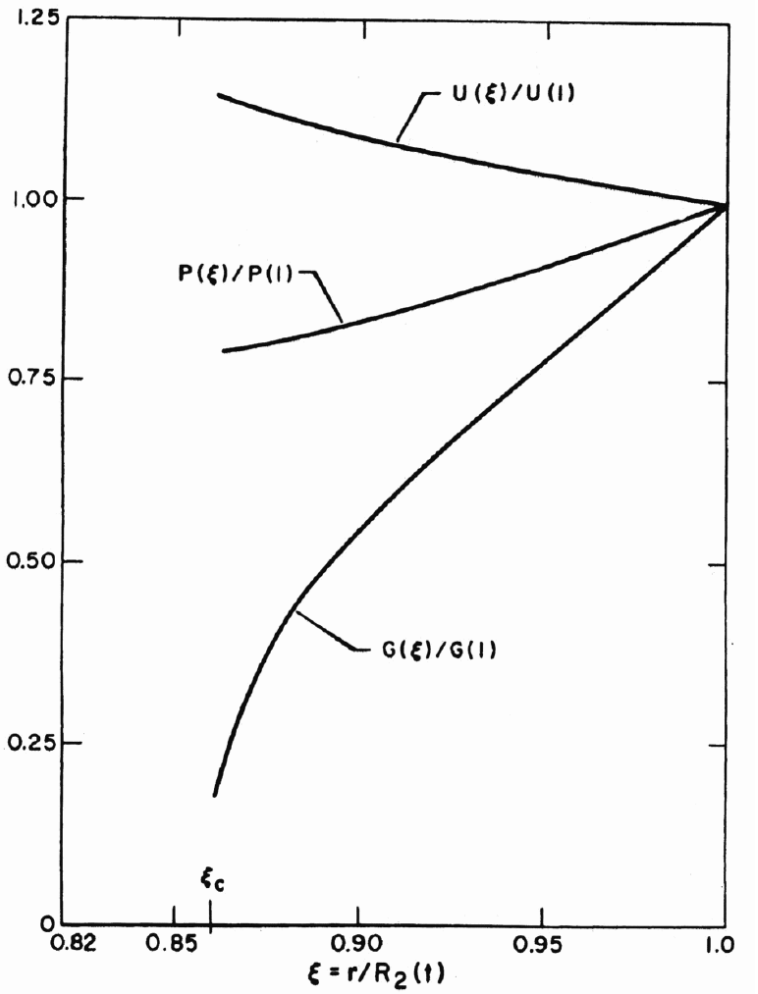

Figure 2.2: The similarity variables for velocity $U(\xi)$, pressure $P(\xi)$, and density $G(\xi)$ in the shell of the swept-up HII region for the adiabatic solution of phase 1. ξ_c denotes the position of the contact surface. The figure is taken from Weaver et al. (1977).

derived the following equations for the description of the bubble evolution in this stage:

$$r_{\rm s1}(t) = \frac{275^{1/5}}{(28\pi)^{3/10}}\,\dot{M}_{\rm w}^{3/10}\,v_{\rm w}^{1/10}\,\rho_0^{-3/10}\,t^{2/5}\ , \tag{2.14}$$

$$r_{\rm s2}(t) = r_{\rm c}(t) = \left(\frac{125}{154\pi}\right)^{1/5}\,L_{\rm w}^{1/5}\,\rho_0^{-1/5}\,t^{3/5}\ , \tag{2.15}$$

with the corresponding velocities

$$v_{\rm s1}(t) = \frac{8800^{1/5}}{5\,(28\pi)^{3/10}}\,\dot{M}_{\rm w}^{3/10}\,v_{\rm w}^{1/10}\,\rho_0^{-3/10}\,t^{-3/5}\ , \tag{2.16}$$

$$v_{\rm s2}(t) = v_{\rm c}(t) = \left(\frac{243}{3850\pi}\right)^{1/5}\,L_{\rm w}^{1/5}\,\rho_0^{-1/5}\,t^{-2/5}\ , \tag{2.17}$$

and for the hot bubble

$$P(t) = \frac{7}{(3850\pi)^{2/5}}\,L_{\rm w}^{2/5}\,\rho_0^{3/5}\,t^{-4/5}\ , \tag{2.18}$$

$$T(r,t) = T_b(t)\left(1-\frac{r}{r_{\rm s2}(t)}\right)^{2/5}\ , \tag{2.19}$$

$$\rho(r,t) = \rho_b(t)\left(1-\frac{r}{r_{\rm s2}(t)}\right)^{-2/5}\ , \tag{2.20}$$

with

$$T_b(t) = \frac{7^{2/7}\,5^{4/35}}{(154\pi)^{8/35}}\,C^{-2/7}\,L_{\rm w}^{8/35}\,\rho_0^{2/35}\,t^{-6/35}\ , \tag{2.21}$$

$$\rho_b(t) = \frac{7^{5/7}\,(154\pi)^{8/35}\,\mu\,m_{\rm H}\,C^{2/7}\,L_{\rm w}^{6/35}\,\rho_0^{19/35}}{5^{4/35}\,(3850\pi)^{2/5}\,k_{\rm B}\,t^{22/35}}\ , \tag{2.22}$$

where $k_{\rm B}$ is the Boltzmann constant, μ the mean molecular weight of the gas, $m_{\rm H}$ the mass of a hydrogen atom, and C the coefficient for the thermal conduction flux (Spitzer 1962)

$$F_c = -CT^{5/2}\frac{\partial T}{\partial r}\ . \tag{2.23}$$

C itself does weekly depend on T, which is neglected here.

The detailed structure of the inner shock front at $r_{\rm s1}$ is poorly understood. As Weaver et al. (1977) pointed out, it is necessary for the derivation of the formulae shown above that the shock front at $r_{\rm s1}$ has negligible thickness. The stopping distance of electrons for "typical" conditions at $r_{\rm s1}$ ($T = 10^6\,{\rm K}, n_{\rm H} = 10^{-2}\,{\rm cm}^{-3}$) is $7.5\times10^{14}\,{\rm cm}$, but in reality the shock is supposed to be of collisionless type, most probable a turbulent electrostatic shock if magnetic fields are absent. In this case two-particle interactions play only a minor role and the shock thickness is of the order $10^9\,{\rm cm}$. This is much shorter than $r_{\rm s1}$, which is typically a few pc.

Cooling in the hot bubble (the third stage of bubble evolution according to Weaver et al. 1977) has not yet been considered. Weaver et al. (1977) make some estimates when and how cooling changes the evolution of the bubble, but the effect of cooling was much more rigorously treated by Koo & McKee (1992a,b). They also distinguish fast stellar winds (the only case discussed by Weaver et al. 1977) and slow stellar winds. In the latter case, cooling may be important for the whole evolution. But in the case of fast stellar winds (e.g., bubbles blown by OB stars as they are examined in this work) the approximation that cooling in the hot bubble is unimportant still holds until there is additional mass injection into the bubble. Koo & McKee (1992a,b) also consider a power-law time dependence of the energy injection (with constant wind velocity) and a power-law profile for the distribution of the ambient gas.

First investigations of stellar wind evolution into an ambient medium with a density gradient have been made by Dyson (1977). The evolution of bubbles in aspherical density profiles has been examined by García-Segura & Mac Low (1995a). This scenario should be appropriate for a Wolf-Rayet (W-R) star that ejects its strong wind into the material that was previously blown off as red supergiant (RSG) wind. The RSG wind itself can be aspherical if it is intrinsically denser at the equator or if the RSG is a member of a binary system. The authors show that these angular density gradients in the RSG wind can explain the observed asphericity of some bubbles around W-R stars.

Although the analytical and semi-analytical solutions for the evolution of SWBs have been improved in recent years (Koo & McKee 1992a,b; García-Segura & Mac Low 1995a; Pittard et al. 2001a,b), a variety of physical effects remain to be included in order to achieve a better agreement of models and observations. For example, the discrepancy between models and observations with regard to the evolution of the hot phase in bubbles has recently been reviewed by Mac Low (2000). See also Chu (2000). It has become evident that the stellar parameters such as the mass-loss rate, the terminal wind velocity, the effective temperature and the luminosity of the star, which drive the evolution of the circumstellar matter, vary strongly over time. Because most previous studies dealt with the evolution of either HII regions or SWBs, little is known about the interaction of these two structures.

2.3 Instabilities

Another effect that can neither be followed analytically nor with the help of one-dimensional numerical models is the development of gas dynamical instabilities, like, e.g., Rayleigh-Taylor instabilities. In case of the SWB shell described above, it can easily be seen from equation 2.17 that the contact discontinuity between the shell of swept-up gas and the hot bubble is already decelerated in phase 2 of the SWB evolution. This means that effective gravity points from the hot, rarefied bubble to the dense shell and the structure is Rayleigh-Taylor stable. A closer examination (García-Segura & Mac Low 1995a) shows that in the case of an ambient density gradient the shell of swept-up material remains decelerated (and, therefore, Rayleigh-Taylor stable) in phase 2 unless

the exponent β in a power-law density profile

$$\rho(r) = \rho_0 \left(\frac{r}{r_0}\right)^{-\beta} \tag{2.24}$$

exceeds 2.

Contrary to Rayleigh-Taylor, another instability (or, more precisely, overstability) is supposed to work in the case of bubble evolution into a homogeneous ambient medium. It is the so-called thin-shell (or Vishniac) overstability (Vishniac 1983; Ryu & Vishniac 1987, 1988; Vishniac & Ryu 1989; Vishniac 1994). The fundamental mechanism is nicely described in Mac Low & Norman (1993) and can easily be explained on the basis of Fig. 2.3: The shell of swept-up material is confined by the forces that act on either side of it, the ram pressure of the swept-up material on the front and the thermal pressure of the hot gas on the back side. The thermal pressure always acts normally to the local shell surface because the sound speed in the hot gas is much higher than the expansion velocity of the shell. The ram pressure on the other side is always anti-parallel to the

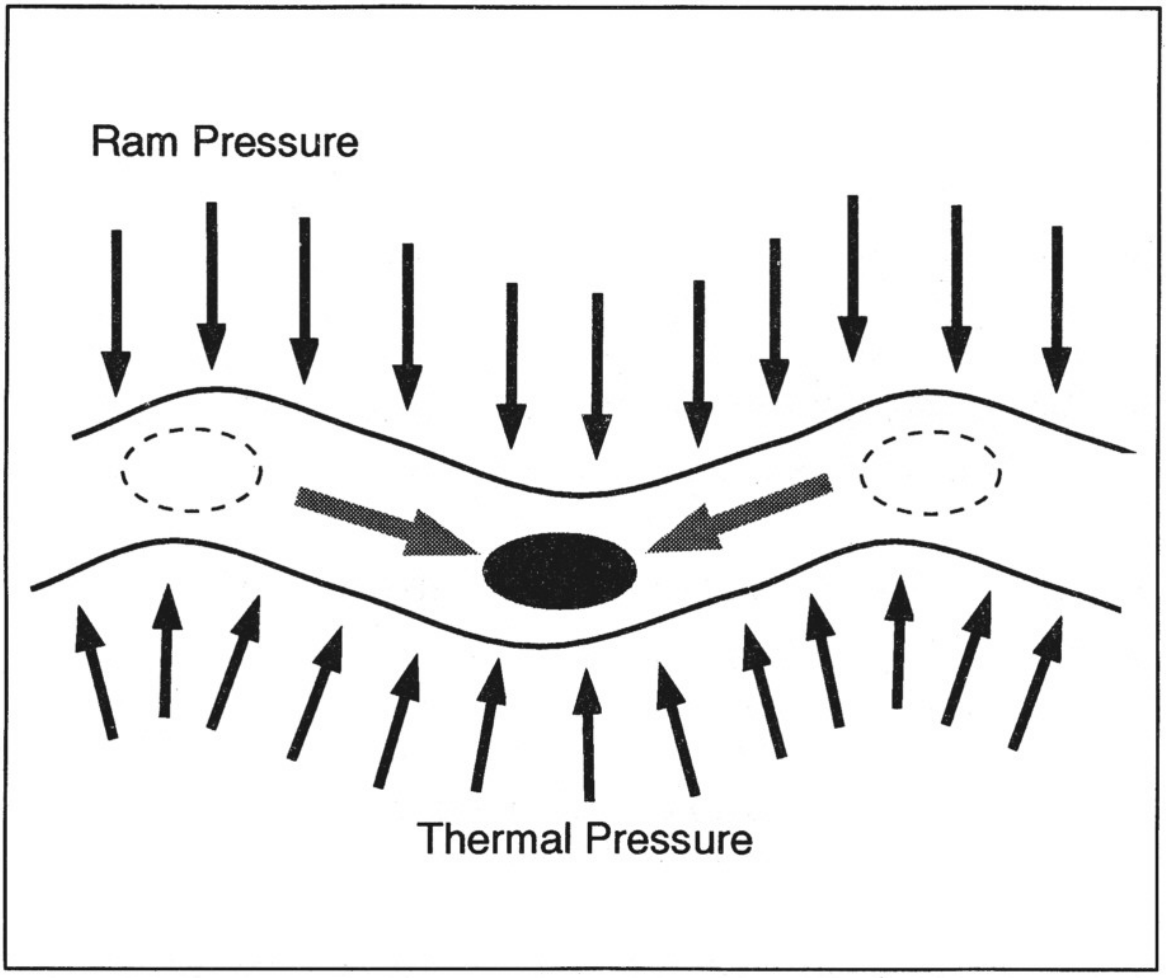

Figure 2.3: Principle of the thin-shell overstability. The figure is taken from Mac Low & Norman (1993).

direction of shell propagation since the velocity of the shell is supersonic with respect to the ambient medium. As long as the shell remains exactly spherical, the thermal and ram pressure are both perpendicular to the shell surface. But in case of a slight distortion of the shell, the thermal pressure is no longer parallel to the direction of shell propagation and the vector sum of both, thermal and ram pressure, has a component parallel to the shell surface. As a result, this drives transverse mass flows from the leading "peaks" to the trailing "valleys" (by analogy). This mass flow enhances the surface density in the "valleys" and reduces it in the "peaks". Because of their larger momentum density, the "valleys" are less decelerated by the ram pressure than the "peaks", so that after some time the former "valleys" move ahead. Now the transverse mass flows in the shell are reversed, mass is accumulated in the "valleys" (the former "peaks") and so an oscillation develops. A linear stability analysis (Vishniac 1983) showed that the amplitude grows with each cycle if the shell is thin enough. It turns out that isothermal wind-driven shocks are overstable if the density contrast across the outer shock front exceeds ≈ 25. Therefore, they are more stable (against the thin-shell overstability) than isothermal blast waves resulting from point-like explosions (e.g., Supernovae), which have a critical density contrast of ≈ 10 (Vishniac & Ryu 1989).

This overstability has also been observed in laboratory plasmas. Grun et al. (1991) induced a point-like explosion in a test chamber filled with xenon gas. The explosion was ignited by irradiating a polystyrene foil with a nanosecond pulse from a high-energy laser. They observed that the growth of the overstability with time follows a power-law, which is in agreement with the theoretical prediction by Vishniac (1983) except for the different exponent. But the growth ceased at late times. No overstabilities were observed with the same instrumental setup when nitrogen was used instead of xenon. This is also in agreement with theory, which predicts overstability for an effective adiabatic index $\gamma < 1.2$, because nitrogen has $\gamma = 1.4$ while xenon has $\gamma = 1.06$ due to radiative cooling.

Mac Low & Norman (1993) have quantitatively confirmed the predictions of Vishniac (1983) and Ryu & Vishniac (1987) for the growth of the overstability in the linear regime using two-dimensional hydrodynamical calculations. They also confirmed the saturation of the overstability that was seen in the laboratory plasma experiments and explained that this happens when transverse shocks form in the shell. The shell is not fragmented by the overstability but density enhancements of more than a factor of two are produced.

However, fragmentation of the shell may occur if an additional ionization front comes into play as has first been studied by Giuliani (1979) and has been shown in numerical calculations by García-Segura & Franco (1996). The density enhancements in the thin shell of the expanding HII region are initially produced by the action of the thin-shell overstability. The optical depth is increased along the lines of sight from the star through the density enhancements and reduced for the lines of sight that pass through the shell at the "peaks" where the density is lowered. Thus, the radiation can easier propagate outwards through the "peaks" than through the "valleys". This steepens the angle between the direction of shell propagation and the normal vector of the shell surface between the "peaks" and the "valleys". Therefore, the pressure imbalance is increased which forces additional mass flux into the "valleys" (see Fig. 2.4). Under the influence of the ionization front the overstability has turned into instability, which becomes catastrophic if the density slope of the ambient medium is decreasing.

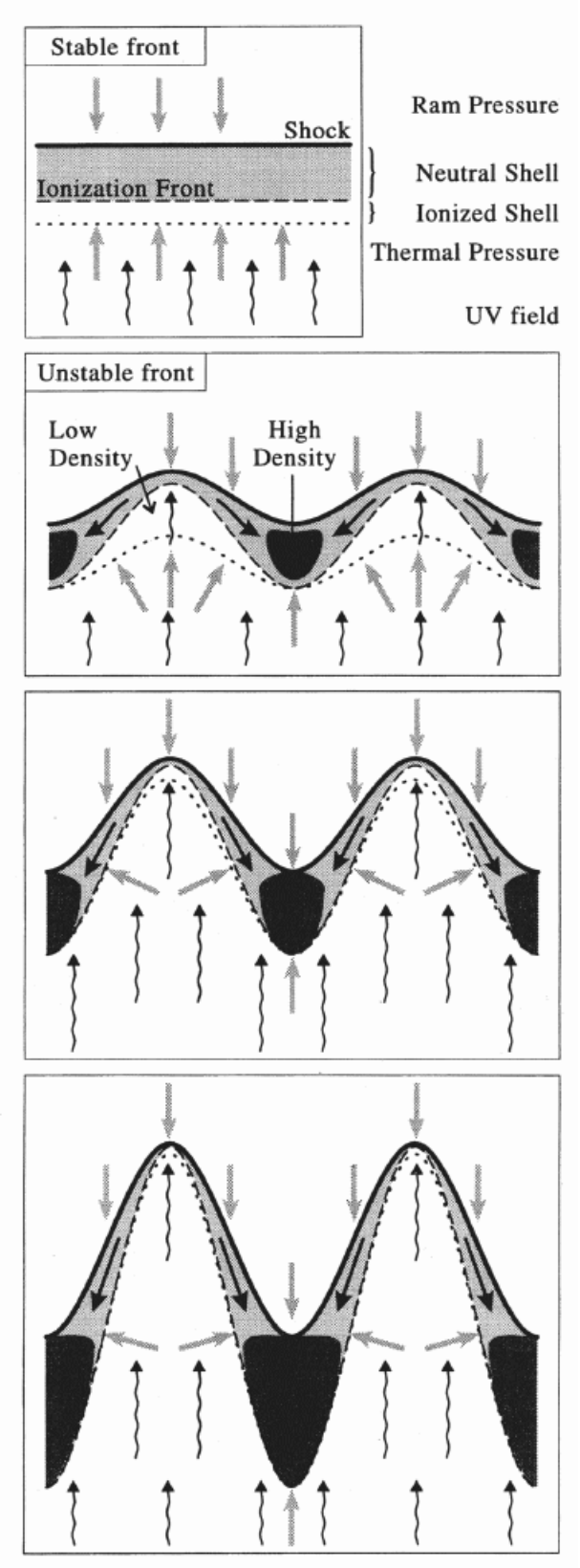

Figure 2.4: Principle of the ionization front instability according to Giuliani (1979). The figure is taken from García-Segura & Franco (1996).

2.4 Observations of Stellar Wind Bubbles

From the theoretical point of view, each star that has a supersonic wind with a sufficiently high mass-loss rate should be capable of blowing an SWB into the ISM. The crucial indicator for the existence of such SWBs is the hot gas produced at the reverse shock. The X-ray emission of the hot ($10^6 - 10^8$ K) gas should be detectable if the surface brightness is high enough for the respective telescope in use. Although theory predicts that even massive stars on the MS are supposed to produce SWBs, they are expected to be large and diffuse with a low surface brightness in X-rays. The vicinities of W-R stars seem to be promising candidates for the observation of SWBs (also called W-R bubbles if the central star is in its W-R stage). Therefore, section 2.5 is entirely dedicated to the observations of W-R bubbles and this section is continued with a brief summary of observations of other SWBs.

2.4.1 Main-Sequence Bubbles

The shells of MS bubbles are also difficult to observe in the optical because they are large and dim (McKee et al. 1984). Nevertheless, shells around MS stars, as well as shells around evolved massive stars (which, based on their radius, expansion velocities, and shell mass, are considered to originate from the MS phase of these stars), have been observed in the optical and IR. Lozinskaya (1982) listed a sample of 28 Of stars with declinations higher than $-43°$, most of them are members of clusters or associations. This sample is thought to be complete in the sense that the environments of all these stars have been surveyed and $m_v - A_v \leq 6$ mag with $A_v \leq 2.5$ mag; i.e., all Of stars within a certain distance to the Sun are in this list, and HII regions associated with the Of stars should also be detectable on the red plates of the *Palomar Sky Atlas*. From this sample of 28 stars, 23 actually have associated HII regions and from these, 11 have a ring-like morphology. The author used the nebula classification scheme introduced by Chu (1981) for W-R-nebulae also for her sample: 50 % of the nebulae around Of stars belong to the group of so-called amorphous HII regions. These often have additional sources of ionization besides the Of star and are supposed to be the classical HII regions. The strong winds of the Of stars may be responsible for the observed supersonic motions in the HII regions. The second group, ring-like HII regions, are also often excited by other early-type stars together with the Of star that provides most of the stellar wind. The ring-like HII regions have radii from 10 to 75 pc. In contrast, SWBs (group 3) are much smaller ($r \approx 1.5 - 15$ pc) and concentrated around single Of stars. This is the classical type of a ring-shaped nebula around a point-like source of strong stellar wind. The fourth class of objets is stellar ejecta. These nebulae are only short-lived.

Oey & Massey (1994) detected two large bubbles in Hα with radii of 66 pc around individual O9 III and O9 I stars in M33. These are distinguished objects as the bubble shells have noticeable spherical shape. Because these bubbles are located in a fairly undisturbed environment 6.6 and 6.9 kpc away from the nucleus of M33 (on the basis of a distance to M33 of 0.84 Mpc) they are pretty good candidates for MS bubbles evolving into a homogeneous medium. The authors compared their observations with analytical

models assuming a power-law wind luminosity profile. They found that good agreement can be obtained between the observation of the nebula around the O9 I star and a model of a 40 $M_\odot$ star in a 0.3 cm^{-3} homogeneous ambient medium, except that the calculated emission measure is too low. The consistency between the observations of the nebula around the O9 III star and the corresponding model is worse because the predicted shell size is too small and the emission measure of the shell is also too low compared with the observed value.

Marston (1996) compiled *Infrared Astronomical Satellite (IRAS)* Skyflux images of the environments of 156 Galactic W-R stars from the van der Hucht et al. (1981) catalog. 49 of them show probable or suspected large shells with diameters $> 20'$. Most of these shells consist of cold, neutral gas (14 of them had already been observed as slowly expanding HI bubbles), but for 8 % of all W-R stars in a southern Galactic survey extended shells can also be identified optically (Marston 1997). These large shells often have smaller shells or bubbles in their interior and together they are supposed to indicate the different mass-loss stages of massive stars. The smaller shells show the interaction of the fast W-R wind with the ejecta of one (or more) previous phases of violent mass loss, namely RSG or luminous blue variable (LBV) phases. The large exterior shells are thought to consist of ambient interstellar medium swept up by the MS bubble during the O star progenitor phase of the W-R stars. Alternative formation scenarios (at least for the large shells around WR 6, WR 40, and WR 136) have been proposed by Nichols & Fesen (1994). They surveyed *International Ultraviolet Explorer (IUE)* spectra of W-R stars for high-velocity UV absorption features (separated from the main component by at least 45 $km\,s^{-1}$) and attributed these features (at least in two cases) to the large *IRAS* shells. They claim that binary W-R stars could be responsible for the formation of a large shell, either by a supernova explosion of the binary companion (WR 136), or by mass ejection due to a Roche Lobe overflow from the W-R star progenitor onto a compact companion (WR 6, WR 40). But Marston (1996) concludes that it is unlikely that either of these alternative formation mechanisms produces many of the large shells observed with *IRAS*. 50 % of the W-R stars without observed high-velocity UV absorption features have large shells observed with *IRAS*. Therefore, contrary to the suggestion of Nichols & Fesen (1994), there seems to be no connection between the high-velocity features and the large *IRAS* shells.

Additional evidence comes from the measurement of the shell expansion velocities of the 14 large *IRAS* shells that have also been observed in the HI 21 cm line: they are expanding at 22 $km\,s^{-1}$ or slower (Marston 1995, and references therein), which is much less than the velocity of the UV absorption features. Finally, there is also no known pulsar within a large *IRAS* shell around a W-R star (Arnal & Mirabel (1991) observed an HI shell that surrounds WR 125 and a pulsar). Marston (1996) also claims that the strong increase of the detection rate for the large *IRAS* shells with Galactic latitude can be explained by confusion with other sources in the Galactic plane and by the fact that the average diameter of the large *IRAS* shells grows with Galactic height $|z|$ (i.e., with decreasing local density). Therefore, the probability that the smaller shells in the Galactic midplane could have been detected by *IRAS* as extended objects is smaller. It is interesting to note that the detection rate of large shells in the Hα CCD survey of Marston (1997) is roughly the same for low and high latitudes.

Closer examinations of the surroundings of individual massive stars in the HI 21 cm line have been performed by, e.g., Cappa et al. (1996) for WR 149 and by Cappa & Benaglia (1998) and Benaglia & Cappa (1999) for a bunch of Of stars. The large bubbles have radii of typically several tens of parsecs, swept-up HI masses of several thousand solar masses and expansion velocities between 7 and 15 $\mathrm{km\,s^{-1}}$. The derived dynamical ages of the bubbles are therefore several million years. All these findings are roughly in agreement with the simple model of a bubble that is blown into the ISM during the MS phase of an O star that will later become a W-R star.

2.4.2 A Young Bubble in the Orion Molecular Cloud

The MS shells are typical results of the interaction of massive stars with their surrounding ISM over a time period of a few megayears. There are also young objects that have influenced their interstellar environment so strongly that they can already be identified as star-gas interactions. One example that should certainly be mentioned here is the so-called Becklin-Neugebauer-Kleinman-Low (BN-KL) nebula in the Orion molecular cloud 1 (OMC-1) behind the Orion nebula. It shows a spectacular, finger-like outflow of molecular hydrogen (Taylor et al. 1984; Allen & Burton 1993; McCaughrean & Mac Low 1997; Salas et al. 1999). As a result of extremely high visual extinction ($A_\mathrm{V} \approx 20 - 50\,\mathrm{mag}$), it can only be observed in the infrared, for example in the [FeII] $a^4F_{5/2} - a^4D_{7/2}$ emission line at 1.64 μm or the $v = 1$–0 S(1) line of molecular hydrogen at 2.12 μm, or at even longer wavelengths.

Most models for the gas outflow proposed so far assume that it is driven by mass ejection from a young star, namely, IRc2 and/or the Becklin-Neugebauer (BN) object, which are both very close to the projected center of the mass outflow. IRc2 has a mass-loss rate $\dot{M}_\mathrm{w} \approx 10^{-3}$ to $10^{-4}\,\mathrm{M_\odot\,yr^{-1}}$ (Downes et al. 1981) and a luminosity $L_\mathrm{phot} \approx (2 - 10) \times 10^4\,\mathrm{L_\odot}$ (Genzel & Stutzki 1989). The mass-loss rate and luminosity of BN are $\dot{M}_\mathrm{w} \approx 4 \times 10^{-7}\,\mathrm{M_\odot\,yr^{-1}}$ and $L_\mathrm{phot} \approx (1 - 2) \times 10^4\,\mathrm{L_\odot}$ (Scoville et al. 1983).

Allen & Burton (1993) proposed an explosive event like a scaled-up FU Orionis-type eruption (strong luminosity increase due to accretion disk instabilities) or a supernova deeply embedded in a molecular cloud to be the cause of the ejection of "bullets" into the surrounding molecular cloud. This might be consistent with the observation of [FeII] emission as a tracer of shocks with speeds of a few hundred $\mathrm{km\,s^{-1}}$ coming mostly from the tips of the finger-like structures. In this case the H_2 emission is produced by slower or oblique shocks because H_2 is dissociated at shock velocities above $24 - 45\,\mathrm{km\,s^{-1}}$, depending on the importance of magnetic fields (Kwan 1977; Draine et al. 1983). The problem with this model is that it seems to be difficult to eject a number of molecular gas clumps from one source almost simultaneously over a wide angle and that the bullet structures remain coherent over long distances within the molecular cloud.

Salas et al. (1999) assume that a $230\,\mathrm{km\,s^{-1}}$ fast wind of IRc2 interacts with a bunch of molecular clumps with a density of $\approx 5.6 \times 10^5\,\mathrm{cm^{-3}}$. The H_2 emission is then produced by slow J-type shocks with approximately $20\,\mathrm{km\,s^{-1}}$ in the clumps. Individual clumps have masses of a few times $10^{-3}\,\mathrm{M_\odot}$ accounting for a total clump mass of $15\,\mathrm{M_\odot}$ within a radius of 0.1 pc. The approach of Stone et al. (1995) to explain the finger-like outflow is quite different. They do not need the clumpy structure of the circumstellar medium. In

their model the fingers appear as hydrodynamical instabilities in a thin, dense shell of gas swept up by a strong, spherical wind of a massive young star. They assume that there is a strong increase of the wind velocity at a certain time, re-accelerating the thin shell so that it becomes Rayleigh-Taylor unstable and fragments, producing bow-shocks and trailing wakes similar to the observed structures. Additionally, the model predicted clumpy shell fragments at the base of the fingers. This feature has also been observationally confirmed by McCaughrean & Mac Low (1997).

For some numerical reason, Stone et al. (1995) used a sound speed of $20\,\mathrm{km\,s^{-1}}$ for the ambient medium. That led to a rapid deceleration of the bullets. Hence, they had to introduce a density gradient in the ambient medium to account for the observed velocities. McCaughrean & Mac Low (1997) slightly modified the Stone et al. (1995) model. They showed that a sound speed in the ambient medium that is lower (and, therefore, more reasonable for a cold molecular cloud) also abolishes the necessity of a density gradient (i.e., the density gradient may be present but it is not absolutely necessary from the model). Another problem of the Stone et al. (1995) model is that there is little observational evidence for the strong time variability of the winds from young massive stars on the required scales. McCaughrean & Mac Low (1997) also overcome this difficulty by assuming that the bubble is powered by two or even more stars, which have slightly different stages of evolution. The older stars sweep up the original shell. The strong increase in wind luminosity needed to reaccelerate the shell then happens by ignition of a new star that drives a wind with a much higher mechanical luminosity.

2.4.3 The Eagle Nebula

Another fairly well studied region where formation of stars and their interaction with the ambient medium take place in an early phase is the Eagle Nebula (M16). Imaging with the WFPC2 on board the *Hubble Space Telescope (HST)* by Hester et al. (1996) and observations in the infrared with ISOCAM (Pilbratt et al. 1998) and NIRSPEC (Levenson et al. 2000) reveal a number of interesting insights into the structure and possible formation history of this active region. The picture of M16 in the optical is dominated by the appearance of the so-called elephant trunks, impressive pillars of dense molecular gas protruding into the HII region. Their surface is partly illuminated by the ionizing light of nearby (distance to the pillars $\approx 2\,\mathrm{pc}$) massive stars so that photoevaporative flows from the surface can be identified on the well-resolved pictures (Hester et al. 1996) as striations extending normally from the surface of the cloud. [SII] as a tracer of the low-ionization zone is strongly limited to sharp zones at the illuminated edges of the molecular trunks. [OIII] emission is much more widespread around the trunks and the transition at the surface is much less pronounced. The distribution of Hα emission is somehow intermediate between [SII] and [OIII] emission. The widespread emission is also visible in Hα as well as the bright rim at the cloud surface, but the rim is wider and less pronounced than in [SII]. These findings support the view of the region as a photoevaporative flow of gas from the illuminated surface of the molecular trunks into the HII region. The flow is driven by the pressure gradient that arises when the ultraviolet photons from the massive star heat the dense gas at the surface of the trunk to a few thousand Kelvin, resulting in a pressure that is higher than in the rest of the (lower density) HII region.

Another interesting feature in M16 is a number of cometary globules with radii up to more than 1000 AU at or close to the surface of the elephant trunks. These globules are supposed to represent density enhancements within the clumpy molecular clouds, which are photoevaporated more slowly than the rest of the cloud and, therefore, protrude from the surface of the trunks. A lot of these globules have neck-like gaseous connections to the trunks in the opposite direction away from the sources of the ionizing photons ("cometary"). In this case, the globules are supposed to cast shadows that prevent the gaseous necks also from evaporation (at least for some time). The fact that only a few of these globules are completely separated from the molecular trunks indicates that their lifetime is fairly short, roughly 10^4 yr after they have been revealed from the parent cloud. Following classical models, one could imagine that these density enhancements within the molecular cloud are the sites of star formation. And indeed, comparing their optical images with K-band images, Hester et al. (1996) found that several globules seem to be associated with young stellar objects (YSOs). Some stars that seem to be associated with globules can already be seen optically on the WFPC2 images. Contrary to the results of Hester et al. (1996), Pilbratt et al. (1998) found no general correlation between discrete IR sources and the globules. They saw evidence for only a low level of ongoing low-mass star formation.

The picture described above raises important questions related to the process of star formation: How important is radiatively driven implosion (Bertoldi 1989) for the transition of dense clumps to protostellar objects? Has photoevaporation limited the mass of protostellar objects or had the cloud cores already stopped accretion before they were exposed to the ionizing radiation? Or has the photoevaporation inhibited the formation of stars in some globules at all? A census in NGC 6611, the host cluster of the Eagle Nebula, showed a large number (several hundred) of intermediate-mass ($3 < M/\mathrm{M}_\odot < 8$) pre-main-sequence stars with ages ranging from 0.25 Myr to at least 1 Myr, generally younger than the massive stars (age 2 ± 1 Myr) that are responsible for the ionization of the Eagle Nebula (Hillenbrand et al. 1993).

An interesting question arises in connection with M16: is the elephant trunk structure a remnant of the original molecular cloud from which the young stars in the region were formed, or has this structure actively been molded by the massive stars as a shell swept up by stellar winds and folded by hydrodynamical instabilities? More detailed observations and better theoretical models are needed to answer this question.

2.5 Observations of Wolf-Rayet Bubbles

Although they are supposed to be good candidates for SWBs, only 1/4 to 1/3 of the known Galactic W-R stars seem to have associated ring nebulae, and only 10 are wind-driven bubbles (Wrigge 1999), according to the optically derived kinematics of the shell (Chu 1981). Up to now only 2 of these SWB candidates have actually been detected in X-rays: NGC 6888 (Bochkarev 1988; Wrigge et al. 1994) and S308 (Wrigge 1999; Chu et al. 2003). Since both central W-R stars are thought to have undergone the MS $\rightarrow$ RSG $\rightarrow$ W-R evolution that we are investigating in this thesis (the $35\,\mathrm{M}_\odot$ case), we briefly review the recent observational work for a careful comparison with our numerical results.

2.5.1 NGC 6888

NGC 6888 was among the first Galactic ring nebulae whose formation have been attributed to mass ejection and radiation from a W-R star (Johnson & Hogg 1965). Its relative proximity and thus large angular size ($18' \times 12'$) has made it to one of the best-studied examples of this class of objects. At a distance of 1.45 kpc (Wendker et al. 1975) the physical radius of the nebula is 3.8 pc (major axis) × 2.5 pc (minor axis). The WN6 star HD 192163 (= WR 136, according to the list of van der Hucht 2001) is close to the center of the nebula. The ellipsoidal shell appears to be geometrically very thin and has a highly filamentary structure. With a mean electron density in the filaments of the nebula of 400 cm^{-3} (Parker 1964), Wendker et al. (1975) derived a mass of 5 $\mathrm{M}_{\odot}$ for the ionized shell and a mean shell thickness of 0.01 pc. The shell expansion velocity varies among different authors in the range $75 - 93$ km s^{-1} (Treffers & Chu 1982; Marston & Meaburn 1988; Moore et al. 2000).

It is important to distinguish two morphological features that are theoretically expected to evolve during the RSG and W-R stage of the star. A thin and dense "RSG shell" forms around the outflowing RSG wind when the reverse shock becomes radiative due to the high density of the wind in this stage. When the fast W-R wind turns on, the nonradiative reverse shock reestablishes itself and the shocked W-R wind sweeps up the RSG wind in the so-called W-R shell. The dynamical age of the W-R shell,

$$t_{\mathrm{dyn}} = \frac{\eta R_{\mathrm{shell}}}{v_{\mathrm{shell}}} \ , \tag{2.25}$$

depends on the expansion velocity and on the assumption of the density profile into which the shell expands. Typically, two cases are considered: a constant ambient density ($\eta = 0.6$ according to Weaver et al. 1977) and a $\rho \propto 1/r^2$ density profile ($\eta = 1.0$ according to García-Segura & Mac Low 1995a). With the expansion velocities quoted above, a mean shell radius of 3.2 pc, and the assumption that the optically visible nebula can be associated with the W-R shell, one obtains a minimum value for the dynamical age of NGC 6888 of 2.0×10^4 yr ($\eta = 0.6$ and $v_{\mathrm{shell}} = 93$ km s^{-1}) and a maximum value of 4.2×10^4 yr ($\eta = 1.0$ and $v_{\mathrm{shell}} = 75$ km s^{-1}).

Moore et al. (2000) used the WFPC2 on the *HST* to examine the filaments of the bright northeast rim of NGC 6888 in the light of the Hα λ6563, [OIII] λ5007, and [SII] $\lambda\lambda$6717, 6731 lines. They found filament densities of $1000 - 1600$ cm^{-3}. The dense shell is enveloped by a skin of emission most evident in [OIII] λ5007 and it is proposed that this skin arises in a cooling regime behind a radiative shock driven into the medium around the shell. For the low density that is expected in the MS bubble without heat conduction a forward shock ahead of the nebula shell would not be visible. Thus, the authors propose that a considerable fraction of the approximately 18 $\mathrm{M}_{\odot}$ wind that was ejected during the RSG phase is possibly present in the MS bubble as a low-density (2 cm^{-3}) exterior layer with low Hα surface brightness, visible only in [OIII] λ5007 postshock emission as the skin engulfing the Hα filaments when it becomes shocked by some combination of nebular shell expansion and the pressure of the postshock W-R wind overtaking the RSG shell. The large discrepancy between the density in the MS bubble of the model and the observed density of the skin could be explained by thermal evaporation of RSG

wind material into the MS bubble. Spectroscopy of the nebular shell shows that the ionized gas is enriched with nitrogen and helium and underabundant in oxygen. Possible explanations might be the transport of chemically enriched material from the core of the star to the outer layers that are ejected during the RSG stage (Esteban & Vílchez 1992) or the mixing of W-R and RSG wind material (Kwitter 1981). The high abundance of nitrogen in the nebula is consistent with the classification of HD 192163 as a WN6 star.

There is some debate on how much neutral gas is present in NGC 6888. The answer to this question has implications on the interpretation of the dynamics of the bubble as being either energy- or momentum-conserving. Marston & Meaburn (1988) found from *IRAS* observations (assuming a gas to dust mass ratio of 100) a shell of 40 $M_\odot$ neutral gas directly outside the ionized shell. The difficulty in the interpretation of the observed data is the correct estimate of the forbidden line contribution in the far-infrared. Van Buren & McCray (1988) concluded that the emission in the *IRAS* 60 and 100 μm bands is predominantly from forbidden [OIII] lines indicating that the continuum emission from the dust and thus the neutral mass would be negligible. Marston (1991) claims that the flux contribution from forbidden [OIII] and [NIII] lines is only $8-20\%$ and that the major reason for these deviating results is the higher flux from the nebula, which he derived because of a differing background removal procedure. However, Moore et al. (2000) conclude from their *HST* WFPC2 observations of the nebula that there cannot be a significant amount of neutral material close to the optical nebula. Their result for the hydrogen ionizing flux of $10^{49.3}\mathrm{s}^{-1}$ is in reasonable agreement with the value of $10^{49}\mathrm{s}^{-1}$ from the W-R models of Crowther & Smith (1996) and does perfectly match the value from GLM2 that we use for our calculations in the $35\,M_\odot$ case, but it is roughly a factor of 50 higher than the Lyman continuum flux of $10^{47.6}\mathrm{s}^{-1}$ that Marston & Meaburn (1988) found as necessary to maintain the observed Hα brightness of the nebula. In other words, only 2% of the ionizing photons from HD 192163 are used to ionize the observable nebular shell of NGC 6888—it is "density-bounded" not "ionization-bounded"—and 98% would still be available to ionize the neutral parts of the shell. Since the shock front ahead of the shell is partially shadowed from the stellar Lyman continuum flux by dense clumps within the shell, it is obvious that there is indeed some neutral material in the shell, but on the other hand the shell is very leaky to Lyman continuum photons, and it is unlikely that there is as much as 40 $M_\odot$ neutral gas present directly outside the ionized shell because that would process a larger fraction of the stellar Lyman continuum flux into Hα emission.

Observational evidence has also been found for the existence of the shell of swept-up ambient ISM around the MS bubble. Using highly resolved *IRAS* images, Marston (1995) discovered an elliptical shell with average radius of 19 pc (assuming a distance to HD 192163 of 1.45 kpc) and mass of $\approx$8000 $M_\odot$ (assuming a gas-to-dust mass ratio of 100). However, this value should be used with some caution since it was obtained with the same techniques that have been applied to produce the controversial result for the amount of neutral mass contained in the W-R bubble.

NGC 6888 was the first SWB that has been observed in X-rays (Bochkarev 1988; Wrigge et al. 1994). The latter authors examined the X-ray emission from NGC 6888 using the PSPC detector of the *ROSAT* satellite and found that it is filamentary and concentrated in the brightest optical features of the nebula. 70% of the total X-ray

emission originates from only $\approx 1-2\%$ of the bubble volume. With their assumed distance to NGC 6888 of 1.8 kpc the X-ray luminosity is estimated to be 1.6×10^{34} erg s^{-1} in the energy band $0.07 - 2.41$ keV and the plasma temperature to be 2×10^6 K. Wrigge & Wendker (2002) also used the HRI detector on board the *ROSAT* satellite to obtain X-ray emission maps with higher spatial resolution. They conclude that approximately half of the total X-ray emission originates from small filaments with typical size of a few tenths of a parsec and typical luminosity in the *ROSAT* HRI band of several 10^{31} erg s^{-1}, corresponding to a hydrogen number density in the filaments of a few cm^{-3}. Wrigge & Wendker (2002) also examined the possibility that the emission of these filaments is produced by clumps of dense gas that evaporate in the bubble of hot gas. They find that this explanation could only be consistent with the observations if the bubble gas is sufficiently hot ($5 - 10 \times 10^6$ K).

2.5.2 S308

S308, surrounding the WN4 star HD 50896 (= EZ CMa = WR 6), is the second SWB that has been observed in X-rays. The optically visible nebula is characterized by an almost spherically symmetric shell with a remarkable protrusion in the northwest quadrant but otherwise with no hints on the formation of pronounced instabilities. The distance to S308 and thus all quantities that scale with the distance are somewhat uncertain. Chu et al. (1982) give $D = 1.5$ kpc. Hamann et al. (1988) found that the range from 0.9 to a few kiloparsecs is in agreement with the results of their spectral analysis, with a preferred value of 2 kpc. Howarth & Schmutz (1995) estimate $D = 1.8$ kpc with an uncertainty of 15% based on their high-resolution observations of the interstellar NaI D lines in the spectra of HD 50896 and several nearby stars. Measurements with the *Hipparcos* satellite indicated $D = 0.6^{+0.4}_{-0.2}$ kpc (Perryman et al. 1997), which seems to be unreasonably close, when compared with the other distance-estimate techniques. The photometric distance to HD 50896 is $D = 1.0 \pm 0.2$ kpc (van der Hucht 2001) and the kinematic distance based on radial velocity information (of S308 and neighboring HII regions) and Galactic rotation is $D = 1.5 \pm 0.2$ kpc (Chu et al. 2003). We subsequently use a distance of 1.5 kpc and all the distance-depending values that we quote from other papers are scaled accordingly.

The radius of the optically visible shell is 9 pc, and the shell expands with $v = 63$ km s^{-1} (Chu et al. 2003). The ionized mass of the shell is 54 M$_\odot$ (Chu et al. 1982, scaled according to the values of radius and expansion velocity used here). The derived average hydrogen number density of the ambient gas that has been swept up is thus ≈ 0.6 cm^{-3}. An interesting implication of the distance and position on the sky is that S308 lies approximately 260 pc above the Galactic plane, an unusual place for a massive star. Since HD 50896 also has a compact companion, possibly the stellar remnant of a SN explosion, it has been proposed that it is a runaway star (Firmani et al. 1979). However, because the location of HD 50896 is almost central within S308 the transverse velocity of HD 50896 with respect to its shell cannot be very high. For an adopted dynamical age of the nebula of 0.14 Myr (Chu et al. 2003) the star can reach its projected displacement from the center of the bubble with a velocity of less than 7 km s^{-1} (Chu et al. 1982). There is no morphological evidence for supersonic transverse motion of the star+shell

system with respect to its local ISM.

Wrigge (1999) used the *ROSAT* PSPC detector to examine the X-ray emission from S308. Despite some technical difficulties, he found that the observed spectrum can be fitted by a two-temperature emission model, one component at $T = 1.5 \times 10^6$ K and the second at $T = 2.8 \times 10^7$ K. A total luminosity of 2.1×10^{33} erg s^{-1} (scaled to the distance of $D = 1.5$ kpc) in the energy band between 0.1 keV and 2.04 keV has been determined. The emitting volume is probably a thick shell with a ratio of inner to outer radius $\approx$0.5.

One of the major conclusions of Wrigge (1999) regarding the theoretical models is that S308 cannot be described by either the Weaver et al. (1977) constant ambient density model or by the two-wind model of García-Segura & Mac Low (1995a). A comparable bubble produced within the two-wind framework would have an X-ray luminosity of 9×10^{33} erg s^{-1}, which is roughly in agreement with the observed value (bearing in mind the uncertainty in the determination of the observed X-ray luminosity). The problem is that the stellar wind luminosity that is necessary to reproduce the bubble in the model is only $\approx$3% of the stellar wind luminosity that Hamann et al. (1993) derived for HD 50896 ($v_w = 1700$ km s^{-1}, $\dot{M}_w = 5.4 \times 10^{-5}$ M$_\odot$ yr^{-1}, scaled to the distance of $D = 1.5$ kpc used here). Even if the lower clumping-corrected mass-loss rate of Nugis et al. (1998) is used to derive the mechanical wind luminosity, the value from the model is still almost an order of magnitude lower. This is called the "missing wind problem". Moreover, the observed X-ray surface brightness profile of S308 is limb-brightened, while the theoretical profile is centrally filled. The result for the classical bubble model according to Weaver et al. (1977) is similar: although the stellar wind luminosity needed to reproduce the observed bubble kinematics is higher than in the two-wind model of García-Segura & Mac Low (1995a), it is still only $\approx$8% of the observed value ($\approx$32% for the clumping-corrected mass-loss rate).

Chu et al. (2003) observed the X-ray emission from the northwest quadrant of S308 using the EPIC CCD cameras of the *XMM-Newton* satellite. They found that the X-ray emission is completely interior to the optical shell and reconfirmed the limb brightening. The brightest X-ray-emitting regions are linked to bright optical filaments. The total X-ray luminosity of S308, extrapolated from the observed flux from the northwest quadrant, is $\leq (1.2 \pm 0.5) \times 10^{34}$ erg s^{-1} in the energy band between 0.25 keV and 1.5 keV. The observed spectrum can be fitted with the emission of an optically thin, nitrogen-enriched plasma of temperature $T = 1.1 \times 10^6$ K. This is quite "cool" compared to the postshock temperature of order 10^8 K that is expected for a rare stellar wind with terminal velocity of a few 1000 km s^{-1}, and it might indicate that the shocked W-R wind has mixed with cold gas by the processes of thermal evaporation and/or dynamic ablation. The spectrum is very soft, so that there is basically no emission beyond 1 keV. The existence of a high-temperature gas component that substantially contributes to the observed emission and that has been claimed to be detected by Wrigge (1999) is ruled out. Less than 6% of the observed X-ray flux (which corresponds to 1.5% of the unabsorbed X-ray flux) can be attributed to the emission of a hotter gas component. The reason for these contradicting results is probably the low signal-to-noise ratio in the *ROSAT* PSPC data that Wrigge (1999) obtained, together with a number of point sources that have not been resolved by the PSPC detector. Since the [O III] λ5007 emission of S308 has a sharp rim, the nebular shell is probably still surrounded by unaffected RSG wind material. This RSG

material cannot extend too much farther out if the protrusion in the northwest quadrant is interpreted as a first blowout. There is a gap between the outer rim of the [OIII] λ5007 emission and the outer edge of the X-ray emission of between 90″ and over 200″, corresponding to $0.7 - 1.5$ pc. Chu et al. (2003) interpret this gap as being filled by the W-R shell and probably a transition layer. This is also indicated by the detection of an interstellar NV absorption line toward HD 50896, which Boroson et al. (1997) attribute to the shell of S308.

The electron density in the X-ray-emitting gas is estimated to be $n_e = 0.28 \pm 0.04$ cm^{-3} or $n_e = 0.63 \pm 0.09$ cm^{-3} for an assumed hot gas volume filling factor of 0.5 or 0.1, respectively. The filling factor is expected to be closer to 0.5 since the limb-brightened X-ray emission profile suggests emission from a thick shell. The resulting mass of the X-ray-emitting gas is 11 ± 5 or 5 ± 3 M$_\odot$ for the two volume filling factors. Assuming that the optical emission that has been used to determine the expansion velocity comes from the W-R shell, the age of the W-R phase can be estimated using equation 2.25. For $R_{\rm shell} = 9$ pc, $v_{\rm shell} = 63$ km s^{-1}, and $\eta = 1.0$ this yields $t_{\rm dyn} = 0.14$ Myr. For a clumping-corrected mass-loss rate of HD 50896 of 1.4×10^{-5} M$_\odot$ yr^{-1} (Nugis et al. 1998, scaled to the distance used here) the mass blown into the bubble by the W-R wind is 2 M$_\odot$. This is less than the X-ray-emitting gas mass, a fact which in turn supports the idea that RSG material is mixed with the shocked W-R wind in the bubble or that the main source of X-rays is different from the shocked W-R wind. Observations of S308 in the optical waveband furthermore show that besides photoionization there is also shock heating present, indicated by the high [OIII] λ5007/Hβ ratio of 20 (Esteban et al. 1992). Similar to the case of NGC 6888, the [OIII] λ5007 emission leads the Hα emission by $16'' - 20''$ (Gruendl et al. 2000) corresponding to $0.12 - 0.15$ pc. Furthermore, S308 is located in an HI cavity swept free by the MS wind of HD 50896 (Arnal & Cappa 1996).

2.6 The Deposition of Energy in the ISM

2.6.1 Analytical Approximations for HII Regions

An important part of this work is concerned with the energetic impact that massive stars have on the ISM. Taking some simplifying assumptions into account, Lasker (1967) derived a simple analytic model that is able to predict the efficiency with which the thermal energy of HII regions is transferred into kinetic energy of expanding shells. We describe the model in some details here. The assumptions are the following: The star that powers the HII region is assumed to have constant effective temperature and luminosity over its whole lifetime, τ, and no stellar wind is considered. The ambient medium around the star is homogeneous, initially neutral, cool, dust-free, and sufficiently extended (i.e., the developing HII region is always ionization bounded rather than density bounded). Therefore, spherical symmetry is applied and the HII region is expected to expand uniformly with a homogeneous density inside, which varies only with time. Effects like hydrodynamical instabilities are not considered. It is furthermore expected that the HII region expands supersonically due to the pressure gradient between the warm, ionized interior and the cold, neutral ambient gas and that the ambient gas is swept up in a cooling, thin

shell behind a strong shock. The ionization front is then located at the inner surface of the shell.

I reproduce the derivation of Lasker's formula here because it reveals some neat insights into the physics of HII regions. The designation of the variables is as follows: the index I refers to the neutral ambient medium, II to the HII region, i to the ionization front, i- to the downstream flow right at the inner side of the ionization front, s to the shock front, and s- to the downstream flow in the shell right at the inner side of the shock front. v indicates velocities with respect to the star (and, therefore, also to the quiescent ambient medium) while u refers to velocities in the frame of the moving shock front. We start our investigation at the time when the initial Strömgren sphere has formed and the HII region starts to expand. (The duration of the first phase that we neglect here is very short compared to the lifetime of the star.) Following a particular shell of ionized gas right downstream the ionization front, mass conservation in the expanding gas yields

$$r^3 \rho_{\rm II} = const(t) \ , \tag{2.26}$$

thus,

$$\frac{d\rho_{\rm II}}{dt} = \frac{\partial \rho_{\rm II}}{\partial r}\frac{dr}{dt} = -3r^{-4} const(t)\, v = -3r^{-1}\rho_{\rm II}\, v \ . \tag{2.27}$$

The gas shell has been examined at $r_{\rm i-} \approx r_{\rm i}$, therefore, we get

$$v_{\rm i-} = \frac{-r_{\rm i}}{3\rho_{\rm II}}\frac{d\rho_{\rm II}}{dt} \ . \tag{2.28}$$

On the other hand, the Strömgren formula 2.2 for the radius of the ionized volume implies the following relation:

$$r_{\rm i}^3 \rho_{\rm II}^2 = const(t) \ , \tag{2.29}$$

where $const(t)$ is in general different from the constant in equation 2.27. The temporal change of the density can then be calculated as

$$\frac{d\rho_{\rm II}}{dt} = \frac{\partial \rho_{\rm II}}{\partial r_{\rm i}}\frac{dr_{\rm i}}{dt} = -\frac{3}{2} r_{\rm i}^{-5/2} const(t)\, v_{\rm i} = -\frac{3}{2}\frac{\rho_{\rm II}}{r_{\rm i}}\, v_{\rm i} \ . \tag{2.30}$$

From that, we get

$$v_{\rm i} = \frac{-2r_{\rm i}}{3\rho_{\rm II}}\frac{d\rho_{\rm II}}{dt} \ . \tag{2.31}$$

Equations 2.28 and 2.31 directly show that

$$v_{\rm i-} = \frac{1}{2} v_{\rm i} \ , \tag{2.32}$$

and, therefore,

$$u_{\rm i-} = -\frac{1}{2} v_{\rm i} \ , \tag{2.33}$$

with $u_{\rm i-}$ being the downstream flow speed in the frame of the ionization front. Additionally we have

$$u_{\rm s+} = -v_{\rm s} \ , \tag{2.34}$$

where u_{s+} is the upstream flow speed in the frame of the shock front and v_s is the shock speed in the frame of the star. Neglecting the small difference between v_s and v_i, we apply the Rankine-Hugoniot pressure jump condition across the shock and ionization front:

$$P_I + \rho_I u_{s+}^2 = P_{II} + \rho_{II} u_{i-}^2 \ . \tag{2.35}$$

Neglecting P_I and using equations 2.33 and 2.34, we get

$$\rho_I v_s^2 = P_{II} + \rho_{II} \left(\frac{1}{2} v_s\right)^2 \ , \tag{2.36}$$

and, thus,

$$\rho_I = \frac{P_{II}}{v_s^2} + \frac{\rho_{II}}{4} \ . \tag{2.37}$$

Introducing the isothermal sound speed,

$$c_s = \sqrt{\frac{P}{\rho}} \ , \tag{2.38}$$

one gets

$$v_s = \frac{c_{s,II}\sqrt{\frac{\rho_{II}}{\rho_I}}}{\sqrt{1 - \frac{\rho_{II}}{4\rho_I}}} \ . \tag{2.39}$$

The denominator is always close to 1, therefore, we can obtain a very simple expression for the shock speed:

$$v_s \approx v_i \approx c_{s,II}\sqrt{\frac{\rho_{II}}{\rho_I}} \ . \tag{2.40}$$

Assuming that ionization equilibrium holds for all times during the expansion of the HII region, equation 2.2 can be generalized to yield

$$r_i = \left(\frac{3 S_u}{4\pi n_H^2 \alpha_B}\right)^{\frac{1}{3}} \ , \tag{2.41}$$

where n_H is now the actual (homogeneous) density of the HII region. Combining the latter one with equation 2.2, we get

$$r_S = \left(\frac{n_H^2 r_i}{n_{H,0}^2}\right)^{\frac{1}{3}} \ , \tag{2.42}$$

where $n_{H,0}$ is the density of the ambient medium. Thus, we get

$$\frac{n_H}{n_{H,0}} = \left(\frac{r_i}{r_S}\right)^{-\frac{3}{2}} \ . \tag{2.43}$$

Inserting this result into equation 2.40, we obtain

$$v_i = c_{s,II}\sqrt{\frac{n_H}{n_{H,0}}} = c_{s,II}\left(\frac{r_i}{r_S}\right)^{-\frac{3}{4}} \ . \tag{2.44}$$

Integration of this equation yields

$$r_{\rm i} = \left(\frac{7}{4} c_{\rm s,II} r_{\rm S}^{3/4} t + r_{\rm S}^{7/4}\right)^{4/7} \quad . \tag{2.45}$$

We now apply the jump conditions for the strong shock ahead of the ionization front. For strong shocks, we have

$$M = \frac{v_{\rm s}}{\sqrt{\gamma} c_{\rm s,I}} \gg 1 \ , \tag{2.46}$$

where M is the so-called upstream Mach number of the shock and γ is the adiabatic exponent. In this case the jump condition for the density reduces to

$$\frac{u_{\rm I}}{u_{\rm s-}} = \frac{\rho_{\rm s-}}{\rho_{\rm I}} = \frac{\gamma+1}{\gamma-1} = 4 \tag{2.47}$$

for an ideal, monoatomic gas with $\gamma = 5/3$. Thus, we get

$$v_{\rm s-} = v_{\rm s} + u_{\rm s-} = v_{\rm s} + \frac{u_{\rm I}}{4} = \frac{3}{4} v_{\rm s} \tag{2.48}$$

because the ambient medium is quiescent and, therefore, $u_{\rm I} = -v_{\rm s}$. The strong shock jump condition yields for the pressure

$$\frac{P_{\rm s-}}{P_{\rm I}} = \frac{2\gamma M^2}{\gamma+1} = \frac{5}{4} M^2 \tag{2.49}$$

and for the temperature

$$\frac{T_{\rm s-}}{T_{\rm I}} = \frac{2\gamma\left(\gamma-1\right) M^2}{\left(\gamma+1\right)^2} = \frac{5}{16} M^2 \ . \tag{2.50}$$

The expanding HII region accelerates and heats the ambient gas in the swept-up shell. We now calculate the thermal energy density behind the shock. With the strong shock relations for density and temperature and the definition of the Mach number M, we get

$$\begin{aligned} \varepsilon_{\rm t} &= \frac{3}{2} n_{\rm s-} k_{\rm B} T_{\rm s-} \\ &= 6 n_{\rm I} k_{\rm B} T_{\rm s-} \\ &= 6 n_{\rm I} k_{\rm B} \frac{5}{16} M^2 T_{\rm I} \\ &= \frac{15}{8} n_{\rm I} k_{\rm B} \frac{v_{\rm s}^2 \rho_{\rm I}}{\gamma P_{\rm I}} T_{\rm I} \ . \end{aligned}$$

Inserting $P_{\rm I} = n_{\rm I} k_{\rm B} T_{\rm I}$, $\rho_{\rm I} = n_{\rm I} m_{\rm H}$, and $\gamma = 5/3$ leads us to the result

$$\varepsilon_{\rm t} = \frac{9}{8} \, n_{\rm I} \, m_{\rm H} \, v_{\rm s}^2 \ . \tag{2.51}$$

The kinetic energy density behind the shock is

$$\begin{aligned} \varepsilon_{\rm k} &= \frac{1}{2}\,\rho_{\rm s-}\,v_{\rm s-}^2 \\ &= 2\,\rho_{\rm I}\,v_{\rm s-}^2 \\ &= 2\,\rho_{\rm I}\,\left(\frac{3}{4}\,v_{\rm s}\right)^2 \\ &= \frac{9}{8}\,\rho_{\rm I}\,v_{\rm s}^2 \\ &= \frac{9}{8}\,n_{\rm I}\,m_{\rm H}\,v_{\rm s}^2\ , \end{aligned} \tag{2.52}$$

where we used the strong shock relation for the density and equation 2.48. It is evident from equations 2.51 and 2.52 that half of the energy transferred to the ISM in the swept-up shell adds up to the kinetic energy while the other half heats the shell.

The expanding HII region acts like a piston and, as we have seen above, half of the work done by the piston is transformed into kinetic energy of the shell. Therefore, the total kinetic energy of the shell can be calculated as:

$$E_{\rm k} = \frac{1}{2}\int_0^{V_{\rm II}(\tau)} P_{\rm II}\,dV_{\rm II}\ , \tag{2.53}$$

where

$$V_{\rm II} = \frac{4\pi}{3}\,r_{\rm i}^3 \tag{2.54}$$

is the volume of the HII region inside $r_{\rm i}$. The pressure in the HII region can be written as

$$P_{\rm II} = \rho_{\rm II}\,c_{\rm s,II}^2 = n_{\rm I}\,m_{\rm H}\,c_{\rm s,II}^2\ .$$

With the help of equations 2.43 and 2.54, $P_{\rm II}$ can then be expressed as a function of $V_{\rm II}$:

$$P_{\rm II} = \left(\frac{4\pi}{3}\right)^{1/2} n_{\rm I}\,m_{\rm H}\,c_{\rm s,II}^2\,r_{\rm S}^{3/2}\,V_{\rm II}^{-1/2}\ . \tag{2.55}$$

Inserting equation 2.55 into equation 2.53 yields

$$\begin{aligned} E_{\rm k} &= \frac{1}{2}\,\left(\frac{4\pi}{3}\right)^{1/2} n_{\rm I}\,m_{\rm H}\,c_{\rm s,II}^2\,r_{\rm S}^{3/2}\,\int_0^{V_{\rm II}(\tau)} V_{\rm II}^{-1/2}\,dV_{\rm II} \\ &= \left(\frac{4\pi}{3}\right)^{1/2} n_{\rm I}\,m_{\rm H}\,c_{\rm s,II}^2\,r_{\rm S}^{3/2}\,\left(V_{\rm II}^{1/2}(\tau) - V_{\rm II}^{1/2}(0)\right)\ . \end{aligned} \tag{2.56}$$

Using equations 2.54 and 2.45, we obtain the result that we were looking for:

$$E_{\rm k} = \frac{4}{3}\,\pi\,n_{\rm I}\,m_{\rm H}\,c_{\rm s,II}^2\,r_{\rm S}^{3/2}\,\left[\left(\frac{7}{4}\,c_{\rm s,II}\,r_{\rm S}^{3/4}\,\tau + r_{\rm S}^{7/4}\right)^{6/7} - r_{\rm S}^{3/2}\right]\ . \tag{2.57}$$

If we additionally assume that the dense shell of swept-up ambient medium remains cool and neutral due to strong radiative energy loss, we can also determine the ionization energy ($\chi_0 = 13.6\,\mathrm{eV}$ per ionized hydrogen atom) that is stored in the HII region:

$$E_\mathrm{i} = V_\mathrm{II}\, n_\mathrm{II}\, \chi_0$$

with equations 2.54 and 2.43

$$= \frac{4}{3}\,\pi\, n_\mathrm{I}\, r_\mathrm{S}^{3/2}\, r_\mathrm{i}^{3/2}\, \chi_0$$

and with 2.45

$$= \frac{4}{3}\,\pi\, n_\mathrm{I}\, \left(\frac{7}{4} c_\mathrm{s,II} r_\mathrm{S}^{5/2} \tau + r_\mathrm{S}^{7/2}\right)^{6/7} \chi_0 \ . \tag{2.58}$$

The same *Ansatz* can be used to estimate the thermal energy of warm gas in the HII region:

$$\begin{aligned} E_\mathrm{t} &= V_\mathrm{II}\, 2\, n_\mathrm{II}\, \frac{3}{2}\, k_\mathrm{B}\, T_\mathrm{II} \\ &= 4\pi\, n_\mathrm{I}\, r_\mathrm{S}^{3/2}\, r_\mathrm{i}^{3/2} k_\mathrm{B}\, T_\mathrm{II} \\ &= 4\pi\, n_\mathrm{I}\, \left(\frac{7}{4} c_\mathrm{s,II} r_\mathrm{S}^{5/2} \tau + r_\mathrm{S}^{7/2}\right)^{6/7} k_\mathrm{B}\, T_\mathrm{II} \ , \end{aligned} \tag{2.59}$$

where we will insert $T_\mathrm{II} = 8000\,\mathrm{K}$ as an appropriate guess for the temperature in the HII region.

Now we can also define the mean efficiency ϵ_L with which thermal energy of HII regions is converted into kinetic energy of bulk motion of interstellar medium (under the assumptions made above):

$$\epsilon_\mathrm{L} = \frac{E_\mathrm{k}}{S_\mathrm{u}\, \tau\, (\langle h\nu \rangle - h\nu_0)} \ , \tag{2.60}$$

where S_u is the number of Lyman continuum photons emitted by the star per unit time, $\langle h\nu \rangle$ is the mean energy of these photons, and $h\nu_0$ is the energy of a Lyman threshold photon.

Lasker (1967) tabulated the energy transfer rate and transfer efficiency resulting from equation 2.60 for massive stars of different spectral types. Since the relations between spectral type and stellar parameters that Lasker used are no longer up-to-date, we re-calculated the energy transfer rate and efficiency for a set of 6 stars with different initial masses and show these results for comparison with our numerical results in Table 2.1 and Figures 2.5 and 2.6. The stellar parameters have now been taken from Maeder (1990), where we have chosen the tracks for stars with solar metallicity. These parameters are also listed in Table 2.1. Since Lasker's analytical model requires constant temperature and luminosity over the whole lifetime of the star and since Maeder (1990) calculates more realistic, time-dependent stellar parameters, we have simply chosen the values for temperature and luminosity at half the lifetime of the star from the tables of Maeder (1990)

Table 2.1: Energy transfer rate $\dot{E}_\mathrm{k}$ and transfer efficiency ϵ_L for HII regions around stars with different initial masses M_ZAMS according to the model of Lasker (1967).

M_ZAMS ($\mathrm{M}_\odot$)	T_eff (K)	L ($10^4\,\mathrm{L}_\odot$)	τ (Myr)	$\dot{E}_\mathrm{k}$ ($10^{34}\,\mathrm{erg\,s^{-1}}$)	ϵ_L (10^{-3})
120	45100	223	3.46	329	2.55
85	42500	136	3.70	225	3.29
60	42600	76.1	4.19	151	3.93
40	40500	34.4	5.15	83.3	5.45
25	35600	12.0	7.74	34.0	9.26
15	29400	3.08	14.1	9.17	19.1

to be representative for the particular star. (The resulting slightly different evolutionary state of the stars explains the surprising fact that in Table 2.1 the effective temperature of the $60\,\mathrm{M}_\odot$ star is slightly higher than the effective temperature of the $85\,\mathrm{M}_\odot$ star.) In accordance with our numerical models, we assumed black-body spectra for the stars. We also take $c_\mathrm{s,II} = 1.15 \times 10^6\,\mathrm{cm\,s^{-1}}$ and $\alpha_\mathrm{B} = 3.37 \times 10^{-13}\,\mathrm{cm^3\,s^{-1}}$, the same values that Lasker (1967) used. The energy transfer rate $\dot{E}_\mathrm{k}$ is here defined as E_k/τ, with E_k from equation 2.57, and the energy transfer efficiency ϵ_L follows from the evaluation of equation 2.60. Both values in Table 2.1 are calculated for an ambient density of $1\,\mathrm{cm^{-3}}$.

The density dependence of the energy transfer rate and efficiency (or, more precisely, the deviation from the major density dependence at high densities, $n_0^{-3/7}$) is shown in Figures 2.5 and 2.6, respectively. The energy transfer rate (for a given ambient density, e.g., $1\,\mathrm{cm^{-3}}$) strongly depends on the initial mass of the star and rises from $9.2 \times 10^{34}\,\mathrm{erg\,s^{-1}}$ for the $15\,\mathrm{M}_\odot$ star to $3.3 \times 10^{36}\,\mathrm{erg\,s^{-1}}$ for the $120\,\mathrm{M}_\odot$ star. But the increase is less steep than the increase of the total stellar luminosity with initial mass of the star. (The relevant increase of the stellar luminosity beyond the Lyman threshold is even stronger.) This fact can also be seen in the strong decrease of the energy transfer efficiency from 1.9 % to 0.26 % with increasing initial mass of the star. Although the numbers change, the general trend that the energy transfer efficiency decreases with increasing initial mass of the star is independent of the ambient density as can be seen in Figure 2.6. Figures 2.5 and 2.6 show that the density dependence of the energy transfer rate and transfer efficiency can be well described as $\propto n_0^{-3/7}$ for higher densities, while for lower densities the gradient is shallower.

Considering the much higher number of less massive stars and the much higher energy input by the most massive stars, one can get an order-of-magnitude estimate for the transfer efficiency from the thermal energy in HII regions to bulk motion of interstellar gas averaged over all massive stars as energy sources for the HII regions. Lasker (1967) did these calculations for an ambient density of $10\,\mathrm{cm^{-3}}$ and got $\langle\epsilon_\mathrm{L}\rangle \approx 10^{-2}$.

For additional discussions about the validity of the solution and the influence of other effects we refer to the original paper of Lasker (1967).

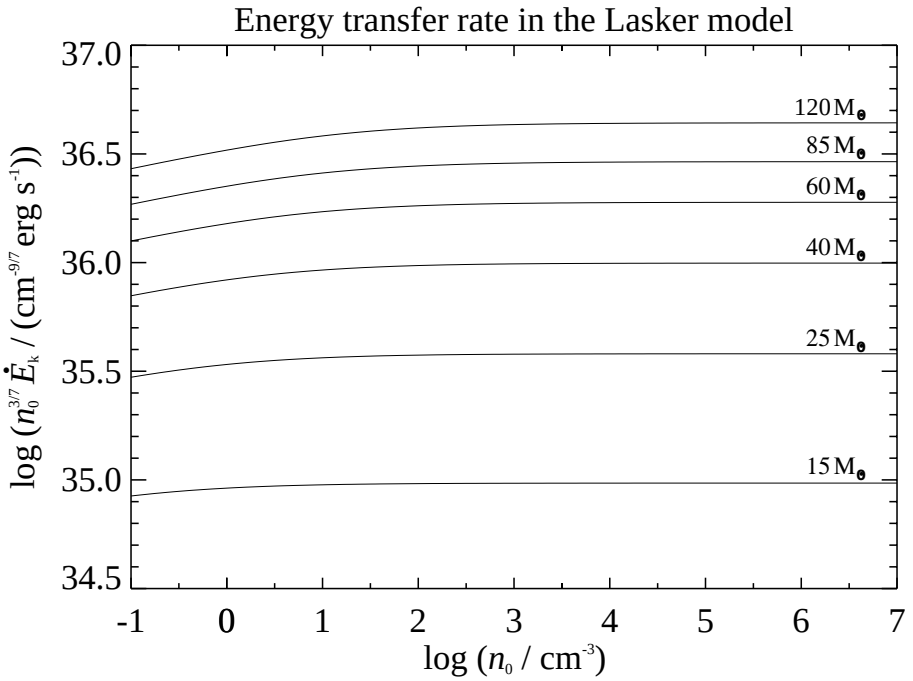

Figure 2.5: The mean rate of energy transfer from thermal energy in an HII region to kinetic energy of the accelerated shell as a function of the ambient density for stars with different initial masses, calculated according to Lasker (1967). The transfer rate has been scaled by $n_0^{3/7}$ to show its major density dependence.

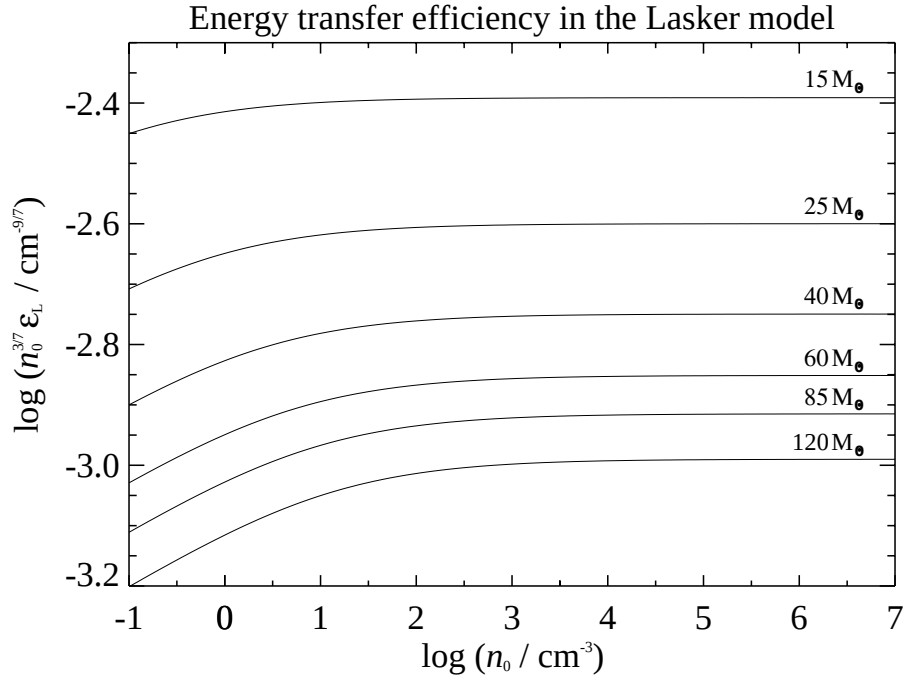

Figure 2.6: The mean efficiency of energy transfer from thermal energy in an HII region to kinetic energy of the accelerated shell as a function of the ambient density for stars with different initial masses, calculated according to Lasker (1967). The transfer efficiency has been scaled by $n_0^{3/7}$ to show its major density dependence.

2.6.2 Analytical Approximations for Stellar Wind Bubbles

It is also possible to obtain an analytical result for the energy that is deposited in the ISM by SWBs. We neglect the first (fully adiabatic) stage of bubble evolution because it is very short. Cooling in the hot bubble strongly depends on the efficiency of heat conduction or how efficiently heat conduction is suppressed by magnetic fields. We will assume for the analytical theory that there is no heat conduction and thus cooling in the hot bubble is unimportant during the lifetime of the star. Then we rely on the similarity solution for the second phase of bubble evolution (thin, dense, strongly cooling outer shell and cooling unimportant in the hot, rarefied bubble) given in section 2.2.

The hot bubble acts like a piston on the ambient medium, and analogous to the case of an HII region it can be shown that the $P\,dV$ work is equally distributed on kinetic energy of shell motion and thermal energy in the shell (which gets immediately lost as a result of cooling). If we furthermore assume that the kinetic energy of the stellar wind is completely transformed into thermal energy at the reverse shock (the strong-jump conditions give 15/16, but clumpiness of the stellar wind, which we completely neglect, might reduce this value), we get for the kinetic energy

$$E_\mathrm{k} \;=\; \frac{1}{2}\int_0^{V_\mathrm{s2}(\tau)} P_\mathrm{b}\,dV_\mathrm{s2}\ .$$

V_s2 is the volume inside r_s2 and can be calculated using equation 2.15:

$$V_\mathrm{s2}(t) \;=\; \frac{4\pi}{3}\,r_\mathrm{s2}^3 \;=\; \frac{4\pi}{3}\left(\frac{125}{154\pi}\right)^{3/5} L_\mathrm{w}^{3/5}\,\rho_0^{-3/5}\,t^{9/5}\ .$$

The pressure in the hot bubble (equation 2.18) can thus be written as a function of V_s2:

$$P_\mathrm{b}(V_\mathrm{s2}) \;=\; \left(\frac{4\pi}{3}\right)^{4/9}\left(\frac{125}{154\pi}\right)^{4/15}\frac{7}{(3850\pi)^{2/5}}\,L_\mathrm{w}^{2/3}\,\rho_0^{1/3}\,V_\mathrm{s2}^{-4/9}\ .$$

Now we get for the kinetic energy:

$$\begin{aligned} E_\mathrm{k} &= \frac{1}{2}\left(\frac{4\pi}{3}\right)^{4/9}\left(\frac{125}{154\pi}\right)^{4/15}\frac{7}{(3850\pi)^{2/5}}\,L_w^{2/3}\,\rho_0^{1/3}\int_0^{V_\mathrm{s2}(\tau)} V_\mathrm{s2}^{-4/9}\,dV_\mathrm{s2} \\ &= \frac{9}{10}\left(\frac{4\pi}{3}\right)^{4/9}\left(\frac{125}{154\pi}\right)^{4/15}\frac{7}{(3850\pi)^{2/5}}\,L_w^{2/3}\,\rho_0^{1/3}\,V_\mathrm{s2}^{5/9}(\tau)\ . \end{aligned}$$

Inserting V_s2 at $t=\tau$ gives the result we were looking for:

$$\begin{aligned} E_\mathrm{k} &= \frac{9}{10}\,\frac{4\pi}{3}\left(\frac{125}{154\pi}\right)^{3/5}\frac{7}{(3850\pi)^{2/5}}\,L_w\,\tau \\ &= \frac{3}{11}\,L_\mathrm{w}\,\tau\ . \end{aligned} \tag{2.61}$$

That enables us also to calculate the thermal energy of hot gas:

$$E_\mathrm{t} \;=\; L_\mathrm{w}\,\tau - \int_0^{V_\mathrm{s2}(\tau)} P_\mathrm{b}\,dV_\mathrm{s2} \;=\; \frac{5}{11}\,L_\mathrm{w}\,\tau\ . \tag{2.62}$$

Besides heat conduction and cooling in the hot bubble, we have also neglected the fact that part of the thermal energy might be used for collisional ionization of gas. Thus, the results for E_k and E_t are upper limits.

2.7 The Energization of the ISM in the Solar Neighborhood

The canonical value of 1 % for the energy transfer efficiency from the thermal energy of HII regions to kinetic energy of bulk motion of interstellar gas has been used by Abbott (1982) in order to examine the energization of the ISM in the solar neighborhood. He compiled observational results and used empirical relations to determine the mass-loss rates and terminal velocities of stellar winds for a complete sample of early-type O stars, W-R stars, and B and A supergiants in the vicinity of the Sun. The transfer of energy into the ISM is estimated from the mechanical wind power of the stars, and it is compared with the energy input by stellar radiation and SNe. Abbott (1982) found that the total wind power is $1.9 \times 10^{38}\,\mathrm{erg\,s^{-1}\,kpc^{-2}}$ with an uncertainty of a factor of 2. 50 % of the wind power is produced by some 50 W-R stars, 47 % by approximately 500 O stars, and the remaining 3 % by B and A supergiants. A few other types of stars with winds are known, but their contribution to the wind power is negligible. The total mechanical power output by SNe is supposed to be $9.9 \times 10^{38}\,\mathrm{erg\,s^{-1}\,kpc^{-2}}$, corresponding to a SN rate of 3 per 100 yr in the Galaxy with a radius of 15 kpc under the assumptions that half of the SNe are of Type I with a mechanical energy release of 5×10^{50} erg while the other half are of Type II with 10^{51} erg mechanical energy release and that the SN rate is the same throughout the plane of the Galaxy (Abbott 1982). Thus, the mechanical power output by SNe is 5 times larger than the mechanical wind power of the stars. The radiative luminosity dominates the power output from the stars and SNe with about $3.4 \times 10^{40}\,\mathrm{erg\,s^{-1}\,kpc^{-2}}$, 6 % coming from W-R stars, 66 % from O stars and 28 % from B and A supergiants. 30 % of the power is emitted in the spectral range above the Lyman threshold.

The fact that radiative luminosity dominates the power **output** from the stars does not necessarily mean that it also dominates the energy **input** into the ISM because that depends on the efficiency of the energy conversion. The stellar Lyman continuum ionizes interstellar gas, but only the photon excess energy above the Lyman threshold can be used to heat the gas. At longer wavelengths, only part of the radiation can contribute at all to the heating via photoelectric heating on dust. And as we have seen above, only a small fraction of the thermal energy in HII regions can be transferred to kinetic energy of bulk motion. Stellar winds and SNe directly heat the ISM by shocks and cloud compression. The hot gas expands, accelerates the ambient medium, and increases its kinetic energy of motion. There is also a secondary heating effect in the way that part of the cooling radiation from the shocked gas is able to ionize and heat ambient material.

As pointed out before, only the excess energy beyond the Lyman threshold of the incident radiation field is converted to thermal energy of an HII region. Spitzer (1978) tabulated this fraction as a function of color temperature of the star and electron temperature of the plasma (which can be set to 8000 K for typical HII regions). For the stars under investigation, Abbott (1982) found an average heating efficiency of 18 % for the Lyman continuum radiation and therefore 6 % for the total radiation energy. As we have seen before, a rough estimate for the mean transfer efficiency from thermal energy in HII regions to bulk motion of ambient gas accelerated by the expansion of the HII region is

1 %.

Photoelectric effect on dust grains by stellar radiation in the energy range below the Lyman threshold is probably the most important heating process in neutral gas. Abbott (1982) simply uses the heating rate derived by de Jong (1977). For the given sample of stars this implies an efficiency of 2 % for the conversion of the total stellar radiative power into heating of HI regions.

The energy transfer efficiency from stellar winds into the ISM has been estimated according to the numerical simulations of Weaver et al. (1977): 30 % of the total wind energy input heats gas to high temperatures, 10 % accelerates ambient material, 27 % is radiated from the hot bubble interior, and 33 % is radiated from the shell of shocked ambient gas. Furthermore, it is assumed that 50 % of the energy radiated from the hot bubble is reused to heat the HII gas while due to the softness of the radiation from the shell only 2 % of that energy heats neutral gas.

For SNe, numerical results from Cowie et al. (1981) for the evolution of supernova remnants into an inhomogeneous medium were used to estimate the energy conversion efficiency: roughly 20 % of the mechanical SN input energy is converted to thermal energy of hot gas, 30 % is used to heat neutral gas by cloud compression, and 6 % is transformed to bulk motion of gas. Once again it is assumed that half of the 40 % fraction that is radiated from the hot gas in the SN remnant heats HII gas.

Thus, the total energy transfer efficiency for stellar radiation is approximately 8 %, for stellar wind it is roughly 54 %, and for the mechanical energy of SNe about 76 %. With all these transfer efficiencies one gets the following picture for the energy transfer rates from stars to the various phases of the ISM in the solar neighborhood: Stellar radiation transfers $2 \times 10^{39}\,\mathrm{erg\,s^{-1}\,kpc^{-2}}$ thermal energy to HII gas, $3 \times 10^{38}\,\mathrm{erg\,s^{-1}\,kpc^{-2}}$ thermal energy to HI gas, and $2 \times 10^{37}\,\mathrm{erg\,s^{-1}\,kpc^{-2}}$ kinetic energy of bulk motion to the ISM. Stellar wind transfers $6 \times 10^{37}\,\mathrm{erg\,s^{-1}\,kpc^{-2}}$ thermal energy to the hot coronal gas, $3 \times 10^{37}\,\mathrm{erg\,s^{-1}\,kpc^{-2}}$ thermal energy to HII gas, $1 \times 10^{36}\,\mathrm{erg\,s^{-1}\,kpc^{-2}}$ thermal energy to HI gas, and $2 \times 10^{37}\,\mathrm{erg\,s^{-1}\,kpc^{-2}}$ kinetic energy of bulk motion to the ISM. SNe transfer $2 \times 10^{38}\,\mathrm{erg\,s^{-1}\,kpc^{-2}}$ thermal energy to the hot coronal gas, $3 \times 10^{37}\,\mathrm{erg\,s^{-1}\,kpc^{-2}}$ thermal energy to HII gas, $3 \times 10^{38}\,\mathrm{erg\,s^{-1}\,kpc^{-2}}$ thermal energy to HI gas by cloud compression, and $6 \times 10^{37}\,\mathrm{erg\,s^{-1}\,kpc^{-2}}$ kinetic energy of bulk motion to the ISM.

From these values one can see that globally the energy transfer to the hot ionized gas is dominated by SNe with a smaller contribution from stellar wind. The heating of the warm ionized medium is primarily due to stellar radiation while SNe and stellar radiation supply roughly the same amount of thermal energy to the neutral gas. The kinetic energy of bulk motion of ISM gas is mainly delivered by SNe, but the contribution of stellar radiation and wind power is significant.

However, this is only the global point of view (global in the sense of averaging over a test volume in the vicinity of the Sun from that we can get sufficiently reliable observational data). It is clear that locally the situation can be very different. For example, in the vicinity of OB associations with stars earlier than O6, stellar winds dominate the energy balance of the ISM (Abbott 1982).

2.8 Previous Numerical Simulations of Stellar Wind Bubbles

Since effects associated with inhomogeneous ambient media or time-dependent stellar parameters, as well as the formation of gasdynamical instabilities, are difficult to handle within an analytical framework, numerical simulations have become a powerful tool to study the evolution of HII regions and SWBs. First two-dimensional numerical calculations of SWBs have been performed by Różyczka (1985) and Różyczka & Tenorio-Tagle (1985a,b) in a series of papers. For the expansion of the bubble into a homogeneous medium the authors described the formation of clumps in the thin shell, but as a result of the lack of resolution, they were unable to completely resolve the dynamics of the shell and to compare it with theoretical predictions. The authors also studied how a change of the wind luminosity (an increase between two fixed levels in a certain time) influences the shell stability and how SWBs break out from a plane-parallel stratified disk. The shell fragmentation due to an increase of the wind luminosity has also been studied by Stone et al. (1995) and has been compared with the observation of "bullets" in the vicinity of young stars.

GML1 and GLM2 focused on the history of the stellar mass loss and the implications for the formation of W-R bubbles. They calculated the evolution of the SWB in one dimension until the star enters the LBV phase (for the case with an initial stellar mass of $60\,M_\odot$) or until the star leaves the RSG stage (for the $35\,M_\odot$ case). The resulting one-dimensional profiles of circumstellar density, pressure, and velocity were used to set up the ambient conditions for two-dimensional calculations of the following stage when the W-R wind interacts with the surrounding structure. The authors found that in both cases the slowly expanding shells originating from prior mass-loss phases are heavily eroded when they are overtaken by the faster W-R wind. This is also the phase in which the resulting nebula shell is considered to be most visible as a result of the high emission measure in the high-density filaments resulting from the collision. The nebula NGC 6888 with its filamentary structure would fit in this picture as being driven by a W-R star that has undergone MS and RSG evolution, and the shell swept up by the W-R wind is currently colliding with the RSG wind shell.

The approach of García-Segura & Franco (1996) is slightly different because they were mainly concerned with the very early evolution of HII regions. They presented two-dimensional gasdynamical calculations for the evolution of HII regions in constant and power-law density profiles and showed the effect of radiative cooling on the thickness of the swept-up shell and therefore also on the development of instabilities. They found that the ionization front can reinforce the growth of the thin-shell instability, and in a power-law density falloff with exponent equal to 2 it can even lead to violent shell disruption.

Brighenti & D'Ercole (1997) investigated the formation of W-R shells resulting from fast W-R winds evolving into slow anisotropic RSG winds. They found that the shell swept up by the W-R wind becomes Rayleigh-Taylor unstable and fragments even before it hits the shell that had previously been piled up by the RSG wind. X-ray maps computed from the numerical models show that the anisotropy of the RSG wind leads to

Table 2.2: Hydrodynamical models of SWBs/HII regions around single early-type stars.

References	Dimensions	Geometry	Linear size (pc)
1.....	2	cylindrical	$7.8 - (3.2 \times 10^{-3})$
2.....	2	spherical	0.1
3.....	1 / 2	spherical	$70 - 45/19 - 3$
4.....	2	spherical	$0.1 - 2$
5.....	2	spherical	6.6/1
6.....	2	cylindrical	0.2
7.....	2	cylindrical	6.5
8.....	2	cylindrical	64/50
References	Resolution[a] (10^{-3})	Duration (Myr)	Ionization
1.....	5	$0.02 - (1.5 \times 10^{-5})$	thermal
2.....	5	10^{-3}	no
3.....	2.5/2.5-1.25	$4 - 5/(28 - 7.2) \times 10^{-3}$	no
4.....	5	$0.02 - 0.33$	PIE[d]
5.....	1.3	0.023	no
6.....	3.9	8×10^{-4}	no
7.....	2.5	0.015	no
8.....	8.0-0.125	4/5	time dependent[e]
References	Heating	Cooling	Wind asymmetry
1.....	mechanical	CIE[b]	no
2.....	mechanical	isothermal EOS[c]	no
3.....	mechanical	CIE + cutoff	no
4.....	mechanical + PIE	CIE + cutoff	no
5.....	mechanical	CIE	yes
6.....	mechanical	CIE	yes
7.....	mechanical	CIE + cutoff	no
8.....	mechanical + radiative	explicit or CIE[f]	no
References	$L_{\rm w}(t)$	$L_{\rm LyC}(t)$	$n_0(r)$
1.....	fixed/two-level	0	constant/composite
2.....	two-level	0	constant
3.....	variable	variable	constant/from one dimension
4.....	0	fixed	constant/power law
5.....	two-level with transition	0	pre–W-R
6.....	three-level	0	constant
7.....	constant	0	constant
8.....	variable	variable	constant

[a] in units of linear size
[b] cooling function based on the assumption of collisional ionization equilibrium
[c] equation of state
[d] photoionization equilibrium calculated assuming that the gas is fully ionized inside the HII region
[e] thermal and radiative ionization of hydrogen
[f] explicit calculation of important cooling processes for lower temperatures and CIE for high temperatures

References.—(1) Różyczka (1985); Różyczka & Tenorio-Tagle (1985a,b). (2) Stone et al. (1995). (3) GML1; GLM2. (4) García-Segura & Franco (1996). (5) Brighenti & D'Ercole (1997). (6) Frank et al. (1998). (7) Strickland & Stevens (1998). (8) This thesis.

a "two-lobe" X-ray morphology that is qualitatively in agreement with the observation of NGC 6888 (Wrigge et al. 1994) but cannot reproduce the small filling factor of the X-ray-emitting gas.

Frank et al. (1998) tried a different approach: they modeled the interaction of an anisotropic fast wind with an isotropic slow wind to explain the morphology of LBV bubbles. They found that anisotropic fast winds can indeed produce strongly bipolar outflows without assuming that the fast wind collides with a slowly expanding disk or torus as previously postulated.

Strickland & Stevens (1998) calculated simple MS bubbles blown by a wind with constant mass-loss rate and terminal velocity into a uniform ISM. Their main goal was to calculate synthetic X-ray spectra from these numerical models as they would be observed with the *ROSAT* satellite, in order to analyze these spectra according to standard procedures and to compare the inferred properties with the original numerical models. Surprisingly (or not), they found that the inferred properties of the bubble can considerably deviate from the "real" properties of the model bubble. This implies that detailed X-ray emission models are necessary, instead of simple one- or two-temperature spectral fits, in order to derive reliable properties of bubbles and superbubbles.

In Table 2.2 we compare the numerical hydrodynamic models of SWBs/HII regions quoted above with respect to the included physics, the covered range of parameters, and some technical properties.

Chapter 3

Numerical Method

3.1 Hydrodynamics

The basic equations that govern the dynamical evolution of a single-fluid, non-viscous gas system are the equations for mass- momentum- and energy conservation:

$$\frac{\partial \rho}{\partial t} + \vec{\nabla} \cdot (\rho \vec{v}) \;=\; 0 \;, \tag{3.1}$$

$$\frac{\partial \vec{v}}{\partial t} + \left(\vec{v} \cdot \vec{\nabla}\right) \vec{v} + \frac{1}{\rho} \vec{\nabla} P + \vec{\nabla} \Phi \;=\; 0 \;, \tag{3.2}$$

$$\frac{\partial e}{\partial t} + \vec{\nabla} \cdot (e \vec{v}) + P \vec{\nabla} \cdot \vec{v} + \Lambda - \Gamma \;=\; 0 \;, \tag{3.3}$$

where $t, \rho, P, \Phi, e, \Lambda, \Gamma$ denote the time, density, thermal pressure, gravitational potential, thermal energy density, energy sink terms (cooling), and energy source terms (heating), respectively. $\vec{v}$ is the velocity. Momentum transfer from radiation to the gas is not considered.

We use cylindrical coordinates (r, ϕ, z) with the z-direction parallel to the rotation axis. We furthermore reduce the problem to 2 dimensions and assume symmetry around the z-axis ($\partial / \partial \phi = 0$). Rotation around the z-axis is also not considered ($v_\phi = 0$). Thus, equations 3.1 to 3.3 reduce to

$$\frac{\partial \rho}{\partial t} + \frac{1}{r} \frac{\partial}{\partial r} (r \rho v_r) + \frac{\partial}{\partial z} (\rho v_z) \;=\; 0 \;, \tag{3.4}$$

$$\frac{\partial v_r}{\partial t} + v_r \frac{\partial v_r}{\partial r} + v_z \frac{\partial v_r}{\partial z} + \frac{1}{\rho} \frac{\partial P}{\partial r} + \frac{1}{\rho} \frac{\partial \Phi}{\partial r} \;=\; 0 \;, \tag{3.5}$$

$$\frac{\partial v_z}{\partial t} + v_r \frac{\partial v_z}{\partial r} + v_z \frac{\partial v_z}{\partial z} + \frac{1}{\rho} \frac{\partial P}{\partial z} + \frac{1}{\rho} \frac{\partial \Phi}{\partial z} \;=\; 0 \;, \tag{3.6}$$

$$\frac{\partial e}{\partial t} + \frac{1}{r} \frac{\partial}{\partial r} (r e v_r) + \frac{\partial}{\partial z} (e v_z) + \frac{P}{r} \frac{\partial}{\partial r} (r v_r) + P \frac{\partial v_z}{\partial z} + \Lambda - \Gamma \;=\; 0 \;, \tag{3.7}$$

with v_r and v_z being the velocity components in the radial and vertical direction, respectively.

The gravitational potential $\Phi_{\rm gas}$ that results from the distribution of gas is given by the solution of the Poisson equation

$$\Delta\Phi_{\rm gas} = 4\pi G\rho \ , \tag{3.8}$$

where G is the gravitation constant. This equation can be solved with an ADI algorithm (Black & Bodenheimer 1975; Press et al. 1992). To obtain the entire gravitational potential Φ, the mass of the star $M_\star$ has to be taken into account:

$$\Phi = \Phi_{\rm gas} - \frac{GM_\star}{r} \ . \tag{3.9}$$

However, we do not consider gravity in the simulations presented in this thesis because owing to the limited mass in our computational domain, gravitation is not an important force term on the timescales we are interested in.

To close the system of equations 3.4 to 3.7, we use the equation of state (EOS) for an ideal gas that consists of molecular, neutral, and ionized hydrogen. In thermal equilibrium, the thermal pressure P in the gas is the sum of the partial pressure of these three components, $P_{\rm H_2}, P_{\rm HI}, P_{\rm HII}$:

$$\begin{aligned} P &= P_{\rm H_2} + P_{\rm HI} + P_{\rm HII} \\ &= n_{\rm H_2}\, k_{\rm B}\, T + n_{\rm HI}\, k_{\rm B}\, T + 2\, n_{\rm HII}\, k_{\rm B}\, T \\ &= \frac{\rho_{\rm H_2}}{2\, m_{\rm H}}\, k_{\rm B}\, T + \frac{\rho_{\rm HI}}{m_{\rm H}}\, k_{\rm B}\, T + \frac{2\,\rho_{\rm HII}}{m_{\rm H}}\, k_{\rm B}\, T \\ &= \frac{\rho\, Y_{\rm H_2}}{2\, m_{\rm H}}\, k_{\rm B}\, T + \frac{\rho\, Y_{\rm HI}}{m_{\rm H}}\, k_{\rm B}\, T + \frac{2\,\rho\, Y_{\rm HII}}{m_{\rm H}}\, k_{\rm B}\, T \\ &= \frac{\rho\, k_{\rm B}\, T}{m_{\rm H}} \left(\frac{1}{2}\, Y_{\rm H_2} + Y_{\rm HI} + 2\, Y_{\rm HII} \right) \ . \end{aligned} \tag{3.10}$$

Here, $n_{\rm H_2}, n_{\rm HI}$, and $n_{\rm HII}$ are the particle number densities of molecular, neutral, and ionized hydrogen, respectively, and $Y_{\rm H_2} = \rho_{\rm H_2}/\rho$, $Y_{\rm HI} = \rho_{\rm HI}/\rho$, and $Y_{\rm HII} = \rho_{\rm HII}/\rho$ are the mass fractions of these three species with the normalization $Y_{\rm H_2} + Y_{\rm HI} + Y_{\rm HII} = 1$. $\rho_{\rm H_2}, \rho_{\rm HI}$, and $\rho_{\rm HII}$ are the mass densities of the three species. T is the equilibrium gas temperature and $k_{\rm B}$ is the Boltzmann constant. $m_{\rm H}$ is the hydrogen atomic mass.

On the other hand, the internal energy density e is the sum of the partial energy densities $e_{\rm H_2}, e_{\rm HI}$, and $e_{\rm HII}$:

$$\begin{aligned} e &= e_{\rm H_2} + e_{\rm HI} + e_{\rm HII} \\ &= \frac{P_{\rm H_2}}{(\gamma_{\rm H_2} - 1)} + \frac{P_{\rm HI}}{(\gamma_{\rm HI} - 1)} + \frac{P_{\rm HII}}{(\gamma_{\rm HII} - 1)} \\ &= \frac{\rho_{\rm H_2}\, k_{\rm B}\, T}{2\, m_{\rm H}\, (\gamma_{\rm H_2} - 1)} + \frac{\rho_{\rm HI}\, k_{\rm B}\, T}{m_{\rm H}\, (\gamma_{\rm HI} - 1)} + \frac{2\,\rho_{\rm HII}\, k_{\rm B}\, T}{m_{\rm H}\, (\gamma_{\rm HII} - 1)} \\ &= \frac{\rho\, Y_{\rm H_2}\, k_{\rm B}\, T}{2\, m_{\rm H}\, (\gamma_{\rm H_2} - 1)} + \frac{\rho\, Y_{\rm HI}\, k_{\rm B}\, T}{m_{\rm H}\, (\gamma_{\rm HI} - 1)} + \frac{2\,\rho\, Y_{\rm HII}\, k_{\rm B}\, T}{m_{\rm H}\, (\gamma_{\rm HII} - 1)} \\ &= \frac{\rho\, k_{\rm B}\, T}{m_{\rm H}} \left(\frac{Y_{\rm H_2}}{2\, (\gamma_{\rm H_2} - 1)} + \frac{Y_{\rm HI}}{(\gamma_{\rm HI} - 1)} + \frac{2\, Y_{\rm HII}}{(\gamma_{\rm HII} - 1)} \right) \ . \end{aligned}$$

With the adiabatic exponents (ratios of specific heats) for molecular gas ($\gamma_{\rm H_2} = 7/5$) and for monoatomic (neutral and ionized) gas ($\gamma_{\rm HI} = \gamma_{\rm HII} = 5/3$), one gets:

$$e \;=\; \frac{\rho\, k_{\rm B}\, T}{m_{\rm H}} \left(\frac{5}{4} Y_{\rm H_2} + \frac{3}{2} Y_{\rm HI} + 3\, Y_{\rm HII} \right) \;. \tag{3.11}$$

From equations 3.10 and 3.11 we obtain the equation of state that we use in our calculations:

$$P \;=\; e \left(\frac{2\, Y_{\rm H_2} + 4\, Y_{\rm HI} + 8\, Y_{\rm HII}}{5\, Y_{\rm H_2} + 6\, Y_{\rm HI} + 12\, Y_{\rm HII}} \right) \;. \tag{3.12}$$

3.2 Radiative Transfer

We consider the transfer of Lyman continuum photons in the gas around the star. The star is the primary source of Lyman continuum photons in our system. These photons move through the circumstellar gas and are absorbed either by gas or by dust, or they are scattered by hydrogen atoms in the course of an ionization and successive recombination directly into the ground state. (Scattering by dust is not considered.) Thus, for the treatment of the radiation transfer we distinguish the two components, Lyman continuum photons emitted by the star and those scattered by hydrogen.

The transfer of the stellar Lyman continuum photons emitted by a point source (the star) is calculated along the radial lines of sight shown in Figure 3.1 according to

$$\vec{\nabla} \cdot \vec{F}_\star \;=\; -\left(n_{\rm HI} \sigma_\star + \kappa_\star \right) F_\star \;. \tag{3.13}$$

In our geometry that translates to

$$\frac{1}{r^2} \frac{\partial}{\partial r} \left(r^2 F_\star \right) \;=\; -\left(n_{\rm HI} \sigma_\star + \kappa_\star \right) F_\star \;. \tag{3.14}$$

We use the gray approximation; i.e., we do not consider the frequency dependence in the transfer equation and use frequency-averaged values instead. Thus, $F_\star = |\vec{F}_\star|$ is the flux of stellar Lyman continuum photons (by number per unit time and unit surface parallel to the surface of the star), $\sigma_\star$ is the photoionization cross section of hydrogen (e.g., Osterbrock 1989) averaged over the Lyman continuum photons emitted by the star, and $\kappa_\star$ is the dust extinction coefficient. We use

$$\kappa_\star \;=\; \rho \times 300\,{\rm cm^2\,g^{-1}} \;, \tag{3.15}$$

the same value that Yorke & Welz (1996) employed.

For simplicity, we assume that the spectrum of the star resembles that of a black body at the effective temperature of the star, $T_{\rm eff}$ (an assumption, which is certainly not true but of acceptable accuracy within the framework of our approach), so that the number of Lyman continuum photons emitted by the star per second can be calculated as

$$S_\star \;=\; L_\star \times \int_{\nu_{\rm LyC}}^{\infty} \frac{B_\nu\left(T_{\rm eff}\right)}{h\nu}\, {\rm d}\nu \;\Big/\; \int_0^\infty B_\nu\left(T_{\rm eff}\right)\, {\rm d}\nu \;, \tag{3.16}$$

where $L_\star$ is the photon luminosity of the star, B_ν the Planck function, and ν_{LyC} the frequency at the Lyman threshold. With the boundary condition

$$F_\star(r_0) \;=\; \frac{S_\star}{4\pi\, r_0^2} \tag{3.17}$$

for an r_0 close to the surface of the star, equation 3.14 has the solution

$$F_\star(r) \;=\; \frac{S_\star}{4\pi\, r^2}\, \exp(-\mathcal{T}) \;, \tag{3.18}$$

with the optical depth

$$\mathcal{T} \;=\; \int_{r_0}^{r} (n_{\mathrm{HI}}\, \sigma_\star + \kappa_\star)\, \mathrm{d}r \;. \tag{3.19}$$

Finally, the space density of Lyman continuum photons $\hat{u}_\star$ can be obtained from

$$\hat{u}_\star \;=\; \frac{F_\star}{c} \;. \tag{3.20}$$

Since we use a gray approximation to the radiation transfer and thus do not account for selective photon absorption (which happens due to the higher photoionization cross section closer to the Lyman threshold), effects like "photon hardening" with its associated temperature gradient within the HII region cannot be expected to be seen in our models. The mean energy of the stellar Lyman continuum photons is everywhere the same within the ionized nebula and can be calculated as

$$\langle h\nu \rangle_\star \;=\; \int_{\nu_{\mathrm{LyC}}}^{\infty} B_\nu\,(T_{\mathrm{eff}})\; \mathrm{d}\nu \;\Big/\; \int_{\nu_{\mathrm{LyC}}}^{\infty} \frac{B_\nu\,(T_{\mathrm{eff}})}{h\nu}\, \mathrm{d}\nu \;. \tag{3.21}$$

The second radiation component are the photons that are emitted in the course of hydrogen recombinations directly into the ground state. The transfer of this diffuse component can be calculated according to Yorke & Welz (1996):

$$\frac{\partial \hat{u}_{\mathrm{rec}}}{\partial t} \;=\; -\,\vec{\nabla}\cdot\vec{F}_{\mathrm{rec}} + \alpha_1(T)\, n_{\mathrm{HII}}^2 - (n_{\mathrm{HI}}\sigma_{\mathrm{rec}} + \kappa_{\mathrm{rec}})\, \hat{u}_{\mathrm{rec}} c \;, \tag{3.22}$$

where $\vec{F}_{\mathrm{rec}}$ is the flux and $\hat{u}_{\mathrm{rec}}$ the space density of the diffuse photons, $\alpha_1(T)$ is the coefficient for hydrogen recombinations directly into the ground state (e.g., Osterbrock 1989), σ_{rec} is the photoionization cross section of hydrogen and κ_{rec} the dust extinction coefficient for the diffuse component. For this, we use the same value as for the stellar photons:

$$\kappa_{\mathrm{rec}} \;=\; \rho \times 300\,\mathrm{cm^2\,g^{-1}} \;. \tag{3.23}$$

In order to solve equation 3.22, it is necessary to find a closure relation that connects $\hat{u}_{\mathrm{rec}}$ with $\vec{F}_{\mathrm{rec}}$. Levermore & Pomraning (1981) proposed the flux-limited diffusion approximation (FLD):

$$\vec{F}_{\mathrm{rec}} \;=\; -\,\frac{\lambda c}{n_{\mathrm{HI}}\sigma_{\mathrm{rec}} + \kappa_{\mathrm{rec}}}\vec{\nabla}\hat{u}_{\mathrm{rec}} \;, \tag{3.24}$$

with the flux limiter

$$\lambda \;=\; \frac{1}{S}\left(\coth S - \frac{1}{S}\right) \;, \tag{3.25}$$

where

$$S \;=\; \frac{|\vec{\nabla}\hat{u}_{\rm rec}|}{(n_{\rm HI}\sigma_{\rm rec}+\kappa_{\rm rec})\,\hat{u}_{\rm rec}}\;. \tag{3.26}$$

For the two extreme cases (optically thick and optically thin) the correct limits for $\vec{F}_{\rm rec}$ are obtained:

$$\vec{F}_{\rm rec} \rightarrow \begin{cases} -\frac{1}{3}\frac{c\,\vec{\nabla}\hat{u}_{\rm rec}}{\chi_{\rm rec}} & : \quad S \rightarrow 0 \quad \text{(diffusion approximation, optically thick)} \\ c\,\hat{u}_{\rm rec}\frac{\vec{\nabla}\hat{u}_{\rm rec}}{|\vec{\nabla}\hat{u}_{\rm rec}|} & : \quad S \rightarrow \infty \quad \text{(streaming approximation, optically thin)} \end{cases}\;, \tag{3.27}$$

with

$$\chi_{\rm rec} \;=\; n_{\rm HI}\sigma_{\rm rec}+\kappa_{\rm rec}\;. \tag{3.28}$$

Inserting equation 3.24 into equation 3.22 yields the remaining partial differential equation to be solved in order to obtain the space density of these recombination photons:

$$\frac{\partial\hat{u}_{\rm rec}}{\partial t} \;=\; \vec{\nabla}\cdot\left(\frac{\lambda\,c}{\chi_{\rm rec}}\vec{\nabla}\hat{u}_{\rm rec}\right)+\alpha_1(T)\,n_{\rm HII}^2-\chi_{\rm rec}\hat{u}_{\rm rec}c\;. \tag{3.29}$$

The mean energy of the diffuse photons, $\langle h\nu\rangle_{\rm rec}$, depends on the gas temperature T and is derived from tables in Osterbrock (1989). In HII regions with their typical temperature of $T \approx 8000\,{\rm K}$ we have $\langle h\nu\rangle_{\rm rec} \approx 14.3\,{\rm eV}$.

An even simpler treatment of this diffuse radiation component is the so-called "on-the-spot" approximation (OSA). Here it is assumed that the photons that are produced by hydrogen recombinations directly into the ground state are re-absorbed by neutral hydrogen on the spot. Since the thermal energy of the free electrons in the HII region is generally small compared to the 13.6 eV ionization potential of hydrogen, the energy of the diffuse photons is close to the Lyman threshold, and since the photoionization cross section is highest for photons just above this threshold, it is plausible that these diffuse photons are absorbed close to their origin rather than moving long distances through the ISM.

The OSA can be implemented very easily in the numerical scheme by replacing the hydrogen recombination coefficient into all states, $\alpha_{\rm A}(T)$, in equation 3.32 with the hydrogen recombination coefficient for recombinations into all states except the ground state, $\alpha_{\rm B}(T)$, and setting $\hat{u}_{\rm rec}$ to 0. In order to save computational time, this method is widely used for the computations presented in this thesis.

3.3 Dissociation and Ionization

The fractions of molecular, neutral, and ionized hydrogen are calculated in every grid cell according to density, temperature, and Lyman continuum photon density. The thermal dissociation of molecular hydrogen is calculated according to Black & Bodenheimer (1975):

$$\frac{\left(1-\hat{Y}_{\rm H_2}\right)^2}{\hat{Y}_{\rm H_2}} \;=\; \frac{2.11}{\rho/({\rm g\,cm^{-3}})}\exp\left(\frac{-52490}{T/{\rm K}}\right)\;, \tag{3.30}$$

with the following limitation by the fraction of ionized hydrogen:

$$Y_{\mathrm{H_2}} = \hat{Y}_{\mathrm{H_2}} \left[(2000\, Y_{\mathrm{HII,lim}} - 300)\, Y_{\mathrm{HII,lim}}^2 + 1 \right] , \tag{3.31}$$

where $Y_{\mathrm{HII,lim}} = \min(Y_{\mathrm{HII}}, 0.1)$. The formation and dissociation of molecular hydrogen is not yet considered in the energy balance because it is assumed that continuum radiation below the Lyman threshold dissociates the molecules before the gas is heated up to temperatures where thermal dissociation occurs.

In order to calculate the degree of hydrogen ionization in the gas, X, the effects of photoionization, collisional ionization (by collisions with electrons), and radiative recombination are considered according to

$$\frac{\partial \rho X}{\partial t} + \vec{\nabla} \cdot (\rho X \vec{v}) = \rho\,(1-X)\,[\sigma_\star \hat{u}_\star + \sigma_{\mathrm{rec}} \hat{u}_{\mathrm{rec}}]\, c + \frac{\rho^2}{m_{\mathrm{H}}} C(T) X (1-X) - \frac{\rho^2}{m_{\mathrm{H}}} \alpha_{\mathrm{A}}(T) X^2 , \tag{3.32}$$

where we use

$$C(T) = 5.949 \times 10^{-11} \sqrt{T/\mathrm{K}} \exp\left(\frac{-1.577 \times 10^5}{T/\mathrm{K}} \right) \ \mathrm{cm^3\,s^{-1}} \tag{3.33}$$

as rate coefficient for ionization of hydrogen from the ground state by collisions with thermal electrons. $\alpha_{\mathrm{A}}(T)$ is the hydrogen recombination coefficient into all states, which has been taken from Osterbrock (1989). The photon density $\hat{u}_{\mathrm{rec}}$ is derived from the solution of the radiation transfer.

3.4 Heating Processes

In equation 3.7 Γ summarizes the heating rates per unit volume due to various microphysical processes. The following heating processes are considered in the models presented in this work.

3.4.1 Heating by Photoionization of Hydrogen

In a photoionization event, the difference between the photon energy and the ionization potential of hydrogen (χ_{HI}) is transferred to the kinetic energy of the liberated electron and thus contributes to the heating of the gas. The resulting heating rate is

$$\Gamma_\star = \frac{\rho}{m_{\mathrm{H}}} (1-X) \sigma_\star\ c\ \hat{u}_\star\, (\langle h\nu \rangle_\star - \chi_{\mathrm{HI}}) \tag{3.34}$$

for the stellar Lyman continuum photons and

$$\Gamma_{\mathrm{rec}} = \frac{\rho}{m_{\mathrm{H}}} (1-X) \sigma_{\mathrm{rec}}\ c\ \hat{u}_{\mathrm{rec}}\, (\langle h\nu \rangle_{\mathrm{rec}} - \chi_{\mathrm{HI}}) \tag{3.35}$$

for the diffuse recombination photons.

3.4.2 Heating by Photoejection of Electrons from Dust Grains by Lyα Photons

A hydrogen recombination into a level above the ground state produces a Lyman series photon in the course of the subsequent de-excitation of the H atom. Since most of the hydrogen atoms remain in the ground state under typical interstellar conditions, this Lyman series photon can be scattered many times by neutral hydrogen atoms before it either leaves the nebula or is absorbed by dust. "Scattered" means that it is absorbed and re-emitted by neutral hydrogen, possibly with further cascading, most likely finally resulting in a Lyα photon.

We follow Maciel & Pottasch (1982) and estimate the binding energy of the electrons in the dust grains to be $E_{\rm bind} \approx 8\,{\rm eV}$. Thus, if the Ly$\alpha$ photon is absorbed by dust, it can lead to the ejection of an electron from the dust grain since the energy of the Lyα photon $E_{{\rm Ly}\alpha} \approx 10.2\,{\rm eV}$ is higher than the binding energy of the electrons in the dust grain. The excess energy $E_{{\rm Ly}\alpha} - E_{\rm bind}$ can be thermalized in the gas. The probability that the impact of a Lyα photon on a dust grain leads to an electron ejection (the so-called grain photoelectric yield) is $Y_{{\rm Ly}\alpha} = 0.11$ (Maciel & Pottasch 1982). We do not calculate the detailed radiation transfer of the Lyα photons, instead we use the "on-the-spot" approximation and thus get the following contribution to the heating rate by this effect:

$$\Gamma_{\rm pe} \;=\; n_{\rm e}\, n_{\rm HII}\, \alpha_{\rm B}(T)\, f_{{\rm Ly}\alpha}\, Y_{{\rm Ly}\alpha}\, (E_{{\rm Ly}\alpha} - E_{\rm bind}) \;, \tag{3.36}$$

where $f_{{\rm Ly}\alpha}$ is the fraction of all hydrogen recombinations into levels above the ground state that produce Lyα photons. We use $f_{{\rm Ly}\alpha} = 0.7$ according to Spitzer (1978).

3.5 Cooling Processes

In equation 3.7 Λ summarizes the cooling rates per unit volume due to various microphysical processes. For the computation of the cooling rates we distinguish two regimes, the high-temperature regime, where $T > 10^5\,{\rm K}$, and the low-temperature regime, where $T < 15000\,{\rm K}$. For the high-temperature regime we use the interstellar cooling function from Sarazin & White (1987) with the correction given by Soker (1990). This cooling function is based on the assumption of collisional ionization equilibrium. For the low-temperature regime the contributions from the most important cooling processes are explicitely calculated. They are described in the following sections. In the intermediate-temperature range between 15000 K and $10^5\,{\rm K}$ we calculate both values and use a weighted average.

3.5.1 Cooling by Recombination of Hydrogen

A recombination of an electron with a proton lowers the thermal energy of the gas by the kinetic energy of the electron, i.e.,

$$\Lambda_{\rm rec} \;=\; n_{\rm e}\, n_{\rm HII}\, \alpha_{\rm A}(T)\, \xi_{\rm A}\, k_{\rm B}\, T \;. \tag{3.37}$$

$\xi_A\, k_B\, T$ is the effective thermal energy loss per recombination and is extracted from tables in Osterbrock (1989). It is always less than $3\, k_B\, T/2$ because the recombination probability is higher for slow electrons. For $T = 8000\,\mathrm{K}$, the typical temperature in HII regions, we have $\xi_A \approx 0.79$.

If the OSA is used instead of the FLD for the treatment of the diffuse Lyman continuum photons, α_A and ξ_A have to be replaced by α_B and ξ_B, the respective values for all recombinations except those directly into the ground state. Then we have $\xi_B \approx 0.69$ for $T = 8000\,\mathrm{K}$.

3.5.2 Cooling by Collisional Ionization of Hydrogen

The collision of a thermal electron with a neutral hydrogen atom can lead to ionization of the hydrogen atom if the electron is fast enough. Each of these collisional ionizations removes 13.6 eV thermal energy from the gas. Thus, we have for the cooling via this process

$$\Lambda_{\mathrm{collion}} \;=\; n_e\, n_{HI}\, C(T)\, \chi_{HI}\ , \tag{3.38}$$

where $C(T)$ is calculated according to equation 3.33.

3.5.3 Cooling by Bremsstrahlung

The cooling due to bremsstrahlung of electrons in the potential of the protons is calculated according to Osterbrock (1989):

$$\Lambda_{\mathrm{brems}} \;\approx\; 1.42\times10^{-27}\, g_{ff} \sqrt{\frac{T}{\mathrm{K}}} \left(\frac{n_e}{\mathrm{cm}^{-3}}\right) \left(\frac{n_{HII}}{\mathrm{cm}^{-3}}\right) \mathrm{erg\ cm^{-3}\ s^{-1}}\ . \tag{3.39}$$

For the sake of simplicity we have used $g_{ff} = 1$ as Gaunt factor for free-free emission.

3.5.4 Cooling by Collisionally Excited Lyα Emission of Hydrogen

For the cooling by collisionally cxcited Lyα emission of hydrogen we use the formula given by Penston (1970):

$$\Lambda_{\mathrm{Ly}\alpha} \;\approx\; 5.27\times10^{-21} \left(\frac{n_{HI}}{\mathrm{cm}^{-3}}\right) \left(\frac{n_e}{\mathrm{cm}^{-3}}\right) \sqrt{\frac{T}{\mathrm{K}}} \left(1+\frac{17500}{T/\mathrm{K}}\right) \exp\left(\frac{-118400}{T/\mathrm{K}}\right) \mathrm{erg\ cm^{-3}\ s^{-1}}\ . \tag{3.40}$$

3.5.5 Cooling by Forbidden Lines of Oxygen and Nitrogen

We have considered cooling by the most important forbidden lines of oxygen and nitrogen. The cooling rate by one of these lines is

$$\Lambda_{\mathrm{forbidden}} \;=\; n_e\, n_{\mathrm{ion}}\, q_{12}\, h\nu_{21} \left[\frac{1}{1+\frac{n_e\, q_{21}}{A_{21}}}\right]\ , \tag{3.41}$$

where the indices "1" and "2" refer to the ground state and the excited state, respectively. The transition probabilities A and the collisional excitation and de-excitation rates q are taken from Osterbrock (1989). The cooling rates according to equation 3.41 are calculated for the ${}^3P_2$–${}^1D_2$ transition of N^+ and O^{++} and the ${}^4S_{3/2}$–${}^2D_{3/2}$ transition of O^+. Simple assumptions have been made about the degree of ionization of nitrogen and oxygen in order to calculate the number density of the ions $n_{\rm ion}$: because of the similar ionization potentials and comparable recombination coefficients of H^0, N^0, and O^0, we set the ratios of ionized to neutral species for nitrogen and oxygen equal to the respective number calculated for hydrogen, i.e., $\rho_{N^+}/\rho_N = X$ and $(\rho_{O^+} + \rho_{O^{++}})/\rho_O = X$, where X is the hydrogen ionization fraction. It is furthermore assumed that the oxygen ions are equally distributed on the ionization stages O^+ and O^{++}, i.e., $\rho_{O^+}/\rho_O = \rho_{O^{++}}/\rho_O = X/2$. The chemical abundance of oxygen and nitrogen is assumed to be solar.

3.5.6 Energy Exchange of Gas and Dust

Collisions of gas particles with dust grains result in an exchange of energy between gas and dust. We have included this energy exchange for the simulations with dust according to Yorke & Welz (1996):

$$\Lambda_{\rm gas-dust} \;=\; n_{\rm H}\, n_{\rm dust}\, 4\pi\, r_{\rm dust}^2\, c_{\rm s}\, k_{\rm B}\, (T - T_{\rm dust})\;, \tag{3.42}$$

where $T_{\rm dust}$ is the temperature of the dust, $c_{\rm s}$ is the sound speed of the gas, and $r_{\rm dust} = 5 \times 10^{-6}\,{\rm cm}$ is the assumed radius of a (spherical) dust grain. With a mass density of the dust of $2.5\,{\rm g\,cm^{-3}}$ and a dust-to-gas mass ratio of 0.01, the number density of dust particles is $n_{\rm dust} = 1.3 \times 10^{-11}\, n_{\rm H}$. We set the dust temperature equal to the initial gas temperature, $T_{\rm dust} = T_0 = 200\,{\rm K}$, and, following Yorke & Welz (1996), assume that the dust temperature changes little during the course of evolution.

3.6 Discretization and Grid Arrangement

The hydrodynamical part of the code is based on algorithms used by Różyczka (1985) who followed the strategy given by Norman (1980). Equations 3.4 to 3.7 and 3.12 are solved numerically on an Eulerian grid in the quadrant with $r \geq 0$ and $z \geq 0$; i.e., we additionally assume mirror symmetry with respect to the equatorial plane. The differencing scheme used to discretize the equations is second-order accurate in space. Because of operator splitting, the accuracy in time is greater than first order. These methods are described in detail in Stone & Norman (1992a,b) and Stone et al. (1992). The advection scheme of van Leer (1977) is employed, and von Neumann–Richtmyer artificial viscosity is used for the treatment of shocks (Richtmyer & Morton 1967).

The star that influences the gas is located in the center of the coordinate system at $r = z = 0$. We use square grids with constant mesh size and insert multiply nested grids in the corner at $r = z = 0$ to enhance the spatial resolution close to the star. All the nested grids are self-similar, and the linear spatial resolution is improved by a factor of 2 for each level of nesting (see Figure 3.1).

The basic code is explicit; therefore, the Courant-Friedrichs-Lewy (CFL) condition determines the maximum time step except when changes in the stellar parameters take place on even smaller timescales. Our integration order starts with the finest grid. The size of the time step satisfies the CFL condition for the finest grid, as well as for all coarser grids (normalized by the appropriate power of 2). After two time steps have been done on the finest grid and the solution has been advanced to $t + \delta t_1 + \delta t_2$, one time step $\delta t_1 + \delta t_2$ is done on the next coarser grid to advance the solution there to the same time. Because of our prior careful choice of δt_1 and δt_2, their sum obeys the CFL condition on the next coarser grid. After the solutions on the two grid levels have been advanced to the same point in time, all coarse grid values that have underlying fine grid values (not from the boundary) are replaced by weighted averages from the fine grid. The outer boundary conditions of the fine grid are interpolated from the corresponding grid

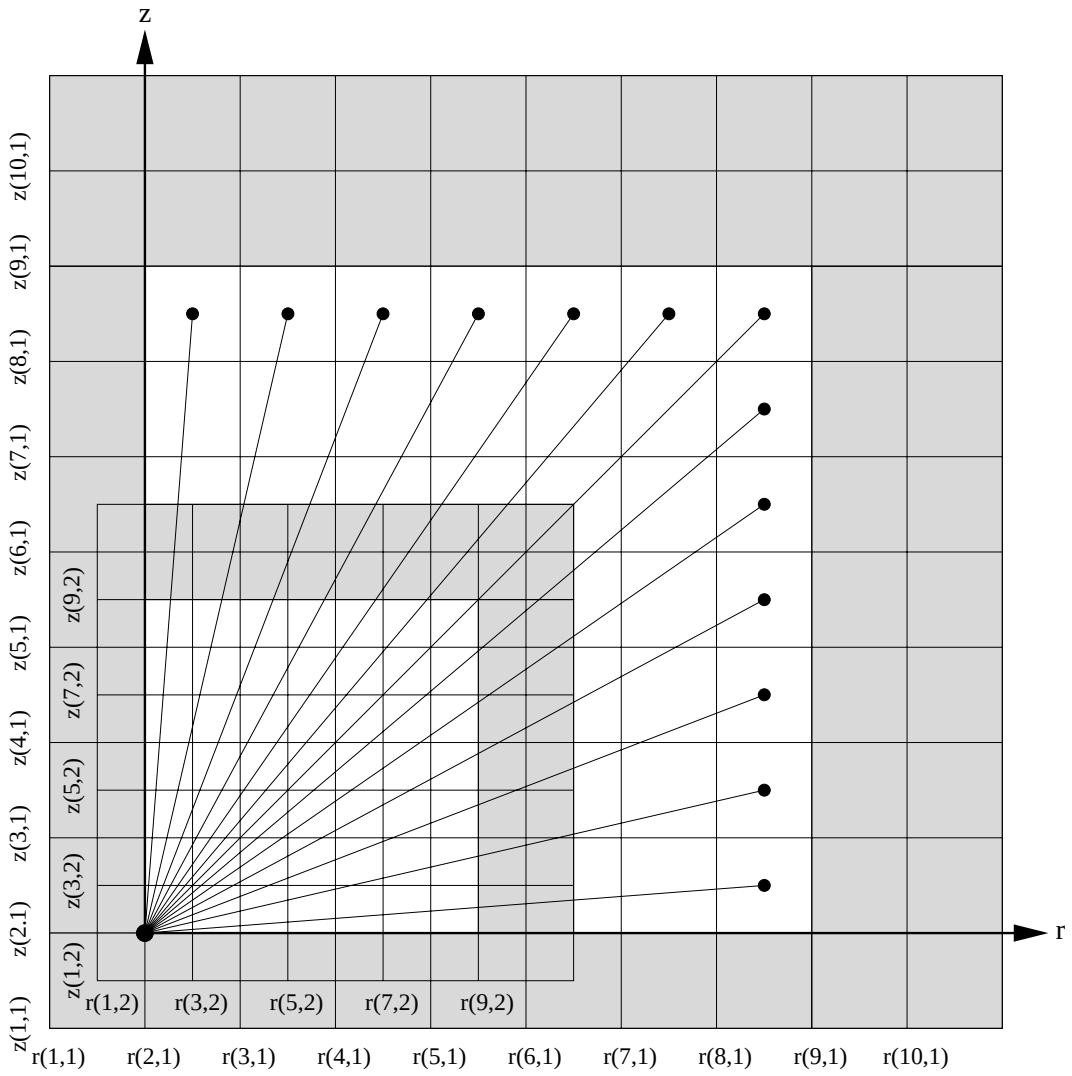

Figure 3.1: Example of the nested grid structure for two nested grids with 10×10 zones each. The ghost zones are gray shaded. 13 lines of sight would be used in this case to perform the radiation transfer. $r-$ and $z-$values of the lower left cell corners are indexed with (n, m), where n is the cell index (along the respective axis) and m the grid index.

values of the coarse grid. After this cycle is repeated (taking into account the new CFL time step constraints), the first integration on the next coarser (third-level) grid can be performed; third-level values are partly replaced by second-level values, and second-level outer boundaries are imposed from third-level values, and so on. We use this recursive scheme for seven grid levels, which means that $\sum_{i=0}^{6} 2^i = (2^7 - 1) = 127$ single integrations have to be done before one time step on the coarsest grid is completed.

The ionization structure of hydrogen is calculated for each hydrodynamical time step by including the effects of photoionization, collisional ionization, and spontaneous recombination, as described in the previous sections. The absorption of the stellar point-source Lyman continuum by neutral hydrogen (and by dust, if included) is calculated along radial lines of sight. We use $N_\mathrm{r} + N_\mathrm{z} - 1$ rays to ensure that every grid cell is traversed by at least one ray, where N_r and N_z are the numbers of grid cells in the r- and z-direction, respectively, without ghost cells (see also Figure 3.1). The optical depth $\mathcal{T}$ is defined at the intersections of the rays with the cell walls. A weighted mean for $\hat{u}_\star$ is calculated if more than one ray crosses a cell.

3.7 Initial Conditions

We start our calculations with the turn-on of the zero-age main-sequence (ZAMS) stellar radiation field and stellar wind in a homogeneous and quiescent ambient medium. This is definitely a gross oversimplification of what can be expected for the structure of the circumstellar gas shortly after the star has been formed at the end of the pre-MS phase. We have two reasons for our approach. The first is that, in order to understand what happens in the circumstellar medium, it is important to start with a well-defined and simple initial configuration. As we will show below, even with this initially homogeneous ambient density and temperature distribution, the interaction of the SWB with the ionizing radiation field produces a variety of interesting morphological structures whose formation processes have to be understood in detail before studies with a more realistic initial setup can be performed. The second reason is that we want to keep our simulations comparable with those of other authors who use different algorithms or incorporate different physical effects in their codes. We choose $n_0 = 20\,\mathrm{cm}^{-3}$ and $T_0 = 200\,\mathrm{K}$ for our quiescent ambient medium. The density is perhaps high for a star that has already left its parental molecular cloud, but we want to keep our results comparable to those of GML1 and GLM2, who also used $n_0 = 20\,\mathrm{cm}^{-3}$ in order to reduce computational expenses. The temperature $T_0 = 200\,\mathrm{K}$ in the ambient medium was chosen to yield a thermal pressure "typical" for the ISM at the solar galactocentric distance.

We use spherical one-dimensional solutions after 1000 yr (60 $\mathrm{M}_\odot$ case) or 700 yr (35 $\mathrm{M}_\odot$ case), respectively, as initial model for the two-dimensional simulations in order to prevent boundary effects from influencing the formation of the very small wind bubble while the development of the self-similar structure is not completed. We switch from one to two dimensions before the swept-up gas collapses into a thin shell that is subsequently subject to instabilities. The one-dimensional profiles used at starting time of the two-dimensional calculations are shown in Figure 3.2 for the $60\,\mathrm{M}_\odot$ case and in Figure 3.3 for the $35\,\mathrm{M}_\odot$ case.

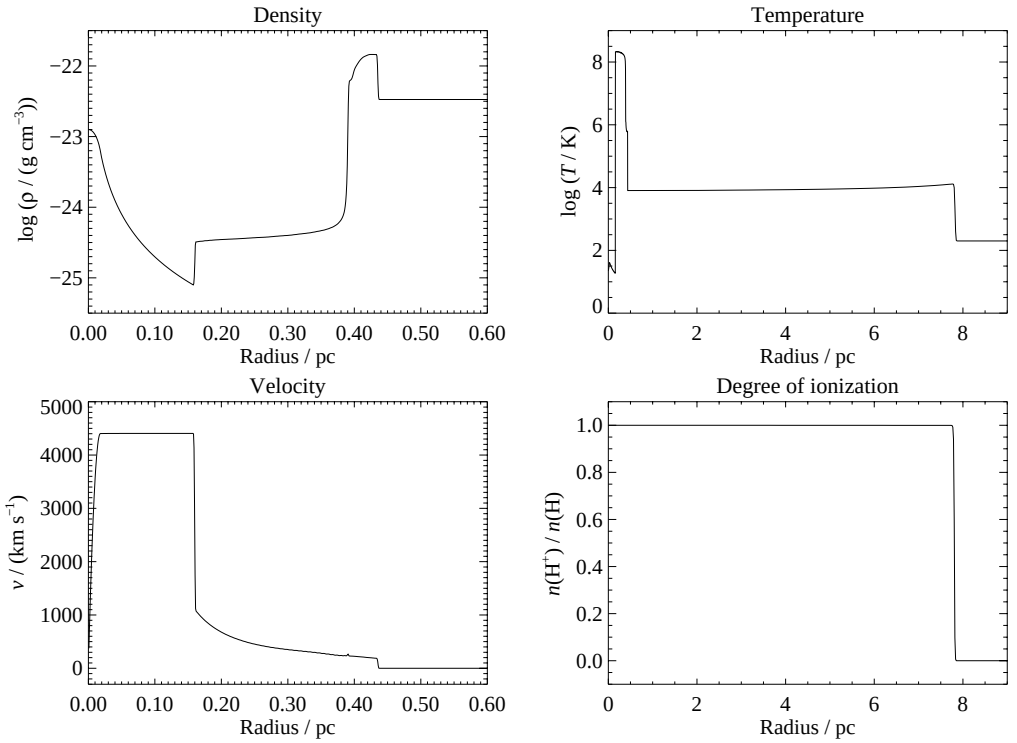

Figure 3.2: Initial conditions for the two-dimensional calculations after 1000 yr in the 60 $M_\odot$ case.

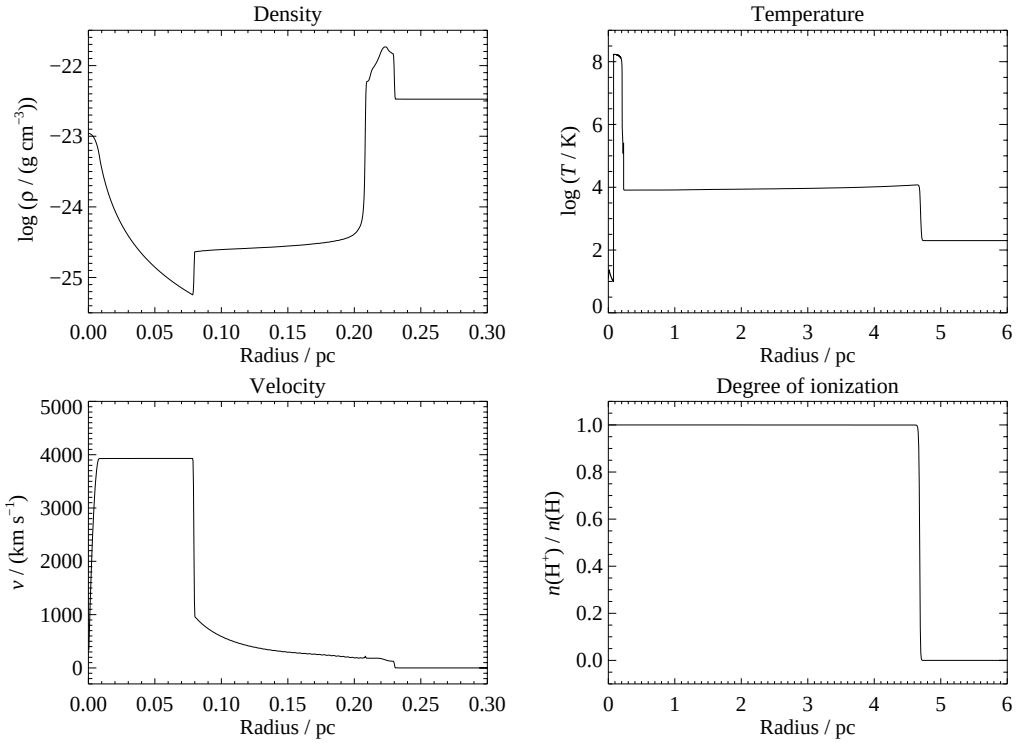

Figure 3.3: Initial conditions for the two-dimensional calculations after 700 yr in the 35 $M_\odot$ case.

3.8 Boundary Conditions

In our models the stellar parameters for mass-loss rate ($\dot{M}_{\rm w}$), terminal velocity of the wind ($v_{\rm w}$), effective temperature ($T_{\rm eff}$), and photon luminosity in the Lyman continuum ($L_{\rm LyC}$) are time-dependent boundary conditions that drive and govern the evolution of the circumstellar gas. In this thesis I present results of calculations for two different stellar tracks with initial masses of 60 and 35 $M_\odot$, respectively. For the 60 $M_\odot$ star we adopt the stellar parameters (see Figure 3.4) given by GML1, and the parameters for the 35 $M_\odot$ star (Figure 3.5) are taken from GLM2 (their version with the "fast" 75 km s^{-1} RSG wind). These stellar parameters are obtained from stellar evolutionary models and from observations. The 60 $M_\odot$ star is supposed to undergo the following evolution: MS O star → H-rich WN star → P Cygni-type LBV → H-poor WN star → H-free WN star → WC star → SN. The MS O phase lasts for about 2.8 Myr, the H-rich WN stage 0.55 Myr, the LBV phase 0.01 Myr, and the final W-R phases 0.705 Myr until the star is supposed to explode as a SN at $\tau = 4.065$ Myr and the calculation stops. For the 35 $M_\odot$ star, the following evolutionary scenario is adopted: MS O star → RSG → W-R star →

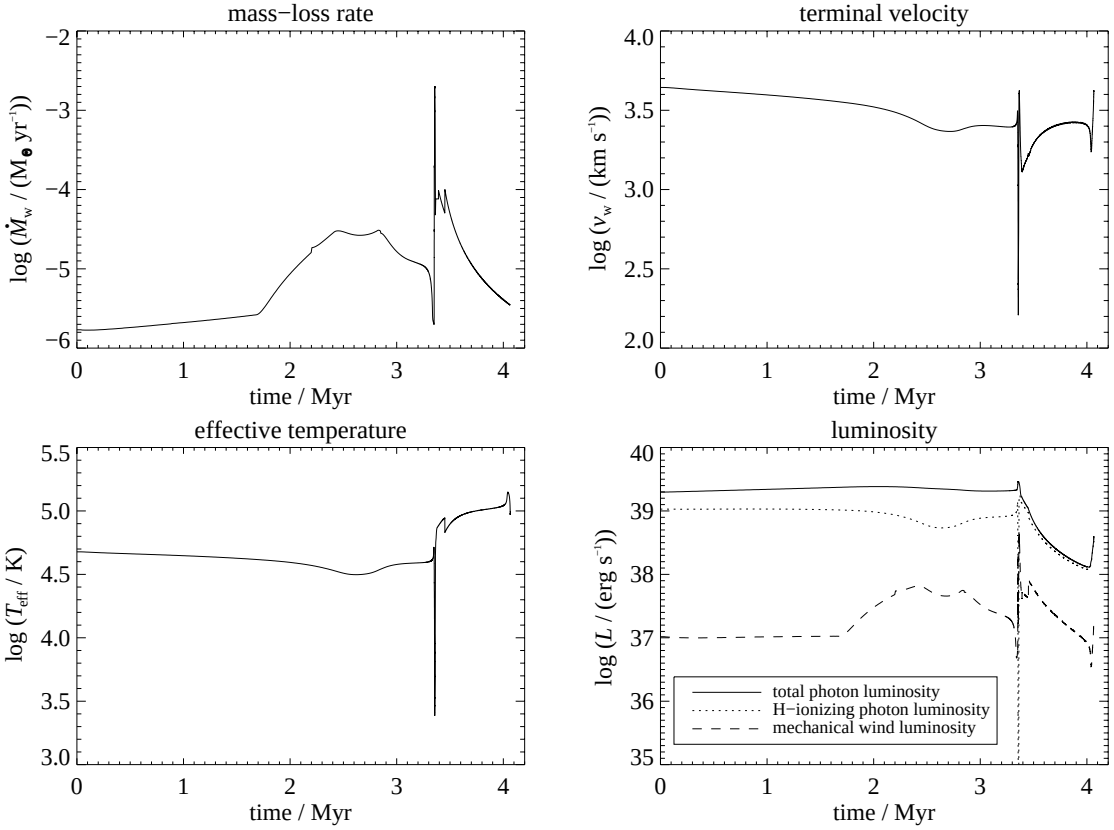

Figure 3.4: Time-dependent stellar parameters used as boundary conditions for the calculation of the 60 $M_\odot$ case: mass-loss rate (top left), terminal velocity of the wind (top right), effective temperature (bottom left), and luminosity (bottom right). All parameters are adopted from GML1.

SN. Here the MS O phase lasts for about 4.52 Myr, the RSG phase 0.234 Myr and the final W-R phase 0.191 Myr. After 4.945 Myr the star explodes as a SN.

According to the mass-loss rate and terminal velocity at time t, appropriate values for density and velocity of the gas are set within the "wind generator region" on the finest grid (a small sphere around the center of the coordinate system where the star is located). The radius of the "wind generator region" is 3.50×10^{17} cm for the 60 $M_\odot$ case and 2.16×10^{17} cm for the 35 $M_\odot$ case.

The other boundary conditions are set up as follows: At the r- and z-axes, reflecting boundary conditions are used. The outer boundaries of the nested grids were taken from the corresponding values on the next coarser grid. The outer boundaries of the outermost (coarsest) grid are semi-permeable; i.e., mass, energy, and momentum can flow out of the computational domain, but not in. Of course, outflow would conflict with our intention to carefully take stock of the energetic processes in our calculations. Thus, we prevent outflow by choosing the coarsest grid large enough that neither the ionization front nor moving material can reach the outer boundary before the star dies and the calculation stops.

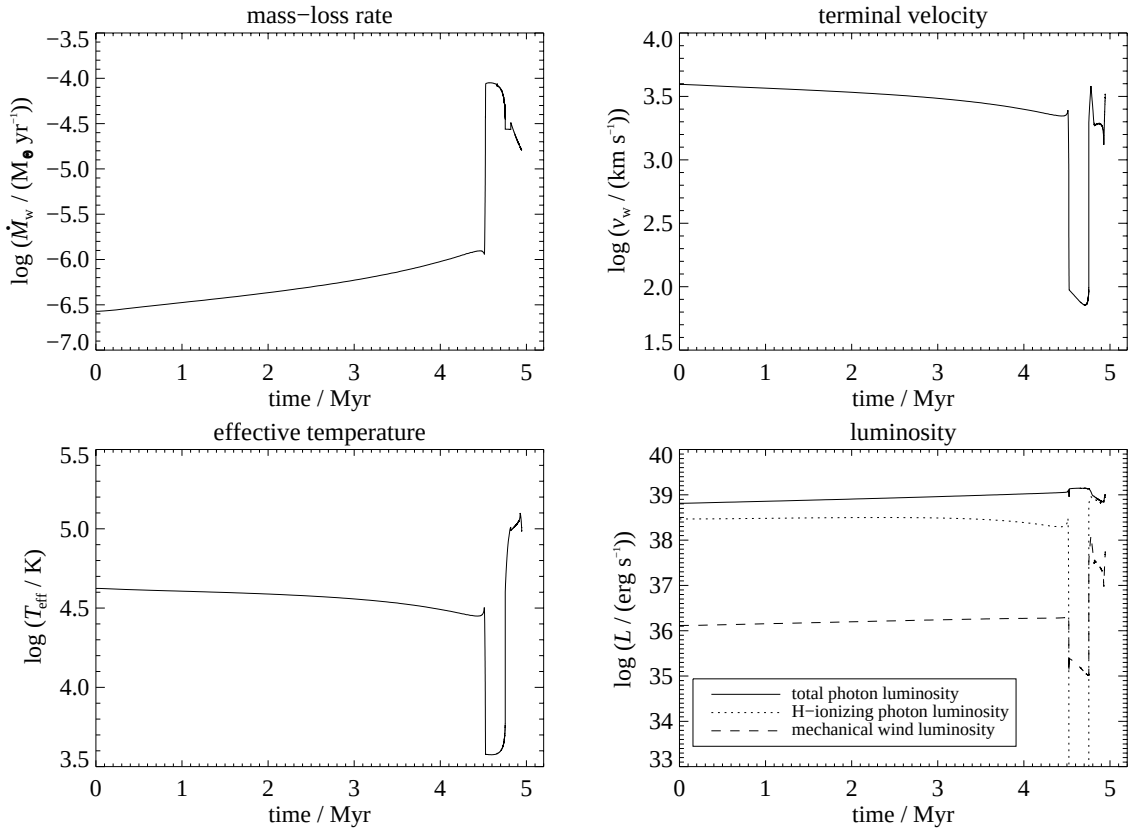

Figure 3.5: Time-dependent stellar parameters used as boundary conditions for the calculation of the 35 $M_\odot$ case: mass-loss rate (top left), terminal velocity of the wind (top right), effective temperature (bottom left), and luminosity (bottom right). All parameters are adopted from GLM2.

3.9 Geometry and Resolution

The size of the computational domain in the 60 $M_\odot$ case is $r_{\max} = z_{\max} = 64$ pc, and in the 35 $M_\odot$ case it is $r_{\max} = z_{\max} = 50$ pc. We use six nested grids within the coarsest grid, resulting in seven grid levels. The simulations have been performed with 125×125 cells on each grid level (excluding ghost cells). For a resolution study we repeat the calculations with 61×61 cells and for the first megayear of evolution with 253×253 cells. Thus, the linear resolution of the medium-resolution run (60 $M_\odot$ case) ranges from 8×10^{-3} pc close to the star to approximately 0.5 pc in the outermost parts of the coarsest grid, which were affected only during the late stages of the bubble evolution. The corresponding resolution values for the 35 $M_\odot$ case are roughly 20 % smaller because we use the same grid setup for the smaller domain.

3.10 Tests

The basic numerical algorithm has already been tested extensively (Yorke & Kaisig 1995). Nevertheless, we performed additional checks and test calculations to discuss the validity and estimate the accuracy of the results that we present in the next chapter.

3.10.1 Conservation of Mass and Energy

We start the discussion with a check of the total mass conservation. On a single grid, the algorithm is completely conservative with respect to the transfer of mass, provided that outflow through the outer boundaries is prohibited. The coupling of the grids within the multiply-nested-grids scheme (the replacement of coarse-grid values by fine-grid values and the interpolation of fine-grid outer boundary conditions from coarse-grid values) as well as a smoothing routine along the z-axis (that prevents the formation of artificial spikes there) lead to deviations from mass conservation. We determined these deviations for various simulations and show the results in Figure 3.6. We plot the deviation from the initial mass, $|\Delta M/M_0|$, where

$$\Delta M = M(\tau) - M_0 - \int_0^\tau \dot{M}_w(t)\, dt \ , \tag{3.43}$$

with $M(\tau)$ being the total mass at lifetime τ in the whole computational domain except for the wind generator region and $M_0 = M(0)$. One can see that the magnitude of the error of mass conservation varies between the different cases. Obviously, it is much lower in the windless cases, but it also depends on the set of stellar parameters and on the fact whether or not dust is considered in the calculation. However, the error is always below 1 %, and for the calculations without dust, which are presented in detail in the next chapter, it is always below 0.1 %.

Since the algorithm for the calculation of the photoionization is not strictly conservative with respect to the energy of the Lyman continuum photons, we additionally checked what fraction of the Lyman continuum luminosity of the star really enters the calculation as photoionizations of hydrogen with excess energy in the form of thermal energy. We

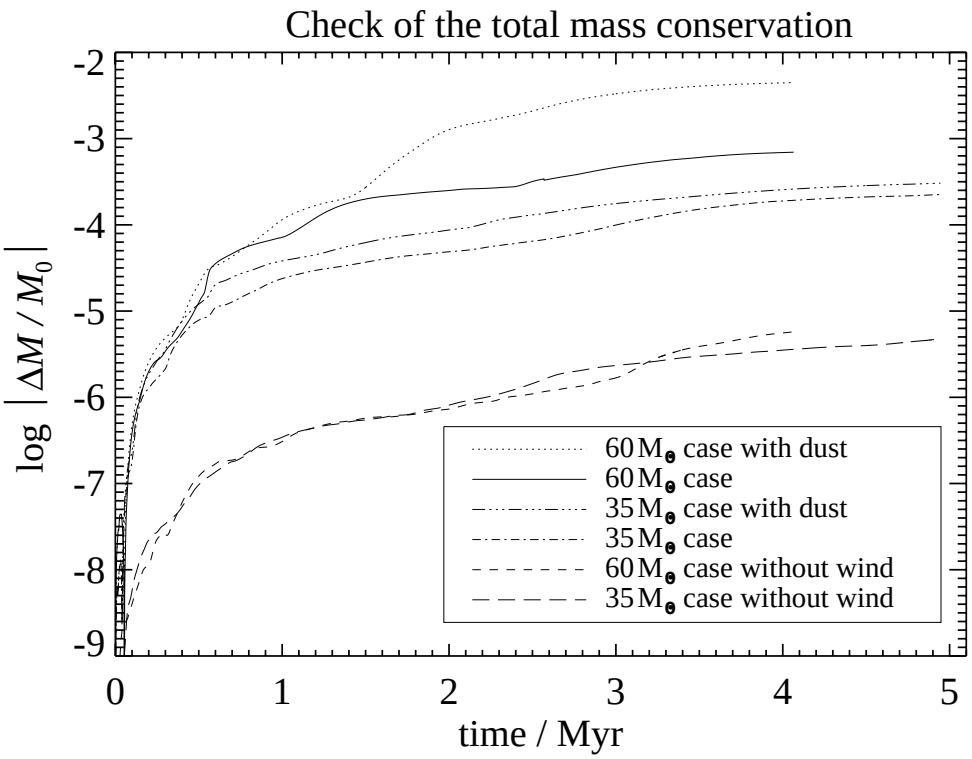

Figure 3.6: Check of the total mass conservation.

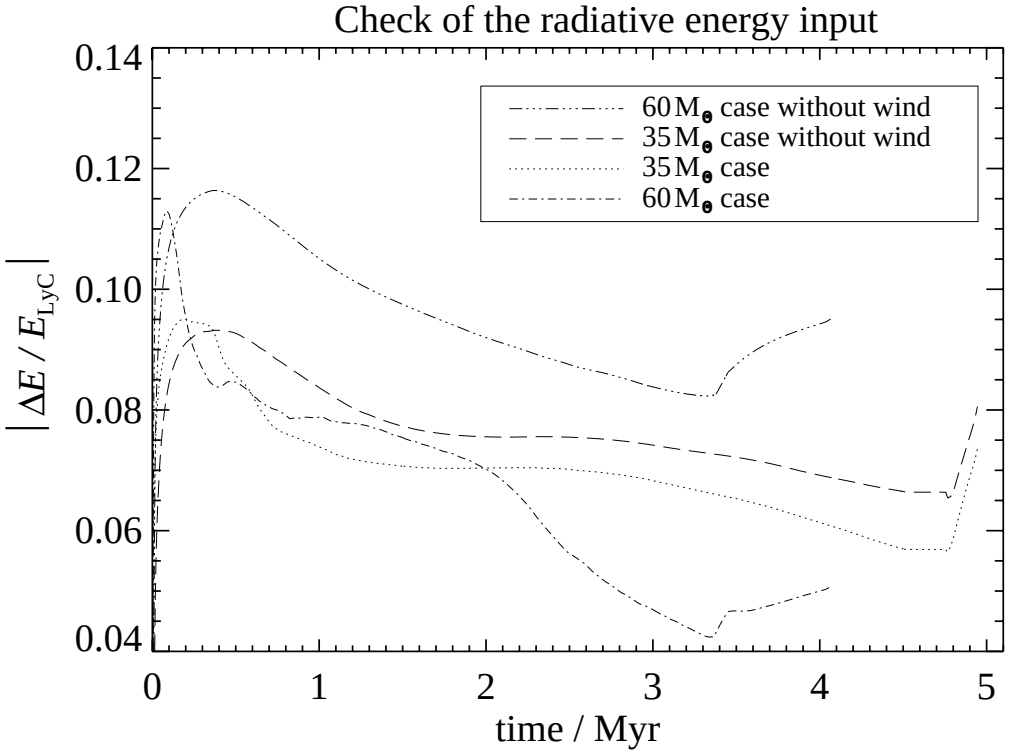

Figure 3.7: Check of the radiative energy input.

show the results in Figure 3.7 as $|\Delta E/E_{\rm LyC}|$. Here,

$$\Delta E = E_{\rm LyC}(\tau) - E_{\rm phion}(\tau) - E_{\rm ph}(\tau) \ , \tag{3.44}$$

where

$$E_{\rm LyC}(\tau) = \int_0^\tau L_{\rm LyC}(t)\, dt \tag{3.45}$$

is the energy emitted by the star in the Lyman continuum over the lifetime τ, $E_{\rm phion}(\tau)$ is the gain of ionization energy by photoionizations in our system, and $E_{\rm ph}(\tau)$ is the gain of thermal energy in the course of these photoionizations. We see that the processing of the H-ionizing radiation in the code is done with an error of 4-12 % (with respect to the total energy in the Lyman continuum radiation). This is not insignificant and it is suggested to improve this part of the algorithm for future simulations, but since this error is of the same order of magnitude than the uncertainty of the Lyman continuum luminosity in the stellar models, it is still tolerable for our calculations.

Finally, we check the total balance of the energy that enters our calculation. The results are shown in Figure 3.8 as $|\Delta E/E_{\rm gain}|$, where

$$\Delta E = E_{\rm k}(\tau) + E_{\rm t}(\tau) + E_{\rm i}(\tau) - E_0 + E_{\rm loss}(\tau) - E_{\rm gain}(\tau) \ . \tag{3.46}$$

E_0 is the thermal energy of the initially unperturbed, neutral ambient medium. $E_{\rm k}(\tau)$, $E_{\rm t}(\tau)$, and $E_{\rm i}(\tau)$ are the kinetic, thermal, and ionization energy in the circumstellar gas, respectively. $E_{\rm loss}(\tau)$ is the energy lost from the system by the various cooling processes accumulated from the beginning of the calculation until lifetime τ, and $E_{\rm gain}(\tau)$ is the

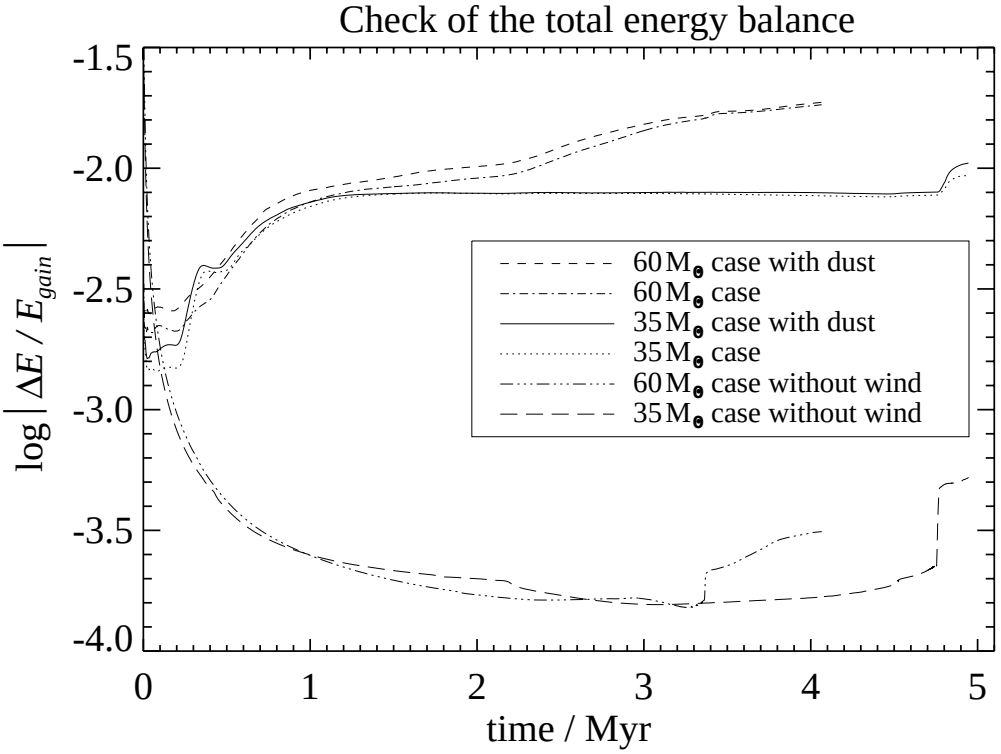

Figure 3.8: Check of the total energy balance.

energy that the circumstellar medium gained from the star via its Lyman continuum radiation and stellar wind during this period of time. It is obvious from Figure 3.8 that the error is much lower for the windless cases. There is also a weaker dependence on the set of stellar parameters. The largest error occurs in the $60\,M_\odot$ case with wind, but it is always below 2 %. This is acceptable, compared with, e.g., the uncertainty of the initial conditions and stellar parameters. It is also considerably lower than the error of the radiative energy input (see above).

3.10.2 Resolution Studies

It is currently impossible to spatially resolve all details of the entire dynamical evolution when modeling an SWB in two or more dimensions over such a long time with all the physics we have included. Especially the modes of the thin-shell overstability (Vishniac 1983; Ryu & Vishniac 1988; Vishniac & Ryu 1989) are extremely difficult to resolve because a sufficient number of grid cells across the thin shell are required to follow the tangential flow of material. Mac Low & Norman (1993) performed purely hydrodynamical simulations of the thin-shell overstability and confirmed the linear stability analysis of Vishniac (1983). Since they completely focused on the hydrodynamical evolution of the thin shell, they made no efforts to treat much more complex systems with more sophisticated physics.

To check the impact of this resolution effect on our results for the energetic evolution of the SWB, we performed resolution studies. We did the same calculations with three different resolutions, medium (125 cells in each dimension), low (61 cells in each dimension), and high (253 cells in each dimension). We compare only the first megayear of the evolution (because the high-resolution model is too CPU intensive). The results for the $60\,M_\odot$ case are displayed in Figure 3.9. The change of kinetic energy due to different resolutions is systematic (at times later than 0.2 Myr) in the sense that a higher resolution increases the kinetic energy that remains in the system. For most of the time the difference in kinetic energy between medium and high resolution ($\lesssim 0.05$ dex) is smaller than between low and medium resolution, which is expected as the value converges toward the limit. The variation of the thermal energy with resolution is only weak; the maximum difference between low and high resolution is $\lesssim 0.05$ dex at any time during the first megayear. The scatter in ionization energy for the three different resolutions is also $\lesssim 0.05$ dex for $0.5\,\mathrm{Myr} \leq t \leq 1.0\,\mathrm{Myr}$ and $\lesssim 0.1$ dex for $t < 0.5\,\mathrm{Myr}$. In the latter case, the deviation of ionization energy between the medium- and high-resolution runs varies but is considerably smaller than between low and medium resolution, indicating that the value of the ionization energy is already close to the actual value.

Figure 3.10 shows the results of the comparable resolution study for the $35\,M_\odot$ case. It can be seen that the quality of the results is comparable to that of the $60\ M_\odot$ case. The variation of the thermal energy with resolution is $\lesssim 0.05$ dex at almost any time during the first megayear. For ionization energy and kinetic energy of bulk motion the deviation between low and high resolution is $\lesssim 0.05$ dex for $0.5\ \mathrm{Myr} \leq t \leq 1.0\ \mathrm{Myr}$ and $\lesssim 0.1$ dex for $t \leq 0.5$ Myr, the latter case with a considerably smaller shift between medium and high resolution than between low and medium resolution, indicating that these values are already close to the actual limit.

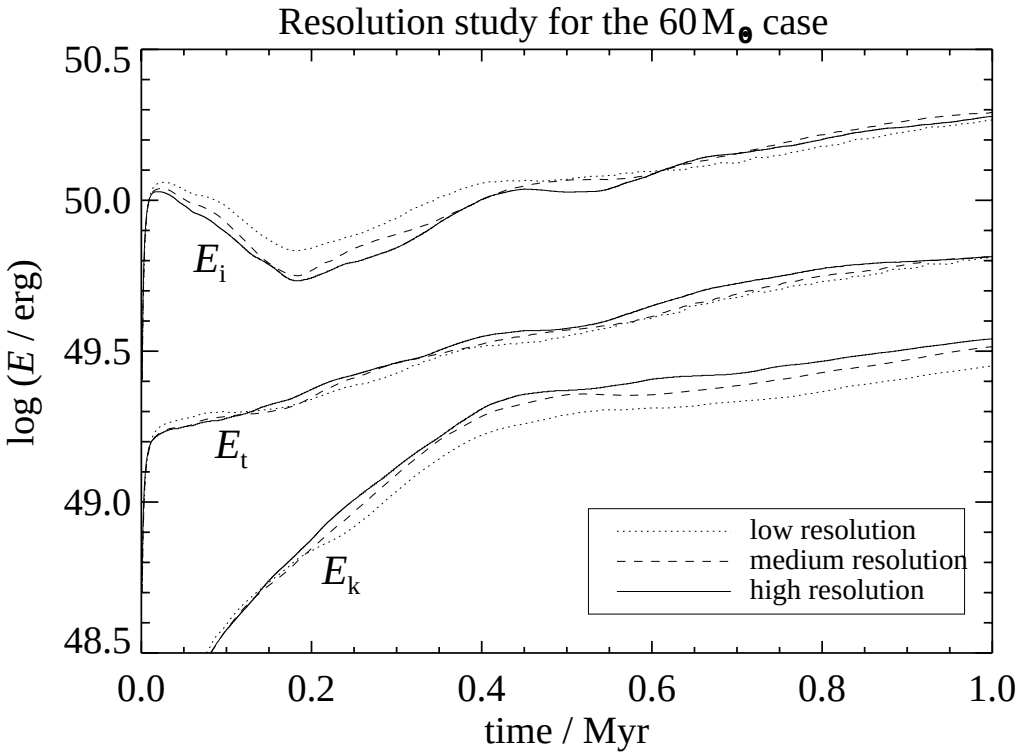

Figure 3.9: Resolution study for the 60 $M_\odot$ case.

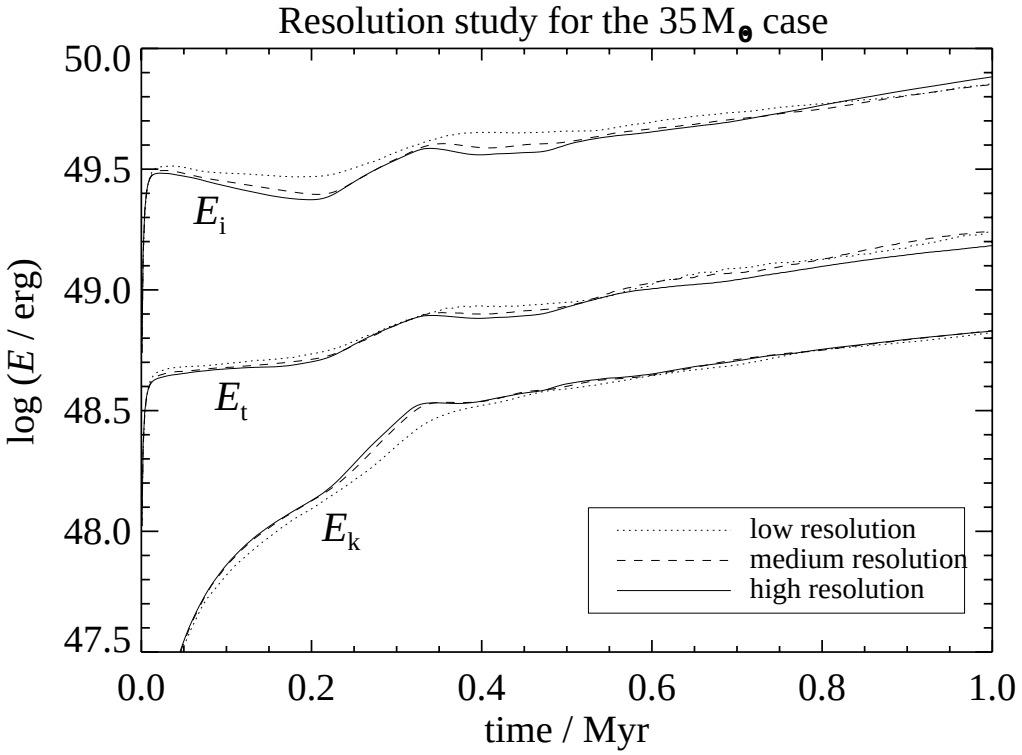

Figure 3.10: Resolution study for the 35 $M_\odot$ case.

These results show that the errors in our energetic analysis due to resolution effects are within an acceptable range, although there are morphological details that remain to be explored in future simulations with even higher resolution.

Chapter 4

Results and Discussion

4.1 The 60 $M_\odot$ Case

In this section I show the results of the 60 $M_\odot$ simulations. Parts of these results have already been published in Freyer et al. (2003).

4.1.1 The Evolution of the Circumstellar Medium

Figures 4.1–4.14 show the evolution of the circumstellar gas around our 60 $M_\odot$ star. The plots show color-coded physical quantities in a quadrant of the (r, z)-plane through the star. The size of the displayed area varies with time as the expansion proceeds outward. The star is located in the center of the coordinate system. We display the mass density together with the velocity field, the gas temperature, and the degree of hydrogen ionization, respectively, for certain stages of evolution. The degree of ionization is not shown for stages after 1 Myr, when the ionized region spatially almost coincides with the hot gas. To prevent confusion, velocity arrows are skipped in the free-flowing wind and (except for Figure 4.1) in the hot bubble.

Figure 4.1 shows the initial model for the two-dimensional calculation that has been set up from the one-dimensional solution after 1000 yr. The fundamental structure of the combined SWB/HII region is well described by the analytical solutions. The ionization front at a distance of about ≈ 8 pc from the star separates the ionized gas at about 8000 K from the undisturbed medium. The front has not yet reached the initial Strömgren radius at about 12.7 pc and is still R type. Thus, there is little dynamical response of the heated gas at this point. The SWB evolves into the preionized and preheated but otherwise undisturbed medium. The free-flowing wind is heated by the reverse shock at $r \approx 0.16$ pc to very high temperatures of about 10^8 K. Although the density in the hot gas is fairly low ($\approx 4 \times 10^{-25}$ g cm^{-3}), the thermal pressure is still much higher than in the HII region and the hot bubble expands supersonically (with respect to the isothermal sound speed in the HII region of ≈ 12 km s^{-1}) at roughly 200 km s^{-1}. The photoionized HII region gas becomes shocked by the expanding hot bubble and compressed into a shell with a density of more than 10^{-22} g cm^{-3} and a temperature of nearly 10^6 K. At this early time, the SWB and the photoionized HII region still evolve independently.

Figure 4.2 depicts the evolution after 2×10^4 yr. The photoionized region has reached

its initial radiative equilibrium size, and gas at the outer edge of the HII region starts to accelerate outward as a result of the pressure gradient between the warm ionized gas and the cold neutral ambient medium. The hot bubble has grown to about 2 pc in radius. The shell has been decelerated to approximately 60 km s^{-1}. Because of the high density and high temperature, strong cooling has led to compression of the swept-up gas into a thin shell. The thin-shell overstability (described in section 2.3) initially produces some dense knots in the shell that imply variations in the optical depth along radial lines of sight indicated by the rippling of the photoionization front. The initial evolution of the SWB (as long as it is independent of the HII region evolution) is very similar to what is described by Strickland & Stevens (1998), except for the deviations due to the different ambient density and stellar parameters.

On the basis of Figure 4.3 ($t = 4 \times 10^4$ yr) and Figure 4.4 ($t = 0.1$ Myr) the structuring impact of the interaction processes between the SWB and the HII region can be well identified: The photoionized HII region has started to expand into the ambient medium at 6–7 km s^{-1}. The isothermal sound speed of the cold neutral gas is about 1 km s^{-1}. Thus, an outer radiative forward shock occurs that sweeps up the ambient gas into a shell. The hot gas bubble has grown to about 5 pc in radius, and the shell expansion velocity is still about 25 km s^{-1} ($t = 0.1$ Myr). The ionization plots nicely illustrate the influence of the density knots in the wind bubble shell on the evolution of the HII region: The gas clumps cast shadows into the HII region. The optical depth for hydrogen-ionizing photons along lines of sight through the clumps is higher than for lines of sight that pass the shell between clumps. As a result of the weakening of the radiation field, the gas behind the clumps starts to recombine, forming neutral spokes within the HII region. The spokes are less prominent in temperature than in degree of ionization because the cooling efficiency breaks down with the disappearance of the free electrons and the shadowed regions remain at several thousand Kelvin for some time.

One could imagine that the shadowed regions are artificial as a result of the use of the on-the-spot approximation for the diffuse radiation field that originates from recombinations directly into the ground state of hydrogen. However, a test calculation that used flux-limited diffusion instead of the on-the-spot approximation yielded qualitatively the same results with respect to the shadowed regions. Only slight morphological differences were obtained as a result of the transfer of the diffuse radiation field.

Considerations about the influence of shadow patterns on ionized regions are not completely new: Capriotti (1973) already discussed the impact of shadows by shell fragments on the formation and appearance of planetary nebulae (PNs). Williams (1999) examined the corrugation of R-type ionization fronts by density inhomogeneities with subsequent formation of dense clumps. Soker (1998) studied the formation of compressed tails in the shadow zones behind dense clumps that are present in the vicinity of the central star of a PN before the ionization starts. In addition, Cantó et al. (1998) presented an analytical model for the partial ionization of the shadow regions behind neutral clumps by the diffuse radiation produced in the nebula along with some gasdynamic simulations. The model is not restricted to PNs and can be generalized to photoionized regions.

For the combined SWB/HII region described in our work we show that the density inhomogeneities needed to cast the shadows can be produced by the action of the stellar wind even after the HII region has already been formed in a completely uniform medium.

In our case the growth of the ionized fingers of the HII region is therefore not only due to the ionization front instability described by García-Segura & Franco (1996). It is strongly triggered by the redistribution of mass (and thus opacity) by the action of the stellar wind shell.

The real nature of the spokes, clumps, and instabilities is three-dimensional rather than two-dimensional, a fact that certainly should influence their size distribution, shapes, and longevity. Three-dimensional simulations, although extremely expensive, would be useful to study these structures in more detail. These two-dimensional simulations should thus be regarded as qualitative indicators that such instabilities exist, a feature missing from one-dimensional calculations.

Another consequence for the structure of the HII region and the shell of the SWB can be seen in Figure 4.5 at 0.2 Myr. The disturbed structure of the HII region, especially the formation of the neutral spokes and the ionized fingers, has induced several flow patterns with velocities up to $\approx 20\,\mathrm{km\,s^{-1}}$. As a result of the pressure gradient between the neutral spokes and the ionized gas, the spokes are compressed by the ionized gas. At the same time the expanding SWB compresses the HII region (and its spokes) as a whole. The clumps in the stellar wind shell originally responsible for the shadows grow in mass and partially merge during the further course of evolution. Photoevaporation of the stellar wind shell and its embedded clumps does not strongly influence the dynamics because the gas in these structures is still warm and its photoionization does not produce large pressure gradients. However, where stellar photons directly impinge upon the cold outer shell through the optically thinner ionized fingers, photoevaporation occurs and leads to significant dynamical effects, as evident in Figures 4.5–4.14.

In the top panel of Figure 4.5 and also in some of the other density plots are swirls of material visible in the hot bubble. These vortices are sometimes generated at the r- and z-axes, possibly as an artifact of the reflecting boundary conditions. Since the total mass involved in these flow patterns is very small, they do not influence the morphological or the energetic evolution significantly.

Proceeding to 0.5 Myr (Fig. 4.6; please note the different scale), we see that the entire HII region has been swept up by the SWB, which has grown to approximately 12 pc in radius. The photoionized HII region (it can best be distinguished from the hot bubble using the temperature plot) consists of 3-7 pc long pillars, the remnants of the ionized fingers. The stellar wind shell loses its structure, becomes more or less dissolved, and merges into the "remnant" HII region because it sweeps up a highly nonuniform medium with an expansion speed that becomes comparable to the sound speed of the HII gas.

Figures 4.7 and 4.8 compare the results of our high- and medium-resolution runs with respect to the morphological structure after 1 Myr. One can easily see that there are significant deviations in the structure of the photoionized region between the two runs. This is not very surprising because, as mentioned above, the formation of density fluctuations due to the thin-shell overstability is very sensitive to the spatial resolution, especially as we have started with a completely undisturbed ambient medium and have not artificially excited any particular unstable mode. We have also seen that exactly these clumps in the stellar wind shell strongly influence the evolution of the HII region as a result of their opacity for Lyman continuum radiation.

Nevertheless, the general structure is very similar for both resolutions: The radius

of the hot bubble is roughly 17 pc (strong deviations from spherical shape appear in both cases). The photoionized gas forms a highly irregular shell around the hot bubble with a mean thickness of ≈ 5 pc, bound on the outside by a swept-up shell of shocked ambient material. It appears as if the phenomenon of "breakout" of the hot gas into the photoionized gas has occurred between the spokes in both cases. However, we see no evidence for further breakout into the undisturbed constant density medium. Had we chosen an ambient environment of limited size, i.e., included cloud edges of decreasing density within the computational grid, we could expect a more dramatic demonstration of breakout.

We now jump to $t = 3.30$ Myr and show in Figure 4.9 the evolutionary state of the circumstellar material shortly before the star enters the LBV phase with its strongly enhanced mass-loss rate. (Please note that we once again changed the plot scale to an appropriate size.) The radius of the hot bubble has grown to approximately 40 pc. Because of the growth of the bubble (and the slight decrease of H-ionizing photon luminosity after 2 Myr), the photoionized HII region has more or less collapsed into a skin with ≈ 2 pc thickness at the inside of the outer shell. The outer shell itself is still corrugated, and so is the photoionized gas. Some small clumps have become detached from the shell.

Figure 4.10 depicts the structure during the LBV eruption. Compared with the earlier plots, one can detect a much higher density in the free-flowing wind zone. That is due to the higher mass-loss rate of the star and the smaller terminal velocity. The rest of the structure is largely unchanged because the time step difference is small.

The LBV phase lasts only for about 10000 yr and is followed by the final W-R phases of the star, which are once again associated with wind terminal velocities of a few times 10^3 km s^{-1}. GML1 describes what happens next: the W-R wind becomes shocked when it hits the much slower LBV wind and the hot, rarefied gas accelerates the dense LBV wind (Fig. 4.11). This is now a highly Rayleigh-Taylor unstable situation, and the shocked W-R wind breaks through the LBV material, fragments it, and blows it into the MS bubble (Fig. 4.12) where it mixes with the hot, rarefied gas, enhancing the density and lowering the temperature there for some time.

Figure 4.13 shows the density and temperature of the circumstellar gas at $t = 3.50$ Myr, some 0.14 Myr after the end of the LBV eruption. The basic structure of the SWB has reestablished. The position of the reverse shock is now at a radius of 15 pc, and it starts to recede because the supply of the bubble with hot gas is resumed and the mechanical wind luminosity decreases during the next $\approx$0.5 Myr. The density especially in the outer parts of the hot bubble is still enhanced by the ejected LBV material.

The last set of pictures for the 60 $M_\odot$ case (Fig. 4.14) shows the structure of the circumstellar gas at the end of our simulation. This is the pre-SN configuration immediately before the star explodes as SNII. The radius of the hot bubble has reached nearly 50 pc, and the photoionized HII region is limited to the illuminated inner skin of the outer shell of swept-up ambient gas.

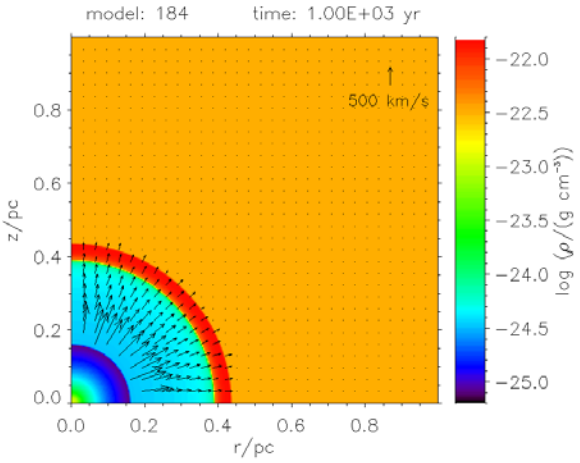

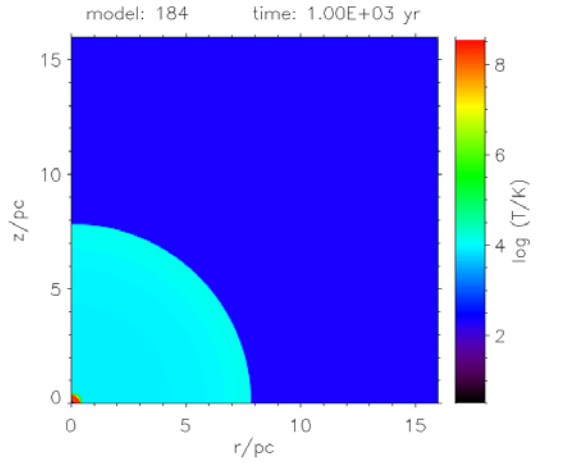

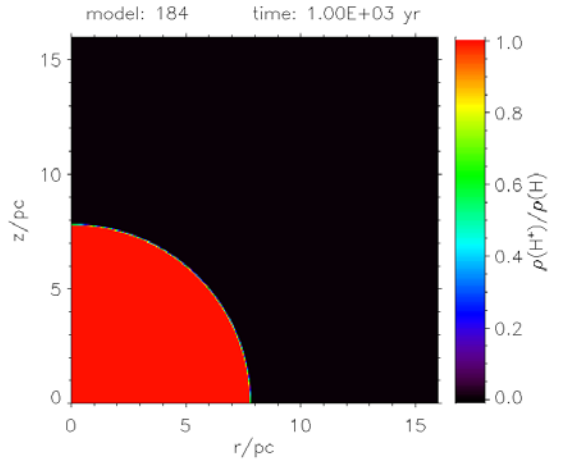

Figure 4.1: Circumstellar mass density and velocity field (top), temperature (middle), and degree of hydrogen ionization (bottom) for the 60 $M_\odot$ case at age 10^3 yr (high-resolution run). The velocity arrows in the free-flowing wind zone have been omitted to prevent confusion. The star is located in the center of the coordinate system. Please note the different length scales.

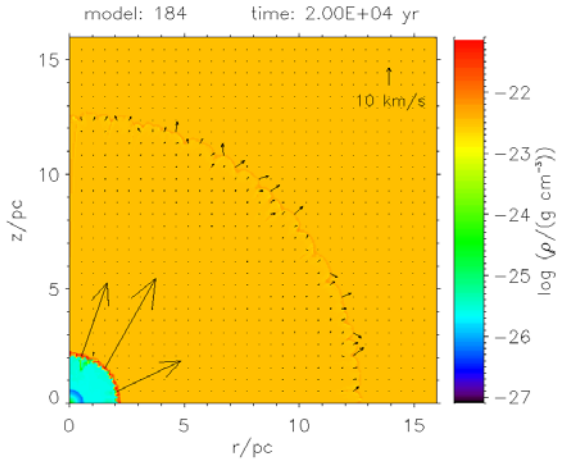

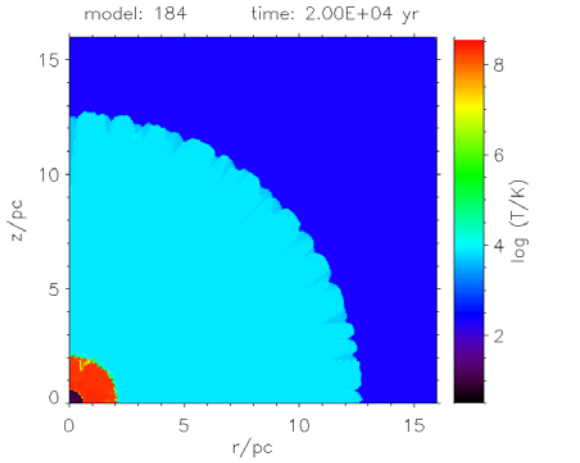

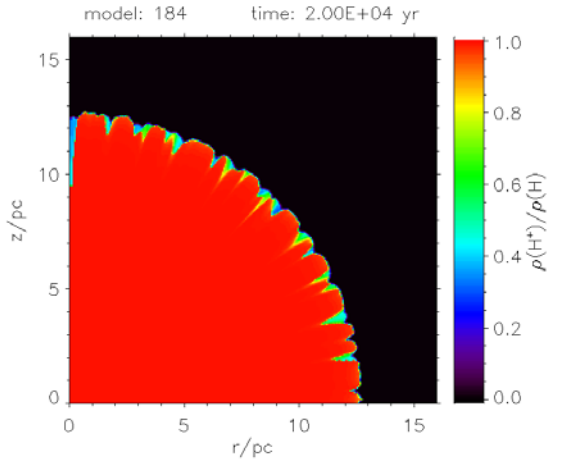

Figure 4.2: Same as Fig. 4.1, but at age 2×10^4 yr. The velocity arrows in the free-flowing wind zone and in the hot bubble have been omitted to prevent confusion.

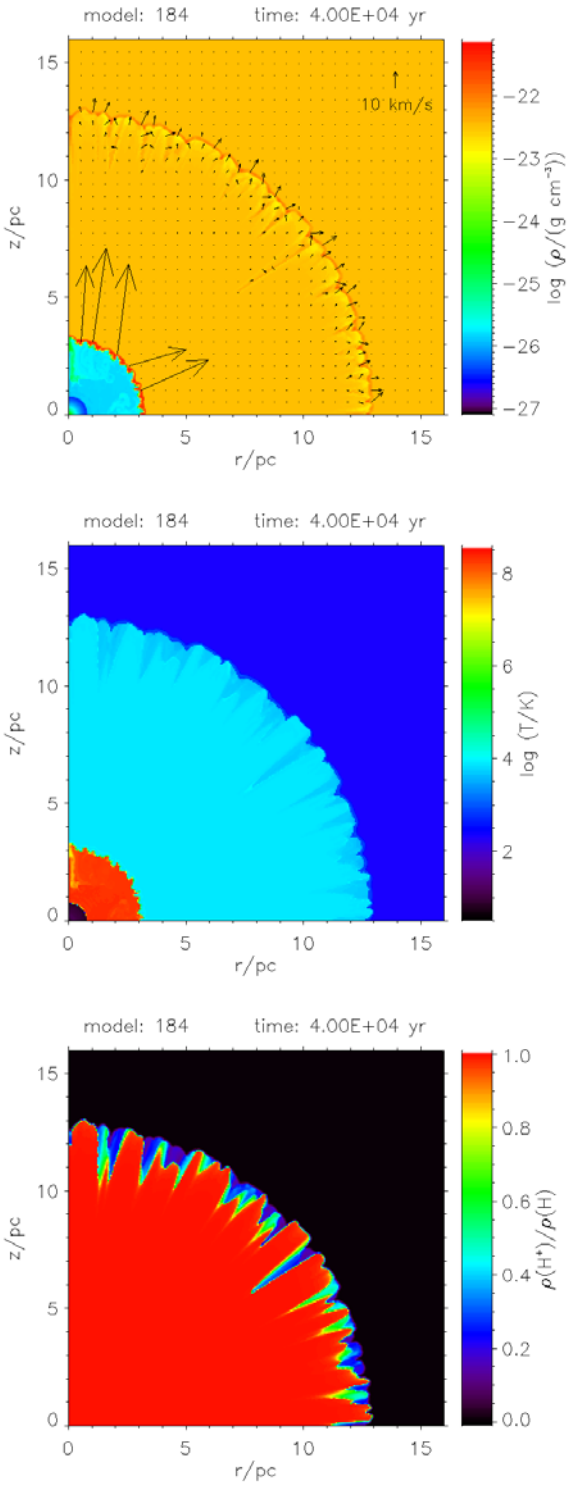

Figure 4.3: Same as Fig. 4.2, but at age 4×10^4 yr.

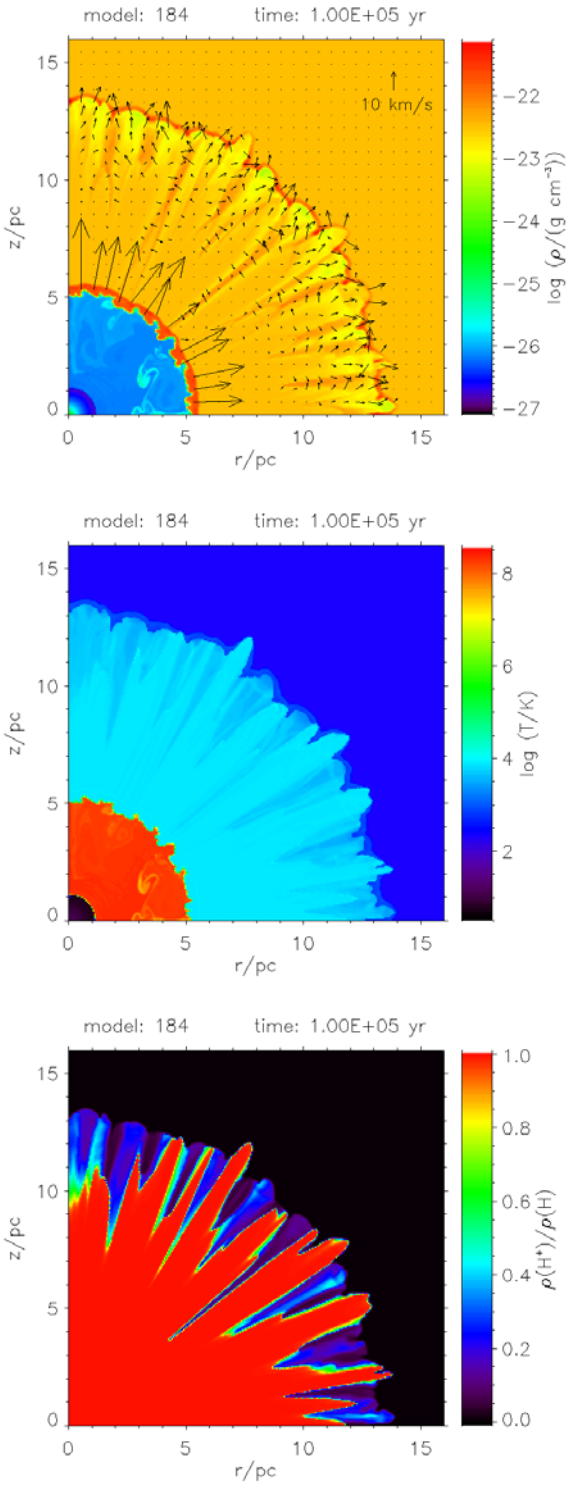

Figure 4.4: Same as Fig. 4.2, but at age 0.1 Myr.

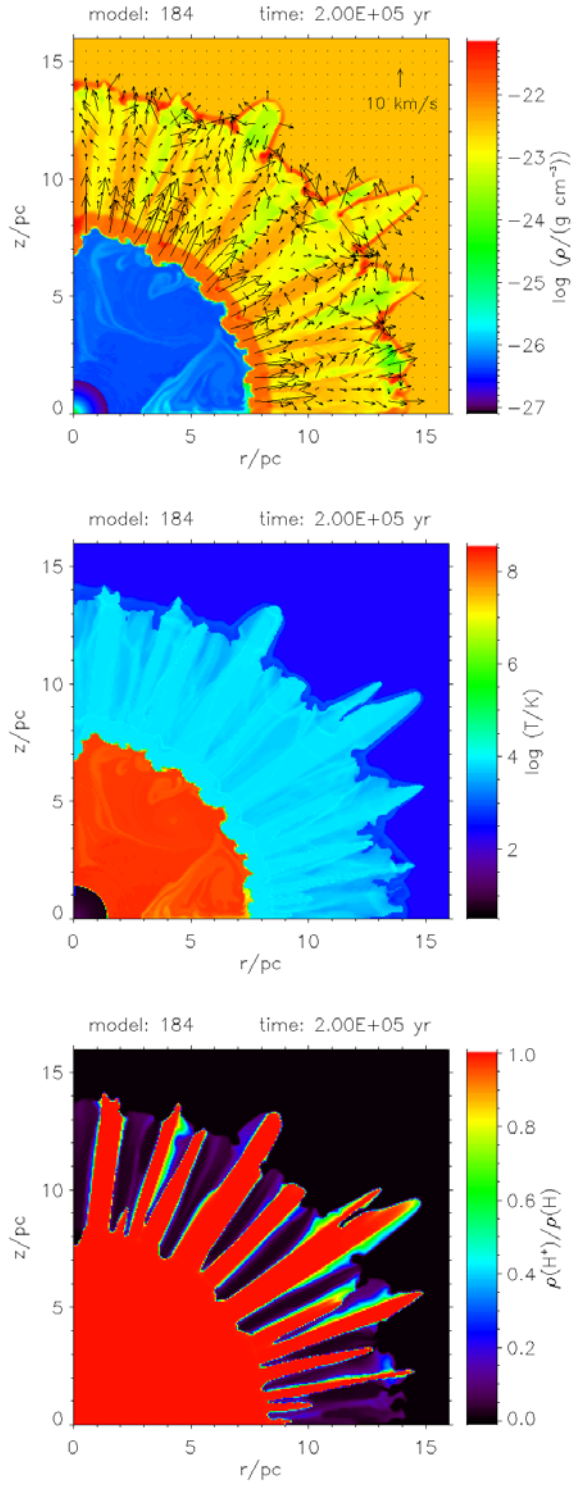

Figure 4.5: Same as Fig. 4.2, but at age 0.2 Myr.

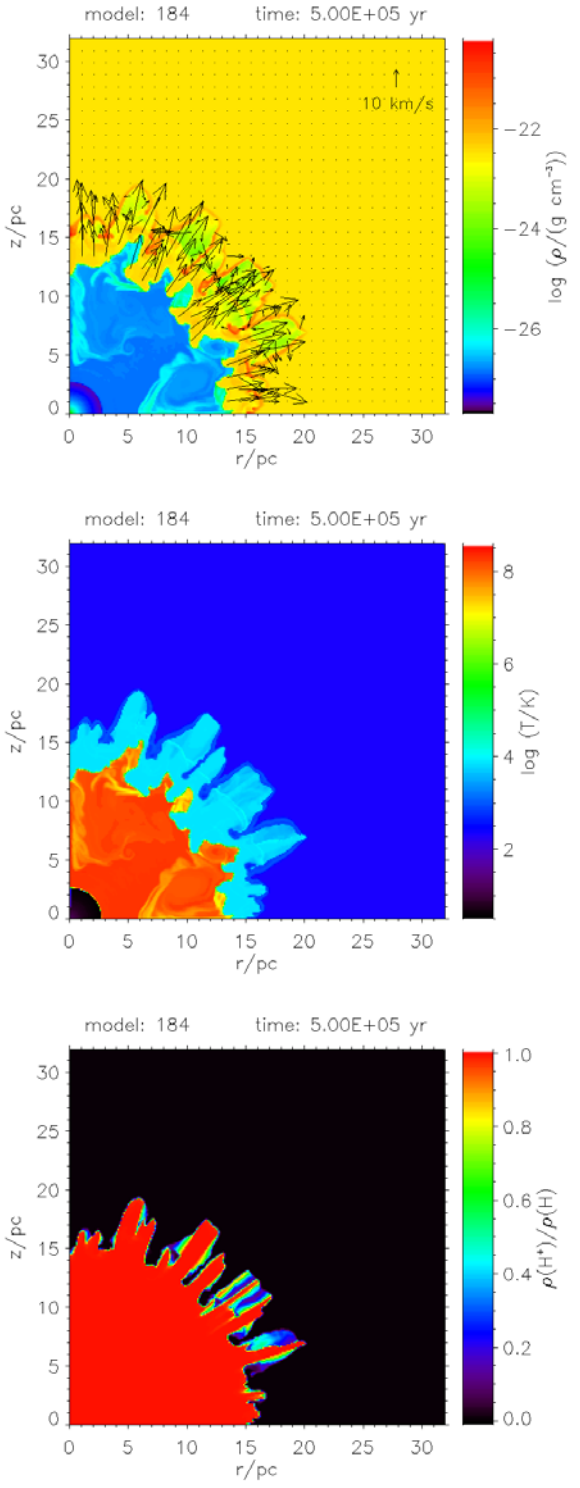

Figure 4.6: Same as Fig. 4.2, but at age 0.5 Myr. Because of the bubble expansion, a larger volume is shown.

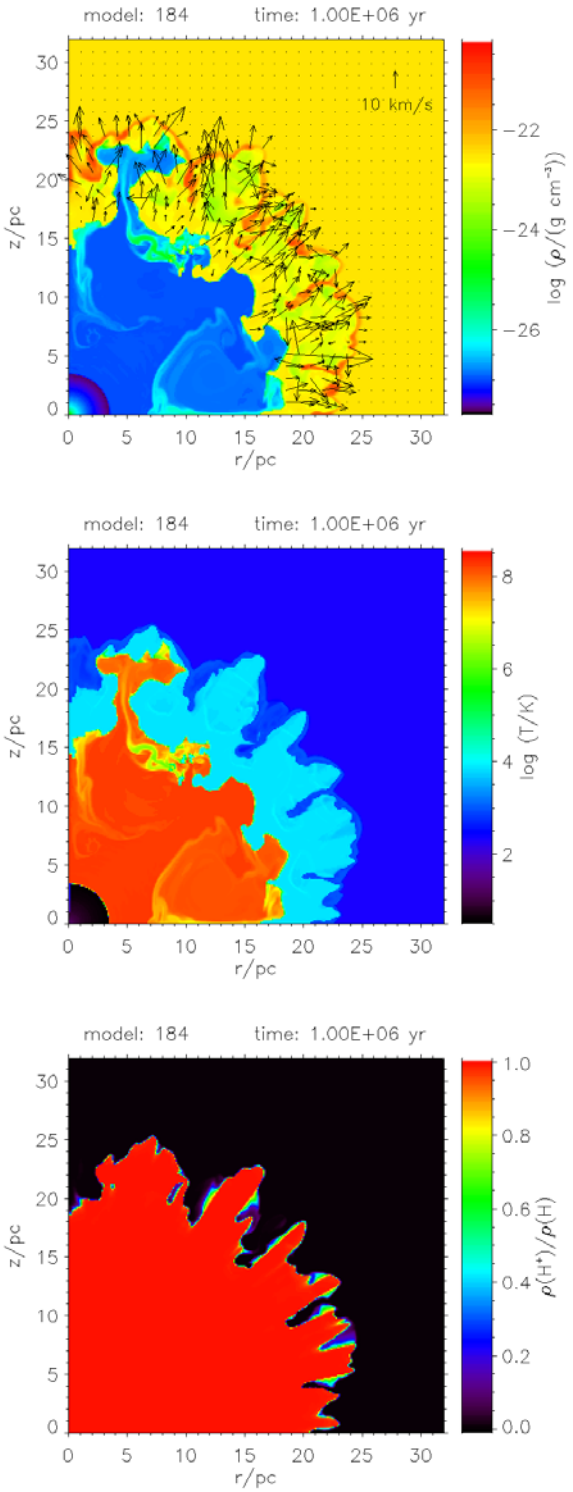

Figure 4.7: Same as Fig. 4.6, but at age 1 Myr.

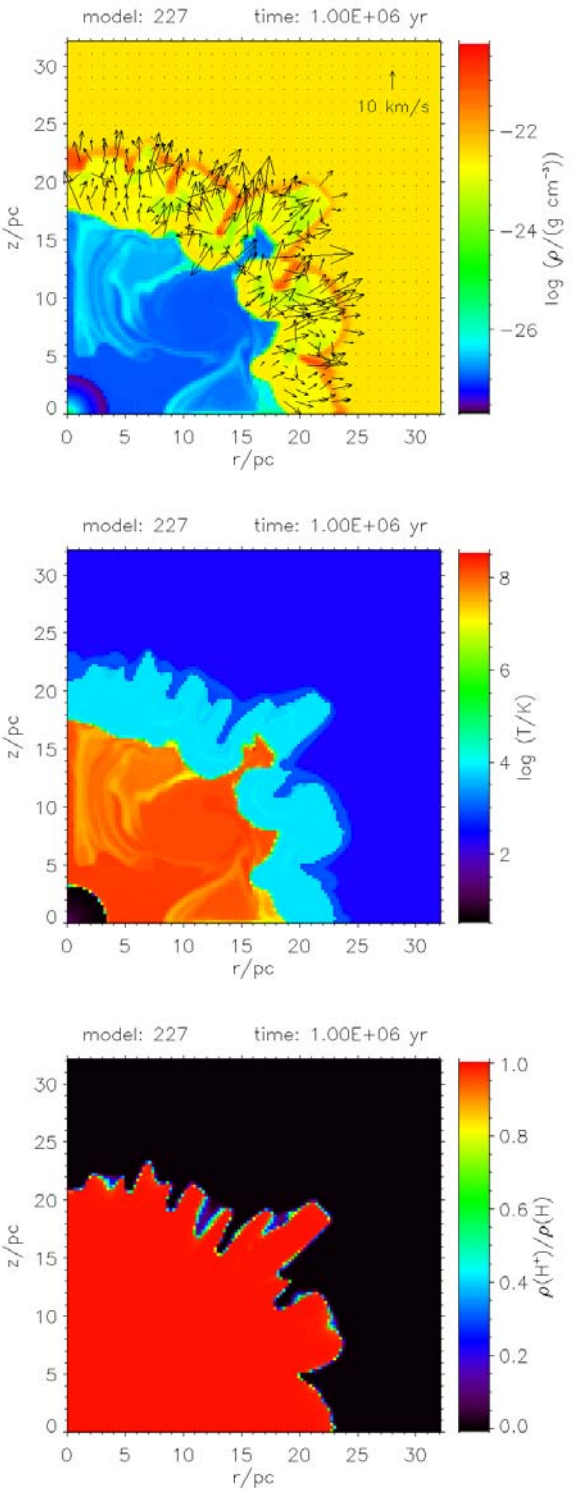

Figure 4.8: Same as Fig. 4.7, but for the medium-resolution run.

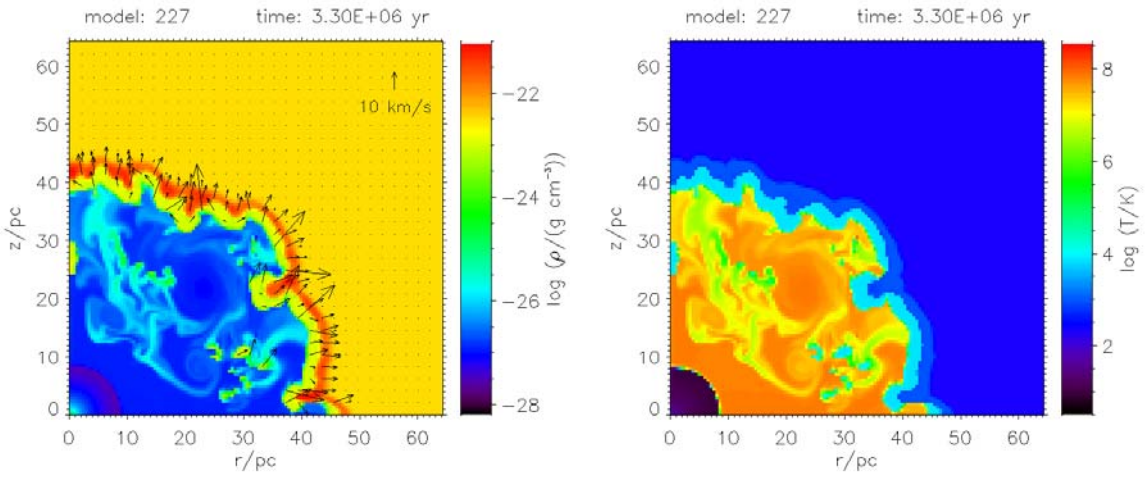

Figure 4.9: Same as Fig. 4.8, but at age 3.30 Myr. Only mass density and velocity field (left) and temperature (right) are shown, and the displayed area is enlarged once again.

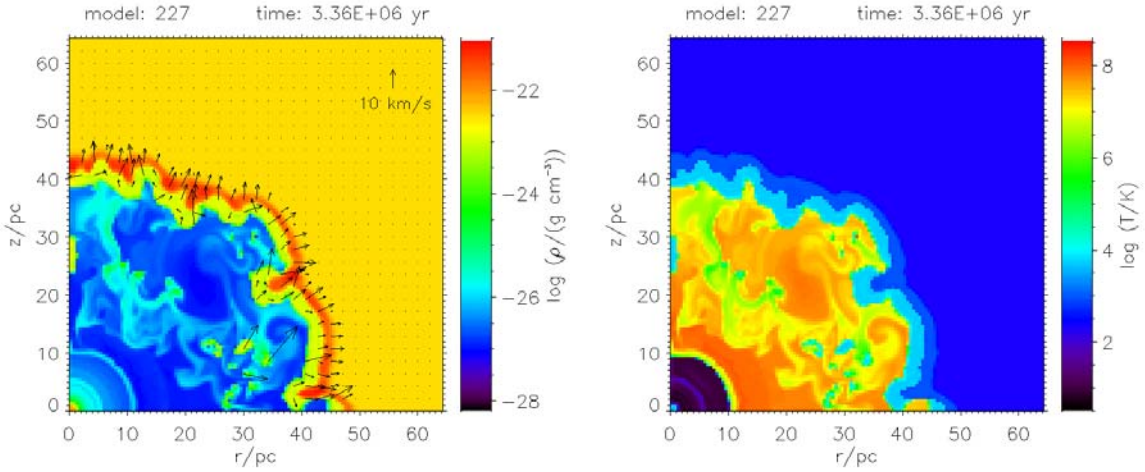

Figure 4.10: Same as Fig. 4.9, but at age 3.36 Myr.

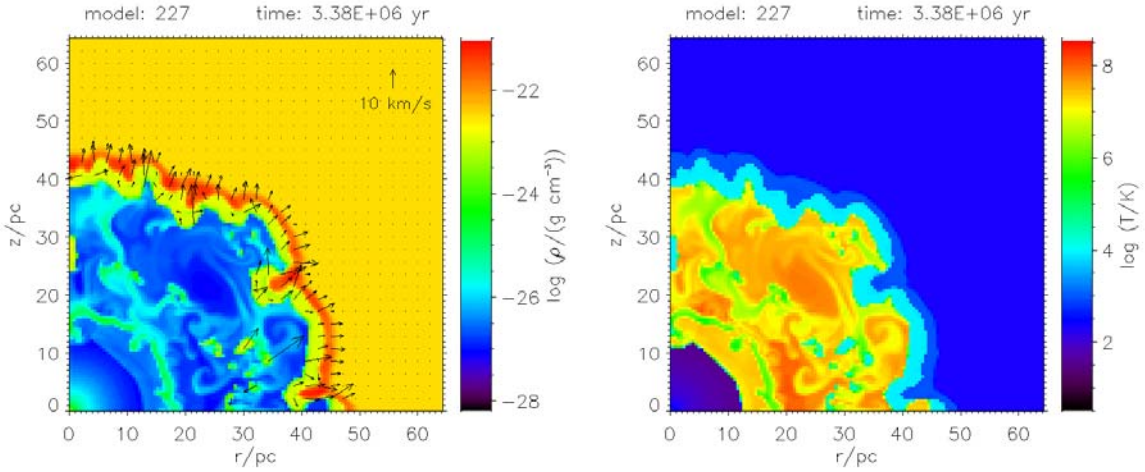

Figure 4.11: Same as Fig. 4.9, but at age 3.38 Myr.

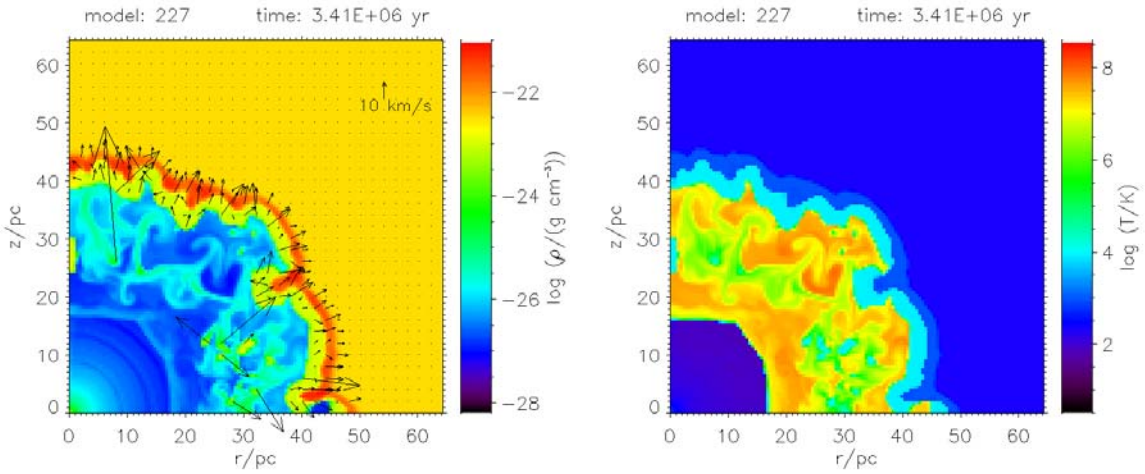

Figure 4.12: Same as Fig. 4.9, but at age 3.41 Myr.

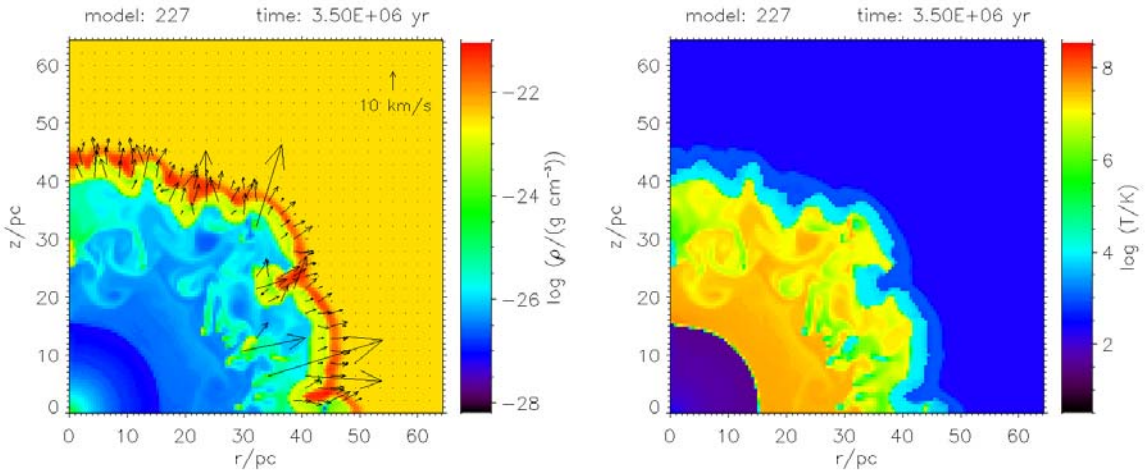

Figure 4.13: Same as Fig. 4.9, but at age 3.50 Myr.

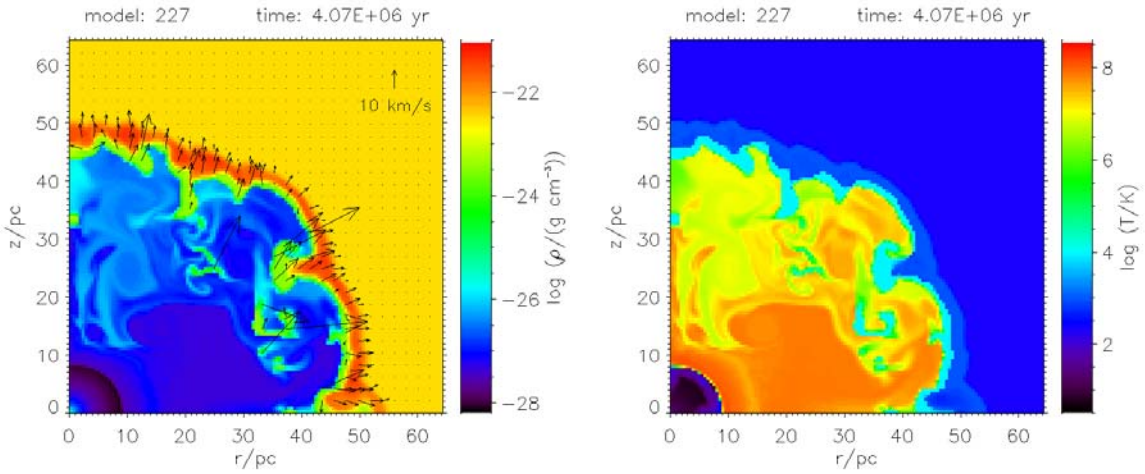

Figure 4.14: Same as Fig. 4.9, but at age 4.07 Myr.

4.1.2 The Energy Balance in the Circumstellar Medium

Numerical Results

Figure 4.15 shows the total energy contributions in the circumstellar gas of the 60 $M_\odot$ case as a function of time. We follow the kinetic energy of bulk motion throughout the computational domain, the ionization energy (13.6 eV per ionized hydrogen atom), and the thermal energy of cold ($T \leq 10^3$ K), warm (10^3 K $< T < 10^5$ K), and hot ($T \geq 10^5$ K) gas. As we have seen before, the ionization and heating of the HII region is the fastest process at the beginning of the evolution. Thus, the ionization energy reaches 1.1×10^{50} erg and the thermal energy of warm gas around 1.5×10^{49} erg very soon after the stellar turn-on.

The evolution of the thermal energy of warm gas follows that of the ionization energy over the lifetime of the star with a shift of 0.7-0.9 dex. This is due to the fact that photoionization by the stellar radiation field is responsible for the bulk production of ionized gas at typically 8000 K. The contribution by shock heating is small because the reverse shock does not heat much mass and the thermal energy of this gas is accounted under "hot gas" rather than "warm gas". Therefore, we will discuss only the ionization energy, bearing in mind that the thermal energy of warm gas behaves quite similarly.

An interesting feature is the drop of ionization energy between its first maximum and $t \approx 0.2$ Myr. This is due to the formation of the dense structures (shell, spokes) in

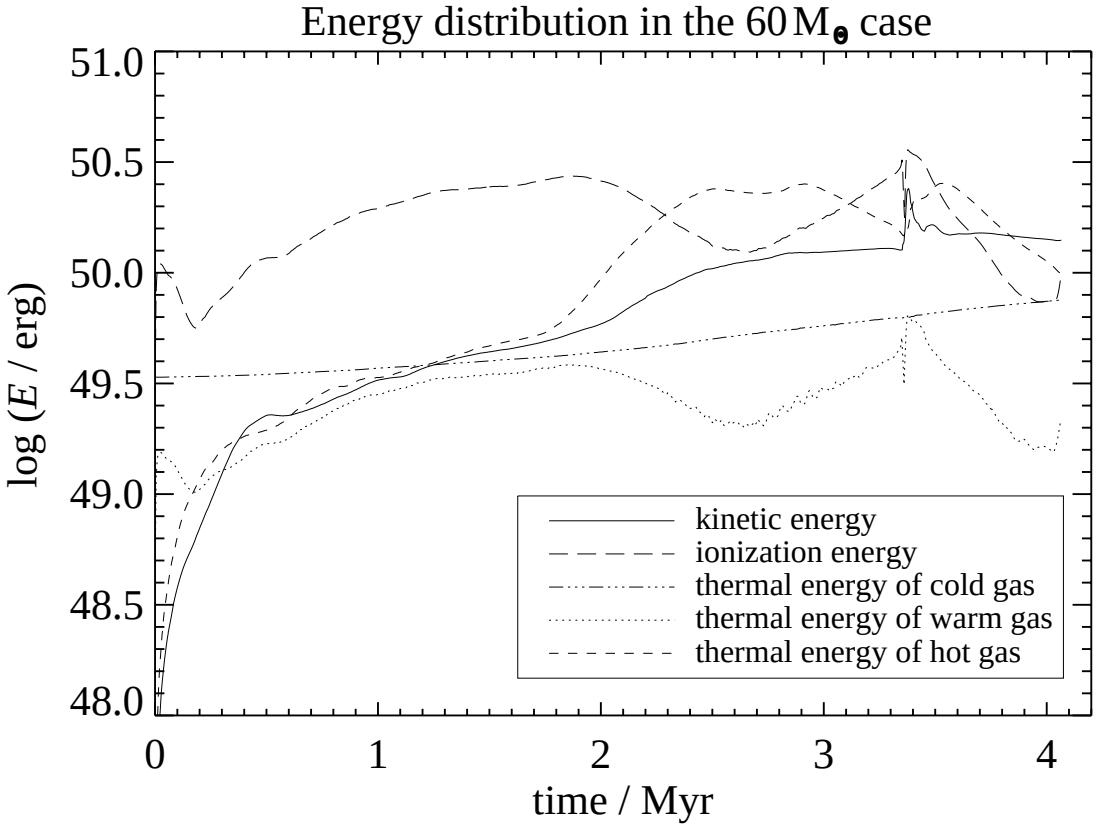

Figure 4.15: Temporal evolution of kinetic, thermal, and ionization energy in the 60 $M_\odot$ case.

the HII region that reduce the recombination time and increase the cooling of the gas (see also Fig. 4.16). Between $t \approx 0.2$ and 1.9 Myr the denser structures dissolve and the pressure decay within the hot bubble together with the HII region expansion result in a decrease of density in the HII region. Thus, the recombination time increases and the ionization energy stored in the system increases accordingly. The ionization energy reaches 2.7×10^{50} erg and the thermal energy of warm gas 3.7×10^{49} erg.

At $t \approx 1.7$ Myr the photon luminosity in the Lyman continuum begins to decrease slightly while the mechanical wind luminosity starts to increase (see Fig. 3.4). The former directly reduces the rate of photons available for photoionization, whereas the latter enhances the pressure in the hot bubble, thus compressing the HII region, which implies higher recombination rates. Thus, ionization energy and thermal energy of warm gas decrease by a factor of 2 and reach local minima at $t \approx 2.6$ Myr. They rise again when the photon luminosity in the Lyman continuum increases and the mechanical wind luminosity decreases until the star reaches the LBV stage.

Although spectacular in appearance, the impact of the LBV phase on the energy balance is only limited as a result of a relatively brief period of time. We note here that the table of stellar parameters that we use is sufficiently time resolved even during the LBV phase, contrary to what could be suspected from Figure 3.4. For a detailed plot of the stellar parameters during the LBV phase see GML1. The ionization energy in the circumstellar gas drops during the LBV stage because the effective temperature of the star decreases significantly, but immediately after the LBV eruption, during the next WN stage, the stellar UV flux drives the circumstellar ionization energy to a global maximum at 3.4×10^{50} erg. The ionization energy follows the stellar UV flux. The final values of ionization energy and thermal energy of warm gas (i.e., at the end of our calculation) are 1.0×10^{50} and 2.1×10^{49} erg, respectively.

The kinetic energy of bulk motion in the circumstellar gas rises from zero at the beginning (because we started with a quiescent medium) as more and more circumstellar gas is accelerated by the expansion of the HII region and the SWB. After some 0.3 Myr it reaches the same level as the thermal energy of warm gas and rises in the same manner. When the mechanical luminosity of the stellar wind increases after $t \approx 1.7$ Myr, it lifts the kinetic energy above 10^{50} erg, close to the ionization energy level. The ejection of the LBV nebula raises the kinetic energy for a short time almost by a factor of 2, but it drops back when the LBV material hits the outer shell and the kinetic energy is dissipated into thermal energy. Its final value is 1.4×10^{50} erg.

The thermal energy of hot gas accounts for the internal energy of the rarefied gas in the SWB that is heated to high temperatures by the reverse shock during the MS and W-R phases of the star. Since there is no hot gas at the very beginning, the thermal energy of this gas phase rises from 0. The behavior of the curve is very similar to that of the kinetic energy, but it increases faster after $t \approx 1.7$ Myr. Between 2.3 and 3.1 Myr it is the dominant form of energy in our system, and after some slight changes in and around the LBV phase it finally decays with the mechanical luminosity of the star to 9.7×10^{49} erg.

The thermal energy of cold gas starts already with the internal energy of the quiescent ambient medium. The value increases smoothly from 3.4×10^{49} erg at the beginning to 7.9×10^{49} erg at the end of the calculation because more and more ambient gas becomes

swept up by the outer shell. The weak shock heats it to several hundred Kelvin, whereas cooling of this neutral gas is very low.

At the beginning the radiative energy input has the strongest influence on the energy distribution. The dynamical response of the circumstellar gas (the expansion of the HII region and the acceleration of the material by the SWB) takes much longer. Thus, the ionization energy dominates the circumstellar energy distribution over the first ≈ 2 Myr. After the kinetic energy and thermal energy of hot gas have caught up with the thermal energy of warm gas, these three forms of energy are comparable between 0.3 and 1.8 Myr. Later, because of the accumulation of kinetic energy in the shell and thermal energy of hot gas in the bubble, these two become comparable with the ionization energy. Between 2.2 Myr and the end of the calculation these three forms of energy differ by not more than a factor of 3, although some changes occur. The LBV phase of the star induces very rapid changes in the relative energy ratios of at most a factor of 3, but they are transitory.

It is interesting to compare the energy stored in the system for the two cases: 1) with wind and 2) the pure HII region evolution without wind (Fig. 4.16). Obviously, the total kinetic energy in the calculation with wind is always higher than in the corresponding calculation without because of the added kinetic energy of the SWB shell. At the end of the simulation, the kinetic energy in the calculation with stellar wind is 4 times higher than in the calculation without.

By contrast, the ionization energy reaches the same level of $\approx 1.1 \times 10^{50}$ erg very soon

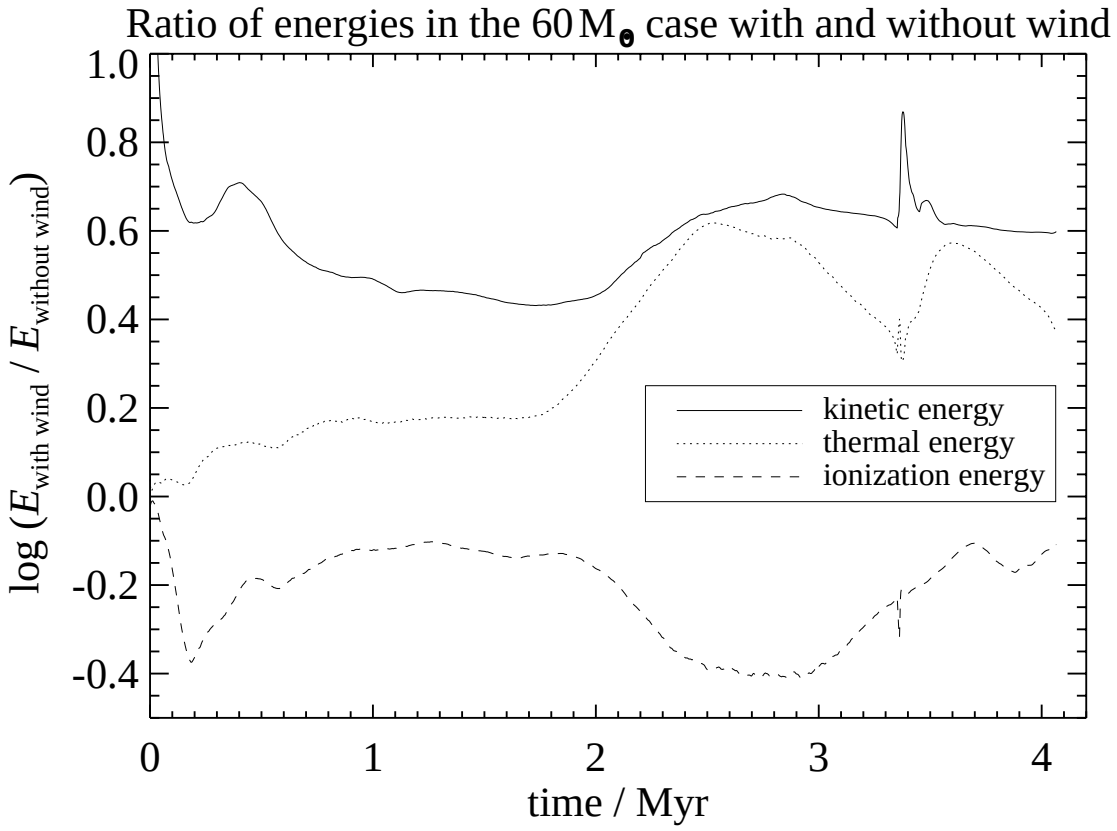

Figure 4.16: Ratio of energies in the 60 $M_\odot$ case with and without a stellar wind.

after the start of the calculation in both cases. As we have already seen in Figure 4.15, the ionization energy in the calculation with wind drops by a factor of 2 during the first 0.2 Myr, whereas in the calculation without wind it continues to grow. This supports our explanation that inhomogeneities in the HII region (shell, spokes) result in shorter recombination times and thus lead to fewer photoionized hydrogen atoms in the system. Although there is additional energy input by the stellar wind, the ionization energy is lower than in the calculation without wind by 0.1–0.4 dex for most of the evolution. This, however, does not imply that the Hα luminosity is different. The Hα luminosity directly mirrors the stellar ionization input.

Although the thermal energy of warm gas (55 % below the respective value of the windless simulation at the end of the calculation) is similarly affected as the ionization energy, the total thermal energy is always higher in the calculation with wind because we have additional energy deposited into the hot and into the cold gas phases.

To gain deeper insight into the temporal variation of the energies, Figures 4.17 to 4.22 show the rates with that the different forms of energy in the circumstellar gas change during the evolution. Triangles indicate energy gain while stars mark energy loss with the indicated rate. We start with the discussion of the ionization energy for the windless case (Figure 4.17) and with stellar wind (Figure 4.18). In the windless case, the change rate of ionization energy basically mirrors the changes of the Lyman continuum luminosity of the star. During the MS phase of the star the ionization energy in the circumstellar gas grows at a relatively constant rate of $4 \times 10^{36}\,\mathrm{erg\,s^{-1}}$. Between 2.2 Myr and 2.6 Myr there is the first phase of ionization energy loss from the system, followed by stages of ionization energy gain and loss according to the variations of the stellar Lyman continuum luminosity. The case with wind (Figure 4.18) shows a similar behavior, but the variation of the ionization energy change rate on small timescales is higher than in the windless case. Additionally, the impact of the stellar wind can be seen, as already described above, resulting in a first phase of ionization energy loss already during the first few 10^5 yr because of the formation of dense structures in the HII region. The second phase of ionization energy loss starts earlier at $\approx$1.9 Myr since the increase of the wind luminosity that starts at this time enhances the thermal pressure in the SWB and therefore increases the density in the HII region, which reduces the average recombination time.

The change rate of thermal energy in the windless case (Figure 4.19) is very similar to the change rate of the ionization energy, except that the thermal energy change rate is lower by 0.7-0.9 dex, as has been explained above. Comparing the change rate of thermal energy in the case with wind (Figure 4.20) to the change rate of ionization energy confirms that the contribution of the hot gas to the thermal energy is significant, while it is not so important for the ionization energy. The first phase of thermal energy loss starts as late as at 2.5 Myr. All of the earlier loss of thermal energy of warm gas (indicated by the loss of ionization energy) is obviously compensated by the increase of the thermal energy in the hot phase.

Finally, we compare the change rate of kinetic energy in the windless case (Figure 4.21) to the one in the case with wind (Figure 4.22). In the windless case, the rate is about constant during the MS phase of the star at $3 \times 10^{35}\,\mathrm{erg\,s^{-1}}$. The variations during the subsequent LBV and W-R phases are also limited until the kinetic energy loss

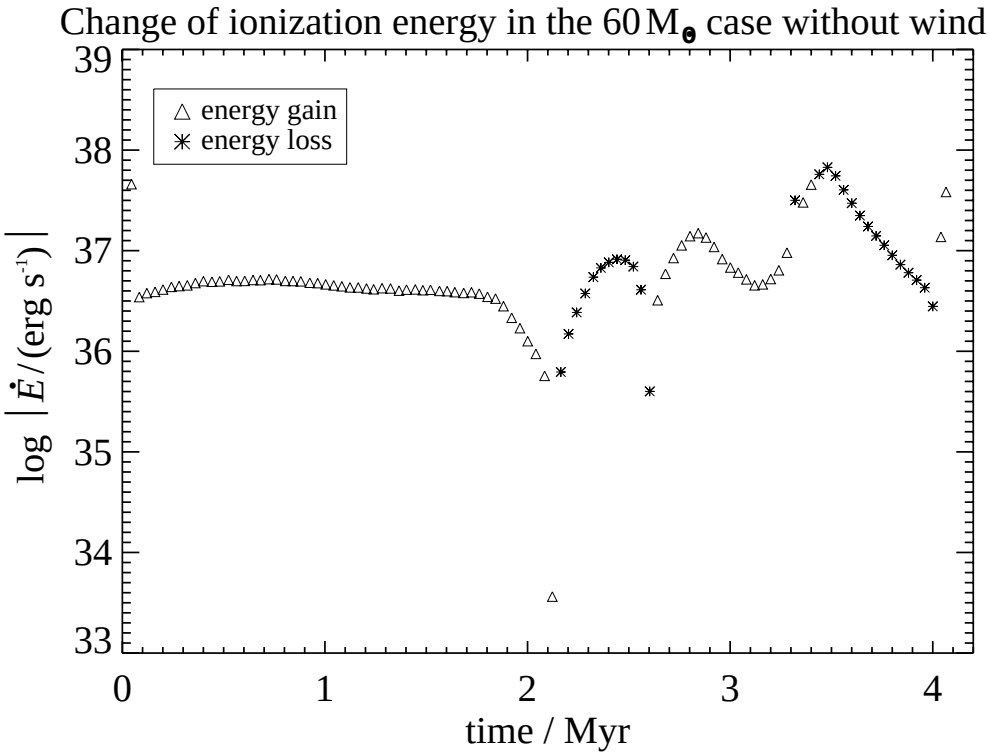

Figure 4.17: Change rate of the ionization energy in the 60 $M_\odot$ case without a stellar wind.

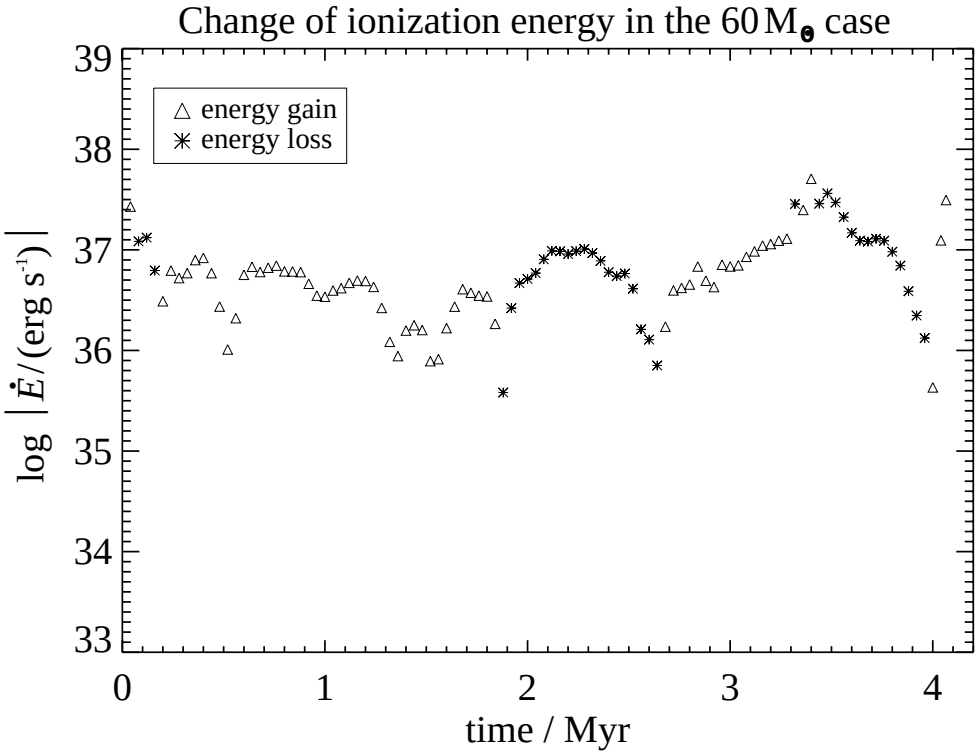

Figure 4.18: Change rate of the ionization energy in the 60 $M_\odot$ case.

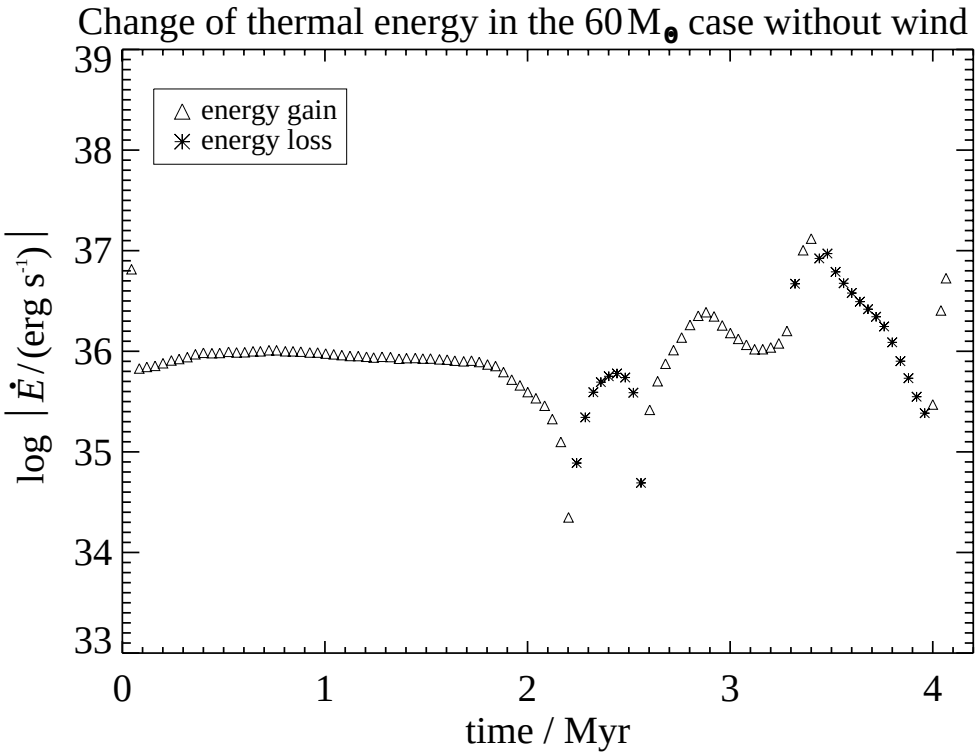

Figure 4.19: Change rate of the thermal energy in the 60 $M_\odot$ case without a stellar wind.

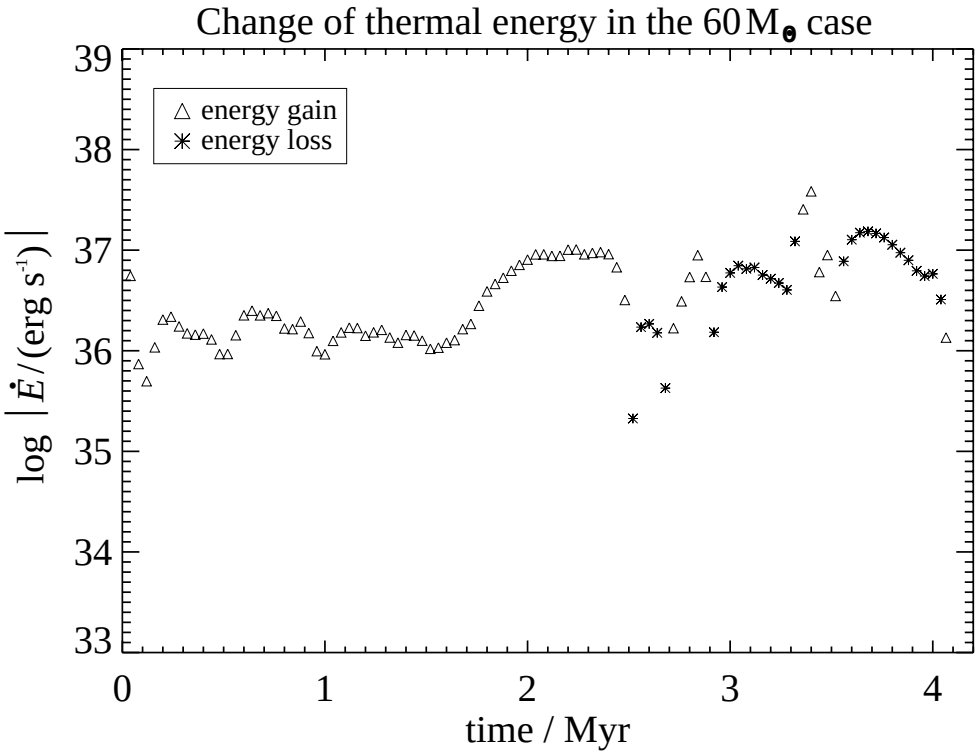

Figure 4.20: Change rate of the thermal energy in the 60 $M_\odot$ case.

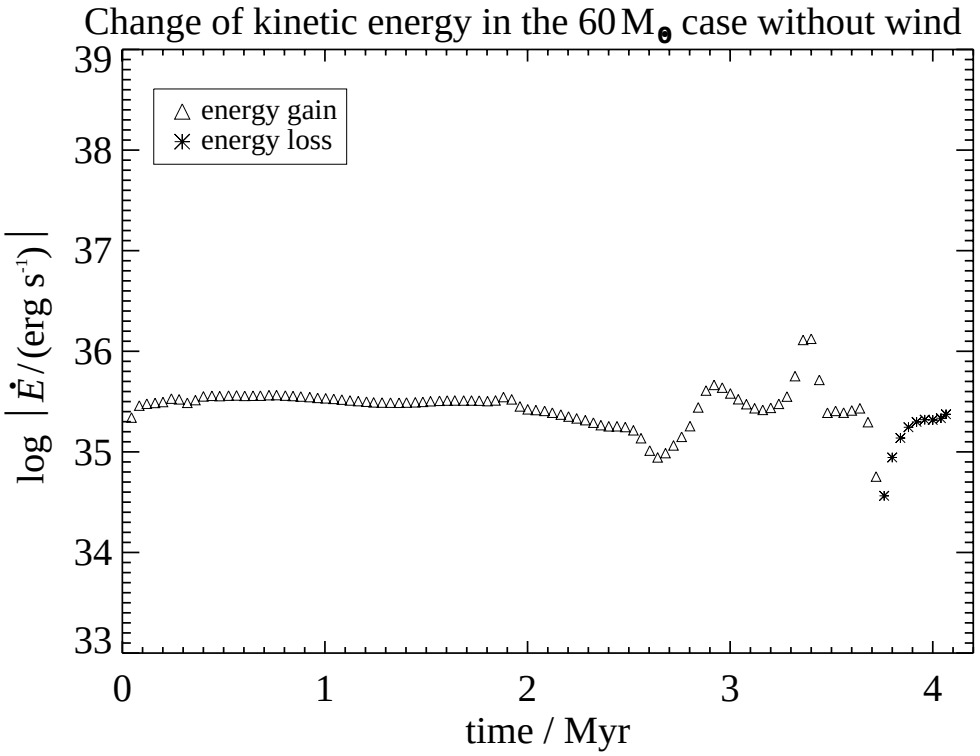

Figure 4.21: Change rate of the kinetic energy in the 60 $M_\odot$ case without a stellar wind.

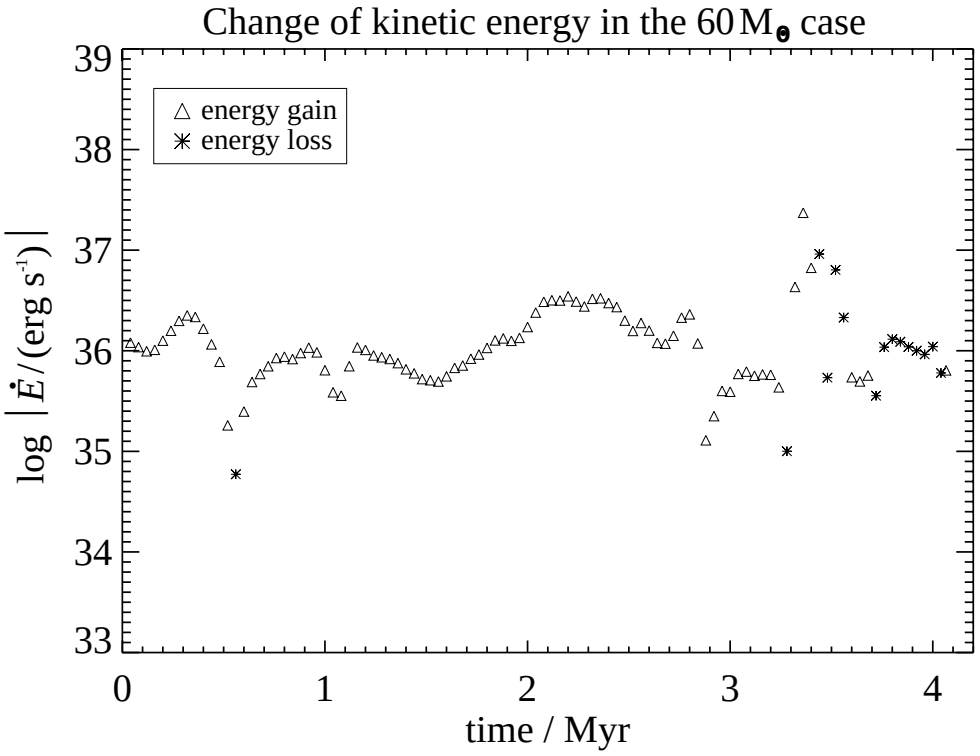

Figure 4.22: Change rate of the kinetic energy in the 60 $M_\odot$ case.

predominates after $t = 3.75\,\mathrm{Myr}$ because of the decrease of the stellar Lyman continuum luminosity. In the case with wind, the variation of the kinetic energy change rate on small timescales is higher than in the windless case. Since there is the additional contribution from the stellar wind, the average gain rates are also higher than in the windless case.

Figure 4.23 shows the transfer efficiency into kinetic, ionization, and thermal energy and their sum for the calculation without wind. We define the transfer efficiency as the cumulative fraction of the input energy that has been converted into a particular form up to the time $t = \tau$. In this case we have only radiative input energy and all values are related to that.

The transfer efficiency into ionization energy has the highest value during the whole calculation. The transfer efficiencies into ionization and thermal energy strongly drop at the beginning of the calculation. This is a consequence of the fact that the photoionization equilibrium has been quickly established and the ionization energy stays constant within an order of magnitude, whereas the transfer efficiency is related to the accumulated input energy that grows continuously in time. The transfer efficiency into ionization energy reaches $\approx 5 \times 10^{-3}$ immediately before the LBV phase and drops as a result of the decreasing photon luminosity in the final W-R phases by almost a factor of 5. The transfer efficiency into thermal energy reaches the level of 10^{-3} before the LBV phase but decreases only by less than a factor of 2 during the remaining evolution. The

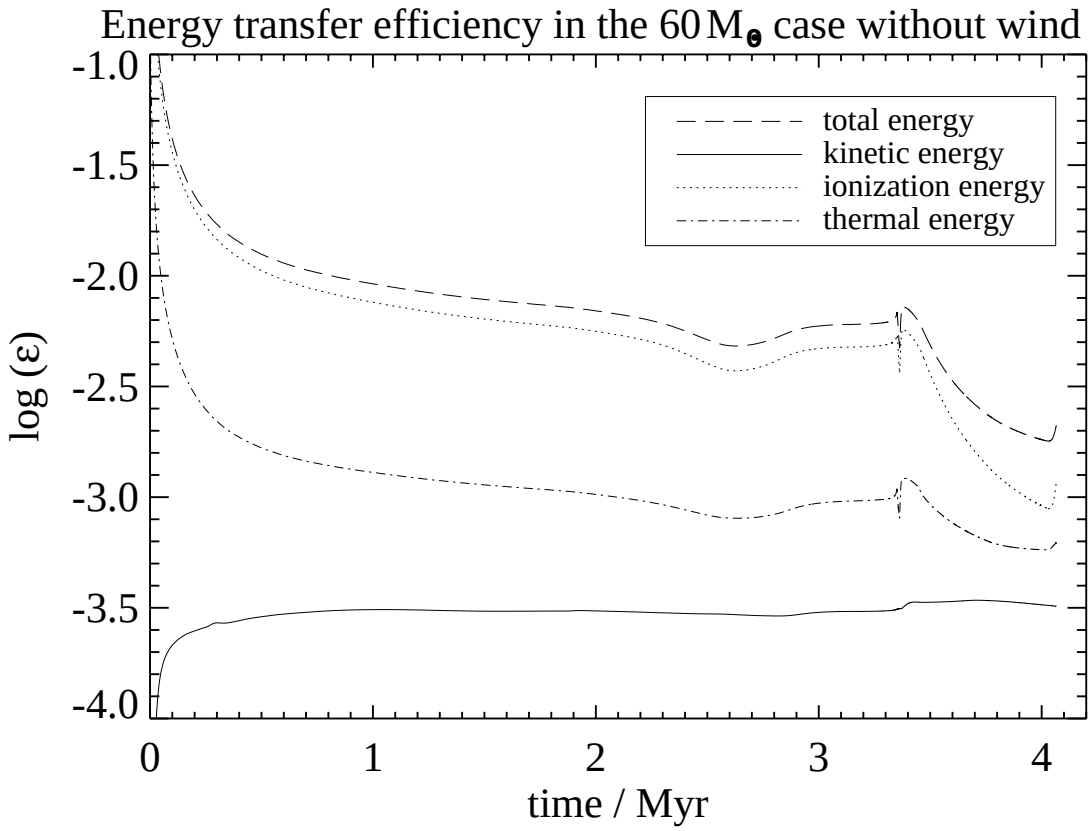

Figure 4.23: Energy transfer efficiency with respect to the total energy input in the $60\,\mathrm{M}_\odot$ case without a stellar wind.

discrepancy between the declines of both values can again be explained by the fact that cooling in formerly photoionized gas is greatly reduced as a result of missing electrons after recombination occurs. Thus, the recombined neutral gas has lost all its ionization energy but can retain a considerable portion of its thermal energy over a relatively long period. The transfer efficiency into kinetic energy has reached a nearly constant level of $\approx 3 \times 10^{-4}$ after 1 Myr and remains at that level until the end of the calculation; i.e., after the first megayear the kinetic energy in the system grows almost proportionally to the total input energy.

Now we check the impact of the stellar wind on the energy transfer efficiencies in the system. Figure 4.24 shows the same transfer efficiencies as Figure 4.23 but for the simulation with wind and radiation. Whereas for the calculation without wind the transfer efficiency into ionization energy dominated the total energy transfer efficiency, for the calculation with wind this is only true during the first ≈ 2.2 Myr. Thereafter the transfer efficiency into thermal energy dominates for about 1 Myr because the photon luminosity in the Lyman continuum decreases and the mechanical wind luminosity increases, thus enhancing the production of hot gas. Curiously, in the LBV phase all three energy transfer efficiencies have the same value of about 2×10^{-3}. As in the case without wind, the transfer efficiency into ionization energy drops more strongly after the LBV phase than that into thermal energy. The drop of the latter one in this calculation is mostly due to energy loss of the hot gas that dominates the thermal energy at late stages of the

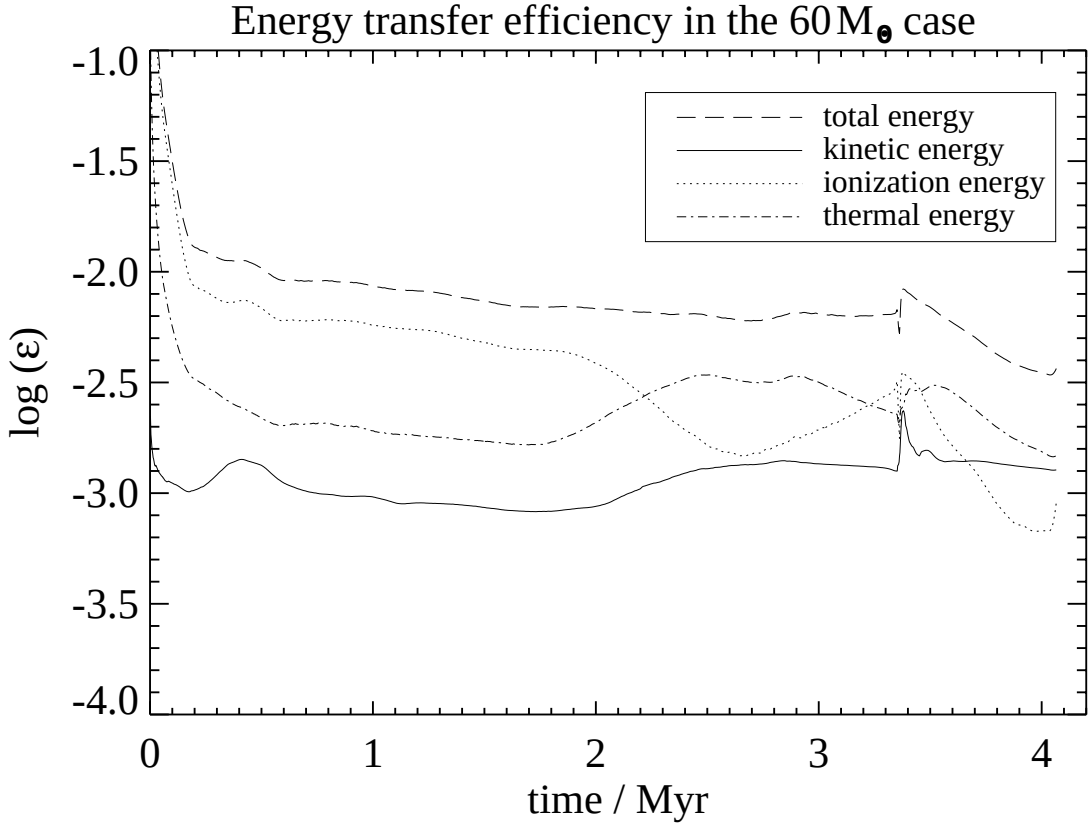

Figure 4.24: Energy transfer efficiency with respect to the total energy input in the 60 $M_\odot$ case.

evolution.

The total energy transfer efficiency reaches approximately 4×10^{-3} at the end of the calculation, about twice as much as in the simulation without wind. This is interesting because we know from Figure 3.4 that the mechanical wind luminosity integrated over the whole lifetime of the star is almost negligible compared to the total radiative energy input in the Lyman continuum. In other words, although the stellar wind itself does not actually inject a considerable amount of energy into the circumstellar gas (compared to the stellar radiation field), its presence almost doubles the total energy that is finally contained in the gas. This difference is due to the fact that the thermal energy deposited increased by a factor of 2.4 and that the kinetic energy rose by a factor of 4 compared to the calculation without wind. The ionization energy actually decreased slightly by some $20\,\% - 30\,\%$.

To facilitate the discussion in the next section, we summarize the values of the individual energy components at the end of the simulation in Table 4.1. Besides the kinetic energy of bulk motion ($E_{\rm k}$) and the ionization energy of hydrogen ($E_{\rm i}$), we list the thermal energy of the cold, warm, and hot gas components ($E_{\rm t,cold}$, $E_{\rm t,warm}$, and $E_{\rm t,hot}$) for the two cases, one with and one without stellar wind. The values of the energy transfer efficiency into kinetic energy ($\varepsilon_{\rm k}$), ionization energy ($\varepsilon_{\rm i}$), and thermal energy ($\varepsilon_{\rm t}$) at the end of the simulation are given in Table 4.2. The total energy of the Lyman continuum radiation emitted by the star is $E_{\rm LyC} = 1.07 \times 10^{53}\,{\rm erg}$, and the mechanical energy injected into the system by the stellar wind, if considered, amounts to $E_{\rm w} = 3.31 \times 10^{51}\,{\rm erg}$.

Table 4.1: The energy components at the end of the $60\,{\rm M}_\odot$ simulations.

Model parameters	$E_{\rm k}$ (10^{49}erg)	$E_{\rm i}$ (10^{49}erg)	$E_{\rm t,cold}$ (10^{49}erg)	$E_{\rm t,warm}$ (10^{49}erg)	$E_{\rm t,hot}$ (10^{49}erg)
Windless.....	3.5	13	5.5	4.7	0
With wind.....	14	10	7.9	2.1	9.7

Note.—The thermal energy of the cold component, $E_{\rm t,cold}$, contains the internal energy of the initially unperturbed ambient medium (3.4×10^{49}erg) that has to be subtracted whenever the input of thermal energy into the system is considered.

Table 4.2: The energy transfer efficiencies at the end of the $60\,{\rm M}_\odot$ simulations.

Model parameters	$\varepsilon_{\rm k}$ (10^{-4})	$\varepsilon_{\rm i}$ (10^{-4})	$\varepsilon_{\rm t}$ (10^{-4})	$\varepsilon_{\rm tot}$ (10^{-4})
Windless.....	3.3	12	6.4	22
With wind.....	13	9.1	15	37

Comparison with Analytical Results

We now calculate the values for the kinetic, ionization, and thermal energy in the system according to the analytical solutions given in section 2.6. The analytical approach cannot handle time-dependent stellar parameters; therefore, we simply choose mean values for effective temperature and luminosity in the Lyman continuum over the lifetime of our model star. With $\langle T_{\rm eff} \rangle = 5.03 \times 10^4\,{\rm K}$, $\langle L_{\rm LyC} \rangle = 8.33 \times 10^{38}\,{\rm erg\,s^{-1}}$, and using $\alpha_{\rm B} = 3.37 \times 10^{-13}\,{\rm cm^3\,s^{-1}}$ as the hydrogen recombination coefficient and $c_{\rm s,II} = 1.15 \times 10^6\,{\rm cm\,s^{-1}}$ for the isothermal sound speed in the HII region (corresponding to $T_{\rm II} = 8000\,{\rm K}$), we obtain the following for $n_0 = 20\,{\rm cm^{-3}}$ after $\tau = 4.065\,{\rm Myr}$ from equations (2.57), (2.58), and (2.59) for the calculation without wind:

$$\begin{aligned} E_{\rm k} &= 4.3 \times 10^{49}\,{\rm erg}\ , \\ E_{\rm i} &= 5.0 \times 10^{50}\,{\rm erg}\ , \\ E_{\rm t} &= 7.7 \times 10^{49}\,{\rm erg}\ . \end{aligned}$$

The energy transfer efficiency in the analytical approach is then defined as

$$\varepsilon = \frac{E}{\tau \langle L_{\rm LyC} \rangle}\ , \tag{4.1}$$

where E can be any of $E_{\rm k}$, $E_{\rm i}$, and $E_{\rm t}$, depending on the efficiency that is calculated. Thus, we obtain

$$\begin{aligned} \varepsilon_{\rm k} &= 4.0 \times 10^{-4}\ , \\ \varepsilon_{\rm i} &= 4.7 \times 10^{-3}\ , \\ \varepsilon_{\rm t} &= 7.2 \times 10^{-4}\ . \end{aligned}$$

Bearing in mind all the assumptions and approximations that have been made to obtain the analytical expression for the kinetic energy of bulk motion (see Lasker 1967, section 2.6.1 in this thesis), the deviation of less than 30 % in $\varepsilon_{\rm k}$ is not too bad. This difference is not due to the constant effective temperature and luminosity that we have chosen to obtain the analytical result. Recalculating $\varepsilon_{\rm k}$ for the first megayear, where the stellar parameters are about constant, makes the discrepancy between the analytical and numerical value of $\varepsilon_{\rm k}$ even larger. The difference is more likely due to temperature deviations from 8000 K in the HII region of the model calculation.

Comparing the analytical and numerical results for the transfer efficiency into ionization energy shows fairly good correspondence immediately before the LBV phase. At the end of the calculation the numerically determined transfer efficiency is about 0.6 dex below the analytical value because the Lyman continuum luminosity of the star drops significantly during the final W-R phases of the star and the ionization energy follows immediately. Of course, the analytical solution cannot reproduce this feature. The correlation between the drop of Lyman continuum luminosity and the thermal energy is weaker because cooling ceases when the plasma becomes neutral, as already mentioned above. Thus, the correspondence between analytical and numerical transfer efficiency into thermal energy is much better and the deviation at the end of the calculation is less than 15 %.

It is more difficult to compare analytical with numerical results in the case of the combined SWB/HII region model because we have only the analytical energy transfer efficiency solutions for the HII region and SWB separately. We simply add up the energy contributions from the HII region and the SWB bearing in mind that this is only a rough approximation, which actually neglects the interactions between both structures. Because we have not considered cooling in the hot bubble, the analytical energy transfer rates into kinetic and thermal energy are upper limits.

We insert the mean value of the mechanical wind luminosity, $\langle L_\mathrm{w} \rangle = 2.58 \times 10^{37}\,\mathrm{erg\,s^{-1}}$, into equations (2.61) and (2.62), and together with the results for the pure HII region we obtain

$$\begin{aligned} E_\mathrm{k} &= 9.5 \times 10^{50}\,\mathrm{erg}\ , \\ E_\mathrm{i} &= 5.0 \times 10^{50}\,\mathrm{erg}\ , \\ E_\mathrm{t} &= 1.6 \times 10^{51}\,\mathrm{erg}\ . \end{aligned}$$

To find the energy transfer efficiency, we relate these values to the sum of Lyman continuum radiation energy and the mechanical wind energy (which, of course, is almost negligible),

$$\varepsilon = \frac{E}{\tau\,(\langle L_\mathrm{LyC} \rangle + \langle L_\mathrm{w} \rangle)}\ , \tag{4.2}$$

where E can again be any of E_k, E_i, and E_t. We get

$$\begin{aligned} \varepsilon_\mathrm{k} &= 8.6 \times 10^{-3}\ , \\ \varepsilon_\mathrm{i} &= 4.6 \times 10^{-3}\ , \\ \varepsilon_\mathrm{t} &= 1.4 \times 10^{-2}\ . \end{aligned}$$

We have already discussed the fact that the ionization energy in the calculation with wind is lower than in the calculation without wind. This slightly enhances the discrepancy between the analytical and the numerical results for the ionization energy in the case with stellar wind. On the other hand, there is no indication that the neglect of the ionization energy in the hot bubble is a bad approximation.

The increase of the thermal energy deposit from the windless HII region simulation to the combined SWB/HII region simulation (factor 2.4) is almost an order of magnitude below the analytical upper limit. Since the conversion of thermal energy by $P\mathrm{d}V$ work is the major source of kinetic energy, the increase of the kinetic energy deposit between the simulations without and with wind (factor of 4 at the end of the calculation) is also 82 % below the analytical upper limit. These findings are supported by the observation that the radius of the bubble at the end of the calculation (≈ 50 pc) is considerably smaller than the analytical result of ≈ 68 pc according to equation (2.15). One reason for the lack of thermal energy in the simulation is the variation of the mechanical luminosity of the star. The LBV wind enhances the density in the bubble, which leads to stronger cooling, and the mechanical luminosity of the stellar wind generally decreases during the last 0.6 Myr. But also during the other stages of evolution, cooling in the hot bubble is not completely negligible for the energetics of the system. The thermal energy of the hot bubble calculated analytically at $t = 1$ Myr is already a factor of 4.5 larger

than the corresponding value in the simulation. Although we have not implemented heat conduction, effects like turbulent mixing between hot and cold gas and numerical diffusion enhance the cooling rate. The resolution-dependent numerical diffusion is not a key factor as we have shown in our resolution study. However, the cooling due to gas mixing is enhanced because the SWB expands at the beginning into the highly nonuniform HII region, a fact that cannot be properly handled by the analytical description. In general, the analytical results for the upper limits of the transfer efficiency into thermal and thus kinetic energy of bulk motion are much higher than the values from the numerical simulations even without heat conduction.

4.1.3 The Impact of Dust

We recalculated the 60 $M_\odot$ simulations considering dust in the ISM according to the very simple description given in chapter 3 and found that the impact of dust (with the employed gas-to-dust mass ratio and gram opacity given in chapter 3) on the results of the model calculations is only very small. As an example, we show in Figure 4.25 the average radius of the ionized volume (assuming sphericity) in the 60 $M_\odot$ cases with wind (with and without dust) and without wind (also with and without dust). After having reached the Strömgren radius very quickly, the radius of the ionized volume in the cases with wind lags behind the respective value in the windless cases during the first few 10^5 yr because

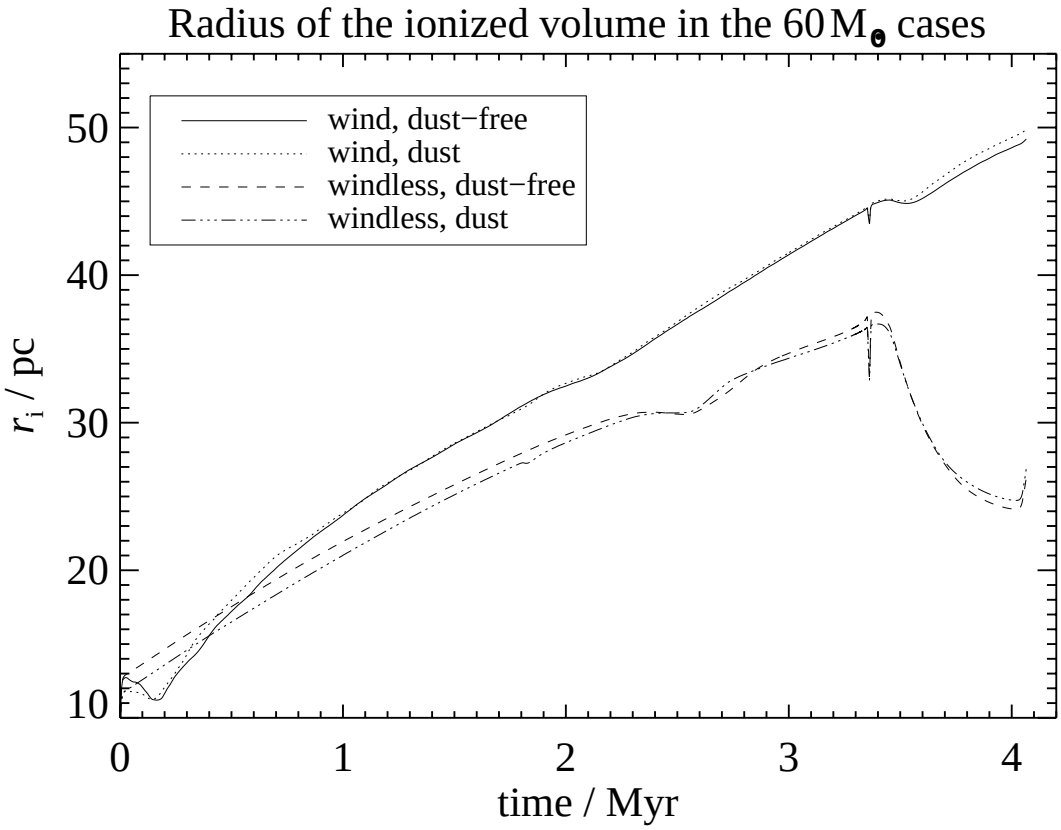

Figure 4.25: Radius of the ionized volume in the 60 $M_\odot$ cases.

of the structure formation and recombination in the HII region that has been described in detail in section 4.1.1. It takes ≈0.5 Myr until the SWB pushes the HII region and the ionization front to a radius greater than that in the windless cases. While the radius of the ionized volume in the windless cases falls off at late stages due to the decreasing Lyman continuum luminosity, it continues to grow in the cases with wind because there it is strongly supported by the size of the SWB, which is widely independent of the radiation field. The difference between the radii of the ionized volumes of the calculations with and without dust is very small. Only in the windless cases during the MS evolution the radius of the ionized volume in the calculation with dust is slightly smaller due to the additional opacity of the dust. In the case with stellar wind, the radius of the ionized volume is dominated by the radius of the SWB, which is almost unaffected by the dust.

We will now discuss the energy loss from the circumstellar gas as another indication that dust is not important within the framework of our model. Whereas the mechanical power of the stellar wind and the radiative power of the star are the energy sources in our system, the only energy sink term is radiative cooling of the gas. All other energetic processes lead to a redistribution of forms of energy within the system but not to a change of the total energy. Figure 4.26 shows the total energy loss of the system due to cooling of the gas and distinguishes 4 different contributions (compare section 3.5): "H ionization loss" refers to the 13.6 eV binding energy per hydrogen recombination into all states above the ground state, while "H thermal loss" accounts for the thermal energy of the electrons

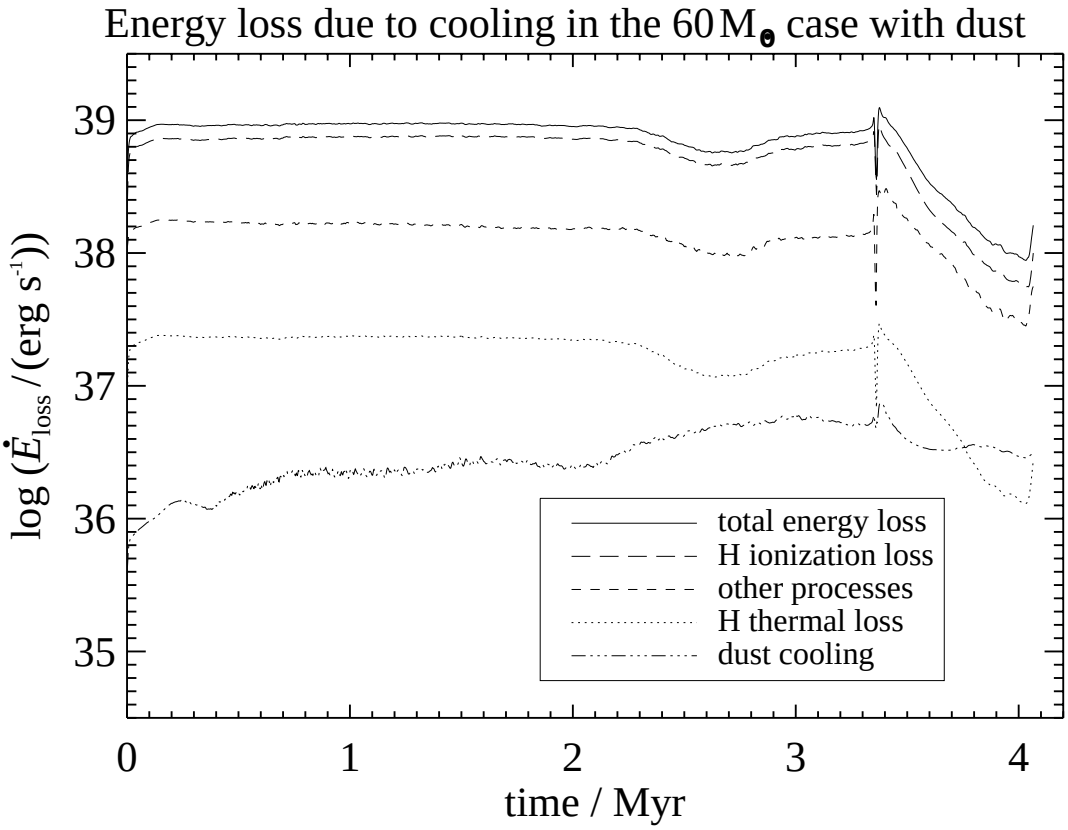

Figure 4.26: Energy loss due to cooling in the 60 $M_\odot$ case with dust.

lost by the same process, "dust cooling" delineates cooling of the gas by collisions with dust grains, and "other processes" include all other cooling processes considered, such as collisionally excited line emission and bremsstrahlung. One can see from Figure 4.26 that the shape of all the curves except "dust cooling" follows the Lyman continuum photon luminosity of the star (see Fig. 3.4). The total energy-loss rate during the MS phase is close to $10^{39}\,\mathrm{erg\,s^{-1}}$, approximately the same as the stellar Lyman continuum luminosity. Although the ionization energy in the system rises to $10^{50}\,\mathrm{erg}$ during the first few times $10^4\,\mathrm{yr}$, it is only a small fraction of the total input energy. "H ionization loss" is the dominant energy sink term during the evolution. It accounts for roughly 80 % of the total emitted power during the MS and first WN stage of the star. After the LBV phase, the relative importance of "other processes" has risen because the LBV ejecta enhanced the density in the hot bubble where collisionally excited lines and bremsstrahlung dominate the energy emission. The contribution from "dust cooling" is negligible during the whole evolution. At the end of the simulation it is comparable to the contribution from "H thermal loss".

These results show that the impact of dust on our results is only very limited. Thus, there was no reason to consider dust in the discussions in the previous sections. Nevertheless, the description of dust in our model is still very simple, and it is worth to include additional effects like, e.g., dust scattering of Lyman continuum photons or a consistent calculation of the dust temperature in future models.

4.1.4 Direct Observational Implications

In this section I discuss some direct observational implications of the model calculations. Since for a correct construction of intensity maps one would need three-dimensional models, the results of our two-dimensional calculations can only give a rough estimate of the observable intensities. Thus, we have calculated angle-averaged intensity profiles for Hα and soft X-ray emission based on the cylindrical symmetry in our models.

The Hα emissivity is calculated according to the table (case B) in Osterbrock (1989). We use a $T_{\mathrm{II}}^{-0.92}$ fit for the temperature dependence and set the emissivity to zero where the degree of hydrogen ionization is below 10^{-4}. We do not account for absorption.

In Figure 4.27 we plot the angle-averaged Hα intensity profiles at two different times ($t = 0.22\,\mathrm{Myr}$, during which intense structure formation occurs in the HII region, and $t = 3.365\,\mathrm{Myr}$, at a late stage after the LBV phase of the star). For comparison, we have also plotted the Hα intensity profiles of the corresponding calculations without stellar wind for the same times.

At $t = 0.22\,\mathrm{Myr}$ the pure HII region calculation without stellar wind shows the intensity profile of a spherical, emitting volume that has just started to expand. On the other hand, the intensity profile of the calculation with stellar wind shows a dominant peak between $r = 8$ and $9\,\mathrm{pc}$. This peak represents the global intensity maximum at that time and is produced by the emission of the dense shell swept up by the hot bubble of shocked stellar wind gas. A secondary, much smaller peak between $r = 13$ and $14\,\mathrm{pc}$ originates from the trapping of the ionization front in the dense outer shell fragments piled up by the expanding HII region.

Comparing these data with the intensity profiles at $t = 3.365\,\mathrm{Myr}$ shows that the

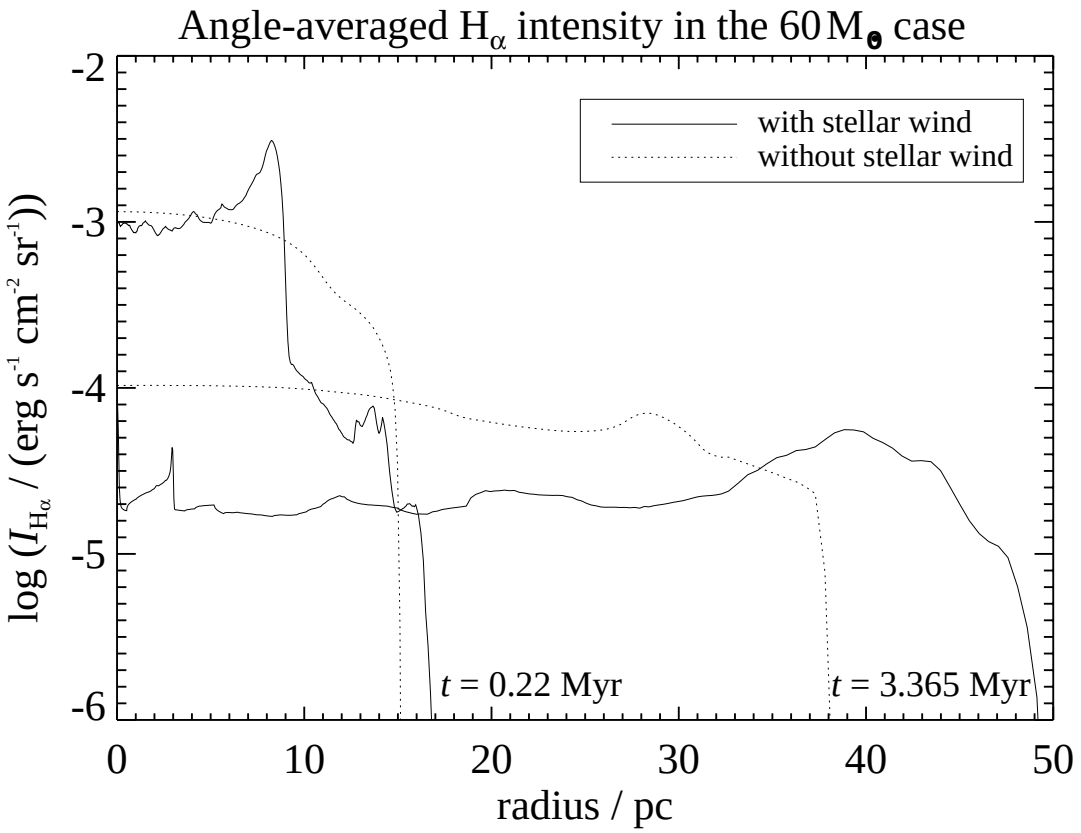

Figure 4.27: Angle-averaged Hα intensity in the 60 $M_\odot$ case with and without a stellar wind compared at two evolutionary times.

further expansion of the bubble and HII region generally lowers the Hα surface brightness, as expected for comparable Lyman continuum fluxes. In particular, when the SWB completely overtakes the HII region and enlarges the whole structure, the Hα surface brightness is lower than in the pure HII region calculation at the same time.

As a result of the facts that the photoionized region is more or less limited to the illuminated inner part of the shell and that the Hα emissivity in the hot cavity is very low, the intensity profile of the combined SWB/HII region appears slightly limb brightened. The Hα emission from the W-R bubble is barely visible above the Hα background from the MS bubble. It might be that in our simulation the shell of the W-R bubble is too hot (e.g., as a result of the neglect of heat conduction) and thus emits more strongly in X-rays (see below) than in the optical.

For the X-ray intensity profiles in the energy range from 0.5 to 3.0 keV we use the emissivity calculated with the Raymond & Smith (1977) program for cosmic chemical composition (Allen 1973). The emissivity is set to zero for temperatures below 10^5 K; absorption is not considered. In Figure 4.28 we display the angle-averaged soft X-ray intensity profiles at $t = 1.0$, 3.30 (before the LBV phase), and 3.365 Myr (after the LBV phase). The two snapshots before the LBV stage show intensities between 10^{-10} and 10^{-8} erg s^{-1} cm^{-2} sr^{-1} for lines of sight through the hot bubble. After the LBV stage, the soft X-ray intensity close to the center of the bubble is strongly enhanced by more than 3

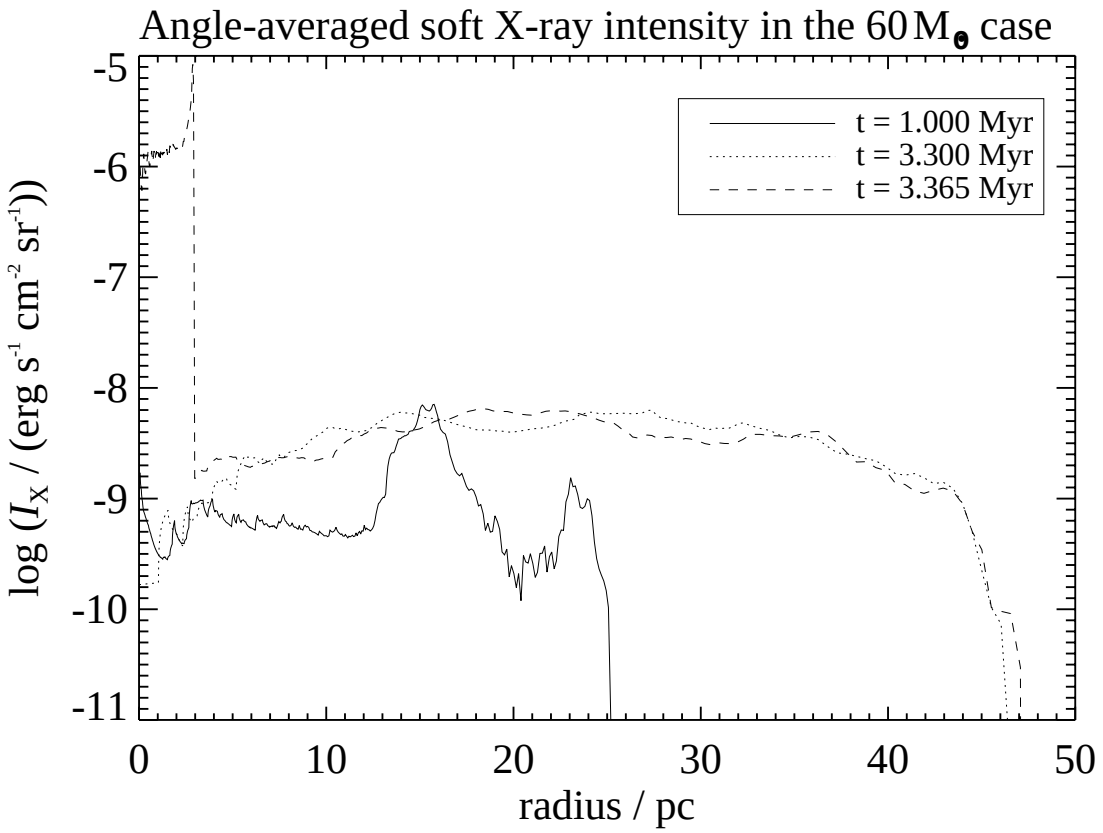

Figure 4.28: Angle-averaged soft (0.5-3.0 keV) X-ray intensity in the 60 $M_\odot$ case with stellar wind at selected evolutionary times.

orders of magnitude to values above $10^{-6}\,\mathrm{erg\,s^{-1}\,cm^{-2}\,sr^{-1}}$ when the shocked W-R wind hits the LBV ejecta. The soft X-ray emission comes mainly from the inside of the shell of the swept-up LBV wind, before it breaks apart.

The W-R nebula RCW 58 around HD 96548 (= WR 40) is a possible candidate for an observed counterpart of the W-R nebula that forms in our model calculation at $t = 3.365\,\mathrm{Myr}$. The W-R star is currently of type WN8 and there are indications that the star passed the LBV stage (GML1; Humphreys 1991). The mean radius of the optical nebula is 3.5 (Chu 1982) or 2.5 pc (Arthur et al. 1996) depending on the estimation of the distance to HD 96548. Thus, the evolutionary state of the nebula should be approximately comparable to the nebula in our model calculation.

Although the strong increase of the surface brightness in our simulation after the LBV phase is basically in agreement with the fact that up to now only W-R bubbles (and no MS bubbles) have been observed in X-rays, the comparison with RCW 58 shows that our model also suffers from the same problem that all analytical and numerical models thus far have: the X-ray luminosity is much higher than observed. In our simulation, the X-ray luminosity of the W-R bubble in the energy range from 0.5 to 3.0 keV is $7 \times 10^{33}\,\mathrm{erg\,s^{-1}}$, whereas Moffat et al. (1982) report that no X-ray emission from RCW 58 was detected with the *Einstein* satellite, meaning that the X-ray luminosity of RCW 58 in this energy range must be below $10^{32}\,\mathrm{erg\,s^{-1}}$ (Arthur et al. 1996).

4.2 The 35 $M_\odot$ Case

4.2.1 The Evolution of the Circumstellar Medium

Figures 4.29 to 4.44 depict the evolution of the gas in the vicinity of and under the influence of the 35 $M_\odot$ model star. The data are plotted in the same manner as in section 4.1.1 for the 60 $M_\odot$ case. Once again, I begin the discussion with the initial model that has been set up from the one-dimensional solution. For the 35 $M_\odot$ case this is done after 700 yr because—due to the lower mechanical wind luminosity of the star—the pressure in the hot bubble is lower. Thus, the forward shock is weaker and the shell of swept-up material is less heated and collapses earlier.

As expected, the basic structure of the SWB/HII region seen in Figure 4.29 is the same as for the 60 $M_\odot$ case except for the length and timescales. The stellar wind flows with the terminal velocity of nearly 4000 km s^{-1} freely out to $r \approx 0.08$ pc, the position of the reverse shock, where it is heated up to about 10^8 K. The forward shock that sweeps up the HII region is at $r \approx 0.23$ pc and moves with some 130 km s^{-1}. Density and temperature immediately behind this shock front are $\rho \approx 1.4 \times 10^{-22}$ g cm^{-3} and $T \approx 2.5 \times 10^5$ K, respectively, which is in good agreement with the jump conditions for a strong shock moving into photoionized gas with $T \approx 8000$ K. The ionization front is still weak R-type at 4.7 pc.

After 5×10^4 yr (Figure 4.30) the hot bubble extends out to about 2.3 pc. The shell of swept-up HII region expands with some 24 km s^{-1}. Density knots have been produced in the thin shell, similar to those seen in the 60 $M_\odot$ case, altering the optical depth along different radial lines of sight. The HII region has begun to expand with almost 10 km s^{-1}, sweeping up the ambient neutral gas, but the ionization front has started to retreat at the places where the clumps in the stellar wind shell cast shadows into the HII region. The basic morphological structure is still comparable to the 60 $M_\odot$ case.

Figure 4.31 shows the evolutionary state of the 35 $M_\odot$ case after 0.2 Myr. The radius of the HII region is approximately 9.5 pc, and it expands into the ambient medium at several km s^{-1}. (When neutral shadows and ionized extensions appear, we define the radius of the HII region as the distance from the star to the "undisturbed" ionization front, which is neither extended along the fingers nor shortened by the shadows.) The hot bubble has grown to $r \approx 4.8$ pc, and the expansion velocity of the stellar wind shell has decelerated to ≈13 km s^{-1}. This is comparable to the sound speed in the HII region; i.e., the outermost side of the stellar wind shell is no longer bound by a shock front and has begun to expand into the HII region as a result of the pressure gradient between the shell and the HII region. (For clarity, we distinguish the stellar wind shell and the HII region. Actually, the stellar wind shell is an important part of the HII region because it is, at least at this point in time, photoionized by the star.) At $t = 0.2$ Myr the geometrical thickness of the stellar wind shell has already grown to 1 pc and the density in the shell is $(6 - 9) \times 10^{-23}$ g cm^{-3}.

As a result of the growth of the geometrical shell thickness, the thin-shell overstability that triggered the formation of density clumps in the shell ceased and the clumps dissolved; the period of time they were present in the stellar wind shell was relatively short. Thus, the shadows in the HII region are much less pronounced and the finger-like

extensions of the HII region are shorter and less numerous than for the 60 $M_\odot$ case. Nevertheless, density fluctuations in the HII region of more than an order of magnitude have been produced. (This may be a lower limit because of restrictions in resolution.) Maximum densities are around $\rho \approx 5 \times 10^{-23}$ g cm^{-3} and minima around $\rho \approx 3 \times 10^{-24}$ g cm^{-3}. At these densities, temperatures, and masses the clumps are not gravitationally bound.

The dissolution of the stellar wind shell can be seen impressively in Figure 4.32 at $t = 0.3$ Myr. The expansion of the stellar wind shell has become a 2 pc broad belt of outflow with density $(2-5) \times 10^{-23}$ g cm^{-3} from the contact discontinuity at $r \approx 6$ pc into the HII region with about sound speed.

Additional processes are triggered by the rarefaction of the gas that previously belonged to the stellar wind shell. Because of the increase of hydrogen recombination time with lower density, excess photons are generated that reionize the shadowed regions (see Fig. 4.32, bottom) and advance the ionization front even further, evaporating additional material from the HII region shell of swept-up ambient medium ahead. This evaporation is visible in the density increase and the disturbed velocity field in the outer parts of the HII region close to the ionization front. As a transient phenomenon, another shell with a density of $(3-6) \times 10^{-23}$ g cm^{-3} develops at $t \approx 0.35$ Myr when the former stellar wind shell gas flowing into the HII region collides with the material photoevaporated from the shell of swept-up ambient gas.

Together with the relics of denser fragments in the HII region, the larger opacity in this dense shell causes once again the formation of small ripples in the ionization front at $t \approx 0.4$ Myr (Figure 4.33). At this time the radius of the hot bubble is about 7.5 pc and the geometrical thickness of the whole HII region is about 4 pc. However, the newly formed shell soon dissolves because of its overpressure with respect to the rest of the HII region, and within certain limits it can thus be said that the dissolution of the stellar wind shell leads to a "rehomogenization" of the HII region.

If we continue our analysis of this case to $t = 0.6$ Myr (Figure 4.34; please note the different scale), we see that the hot bubble has grown to almost 10 pc in radius. The shell-like HII region, still expanding into the ambient medium at about 10 km s^{-1}, becomes more and more homogeneous. Nevertheless, remaining density fluctuations from the previous formation and destruction processes are still in the range from 7×10^{-24} to 4×10^{-23} g cm^{-3}.

We compare the morphological characteristics of the circumstellar gas that result from our runs with different resolution after 1 Myr in Figure 4.35 (high resolution) and Figure 4.36 (medium resolution). As can be expected, the overall structure in both runs is the same. The radius of the shell of swept-up ambient gas around the HII region is $\approx$17 pc, and it expands at almost 10 km s^{-1}. The geometrical thickness of the HII region itself is slightly larger in the high-resolution run, the velocity field in the HII region is stronger perturbed than in the medium-resolution run, and some fragments of the photoionized gas protrude and get mixed into the hot gas. All the latter deviations can be understood in terms of the finer substructures in the HII region, which were able to form in the high-resolution run. However, the trend toward a rehomogenization of the HII region continues. The density fluctuations in the HII region are only in the range of 9×10^{-24} to 2×10^{-23} g cm^{-3}, except for very small regions at the inner side of the shell of swept-up ambient gas. Here the density is reduced after neutral clumps from the shell

have been evaporated "explosively". Subsequently, for $t > 1$ Myr we consider only the medium-resolution model.

Since the stellar parameters vary only very gradually during the MS phase until the star enters the RSG stage (see Figure 3.5), the basic structure of the SWB/HII region remains the same during the next 3 Myr except that it continues to grow. Thus, we can procede very fast with our description of the evolution, showing snapshots of the evolutionary state only every megayear.

After 2 Myr (Fig. 4.37, please note once again the larger scale) the radius of the hot bubble extends out to 17 pc. The thickness of the HII region shell has grown to approximately 7 pc due to the decrease of thermal pressure in the HII region. The hot bubble and the photoionized HII region are already in pressure equilibrium; as the pressure of the hot bubble decreases through expansion, the pressure of the HII region drops, too. Because the temperature in the HII region is nearly constant in time, the density has decreased to $(7.3 - 11) \times 10^{-24}\,\mathrm{g\,cm^{-3}}$. This is not only a lower mean value, the density spread also continues to shrink. The thermal pressure of the SWB/HII region is still 40 times higher than that of the ambient medium and the HII region still expands into the ambient medium at about $6\,\mathrm{km\,s^{-1}}$.

Figure 4.38 shows the state of the circumstellar gas after 3 Myr. The radius of the hot bubble measures now almost 22 pc and the thickness of the HII region shell about 8 pc. The density in the HII region covers the range $(5.2 - 7.5) \times 10^{-24}\,\mathrm{g\,cm^{-3}}$. The outer shell of swept-up ambient medium still expands at $\approx 5\,\mathrm{km\,s^{-1}}$. As a result of the decrease of pressure in the HII region and the increase of total mass in the outer shell, the geometrical thickness of the outer shell has grown to about 2 pc. The density in the outer shell is $\rho \approx 2 \times 10^{-22}\,\mathrm{g\,cm^{-3}}$.

One megayear later, at the age of 4 Myr (Fig. 4.39), the basic picture is still similar. The radius of the hot bubble is now about 27 pc, the HII region extends out to ≈35 pc, and the density in the HII region is $(3.9 - 5.5) \times 10^{-24}$ g cm^{-3}. A few dense clumps are visible in the hot bubble that have detached from the HII region. The thermal pressure of the SWB/HII region is still ≈20 times higher than that of the ambient medium, and the whole structure still expands at about $4 - 5$ km s^{-1}. As a result of the additionally swept-up material, the reduced pressure in the HII region, and the deceleration of the expansion, the geometrical thickness of the outer shell has increased to almost 3 pc while its density has decreased to $\rho \approx (1 - 2) \times 10^{-22}$ g cm^{-3}. Thus, the mass collected in this shell is about 2×10^{38} g. This result is in good agreement with the picture that most of the ambient gas that has been swept up during the expansion since the ionization front turned to D-type is still stored in the outer shell and that only a minor fraction has been evaporated into the HII region.

At $t \approx 4.52$ Myr the star enters the RSG phase. The effective temperature of the star decreases to a few thousand Kelvin and the Lyman continuum flux drops by many orders of magnitude. The mass-loss rate strongly increases and the terminal velocity of the wind decreases; i.e., the star blows a dense and slow wind into the hot bubble. This can be seen in Figure 4.40, which depicts the state of the circumstellar gas at $t \approx 4.59$ Myr. At this time the dense RSG wind fills the inner 5 pc of the volume and expands at about 90 km s^{-1} into the hot bubble extending out to about 30 pc. Although the wind speed during the RSG phase is relatively low (compared to the MS and W-R phases),

the material becomes shocked when it is decelerated by the pressure of the MS bubble because the sound speed in the RSG wind is also low. (The gas is cold and neutral, or even molecular, because the soft stellar radiation field in the RSG phase is incapable of ionizing and heating it.) Since the density of the RSG wind is fairly high, this reverse shock is radiative and forms the very thin and dense RSG shell, which is not completely resolved in our calculation (compare to GLM2, the case of the fast RSG wind). Because of the reduction of Lyman continuum flux, the hydrogen in the former HII region in the range $30\,\mathrm{pc} \lesssim r \lesssim 38\,\mathrm{pc}$ starts to recombine. The degree of hydrogen ionization drops to $\approx$0.3 as the gas cools from about 6600 K at $t = 4$ Myr to some 4800 K. Thus, the thermal pressure in the (former) HII region drops significantly, leading to a further broadening and slowing down of the outer shell of swept-up ambient medium, which at this time has a thickness of about 3 pc and a velocity of $\approx$4 km s^{-1}.

The transition from the RSG phase of the star to the W-R phase occurs at $t \approx 4.754$ Myr. In the W-R phase the mass-loss rate is somewhat lower than in the RSG stage (see Figure 3.5), but the terminal velocity of the W-R wind is much higher (a few thousand km s^{-1}). The mechanical luminosity of the W-R wind is thus much higher than that of the RSG wind. Because of the increase of effective temperature to about 10^5 K, the stellar photon output occurs largely beyond the Lyman continuum limit; the star's Lyman continuum luminosity $\approx 10^{39}$ erg s^{-1} is higher than during the MS phase of the star. Figure 4.41 shows the structure of the circumstellar gas at $t = 4.78$ Myr, some 2.6×10^4 yr after the start of the W-R wind. The fast (and thus less dense) W-R wind reestablishes a nonradiative reverse shock that heats the W-R wind to about 10^8 K. The expansion of the hot gas sweeps up the slow RSG wind in the W-R shell. The expansion velocity of the W-R shell is high, almost 400 km s^{-1}. Therefore, a strong shock ahead of the W-R shell heats the RSG wind material and the W-R shell is thick (of the order 1 pc) and hot ($\approx 10^6$ K). Figure 4.41 pinpoints the moment when the W-R shell and the RSG shell collide so that only one shell of swept-up RSG wind is visible within the MS bubble (see GLM2). Please note that the shell distortion at the z-axis is a result of the dense clump that has been there before. Stellar Lyman continuum photons ionize the RSG wind gas (before it is shock heated by the W-R shell) and reionize the former HII region, which can be seen by comparison of the lower panels of Figures 4.40 and 4.41.

As long as the W-R shell moves through the RSG wind material, the thermal pressure of the shocked W-R wind inside the W-R shell is counterbalanced by the ram pressure of the RSG material it sweeps up. When the shock passes over the boundary between the RSG and MS winds and moves into the lower density medium, it speeds up as a rarefaction wave travels back into the W-R shell. It is the overpressure of the shocked rarefied W-R gas which is accelerating the much denser W-R shell. This is the classical case of a Rayleigh-Taylor unstable configuration and the W-R shell is torn into long filaments as the shocked W-R wind breaks through it. This can be seen very impressively in Figure 4.42 at $t = 4.80$ Myr and in Figure 4.43 at $t = 4.82$ Myr.

Figure 4.44 shows the final, presupernova state of the circumstellar gas after 4.945 Myr of evolution. The wind flows freely out to $9 - 10$ pc. This value is somewhat uncertain, however, due to the very complex flow pattern. The freely flowing wind is surrounded by the hot bubble that extends out to $31 - 37$ pc (on average 34 pc). The gas density in the hot bubble is $(1 - 30) \times 10^{-27}$ g cm^{-3}. This is fairly high (compared to the density at

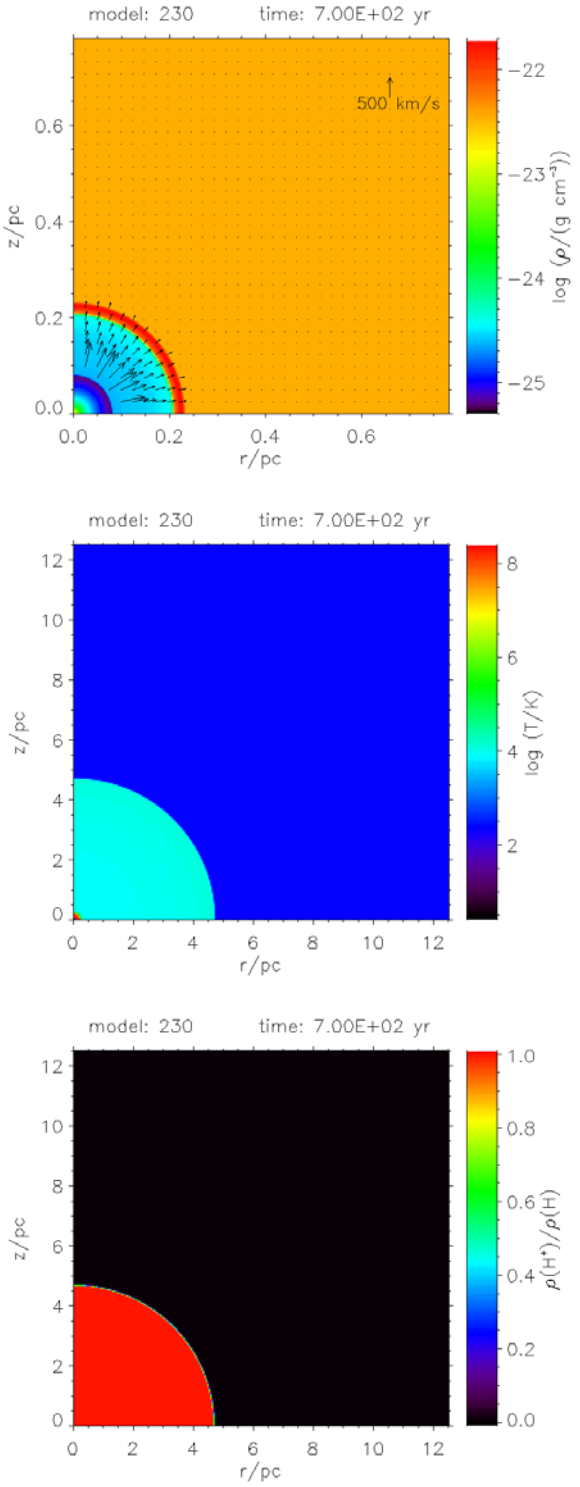

Figure 4.29: Circumstellar mass density and velocity field (top), temperature (middle), and degree of hydrogen ionization (bottom) for the $35\,M_\odot$ case at age 700 yr (high-resolution run). The velocity arrows in the free-flowing wind zone have been omitted to prevent confusion. The star is located in the center of the coordinate system. Please note the different length scales.

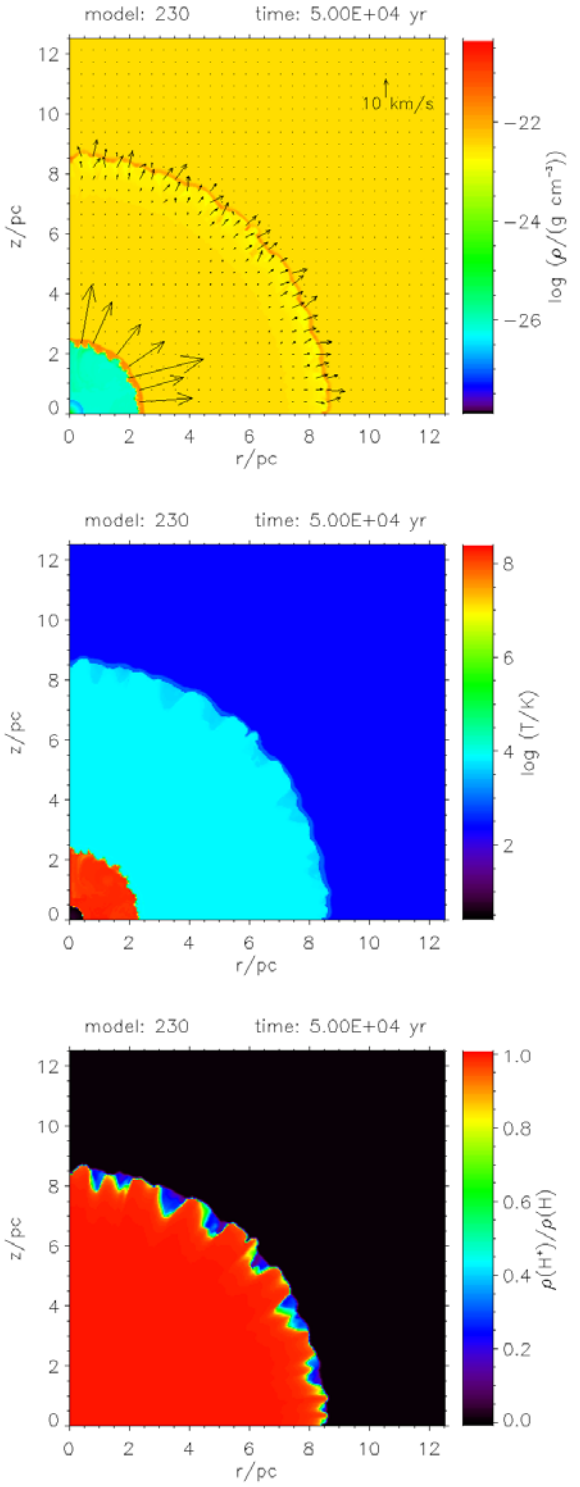

Figure 4.30: Same as Fig. 4.29, but at age 5×10^4 yr. The velocity arrows in the free-flowing wind zone and in the hot bubble have been omitted to prevent confusion.

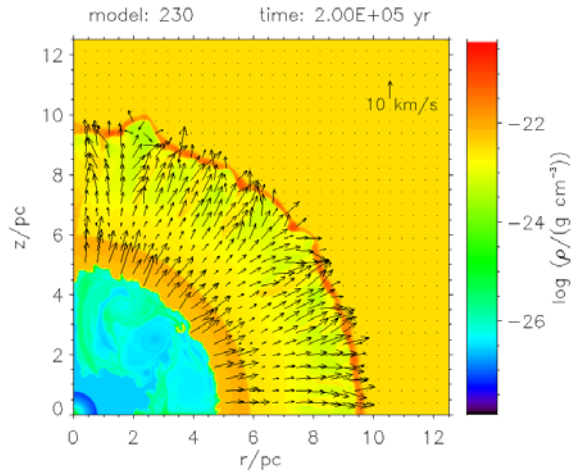

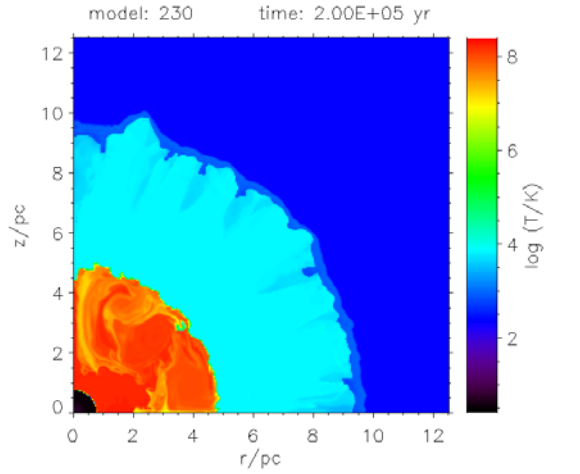

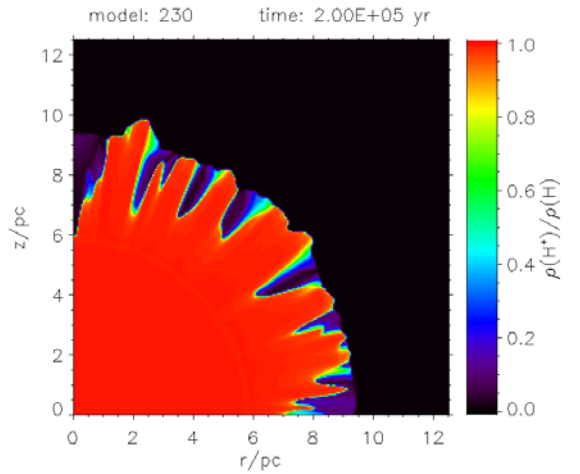

Figure 4.31: Same as Fig. 4.30, but at age 0.2 Myr.

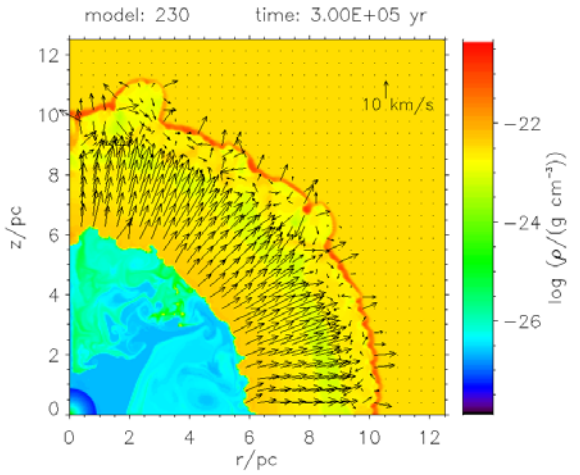

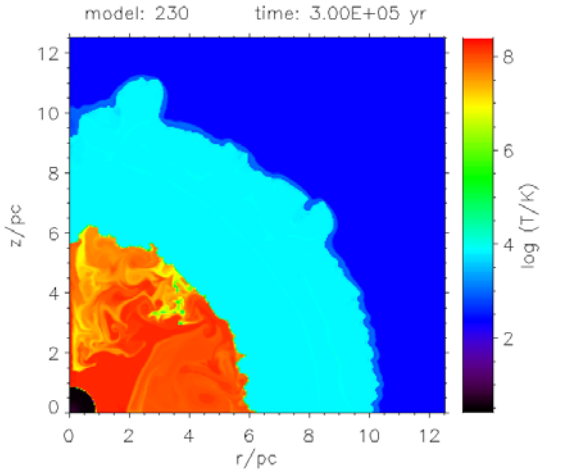

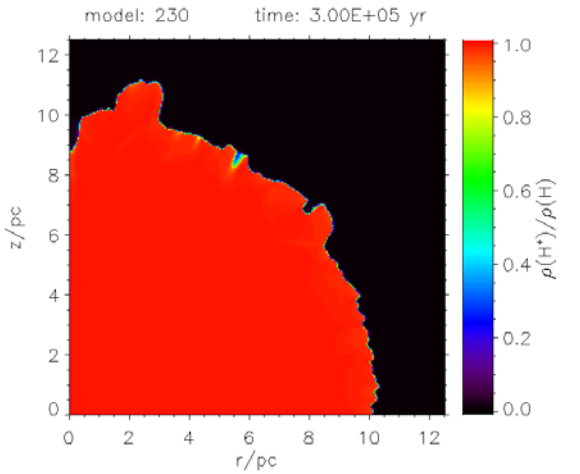

Figure 4.32: Same as Fig. 4.30, but at age 0.3 Myr.

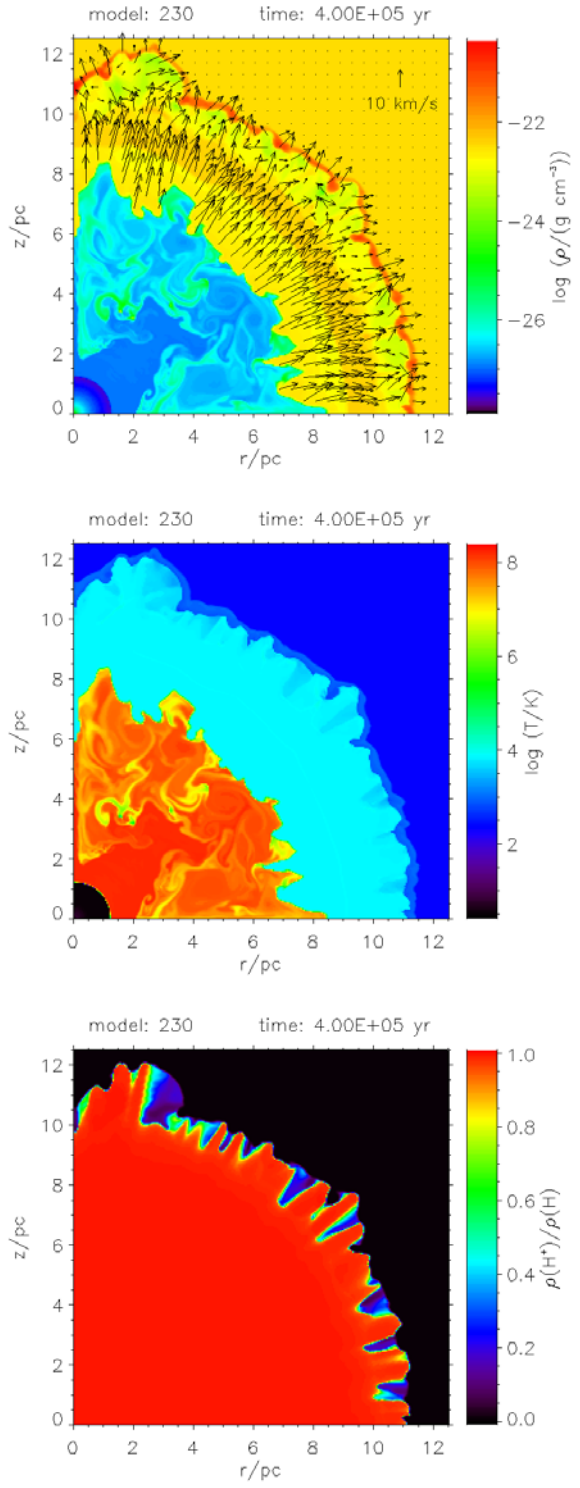

Figure 4.33: Same as Fig. 4.30, but at age 0.4 Myr.

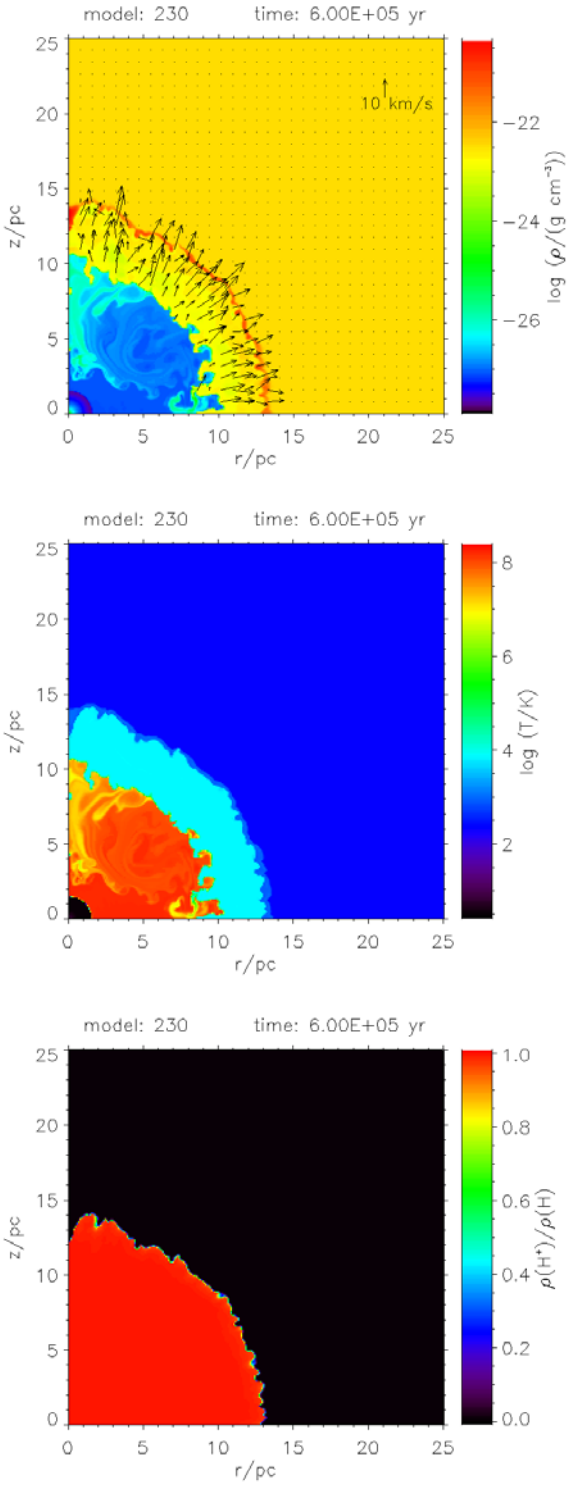

Figure 4.34: Same as Fig. 4.30, but at age 0.6 Myr. Because of the bubble expansion, a larger volume is shown.

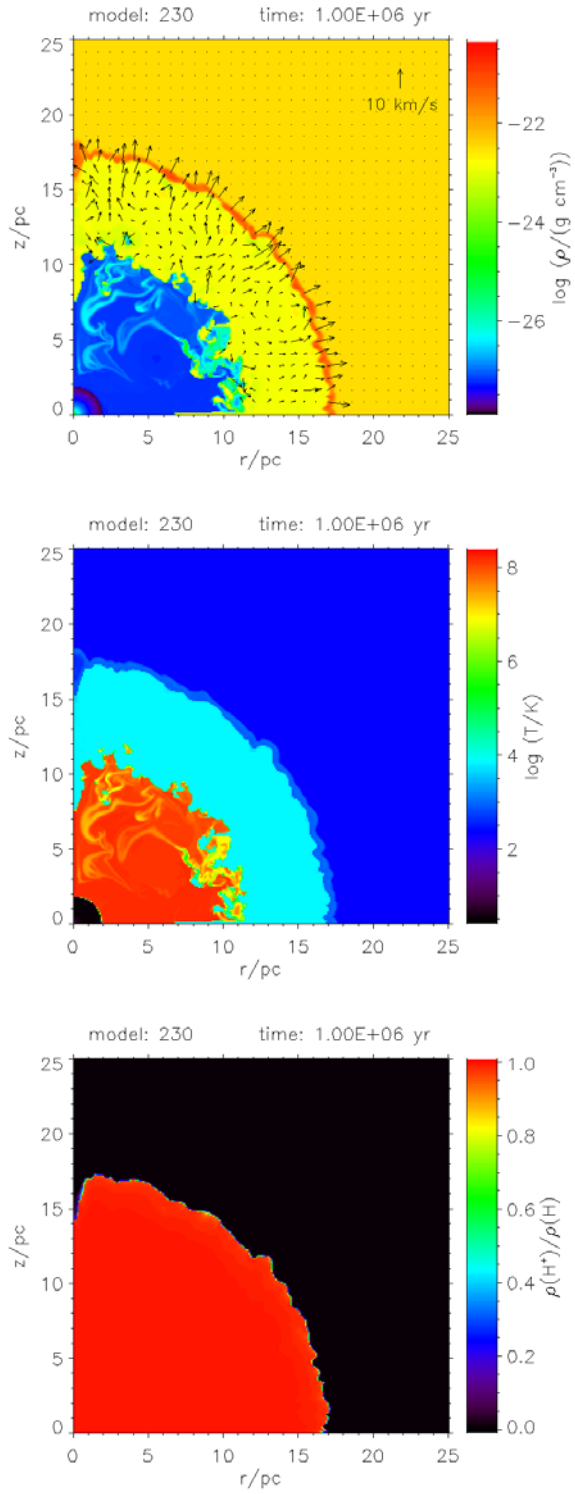

Figure 4.35: Same as Fig. 4.34, but at age 1.0 Myr.

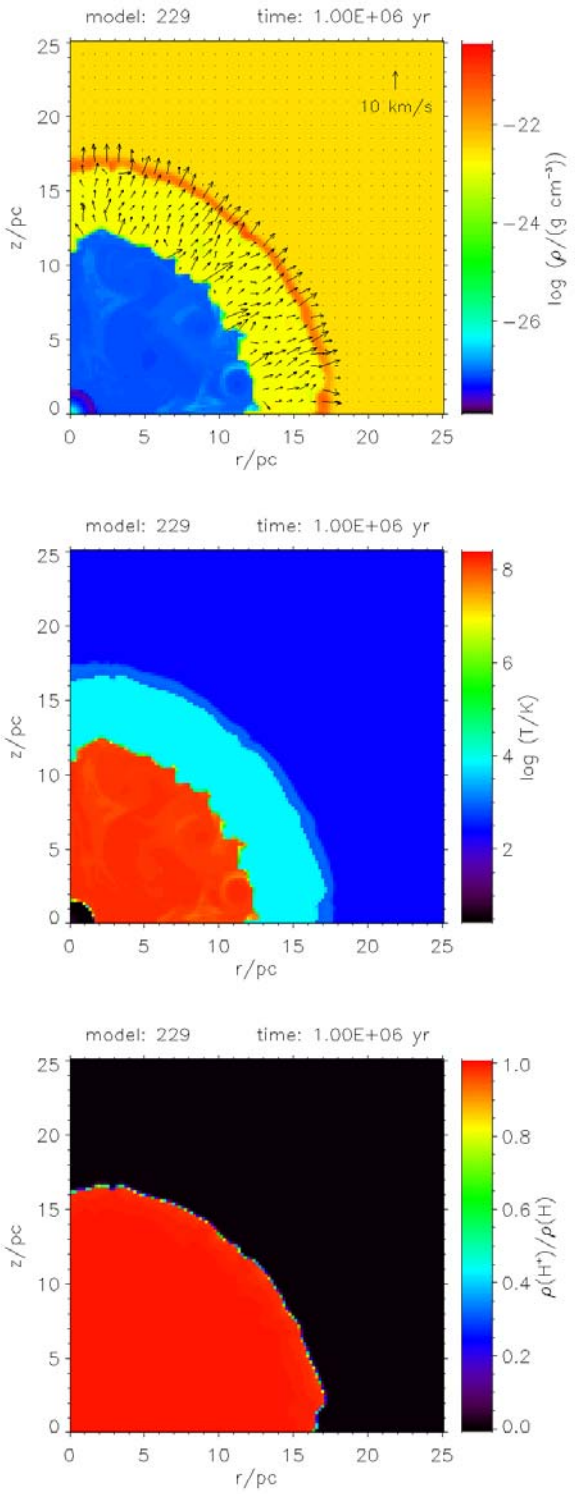

Figure 4.36: Same as Fig. 4.35, but for the medium-resolution run.

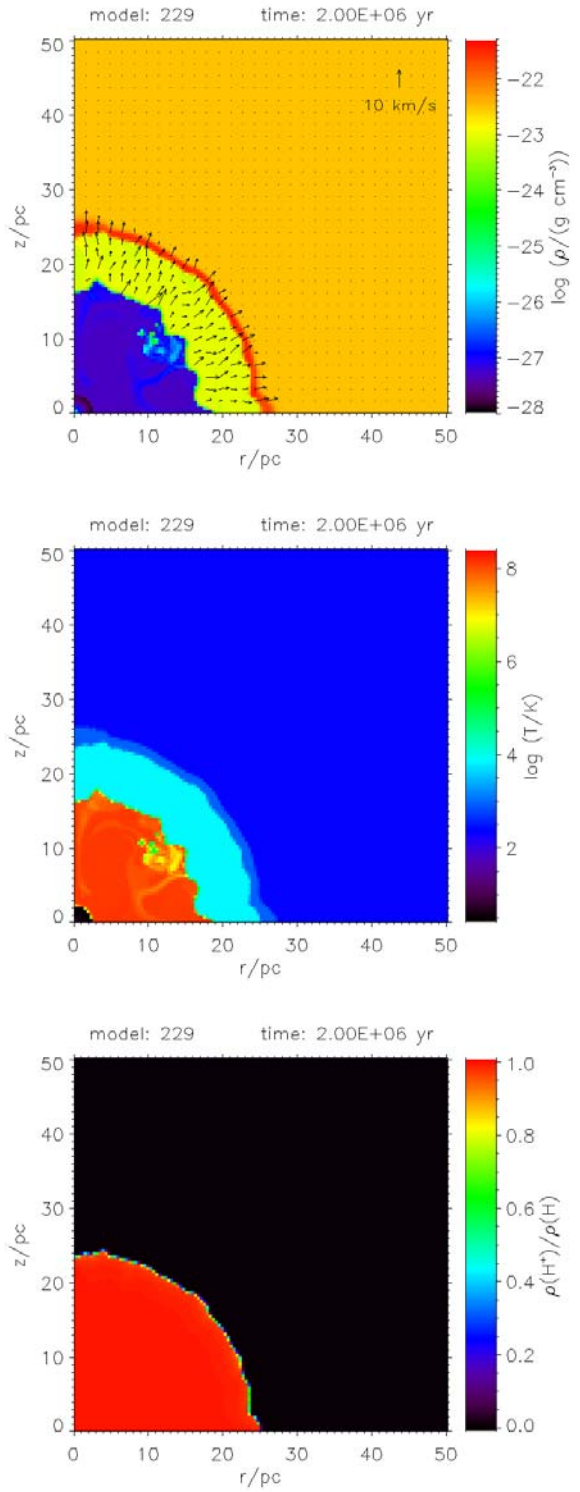

Figure 4.37: Same as Fig. 4.36, but at age 2.0 Myr, and the displayed area is enlarged once again.

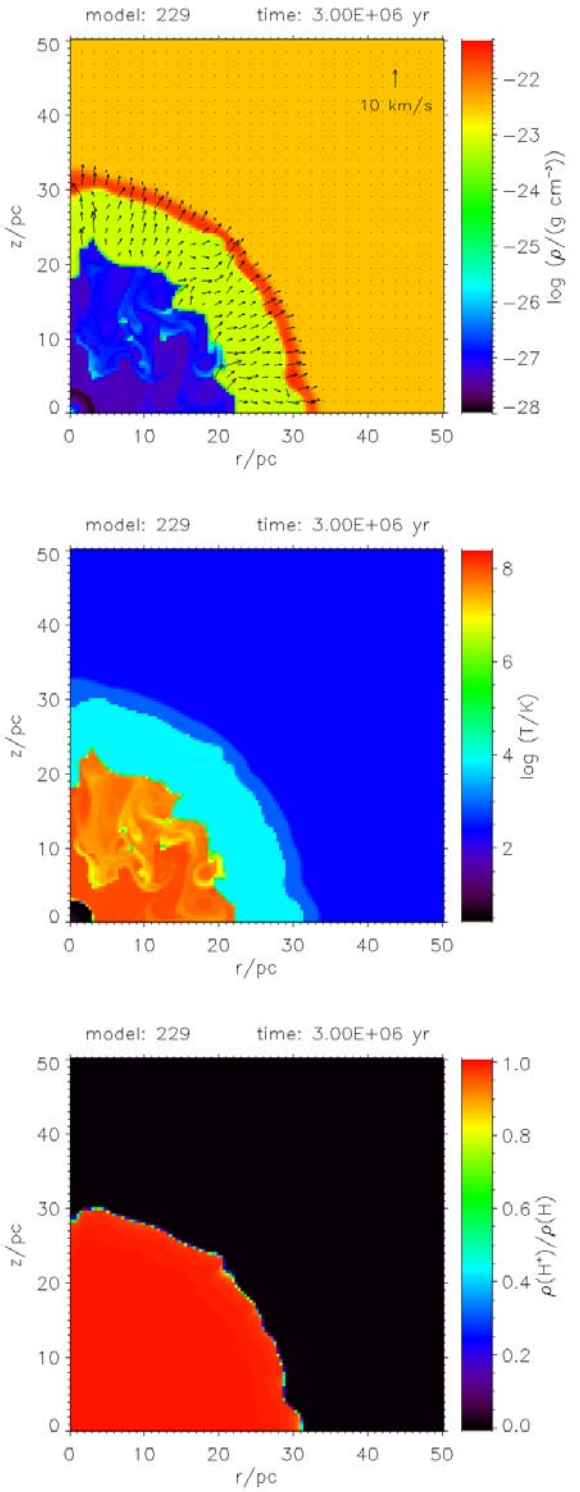

Figure 4.38: Same as Fig. 4.37, but at age 3.0 Myr.

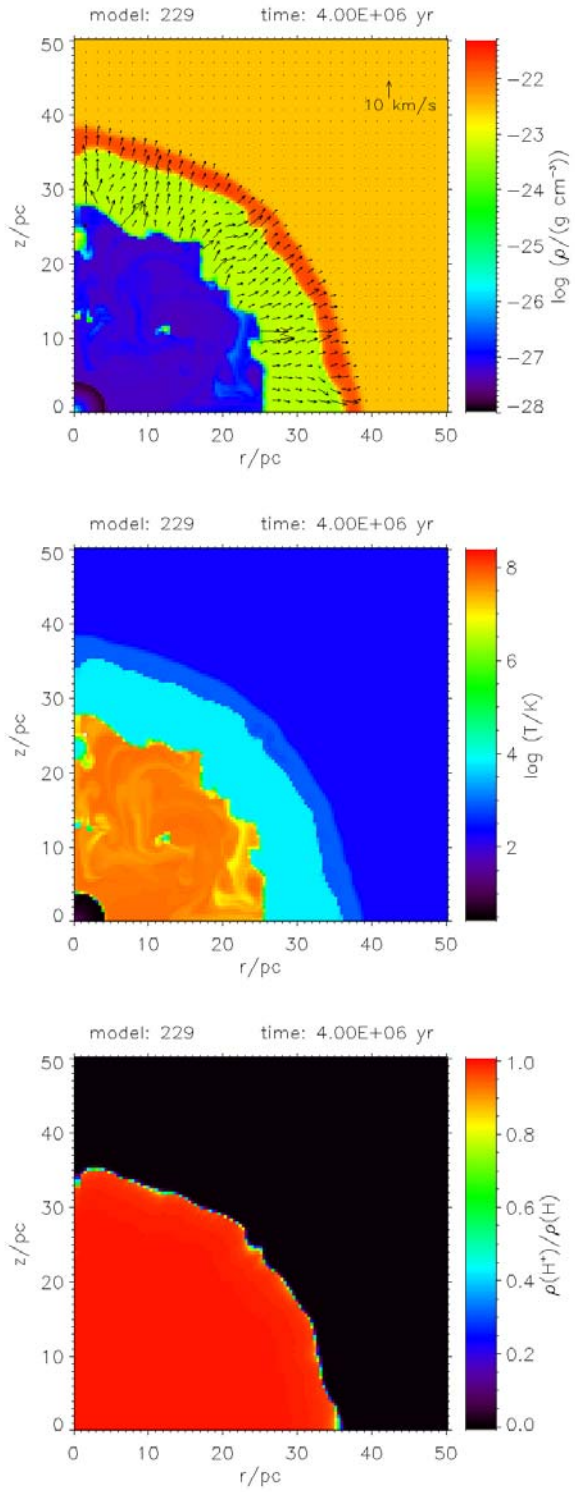

Figure 4.39: Same as Fig. 4.37, but at age 4.0 Myr.

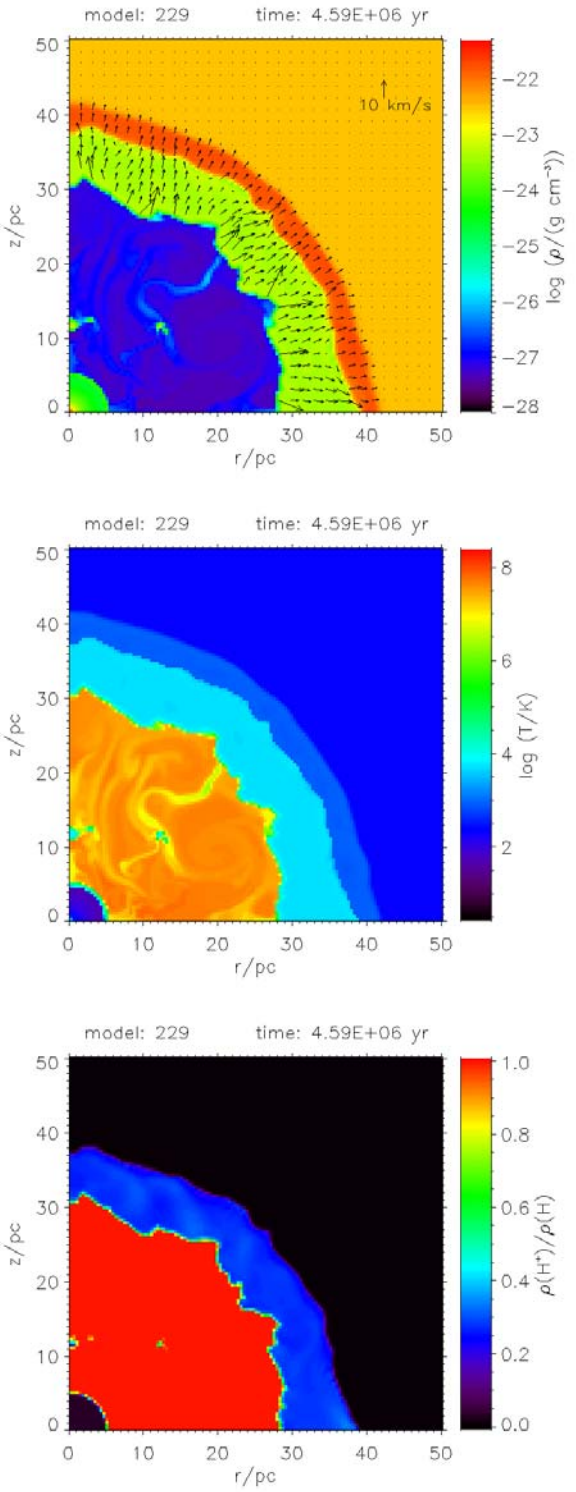

Figure 4.40: Same as Fig. 4.37, but at age 4.59 Myr.

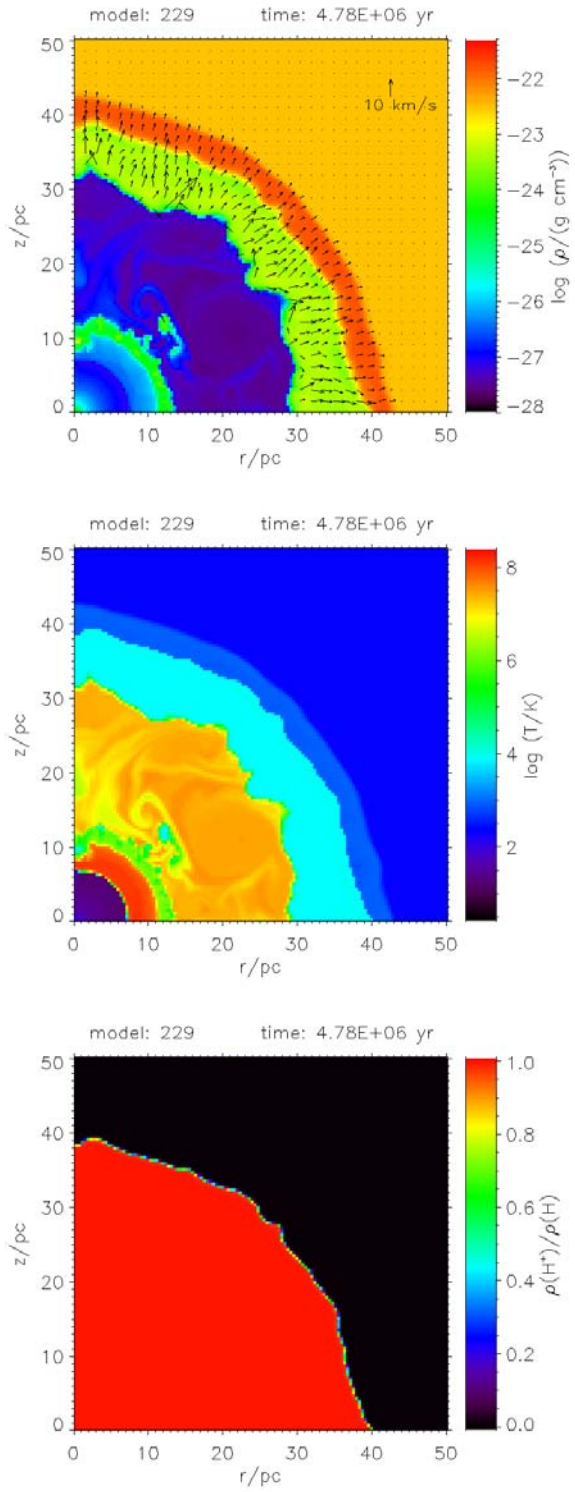

Figure 4.41: Same as Fig. 4.37, but at age 4.78 Myr.

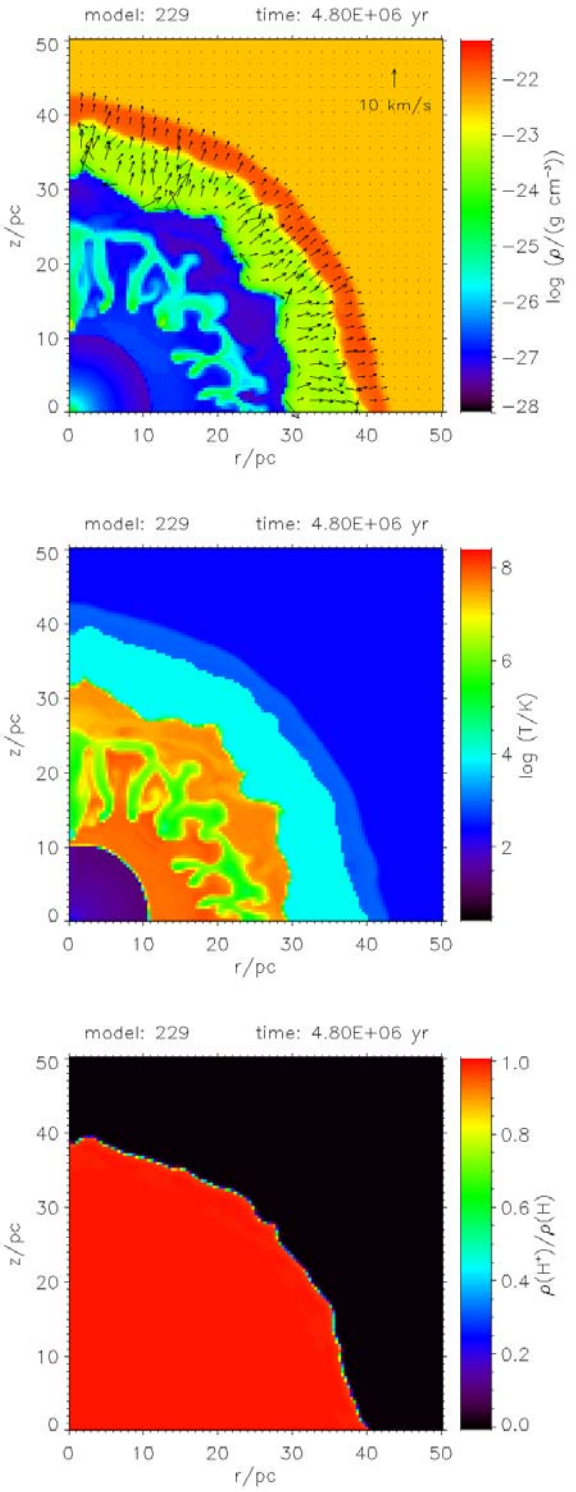

Figure 4.42: Same as Fig. 4.37, but at age 4.80 Myr.

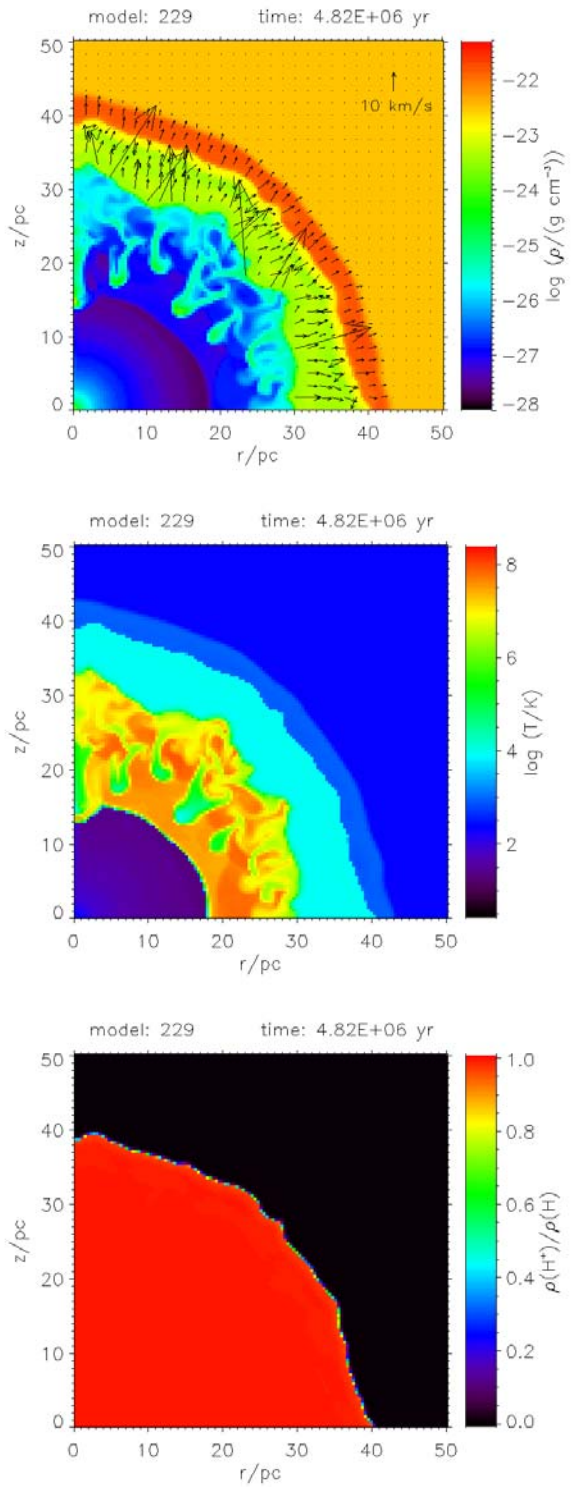

Figure 4.43: Same as Fig. 4.37, but at age 4.82 Myr.

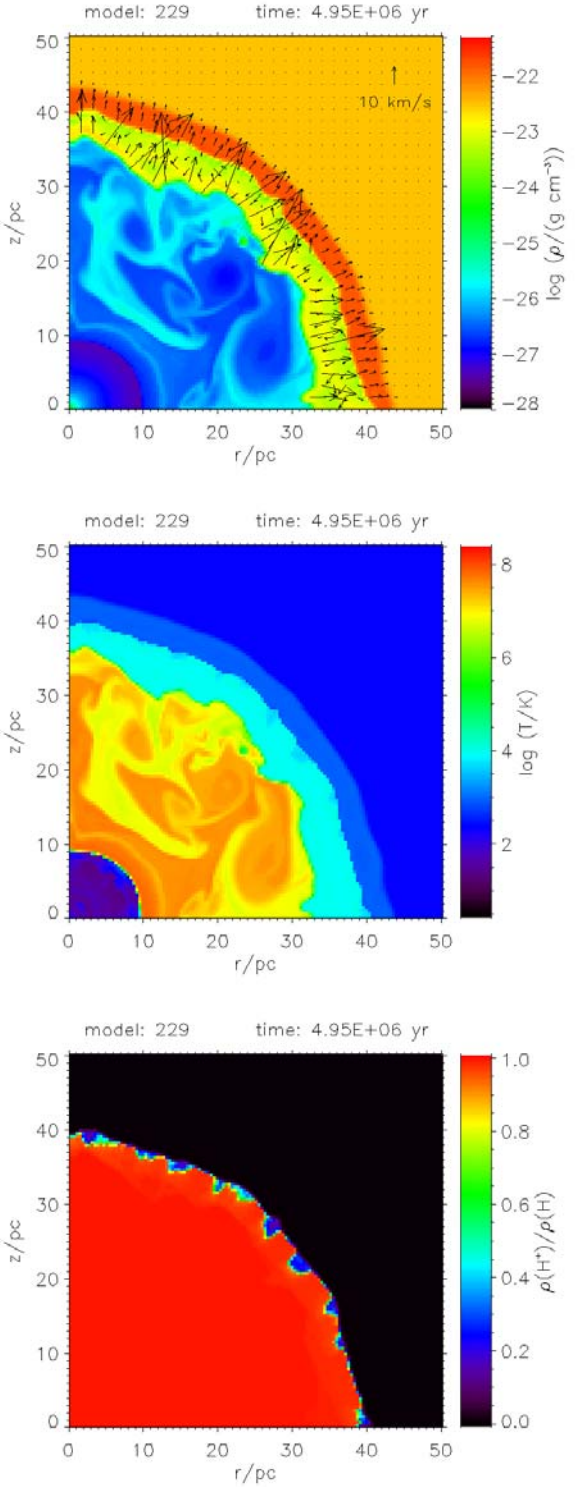

Figure 4.44: Same as Fig. 4.37, but at age 4.95 Myr.

the end of the MS phase of the star) because some of the RSG/W-R ejecta mixes with the hot bubble gas, enhancing the density significantly and lowering the temperature.

The thickness of the shell-like HII region has shrunk to $3-8$ pc with an average of 5.5 pc, after the RSG ejecta hit it and the pressure in the hot bubble has risen. This also enhances the density in the HII region to $(2-20)\times10^{-24}$ g cm^{-3}. The higher spread is a result of the higher W-R Lyman continuum flux (compared to the MS phase), leading to increased photoevaporation of the swept-up ambient material. Finally, the shell of swept-up ambient gas is $3-4$ pc thick, and the gas density in the shell is $(1-2)\times10^{-22}$ g cm^{-3}. The expansion velocity of this shell is $3-4$ km s^{-1} and therefore still supersonic with respect to the cold ambient ISM. The outermost shock moving into the ISM heats the swept-up ISM gas to almost 10^3 K. Thus, the whole structure extends out to a distance of $43-44$ pc from the star at this evolutionary time.

4.2.2 The Energy Balance in the Circumstellar Medium

Numerical Results

I discuss the energization of the circumstellar gas around the $35\,M_\odot$ star on the basis of Figure 4.45 and compare it with its counterpart for the $60\,M_\odot$ case (Figure 4.15 in section 4.1.2). The plot shows the energy contributions in the circumstellar gas as a function of time, namely, the kinetic energy of bulk motion in the whole computational domain, the ionization energy (13.6 eV per ionized hydrogen atom), and the thermal energy of cold ($T \leq 10^3$ K), warm (10^3 K $< T < 10^5$ K), and hot ($T \geq 10^5$ K) gas, respectively.

The ionization energy dominates after several thousand years, when the ionization front reaches the Strömgren radius. Here it attains a value of approximately 3.1×10^{49} erg, which is about half an order of magnitude less than for the $60\,M_\odot$ case due to the lower Lyman continuum luminosity of the $35\,M_\odot$ star. The subsequent dip in ionization energy is much less pronounced than for the $60\,M_\odot$ case, since at that time there is less structure formation in the HII region of the $35\,M_\odot$ case, as is evident in Figures 4.31 through 4.33. Afterward, the ionization energy rises smoothly to 1.8×10^{50} erg before the star enters the RSG stage. During the RSG stage the ionization energy drops by an order of magnitude since the H-ionizing radiation from the star is completely switched off and the photoionized gas recombines. The gas is reionized when the star evolves to the W-R phase; the ionization energy reaches a global maximum of 2.8×10^{50} erg. Contrary to the $60\,M_\odot$ case, the ionization energy remains the dominant form of energy in the system for the entire evolution except for a brief period at the end of the RSG phase.

A feature that we already described for the $60\,M_\odot$ case can also be seen in the $35\,M_\odot$ case: the evolution of the thermal energy of warm gas follows that of the ionization energy over the lifetime of the star with a shift of $0.7-0.9$ dex due to the fact that for both cases, photoionization is responsible for the bulk production of ionized gas at typically 8000 K. The shift is smaller during the RSG phase of the star because cooling is less efficient in the formerly photoionized regimes when the hydrogen recombines and the plasma becomes neutral.

The evolution of the kinetic energy of bulk motion and the thermal energy of hot gas are also very similar; they do not deviate from each other by more than 0.2 dex until

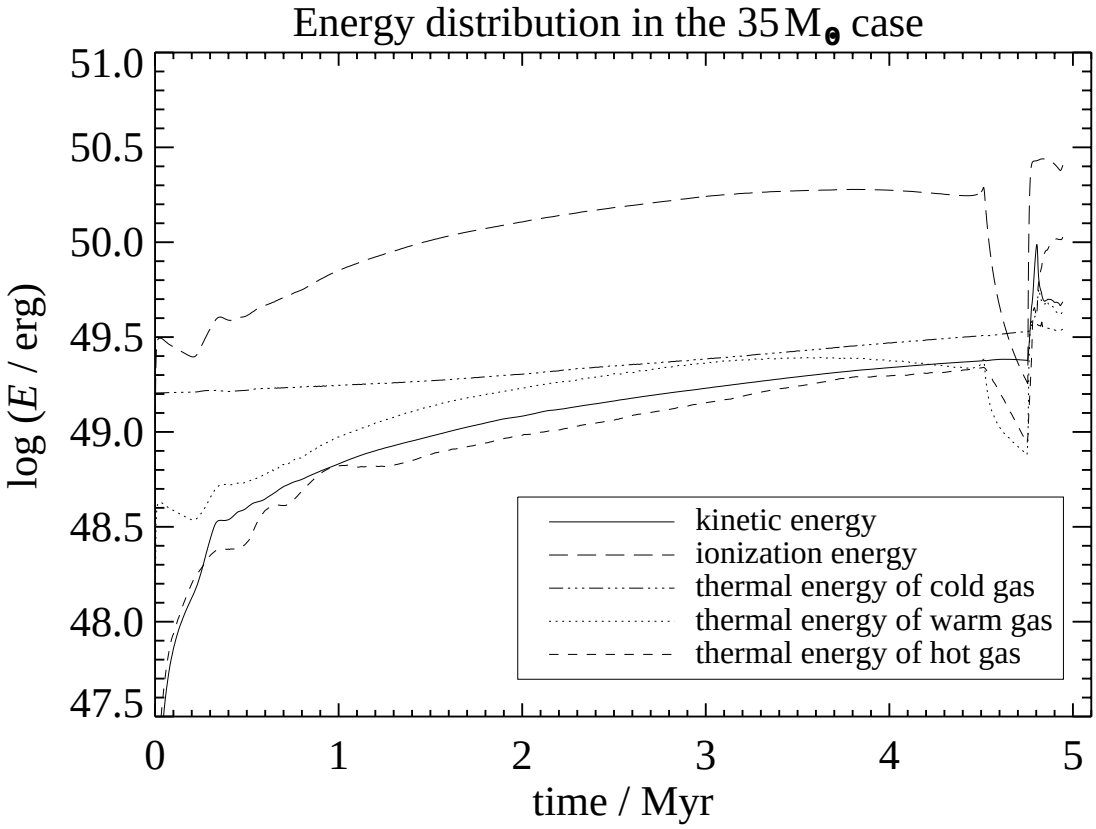

Figure 4.45: Temporal evolution of kinetic, thermal, and ionization energy in the 35 $M_\odot$ case.

the star enters the RSG phase. Whereas the kinetic energy remains basically constant during the RSG phase, the thermal energy of hot gas decreases as the supply of hot gas by the reverse shock dies off. The cooling of the hot gas and mixing with cooler gas continues. Both values rise when the nonradiative reverse shock reestablishes itself in the W-R phase. When the calculations are stopped, the kinetic energy is 4.9×10^{49} erg and the thermal energy of hot gas 1.1×10^{50} erg; the latter value is almost the same as at the end of the 60 $M_\odot$ calculation at 4.065 Myr.

The thermal energy of cold quiescent gas in the entire computational domain at the beginning of the calculation is 1.6×10^{49} erg (the same energy density as in the 60 $M_\odot$ case, but with a smaller computational volume). This value grows smoothly during the lifetime of the star as more and more ambient gas becomes swept up and weakly shocked by the outer shell. The thermal energy of the cold gas at the end of the calculation is 3.5×10^{49} erg; i.e., 1.9×10^{49} erg have been added during the evolution.

To study the impact of the stellar wind on the energy transfer in the circumstellar gas, we compare the energy in the system as a function of time for the two cases: 1) the standard case with wind and 2) the HII region evolution without wind (Figure 4.46; see also Figure 4.16). The kinetic energy of bulk motion is enhanced due to the added kinetic energy of the stellar wind shell. On the other hand, the compression of the HII region into a shell with higher density reduces the amount of ionization energy stored in the system compared to the windless case. Thus, the ratio of ionization energy for the calculation

with wind to that of the windless model is below 1 throughout the lifetime of the star. Both features are well recognized from the $60\,M_\odot$ case. In general, the deviations of the energies between the models with and without stellar wind are smaller in the $35\,M_\odot$ case, especially during the MS evolution. For most of the MS time the ratios are well within the interval $0.5 - 2.0$. This difference to the $60\,M_\odot$ case exists because the ratio of mechanical luminosity to Lyman continuum luminosity of the $35\,M_\odot$ star is smaller than that of the $60\,M_\odot$ star.

There is a drop in the ratio of the ionization energies with and without wind during the RSG phase of the star. At first glance, this is surprising since in the calculation with stellar wind there is additional ionization energy in the hot bubble. But the density in the hot bubble is very low, and although the thermal energy of the hot gas in the bubble is important, there is not much ionization energy involved. The reason for the drop in the ratio of the ionization energies with and without wind is the fact that in the calculation with wind the HII region is compressed into a shell surrounding the hot bubble and the density in this shell is higher than in the spherical HII region of the windless simulation. The higher density results in shorter recombination times and thus a faster loss of ionization energy when the Lyman continuum radiation of the star ceases at the beginning of the RSG phase.

Due to the acceleration of the slow RSG wind by the shocked W-R wind, there is a strong peak in the ratio of the kinetic energies with and without wind. This additional

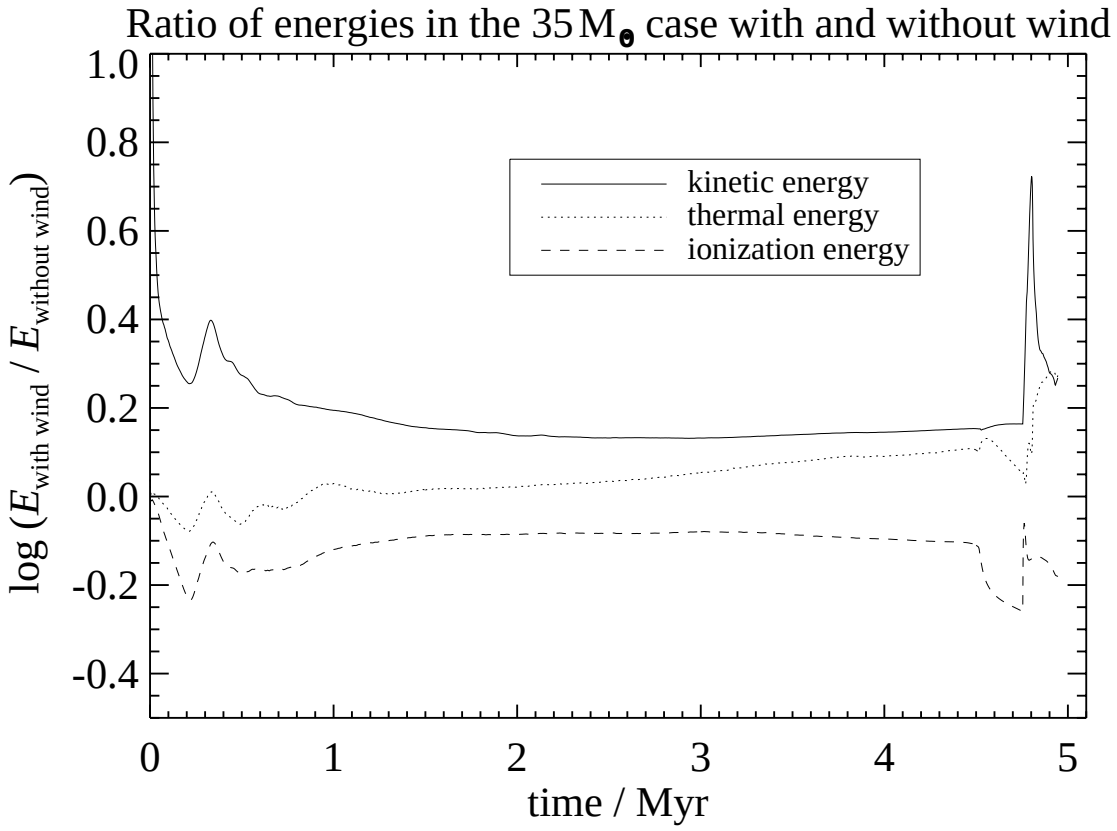

Figure 4.46: Ratio of energies in the $35\,M_\odot$ case with and without a stellar wind.

kinetic energy is partially dissipated when the accelerated RSG wind material hits the HII region. At the end of the simulation the kinetic energy in the calculation with stellar wind is enhanced by 85 %, whereas the ionization energy is reduced by 34 %, and the thermal energy that is added to the system during the evolution is increased by 88 % compared to the calculation without stellar wind.

One of the goals of this work is to determine the efficiencies with which the stellar input energy is converted into the different forms of energy in the circumstellar medium. We show these values for the 35 $M_\odot$ case in Figure 4.47 (compare Figure 4.24 in section 4.1.2). We recall here that we define the transfer efficiency as the cumulative fraction of the stellar input energy that has been converted into a particular form of energy in the circumstellar medium up to the time $t = \tau$, where τ is the age of the star. Figure 4.47 shows the transfer efficiencies into kinetic, ionization, and thermal energy and their sum for the 35 $M_\odot$ case.

As we have already seen in Figure 4.45, the energization of the circumstellar gas occurs fairly smoothly until the star reaches the RSG stage. The transfer efficiency into kinetic energy reaches 5.6×10^{-4} before and during the RSG phase and peaks up to 2.2×10^{-3} when the shocked W-R wind accelerates the RSG wind. At the end of the simulation it is 1.0×10^{-3}. The transfer efficiency into thermal energy is higher than that into kinetic energy by a factor of 2–3 during most of the MS time. It reaches 1.4×10^{-3} before the RSG phase, drops by almost a factor of 2 during the RSG phase, rises again when the

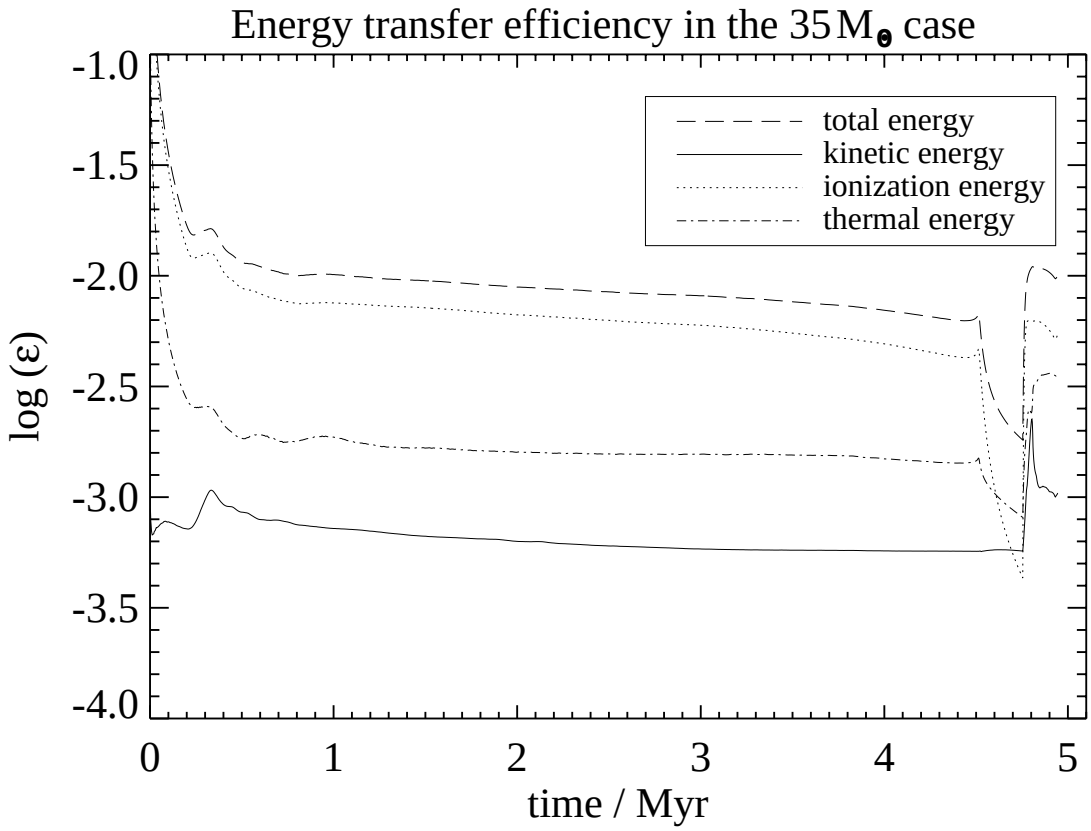

Figure 4.47: Energy transfer efficiency with respect to the total energy input in the 35 $M_\odot$ case.

star enters the W-R stage, and ends up at 3.6×10^{-3} at the end of the simulation. The transfer efficiency into ionization energy is the highest except during the RSG stage of the star. Before the RSG phase it is 4.4×10^{-3} and at the end of the simulation it is 5.5×10^{-3}.

For comparison, we also show the respective values for the $35\,M_\odot$ case without wind in Figure 4.48 (compare Figure 4.23 in section 4.1.2). In the windless case, there is only radiative energy input and all values are related to that. Since there is no additional structuring impact of the stellar wind, the transfer efficiencies into ionization energy and thermal energy develop even more smoothly than in the case with wind and reach values of 6×10^{-3} and 1×10^{-3}, respectively, before the star enters the RSG stage. The efficiencies decrease when the Lyman continuum luminosity of the star ceases during the RSG stage. They rise again with the onset of the W-R stage and reach final values of 8.4×10^{-3} and 1.9×10^{-3}, respectively. The energy transfer efficiency into kinetic energy is almost constant at $4 - 5 \times 10^{-4}$ during most of the MS and RSG lifetime of the star and jumps to 5.7×10^{-4} at the end of the simulation as a dynamical response of the HII region to the high Lyman continuum luminosity of the star during the final W-R phase.

The total energy transfer efficiency (into kinetic, thermal, and ionization energy) at the end of the simulation with wind is 10^{-2}; i.e., 1% of the total input energy from the star is transferred to the circumstellar gas. This is comparable to the net efficiency of the windless simulation. This result shows that, globally speaking, the role of the stellar

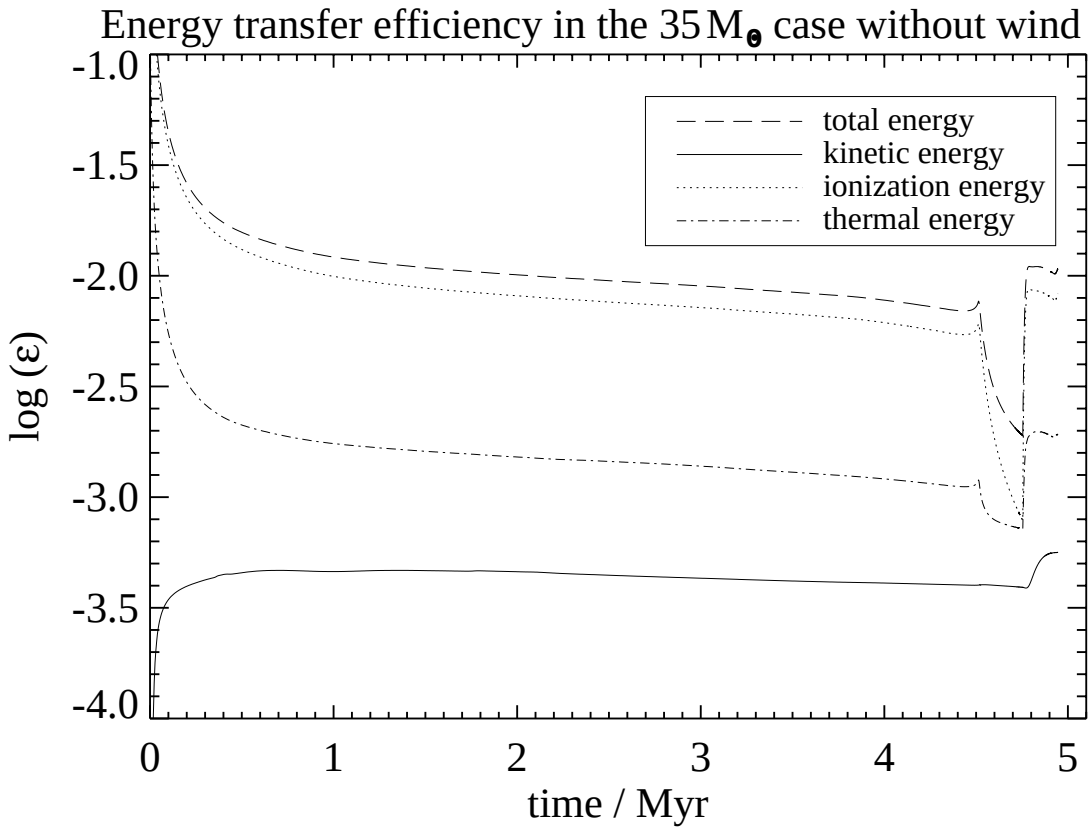

Figure 4.48: Energy transfer efficiency with respect to the total energy input in the $35\,M_\odot$ case without a stellar wind.

wind is less important than for the 60 $M_\odot$ case, in which its presence doubled the total energy transfer efficiency at the end of the calculation. However, the total energy transfer efficiency at the end of the 35 $M_\odot$ calculation is 2.7 times as high as for the 60 $M_\odot$ case. Since the circumstellar energy in the 35 $M_\odot$ case is dominated by ionization energy, a substantial fraction will be lost quickly when the star ultimately turns off. On the other hand, the SN will inject a huge amount of additional energy into the circumstellar gas. Both processes are beyond the scope of this thesis.

We summarize the values of the individual energy components (E_k, E_i, $E_\mathrm{t,cold}$, $E_\mathrm{t,warm}$, and $E_\mathrm{t,hot}$) at the end of the 35 $M_\odot$ simulations with and without stellar wind in Table 4.3. The values of the energy transfer efficiency into kinetic energy (ε_k), ionization energy (ε_i), thermal energy (ε_t), and their sum (ε_tot) at the end of the 35 $M_\odot$ simulations with and without stellar wind are given in Table 4.4. During the lifetime of the 35 $M_\odot$ star, the total energy emitted in the Lyman continuum is $E_\mathrm{LyC} = 4.61 \times 10^{52}$ erg and the mechanical energy of the stellar wind amounts to $E_\mathrm{w} = 4.77 \times 10^{50}$ erg.

Table 4.3: The energy components at the end of the 35 $M_\odot$ simulations.

Model parameters	E_k (10^{49}erg)	E_i (10^{49}erg)	$E_\mathrm{t,cold}$ (10^{49}erg)	$E_\mathrm{t,warm}$ (10^{49}erg)	$E_\mathrm{t,hot}$ (10^{49}erg)
Windless.....	2.6	39	3.0	7.6	0
With wind.....	4.9	25	3.5	4.3	11

Note.—The thermal energy of the cold component, $E_\mathrm{t,cold}$, contains the internal energy of the initially unperturbed ambient medium (1.6×10^{49}erg) that has to be subtracted whenever the input of thermal energy into the system is considered.

Table 4.4: The energy transfer efficiencies at the end of the 35 $M_\odot$ simulations.

Model parameters	ε_k (10^{-4})	ε_i (10^{-4})	ε_t (10^{-4})	ε_tot (10^{-4})
Windless.....	5.7	84	19	109
With wind.....	10	55	36	101

Comparison with Analytical Results

Taking mean values for the relevant stellar parameters over the lifetime of the 35 $M_\odot$ star, we can calculate the kinetic, ionization, and thermal energy in the system according to the analytical solutions given in section 2.6. With $\langle T_\mathrm{eff} \rangle = 3.78 \times 10^4$ K, $\langle L_\mathrm{LyC} \rangle = 2.95 \times 10^{38}$ erg s^{-1}, and using $\alpha_\mathrm{B} = 3.37 \times 10^{-13}$ cm^3 s^{-1} as hydrogen recombination coefficient and $c_\mathrm{s,II} = 1.15 \times 10^6$ cm s^{-1} for the isothermal sound speed in the HII region

(corresponding to $T_{\rm II} = 8000$ K), we obtain for $n_0 = 20$ cm^{-3} after $\tau = 4.945$ Myr from equations (2.57), (2.58), and (2.59) in section 2.6.1 for the $35\,{\rm M}_\odot$ case without wind:

$$\begin{aligned} E_{\rm k} &= 2.7 \times 10^{49} \text{ erg} , \\ E_{\rm i} &= 2.9 \times 10^{50} \text{ erg} , \\ E_{\rm t} &= 4.5 \times 10^{49} \text{ erg} . \end{aligned}$$

With the same definition of the energy transfer efficiency, according to equation (4.1) we get the corresponding energy transfer efficiencies in the analytical approach:

$$\begin{aligned} \varepsilon_{\rm k} &= 5.8 \times 10^{-4} , \\ \varepsilon_{\rm i} &= 6.4 \times 10^{-3} , \\ \varepsilon_{\rm t} &= 9.7 \times 10^{-4} . \end{aligned}$$

The analytical value for the transfer efficiency into kinetic energy deviates from the numerical result by less than 2 %. Bearing in mind all the approximations that were made in order to obtain the analytical solution, it is clear that the almost perfect correspondence between the analytical and numerical results is certainly by chance. This is supported by the fact that the numerical value for $\varepsilon_{\rm k}$ is almost constant during most of the MS and RSG lifetime, but jumps up by ≈40 % during the final W-R stage. Analytical and numerical results for the transfer efficiency into thermal energy show fairly good correspondence immediately before the RSG phase (not shown here), but since the final W-R stage boosts the thermal energy and thus also the transfer efficiency into thermal energy, the final value deviates from the analytical one by approximately a factor of 2. The comparison of analytical and numerical results for the transfer efficiency into ionization energy bears similar results. The values are fairly close to each other before the star turns to the RSG stage, and the deviation at the end of the simulation is also only ≈30 %.

As we have already discussed in section 4.1.2, the comparison of analytical with numerical results is much more difficult in the case of the combined SWB/HII region calculation because no analytical solution is yet known for energy transfer efficiencies in the case of HII regions with stellar winds. Again, we construct an analytical approximation by simply adding up the energy contributions from the HII region and the SWB, bearing in mind that this is only a rough estimation, which actually neglects the mutual interactions. In any case the analytical energy transfer efficiencies into kinetic and thermal energy are upper limits, since cooling in the hot bubble is not considered in the analytical approach.

Equations (2.61) and (2.62) yield the kinetic and thermal energy for the SWB only. Inserting the mean value of the mechanical wind luminosity, $\langle L_{\rm w} \rangle = 3.05 \times 10^{36}$ erg s^{-1}, and adding up the results for the pure HII region, we obtain

$$\begin{aligned} E_{\rm k} &= 1.6 \times 10^{50} \text{ erg} , \\ E_{\rm i} &= 2.9 \times 10^{50} \text{ erg} , \\ E_{\rm t} &= 2.6 \times 10^{50} \text{ erg} . \end{aligned}$$

Related to the sum of Lyman continuum radiation energy and mechanical wind energy (which is almost negligible also for the $35\,\mathrm{M}_\odot$ star), we get the corresponding energy transfer efficiencies according to equation (4.2):

$$\begin{aligned} \varepsilon_\mathrm{k} &= 3.4 \times 10^{-3} \ , \\ \varepsilon_\mathrm{i} &= 6.3 \times 10^{-3} \ , \\ \varepsilon_\mathrm{t} &= 5.6 \times 10^{-3} \ . \end{aligned}$$

Comparing these values with the results of the analytical solution for the windless case and the simulations with and without wind, one can see that the increase of the kinetic energy deposit from the windless to the combined SWB/HII region simulation (almost doubled) as well as the increase of the thermal energy deposit (also almost doubled) is about a factor of 3 below the analytical upper limits.

4.2.3 Comparison with Observations

In section 2.5 we point out the importance of X-ray observations of the hot gas in SWBs to study the physics of SWBs. Thus, we have also examined the X-ray properties of our numerical model in the $35\,\mathrm{M}_\odot$ case. In Figure 4.49 we plot the total X-ray luminosity of our model bubble in the energy band $0.1 - 2.4$ keV as a function of time. The emissivity $j_\nu(\rho, T, Z)$ in each grid cell is calculated with the Raymond & Smith (1977) program. For temperatures below 10^5 K the emissivity is set to zero. The total X-ray luminosity at time t is calculated as

$$L_X(t) = \sum_{\mathrm{cells}} \int_{h\nu=0.1\ \mathrm{keV}}^{h\nu=2.4\ \mathrm{keV}} 4\pi j_\nu(\rho_\mathrm{cell}(t), T_\mathrm{cell}(t), Z) V_\mathrm{cell}\ d\nu \ , \tag{4.3}$$

where $\rho_\mathrm{cell}(t)$ and $T_\mathrm{cell}(t)$ are the plasma density and temperature in the grid cell, respectively, V_cell is the volume of the grid cell, and $h\nu$ the energy of the X-ray photons. For the summation over grid cells the finest grid that is available for the respective coordinates is always used. As for the calculation of all the other global quantities, the grid data are mirrored at the equator. We assume optically thin emission; absorption is neglected. For the set of chemical abundances, Z, we use the same values that Chu et al. (2003) used for their spectral X-ray fits of S308, which are based on the abundance determination of Esteban et al. (1992) for the optically visible shell. We assume that the elements not mentioned by Chu et al. (2003) have the same abundance relative to the solar value as oxygen (0.13). Thus, for the computation of the X-ray emissivity the following elements are considered: H, He, C, N, O, Ne, Mg, Si, S, Ar, Ca, Fe, Ni with the following abundances relative to the solar values (Anders & Grevesse 1989): 1.0, 2.1, 0.1, 1.6, 0.13, 0.22, 0.13, 0.13, 0.13, 0.13, 0.13, 0.13, 0.13. This set of elemental abundances is intended to represent the chemistry in the RSG wind. The composition of the hot gas in the MS bubble may be different because the radiating material is supposed to originate from the MS wind of the star and (if thermal evaporation or ablation is important) also from the ambient medium. However, for the sake of simplicity we use the same chemical composition for all the emitting gas during the whole evolution. We briefly discuss impacts of

this choice below. The chemical composition employed for this diagnostic purpose is thus inconsistent with the solar chemical composition that is used to calculate the cooling of the gas (energy sink term in the radiation-hydrodynamical equations).

Figure 4.49 shows that the X-ray luminosity assumes the value 10^{32} erg s^{-1} soon after the turn-on of the stellar wind. It remains remarkably constant during the MS phase and the associated growth of the SWB. The deviation from 10^{32} erg s^{-1} is less than a factor of 2.5 during this period. Most of the X-ray emission originates at the interface between the hot gas in the SWB and the swept-up HII shell. Although He and N are overabundant, the strong underabundance of the other metals reduces the X-ray luminosity. Using a solar chemical composition instead of the abundances described above would increase the luminosity in Figure 4.49 by a factor $3-4$. With the onset of the RSG phase the total X-ray luminosity decreases by a factor of $3-4$ until the star reaches the W-R stage. This happens because the hot gas (or more precisely the gas in the interface region close to the shell of swept-up ambient gas) cools and the supply of the bubble with hot gas ceases during the RSG phase.

The subsequent onset of the fast W-R wind drives up the total X-ray luminosity by approximately 3 orders of magnitude. It reaches a few times 10^{34} erg s^{-1}, but varies quite strongly. It is interesting to note that in this phase almost all of the X-ray emission comes from the W-R shell (instead of the shocked W-R wind). At $t = 4.775$ Myr the radius of

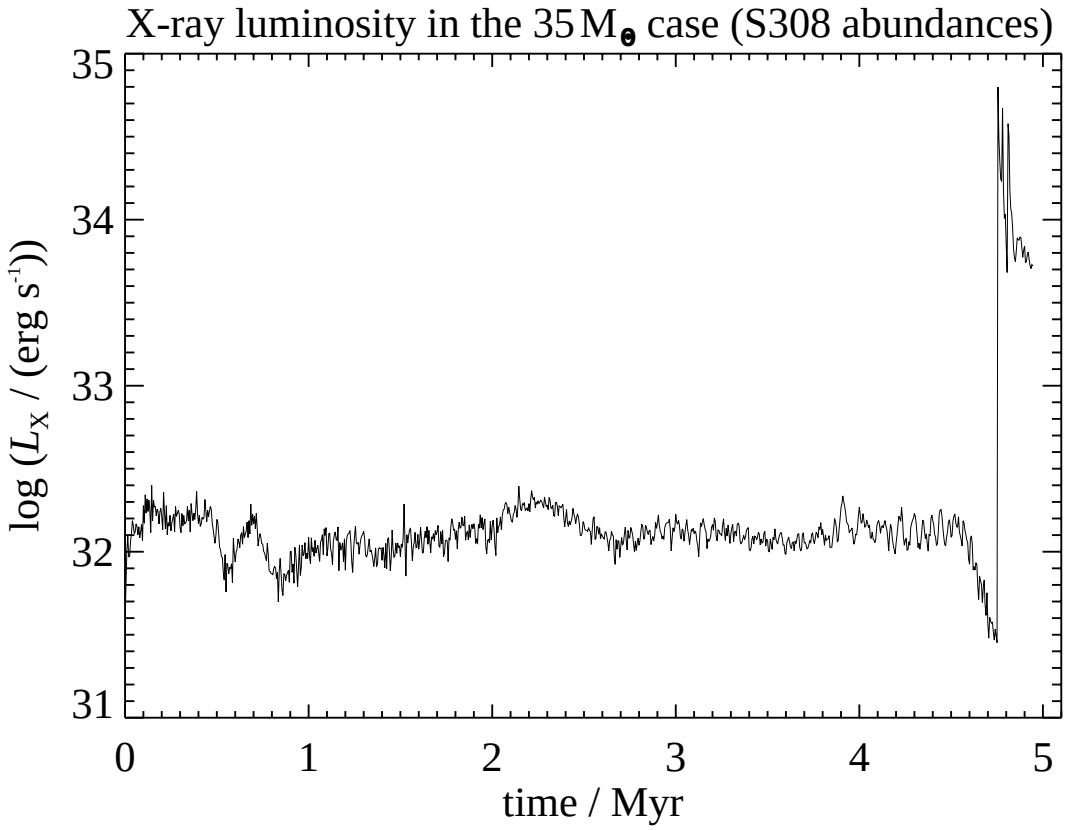

Figure 4.49: X-ray luminosity in the energy band $0.1-2.4$ keV in the $35\,M_\odot$ case with stellar wind. The chemical abundances are chosen according to the abundances observed in the W-R bubble S308.

this X-ray-emitting shell is approximately 10 pc with a thickness of $1.0 - 1.3$ pc. The temperature drops from 2.5×10^6 K behind the shock to 6×10^5 K at the inside of the shell, the density rises from 2×10^{-25} to 1.2×10^{-24} g cm^{-3}, and the velocity rises from 300 to 500 km s^{-1}. The shocked W-R wind has (from the reverse shock to the contact discontinuity) a density of 5×10^{-27} to 1.4×10^{-26} g cm^{-3}, a temperature of 1.0×10^8 to 5×10^7 K, and a velocity of 1000 to 500 km s^{-1}. The Hα emission comes mostly from the RSG shell. The density in this shell is $(3 - 12) \times 10^{-25}$ g cm^{-3}, which may be seen as a lower limit since this shell is not completely resolved in our calculations. The temperature in the shell is $(8 - 20) \times 10^3$ K, indicating that there is shock heating present in addition to photoionization. The shell's velocity has slowed to 25 km s^{-1} due to its interaction with the MS wind material.

Judging by the geometrical extent, the evolutionary state of the W-R bubble at this time is approximately comparable to the currently observable stage of S308. The model data show surprisingly good agreement with the X-ray observations of S308 described in section 2.5. The total X-ray luminosity of a few times 10^{34} erg s^{-1} is slightly higher but of the same order of magnitude as the $\leq 1.2 \pm 0.5 \times 10^{34}$ erg s^{-1} observed by Chu et al. (2003). Since almost all of the X-ray emission in our model comes from the W-R shell, the temperature range of $(0.6 - 2.5) \times 10^6$ K agrees quite well with the 1.1×10^6 K that results from the spectral fit of the observed X-rays. Although the observational proof for the existence of a substantially hotter gas component is still under debate, in our model it could well be identified with the shocked, hot W-R wind, which contributes only a small fraction to the total soft X-ray emission. The average density in the X-ray-emitting W-R shell is $n_e \approx 0.4$ cm^{-3}, which is well within the observationally determined range of $n_e = 0.28 - 0.63$ cm^{-3} for the assumed range $0.5 - 0.1$ of the hot gas volume filling factor (Chu et al. 2003). The total mass of the W-R shell is approximately 15 $M_\odot$; i.e., most of the 18.6 $M_\odot$ RSG wind has already been swept up. This is at the upper end of the observationally supported range of 11 ± 5 $M_\odot$ for an assumed volume filling factor of 0.5. The fact that the W-R shell supplies most of the X-ray emission alleviates the necessity to assume that thermal evaporation of RSG wind gas raises the mass of the X-ray-emitting shocked W-R wind. The process of thermal evaporation, which is not implemented in our numerical model, would not be very efficient anyway, since the temperature gradient between the $\approx 10^6$ K W-R shell and the shocked W-R wind at several times 10^7 K is rather modest.

The conclusion of Wrigge (1999) that S308 cannot be described by the two-wind model seems to be vulnerable because he assumed that the X-ray emission originates from the shocked W-R wind and that the energy in the forward shock ahead of the W-R shell is completely dissipated in a different wavelength range. Consequently, using the formula for the X-ray luminosity of the shocked W-R wind under the impact of conductive evaporation from García-Segura & Mac Low (1995a) in order to reproduce the observed X-ray luminosity, he derived values for the mechanical wind luminosity that are much too low compared to the actually observed values of the central W-R star. By contrast, the mechanical wind luminosity in our model calculation during the first 2×10^4 yr of the W-R stage is in the range $(3 - 10) \times 10^{37}$ erg s^{-1}, which is in reasonable agreement with the observed stellar wind luminosity (scaled to the distance of $D = 1.5$ kpc used here) of 4.9×10^{37} erg s^{-1} (Hamann et al. 1993) or 1.3×10^{37} erg s^{-1} for a clumping-corrected

mass-loss rate (Nugis et al. 1998).

Because the X-ray-emitting volume is a thick shell ($1.0-1.3$ pc), another observational constraint that is well reproduced in our model is the limb brightening of the X-ray emission. In Figure 4.50 we display the unabsorbed angle-averaged X-ray intensity profile in the energy range $0.1-2.4$ keV at three evolutionary times during the early W-R stage, namely, $t = 4.765$, 4.770, and 4.775 Myr, the latter corresponding to the phase discussed above. We see that the "background" intensity produced by the hot gas in the MS bubble is of order 10^{-10} erg s^{-1} cm^{-2} sr^{-1}. The intensity for lines of sight through the W-R shell is higher by $3-5$ orders of magnitude. The limb brightening within the W-R shell can be seen for all three profiles, as well as the decrease of the peak intensity with time. The consideration of absorption would not alter this result because the limb brightening is due to the geometry of the emitting plasma rather than due to varying absorption.

Since the shocked W-R wind in our model calculation has not yet swept up the entire RSG wind, the X-ray-emitting shell is interior to the optical shell as has been found in the observations. Differing from Chu et al. (2003), we interpret the gap between the outer rim of the optical emission and the outer edge of the X-ray emission as being the RSG ejecta in front of the W-R shell rather than being the W-R shell itself. The thickness of the gap in our model at this time is approximately 0.5 pc, which is smaller than the

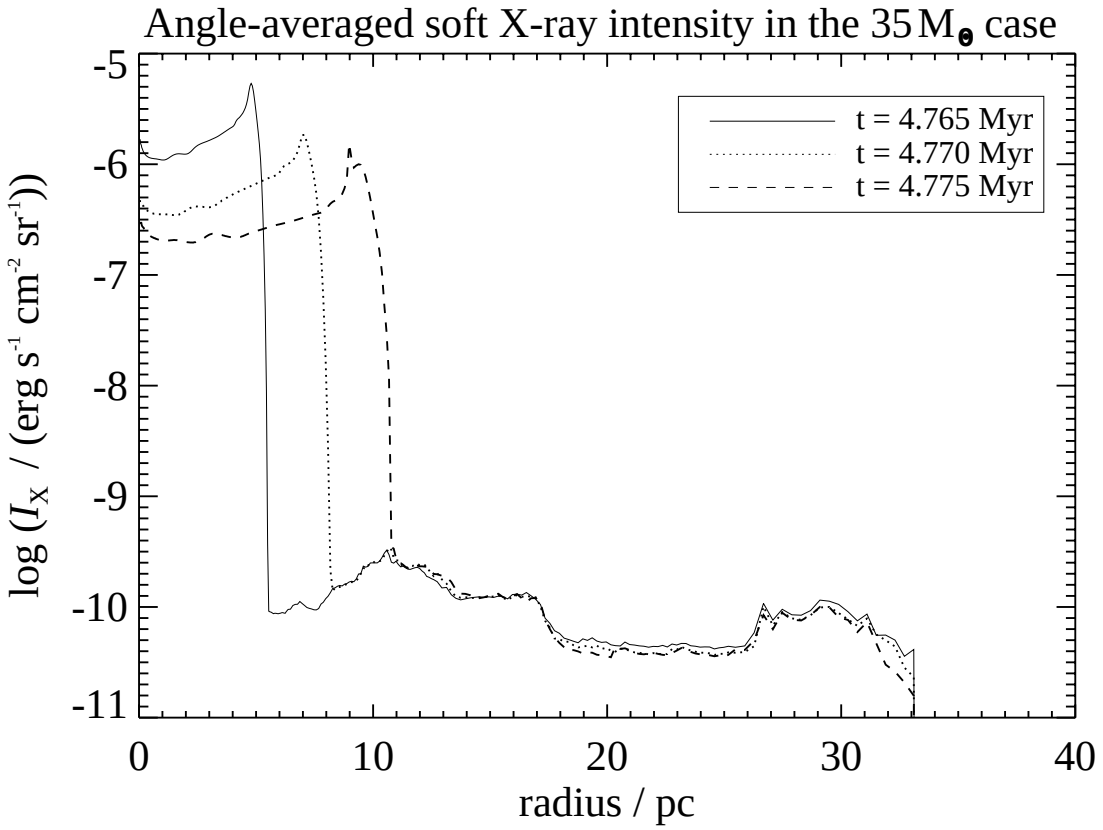

Figure 4.50: Angle-averaged unabsorbed X-ray intensity in the energy band $0.1-2.4$ keV in the $35\,M_\odot$ case with stellar wind at selected evolutionary times. The chemical abundances are chosen according to the abundances observed in the W-R bubble S308.

observed gap ($0.7 - 1.5$ pc). However, this strongly depends on the exact instant of time and on the exact duration of the RSG phase as well as the velocity of the RSG wind.

If our interpretation of the dynamical evolution is true, the age that has been attributed to the W-R bubble is probably significantly overestimated because of the assumption that the observed velocity 63 km s^{-1} is the velocity of the W-R shell rather than the velocity of the RSG shell. Based on our model the age of the bubble is $\approx 2 \times 10^4$ yr for the stage described above, much less than the 1.4×10^5 yr derived from the observed velocity of 63 km s^{-1}.

The appearance of NGC 6888 is harder to explain within the framework of our model. The observed geometrical size implies that the nebula is younger than S308, provided that the temporal evolution of the stellar parameters during the RSG and W-R stage is about the same. A maximum value of ≈8000 yr can be derived under the assumptions that the optically visible nebula has not yet been swept up by the expanding W-R bubble and that our stellar model parameters are appropriate for NGC 6888. The observed X-ray luminosity 1.6×10^{34} erg s^{-1}, as well as the emitting plasma temperature 2×10^6 K (Wrigge et al. 1994) are in reasonable agreement with the model data, but the X-ray emission in the model originates from a thick shell that is more or less homogeneous rather than from small filaments with a volume filling factor of only a few percent. Although the hot W-R shell is able to "hide" mass from optical observations and thus helps to find the yet undetected portion of RSG wind mass, 8000 yr after the onset of the W-R wind it contains only ≈3 $M_\odot$, which is not enough to solve the problem completely (assuming that the RSG mass loss used in the model is appropriate for NGC 6888). The biggest difficulty is probably the appearance of the optical shell. In the numerical model the RSG shell already has a radius greater than 10 pc and the unaffected RSG wind between the W-R shell and the RSG shell contributes significantly to the Hα emission. This conflicts with the observation of a very thin, filamentary shell with hydrogen number densities as high as 1000 cm^{-3}.

There may be various reasons for this mismatch between our model and the observations of NGC 6888. It is possible that physical effects not yet covered in our model are more important for NGC 6888, or that the resolution applied in our calculations is not yet high enough to allow for the formation of high-density filaments. Another possibility is that the actual mass-loss history of HD 192163 differs from what is expected and used in our calculations.

Apart from the detailed comparison, Figure 4.49 illustrates another aspect. The fact that up to now only W-R bubbles have been observed in X-rays is not only by chance. At least for the MS → RSG → W-R sequence the X-ray luminosity during the final W-R stage exceeds that of the rest of the stellar lifetime by more than an order of magnitude. Moreover, during the early W-R phase the emission comes from a relatively small volume (compared to most of the MS lifetime), resulting in an even higher X-ray surface brightness, which is easier to detect.

4.3 Unconsidered Physics and Differing Parameters

In this section I briefly discuss the changes of the results that are expected if the ambient medium is modified or if the stellar parameters differ from those used in the model calculations. I also outline the possible influence of physical processes that are not yet considered in the models.

Because of the immense computational efforts, we can only show results for one set of ambient medium parameters ($n_0 = 20\,\mathrm{cm}^{-3}$ and $T_0 = 200\,\mathrm{K}$) for each model star. Separating the evolution of the HII region and SWB, an increase of the density in the ambient medium results in a decrease of the size of the HII region. A closer examination of equations 2.57 to 2.59 shows that an increase of the ambient density always leads to a decrease of the rate with that ionization, thermal, and kinetic energy is accumulated by the expansion of the HII region. Modifying the temperature of the ambient medium does not strongly affect the evolution as long as the gas is not ionized and the pressure in the HII region is much higher than the pressure of the ambient medium.

With respect to the SWB, equation 2.15 shows that the radius of the SWB is proportional to $\rho_0^{-1/5}$; i.e., at comparable times it is also smaller in the case of a higher ambient density. In contrast to the HII region, the growth of the thermal and kinetic energy of the SWB does not depend on the ambient density, as long as the assumptions under which equations 2.61 and 2.62 were derived remain fulfilled (e.g., the thermal pressure in the hot bubble is much higher than the thermal pressure in the ambient medium).

It is difficult to estimate the impact of a variation of the ambient conditions on the highly nonlinear SWB/HII region interaction effects. Basically, an increase of the density in the ambient medium leads to both a smaller SWB and a thicker shell of swept-up material. Thus, the ratio of shell thickness to SWB diameter grows, which increases the unstable length scales and tends to inhibit thin-shell overstabilities with all their associated effects. On the other hand, clumpiness in the circumstellar medium may exist anyway, abolishing the need to trigger the interaction effects by shell instabilities. It is clear that numerical simulations under a variety of different ambient conditions are highly desirable in order to study these effects in more detail. They will become available with increasing computer power.

It should also be noted here that the stellar parameters that we use as time-dependent boundary conditions in our simulations are still somewhat uncertain. For example, Martins et al. (2002) showed that the determination of the effective temperature of O dwarfs based on non-LTE line-blanketed atmosphere models including stellar winds results in differences to previous calibrations up to a few times $10^3\,\mathrm{K}$. The mass-loss rate and its temporal variation in the short and violent evolutionary stages like the LBV phase are probably even less well known. We have chosen the sets of stellar parameters from GML1 and GLM2 because they are currently state of the art, sufficiently time resolved, and we wanted to directly compare our two-dimensional simulations to their one-dimensional calculations.

Nevertheless, deviations of the stellar parameters from this set will certainly influence the results of the model calculations. Basically, a larger rate of hydrogen-ionizing photons emitted by the star will increase the size of the HII region and thus the energy input into the ISM. In a similar manner, a higher stellar wind luminosity will increase the size of

the SWB and the energy transferred to the shell at a given time. Note that although the analytical description of the SWB evolution depends on the stellar wind luminosity, i.e., only on the product of mass-loss rate and wind terminal velocity squared, this does not account for cooling in the hot bubble, which will be enhanced when the mass-loss rate rises without a proportional increase in wind velocity.

The impact of changes in the temporal evolution of the stellar parameters (e.g., a different number of outbursts of varying length) on the results of our calculations is difficult to estimate. Highly nonlinear effects appear when, e.g., a slow shell is overtaken by a fast wind and instabilities arise. Interaction processes between the SWB and the HII region may also be amplified or damped by variations of the stellar parameters. Numerical simulations for different stellar evolutionary histories are necessary to study these effects in detail.

Some physical processes are not yet considered in our models, and we want to briefly discuss their possible influence here. One of these processes is heat conduction, which may play a role for the energy transfer in the system. Although classical theory and our numerical models without heat conduction predict that the cooling time for the interior of the MS bubble is longer than the lifetime of the star, there is indirect evidence that, at least in NGC 6888, the MS bubble is cold at the time when the W-R wind blows out into the MS bubble (Mac Low 2000). A possible explanation is mass loading of the MS bubble: heat conduction evaporates cold material from the shell or from immersed clouds, which enhances the density in the bubble. The higher density reduces the cooling time of the bubble. Such evaporation from a cloud embedded in hot interstellar gas has recently been observed (Chu 2000).

On the other hand, magnetic fields provide an efficient mechanism to reduce the efficiency of heat conduction. In a plasma the electrons are constrained to move along magnetic field lines. If the magnetic field lines are aligned with the shell or if they are tangled, the effective path lengths for fast electrons moving from the hot to the cold gas are much longer and heat conduction by electrons is less efficient. Saturation effects of heat conduction due to electric fields arising from charge separation further complicate the situation. All these effects are worthy to be studied in detail, but the simultaneous inclusion into multidimensional hydrodynamical simulations remains a computational challenge for the future.

We only allowed for isotropic winds in our models. However, line-driving theory for rotating stars suggests that mass outflow from the poles should be both more vigorous and faster. As already mentioned in section 2.8, Brighenti & D'Ercole (1997) and Frank et al. (1998) showed that anisotropic winds can indeed influence the formation and appearance of circumstellar shells, producing lobes or bipolar outflows. Similar effects may be expected for our models when anisotropic winds are employed, but details remain to be explored.

Other physical effects not yet considered in our models include variations of the metallicity in the circumstellar gas and the photodissociation of molecular hydrogen. In its later stages, the star is expected to eject gas that is enriched with metals. This enhancement of the metallicity in the circumstellar medium leads to stronger cooling and thus influences the circumstellar evolution. The dissociation of molecular hydrogen by stellar photons with energies below the Lyman threshold adds additional (exterior) layers to the

basic structure shown in Figure 2.1. The HII region evolves into the photodissociated region, which itself expands into the molecular gas. Interaction processes between the photodissociated region and the HII region similar to those between the HII region and the SWB may arise.

Chapter 5

Summary and Conclusions

In this thesis I present results of numerical simulations carried out with a two-dimensional radiation hydrodynamics code in order to study the impact of massive stars on their surrounding interstellar medium. These simulations are, to my best knowledge, the first numerical models in more than one dimension that cover the whole evolution from the ZAMS phase of the star until it explodes as a supernova, considering time-dependent stellar parameters, radiation transfer, nonequilibrium ionization of hydrogen in the circumstellar gas, and a fairly sophisticated treatment of heating and cooling.

The evolution is studied for two different model stars. The first one has an initial mass of $60\,M_\odot$ and develops from a main-sequence O star through a hydrogen-rich WN stage, a P Cygni-type LBV phase, hydrogen-poor and hydrogen-free WN stages to a WC star, which finally explodes as a supernova of Type II. The second model star, initially having a mass of $35\,M_\odot$, is supposed to undergo the evolution from the main-sequence O star to the RSG and finally the W-R star, until it also explodes as a supernova of Type II.

The numerical models for the evolution of the circumstellar gas around the $60\,M_\odot$ star show that the interaction of the SWB with the stellar radiation field can strongly influence the morphology of the circumstellar medium. The rearrangement of circumstellar gas by the stellar wind influences the way it reacts to the ionizing radiation. Density clumps formed in the shell of gas swept up by the SWB cast shadows into the HII region. The resulting pressure gradients force material into the shadowed regions, enhancing their density and forming neutral "spokes", which subsequently raise the mass of the clumps in the shell. The HII region is extended in directions free of clumps. Thus, the formation of these elongated HII region "fingers" in our model not only occurs as a result of the ionization front instability described by García-Segura & Franco (1996) but is triggered and amplified by the redistribution of mass by the action of the stellar wind shell.

These results document the necessity to consider both ionizing radiation and stellar winds for an appropriate description of the interaction of OB stars with their circumstellar environment. They also shed light on the open question of whether the complex structures that can be found in HII regions are primordial, i.e., relics from the time before the gas became ionized, or formed by dynamical processes in the course of the HII region evolution. While there are strong observational indications that the former plays an important role, our results give support to the idea that the latter cannot be completely

excluded: intense structure formation in HII regions with strong stellar winds can occur even if the neutral ambient medium was initially homogeneous.

Nevertheless, these structures are only a temporary phenomenon because the extended HII region is eventually swept up by the stellar wind shell. If we compare our results for the $60\,M_\odot$ case at $t = 3.30$ Myr with the one-dimensional solution of GML1, we see that, from a morphological point of view, there is basically little difference in the overall structure except for the appearance of an HII region at the inner part of the remnant shell and a few filaments in the hot bubble. Thus, the approach of GML1 and GLM2 to use the one-dimensional solution for the estimation of the initial conditions for closer studies of the LBV and subsequent W-R stage appears to be valid.

The structure formation induced by the interaction of the stellar radiation field with the SWB also has implications for the energy balance of the circumstellar gas, mostly via the effect that denser gas has a shorter recombination time and a higher cooling efficiency. This can be seen in the decrease of ionization and thermal energy of warm photoionized gas in the circumstellar medium during the time when the structure formation occurs in the first few times 10^5 yr. Furthermore, the ionization energy lags behind the corresponding value in the calculation without wind by $0.1 - 0.4$ dex and the thermal energy of warm gas by $0.2 - 0.6$ dex for almost the entire lifetime of the $60\,M_\odot$ star. This also implies that the HII regions around stars with winds can have a higher emission measure than undisturbed ones.

Although the total mechanical wind energy of the star is negligible compared to the accumulated energy of the Lyman continuum photons, in the $60\,M_\odot$ case the simulation with a stellar wind results in a kinetic energy of bulk motion in the circumstellar medium that is 4 times higher than in the calculation without wind. The total thermal energy is almost twice as high (or, subtracting the initial thermal energy of the background gas, the thermal energy that is added to the system is enhanced by a factor of 2.4). The energy transfer efficiency of the stellar Lyman continuum radiation over long timescales is so low because this radiative energy is mostly used to maintain the photoionization of hydrogen; it is lost from the system when the hydrogen recombines into levels above the ground state. By contrast, most of the energy of the stellar wind is converted into thermal energy of hot gas that accelerates the shell. The kinetic energy can be accumulated in the system for a long time unless it is dissipated, and the thermal energy of hot gas can also be saved if the density in the bubble is sufficiently low. For a plasma of solar chemical composition with $T = 10^7$ K and $n = 10^{-2}$ cm^{-3}, the cooling time in collisional ionization equilibrium is several times 10^7 yr. Although the LBV phase of the star induces very rapid changes in the energy balance of the circumstellar medium, its impact over longer timescales is limited as a result of the brevity of the LBV eruption.

The above conclusions regarding the inefficiency of converting the energy flux of photoionizing UV photons into kinetic energy are modified in the presence of large-scale density gradients (i.e., at the edge of a molecular cloud). Generally speaking, the resulting "champagne flow" can lead to an efficiency of about 1 % for converting the stellar UV flux into kinetic energy of expansion (see Yorke 1986). The exact value for efficiency depends on the details of the problem, however; it is conceivable in some cases that the champagne phase is negligibly short compared to the lifetime of the star. We note that simulations that assess the role of stellar winds in the presence of champagne flows are

currently rare. Comerón (1997) examined the evolution of wind-driven HII regions across a density discontinuity for various parameters but without the consideration of energy transfer efficiencies.

For the simulations of HII region evolution without a stellar wind the analytical prediction for the kinetic energy in the system at the end of the star's lifetime differs from our numerical result in the case of the $60\,M_\odot$ star by less than 30 %. The analytical solution for the energy transfer efficiency in the case of the combined SWB/HII region is just an upper limit and overestimates the transfer efficiencies into kinetic energy and thermal energy by factors of 6.7 and 9.7, respectively.

The setup of the $35\,M_\odot$ simulation differs from that of the $60\,M_\odot$ case only by the deviating time-dependent stellar parameters that drive and govern the evolution of the circumstellar gas. The fundamental structures that evolve are basically the same as observed in the $60\,M_\odot$ case. They are generally smaller because for most of the time the stellar wind luminosity and the Lyman continuum luminosity are lower than in the $60\,M_\odot$ case. At the end of the simulation the entire bubble structure has a radius of $\approx$44 pc, which is some 6 pc smaller than the final bubble of the $60\,M_\odot$ case, although the $35\,M_\odot$ star lives 0.88 Myr longer than the $60\,M_\odot$ star.

Instability-driven structure formation during the early MS phase of the star (the formation of ionized fingers corrugating the ionization front and the formation of neutral spokes shadowed by dense clumps), which we found to be quite prominent in the case of the $60\,M_\odot$ calculation, is also visible in the $35\,M_\odot$ case, but it is much less pronounced and only short-lived, because of the lower mechanical wind luminosity of the star. The lower mechanical wind luminosity of the star reduces the thermal pressure of the hot gas in the bubble. The lower pressure in the hot bubble increases the geometrical thickness of the shell of swept-up HII gas, making it less sensitive to thin-shell overstabilities that could trigger the formation of the morphological structures described above. Since this behavior better preserves the basic spherical structure, other morphological effects become visible, which might be prohibited in the $60\,M_\odot$ case by the strong corrugation of the bubble shell. When the swept-up HII shell broadens geometrically, the plasma density in the shell decreases. This rarefaction reduces the rate of Lyman continuum photons necessary to sustain the photoionization of the shell and excess photons become available, which drive the ionization front outward and photoevaporate additional material from the neutral shell of swept-up ambient medium. The inward flow of evaporated material collides with the outward flow of the dissolving swept-up HII shell, temporarily forming a new shell of enhanced density. Since all the plasma within the HII region is almost isothermal, this density fluctuation vanishes soon.

Another consequence of the reduced stellar wind luminosity (compared to the $60\,M_\odot$ case) is the fact that for most of the time the shape of the HII region is more or less preserved as a broad shell interior to the thin shell of swept-up ambient material rather than being so thin as in the $60\,M_\odot$ case where the HII region is compressed into the illuminated inner part of the outer shell. Nevertheless, the geometrical thickness of the photoionized shell shrinks at the end of the simulation when the stellar wind luminosity reaches its maximum during the final W-R stage.

The morphological impact of the low-velocity mass-loss phase (the RSG stage) is more prominent than that of the $60\,M_\odot$ star (the LBV stage), because the total mass

loss during the RSG stage is higher (≈18.6 $M_\odot$) than during the LBV stage of the 60 $M_\odot$ star (≈7.3 $M_\odot$). The slowly expanding RSG wind material is subsequently swept up and accelerated by the shocked W-R wind so that Rayleigh-Taylor instabilities break it into filaments.

The final, presupernova structure that shows up in the 35 $M_\odot$ case after 4.945 Myr is basically comparable to that of the 60 $M_\odot$ case at its end. The entire bubble is slightly smaller, the HII shell at the inside of the outer neutral swept-up shell is more extended than in the 60 $M_\odot$ case. Outer shell and HII region are less clumpy and show less rippling as a consequence of the different evolutionary scenarios.

The reduced substructure formation during the early MS phase is also reflected in the circumstellar energetics. The decrease of ionization energy and thermal energy of warm gas (compared to the respective case without stellar wind) resulting from the formation of dense photoionized structures with short recombination times is smaller than for the 60 $M_\odot$ case. Ionization energy dominates the energy in the circumstellar gas for most of the evolution. The kinetic energy of bulk motion stays fairly close together with the warm and the hot component of thermal energy from $t \approx 0.3$ Myr until the star enters the RSG phase.

The energetic variations during the RSG stage are stronger than those during the LBV stage of the 60 $M_\odot$ star because, due to the duration of the RSG phase, the ionizing radiation of the star is switched off for a considerable period of time so that the photoionized regions recombine. In addition, the mass that is ejected during the RSG stage and accelerated during the subsequent W-R stage is about 2.5 times higher than the mass ejected during the LBV stage of the 60 $M_\odot$ star.

At the end of the 35 $M_\odot$ simulation the total energy transfer efficiency is 1 %. This value is about the same as in the corresponding simulation without stellar wind, but it is 2.7 times higher than the value at the end of the 60 $M_\odot$ calculation. 54 % of the net energy that has been added to the system until the end of the simulation is then in the form of ionization energy, 36 % in thermal energy, and 10 % in kinetic energy of bulk motion. The corresponding values at the end of the 60 $M_\odot$ calculation are 25 %, 40 %, and 35 %, respectively. This is another indication that the stellar wind plays a more prominent role in the 60 $M_\odot$ case.

Remarkable agreement of the X-ray properties is found when comparing our 35 $M_\odot$ case during the early W-R phase with observations of S308. The order of magnitude of the observed X-ray luminosity, as well as the temperature of the emitting plasma and the limb brightening of the intensity profile, is well reproduced. The obvious explanation that our model overcomes the "missing wind problem" described in section 2.5 is that almost the entire X-ray emission during this phase comes from the W-R shell rather than from the shocked W-R wind. Analytical models constructed so far (see, e.g., García-Segura & Mac Low 1995a) assume the W-R shell to be thin and cool so that the energy in the forward shock is completely dissipated in the low-energy wavelength range. The source of X-rays in these models is the shocked W-R wind, and the efficiency of heat conduction and thermal evaporation between the hot gas and the cold W-R shell strongly influences the luminosity and the spectral shape of the X-ray emission. If heat conduction is efficient enough to cool the hot shocked W-R wind down to the observed temperature and if the W-R wind luminosity in the models is adjusted to reproduce the observed X-ray luminosity,

the W-R wind luminosity is usually much lower than observed (Wrigge 1999).

Another factor that reduces the X-ray luminosity in our model to values roughly comparable with S308 is the assumed set of chemical abundances. Although He and N are overabundant according to the observations in the nebula, the underabundance of the other metals reduces the X-ray luminosity by a factor of $3-4$ compared to what can be expected from solar chemical composition.

A further consequence of this interpretation of our results is that the Hα emission originates mostly from the RSG shell. This is in agreement with the finding of Chu et al. (2003) that the X-ray emission is completely interior to the optical shell. Since the age of S308 (and other W-R bubbles) was hitherto derived from the expansion velocity of the optical nebula under the assumption that the nebula is part of the W-R shell, our results imply an age of S308 that is much younger ($\approx 2 \times 10^4$ yr) than assumed so far.

However, the match of our model data and the observations is worse for the case of NGC 6888. Besides numerical or model restrictions, differences of the mass-loss and luminosity history between the central star of NGC 6888 and the $35\,M_\odot$ model star might be responsible for the discrepancies.

This detailed examination is suitable to improve studies of the energization of the ISM in the solar neighborhood (e.g., Abbott 1982), which use energy transfer efficiencies as theoretical input. It is also important when considering the heating of the Galactic disk as a global phenomenon self-regulated by star formation. To address this, the effects of overlapping HII regions and SWBs in OB clusters and associations still need to be assessed, which is the subject of future investigations.

References

Abbott, D. C. 1982, ApJ, 263, 723

Allen, C. W. 1973, Astrophysical Quantities (3d ed.; London: Athlone)

Allen, D. A., & Burton, M. G. 1993, Nature, 363, 54

Anders, E., & Grevesse, N. 1989, Geochim. Cosmochim. Acta, 53, 197

Arnal, E. M., & Cappa, C. E. 1996, MNRAS, 279, 788

Arnal, E. M., & Mirabel, I. F. 1991, A&A, 250, 171

Arthur, S. J., Henney, W. J., & Dyson, J. E. 1996, A&A, 313, 897

Avedisova, V. S. 1972, Soviet Astronomy, 15, 708

Beltrametti, M., Tenorio-Tagle, G., & Yorke, H. W. 1982, A&A, 112, 1

Benaglia, P., & Cappa, C. E. 1999, A&A, 346, 979

Bertoldi, F. 1989, ApJ, 346, 735

Black, D.C., & Bodenheimer, P. 1975, ApJ, 199, 619

Bochkarev, N. G. 1988, Nature, 332, 518

Boroson, B., McCray, R., Clark, C. O., Slavin, J., Mac Low, M.-M., Chu, Y.-H., & Van Buren, D. 1997, ApJ, 478, 638 (erratum 485, 436)

Brighenti, F., & D'Ercole, A. 1997, MNRAS, 285, 387

Cantó, J., Raga, A., Steffen, W., & Shapiro, P. R. 1998, ApJ, 502, 695

Cappa, C. E., & Benaglia, P. 1998, AJ, 116, 1906

Cappa, C. E., Niemela, V. S., Herbstmeier, U., & Koribalski, B. 1996, A&A, 312, 283

Capriotti, E. R. 1973, ApJ, 179, 495

Castor, J., McCray, R., & Weaver, R. 1975, ApJ, 200, L107

Chevalier, R. A., & Theys, J. C. 1975, ApJ, 195, 53

Chu, Y.-H. 1981, ApJ, 249, 195

Chu, Y.-H. 1982, ApJ, 254, 578

Chu, Y.-H. 2000, in Astrophysical Plasmas: Codes, Models, and Observations, ed. J. Arthur, N. Brickhouse, & J. Franco, Rev. Mex. Astron. Astrofis. (Serie de Conferencias), 9, 262

Chu, Y.-H., Guerrero, M. A., Gruendl, R. A., García-Segura, G., & Wendker, H. J. 2003, ApJ, 599, 1189

Chu, Y.-H., Gull, T. R., Treffers, R. R., Kwitter, K. B., & Troland, T. H. 1982, ApJ, 254, 562

Comerón, F. 1997, A&A, 326, 1195

Cowie, L. L., McKee, C. F., & Ostriker, J. P. 1981, ApJ, 247, 908

Crowther, P. A., & Smith, L. J. 1996, A&A, 305, 541

de Jong, T. 1977, A&A, 55, 137

Downes, D., Genzel, R., Becklin, E. E., & Wynn-Williams, C. G. 1981, ApJ, 244, 869

Draine, B. T., Roberge, W. G., & Dalgarno, A. 1983, ApJ, 264, 485

Dyson, J. E. 1973, A&A, 23, 381

Dyson, J. E. 1977, A&A, 59, 161

Dyson, J. E. 1978, A&A, 62, 269

Dyson, J. E., & de Vries, J. 1972, A&A, 20, 223

Esteban, C., & Vílchez J. M. 1992, ApJ, 390, 536

Esteban, C., Vílchez, J. M., Smith, L. J., & Clegg, R. E. S. 1992, A&A, 259, 629

Falle, S. A. E. G. 1975, A&A, 43, 323

Firmani, C., Koenigsberger, G., Bisiacchi, G. F., Ruiz, E., & Solar, A. 1979, in IAU Symp. 83, Mass Loss and Evolution of O-Type Stars, ed. P. S. Conti, & C. W. H. de Loore (Dordrecht: Reidel), 421

Franco, J., Díaz-Miller, R. I., Freyer, T., & García-Segura, G. 1998, in ASP Conf. Ser. 141, Astrophysics from Antarctica, ed. G. Novak, & R. H. Landsberg, 154

Frank, A., Ryu, D., & Davidson, K. 1998, ApJ, 500, 291

Freyer, T., Hensler, G., & Yorke, H. W. 2003, ApJ, 594, 888

García-Segura, G., & Franco, J. 1996, ApJ, 469, 171

García-Segura, G., & Mac Low, M.-M. 1995a, ApJ, 455, 145

García-Segura, G., & Mac Low, M.-M. 1995b, ApJ, 455, 160

García-Segura, G., Mac Low, M.-M., & Langer, N. 1996a, A&A, 305, 229 (**GML1**)

García-Segura, G., Langer, N., & Mac Low, M.-M. 1996b, A&A, 316, 133 (**GLM2**)

Genzel, R., & Stutzki, J. 1989, ARA&A, 27, 41

Giuliani, J. L. 1979, ApJ, 233, 280

Gruendl, R. A., Chu, Y.-H., Dunne, B. C., & Points, S. D. 2000, AJ, 120, 2670

Grun, J., Stamper, J., Manka, C., et al. 1991, Phys. Rev. Lett., 66, 2738

Hamann, W.-R., Koesterke, L., & Wessolowski, U. 1993, A&A, 274, 397

Hamann, W.-R., Schmutz, W., & Wessolowski, U. 1988, A&A, 194, 190

Hester, J. J., Scowen, P. A., Sankrit, R., et al. 1996, AJ, 111, 2349

Hillenbrand, L. A., Massey, P., Strom, S. E., & Merrill, K. M. 1993, AJ, 106, 1906

Howarth, I. D., & Schmutz, W. 1995, A&A, 294, 529

Humphreys, R. M. 1991, in IAU Symp. 143, Wolf-Rayet Stars and Interrelations with Other Massive Stars in Galaxies, ed. K. A. van der Hucht, & B. Hidayat (Dordrecht: Kluwer), 485

Johnson, H. M., & Hogg, D. E. 1965, ApJ, 142, 1033

Koo, B.-C., & McKee, C. F. 1992a, ApJ, 388, 93

Koo, B.-C., & McKee, C. F. 1992b, ApJ, 388, 103

Kwan, J. 1977, ApJ, 216, 713

Kwitter, K. B. 1981, ApJ, 245, 154

Lasker, B. M. 1967, ApJ, 149, 23

Levenson, N. A., Graham, J. R., McLean, I. S., et al. 2000, ApJ, 533, L53

Levermore, C. D., & Pomraning, G. C. 1981, ApJ, 248, 321

Lozinskaya, T. A. 1982, Astrophysics and Space Science, 87, 313

Maciel, W. J., & Pottasch, S. R. 1982, A&A, 106, 1

Mac Low, M.-M. 2000, in Astrophysical Plasmas: Codes, Models, and Observations, ed. J. Arthur, N. Brickhouse, & J. Franco, Rev. Mex. Astron. Astrofis. (Serie de Conferencias), 9, 279

Mac Low, M.-M., & Norman, M. L. 1993, ApJ, 407, 207

Maeder, A. 1990, A&AS, 84, 139

Marston, A. P. 1991, ApJ, 366, 181

Marston, A. P. 1995, AJ, 109, 2257

Marston, A. P. 1996, AJ, 112, 2828

Marston, A. P. 1997, ApJ, 475, 188

Marston, A. P., & Meaburn, J. 1988, MNRAS, 235, 391

Martins, F., Schaerer, D., & Hillier, D. J. 2002, A&A, 382, 999

McCaughrean, M. J., & Mac Low, M.-M. 1997, AJ, 113, 391

McKee, C. F., Van Buren, D., & Lazareff, B. 1984, ApJ, 278, L115

Moffat, A. F. J., Firmani, C., McLean, I. S., & Seggewiss, W. 1982, in IAU Symp. 99, Wolf-Rayet Stars: Observations, Physics, Evolution, ed. C. W. H. de Loore, & A. J. Willis (Dordrecht: Reidel), 577

Moore, B. D., Hester, J. J., & Scowen, P. A. 2000, AJ, 119, 2991

Nichols, J. S., & Fesen, R. A. 1994, A&A, 291, 283

Norman, M. L. 1980, Ph.D. Thesis, L. Livermore Lab. Report UCRL 52946

Nugis, T., Crowther, P. A., & Willis, A. J. 1998, A&A, 333, 956

Oey, M. S., & Massey, P. 1994, ApJ, 425, 635

Osterbrock, D. E. 1989, Astrophysics of Gaseous Nebulae and Active Galactic Nuclei (Mill Valley: University Science Books)

Parker, R. A. R. 1964, ApJ, 139, 493

Penston, M. V. 1970, ApJ, 162, 771

Perryman, M. A. C., et al. 1997, A&A, 323, L49

Pikel'ner, S. B. 1968, Astrophysical Letters, 2, 97

Pilbratt, G. L., Altieri, B., Blommaert, J. A. D. L., et al. 1998, A&A, 333, L9

Pittard, J. M., Dyson, J. E., & Hartquist, T. W. 2001a, A&A, 367, 1000

Pittard, J. M., Hartquist, T. W., & Dyson, J. E. 2001b, A&A, 373, 1043

Press, W. H., Teukolsky, S. A., Vetterling, W. T., & Flannery, B. P. 1992, Numerical Recipes: The Art of Scientific Computing, 2nd ed. (Cambridge: University Press)

Raymond, J. C., & Smith, B. W. 1977, ApJS, 35, 419

Richling, S., & Yorke, H. W. 2000, ApJ, 539, 258

Richtmyer, R. O., & Morton, K. W. 1967, Difference Methods for Initial Value Problems, 1d ed. (New York: Interscience)

Różyczka, M. 1985, A&A, 143, 59

Różyczka, M., & Tenorio-Tagle, G. 1985a, A&A, 147, 202

Różyczka, M., & Tenorio-Tagle, G. 1985b, A&A, 147, 209

Ryu, D., & Vishniac, E. T. 1987, ApJ, 313, 820

Ryu, D., & Vishniac, E. T. 1988, ApJ, 331, 350

Salas, L., Rosado, M., Cruz-Gonzáles, I., et al. 1999, ApJ, 511, 822

Sarazin, C. L., & White, R. E. 1987, ApJ, 320, 32

Scoville, N., Kleinmann, S. G., Hall, D. N. B., & Ridgway, S. T. 1983, ApJ, 275, 201

Soker, N. 1990, AJ, 99, 1869

Soker, N. 1998, MNRAS, 299, 562

Spitzer, L. 1962, Physics of Fully Ionized Gases (New York: Interscience)

Spitzer, L. 1978, Physical Processes in the Interstellar Medium (New York: Wiley)

Stone, J. M., Mihalas, D., & Norman, M. L. 1992, ApJS, 80, 819

Stone, J. M., & Norman, M. L. 1992a, ApJS, 80, 753

Stone, J. M., & Norman, M. L. 1992b, ApJS, 80, 791

Stone, J. M., Xu, J., & Mundy, L. G. 1995, Nature, 377, 315

Strickland, D. K., & Stevens, I. R. 1998, MNRAS, 297, 747

Strömgren, B. 1939, ApJ, 89, 529

Taylor, K. N. R., Storey, J. W. V., Sandell, G., Williams, P. M., & Zealey, W. J. 1984, Nature, 311, 236

Tenorio-Tagle, G., Beltrametti, M., Bodenheimer, P., & Yorke, H. W. 1982, A&A, 112, 104

Treffers, R. R., & Chu, Y.-H. 1982, ApJ, 254, 569

Van Buren, D., & McCray, R. 1988, ApJ, 329, L93

van der Hucht, K. A., Conti, P. S., Lundström, I., & Stenholm, B. 1981, Space Science Reviews, 28, 227

van der Hucht, K. A. 2001, New Astronomy Reviews, 45, 135

van Leer, B. 1977, Journal of Computational Physics, 23, 276

Vishniac, E. T. 1983, ApJ, 274, 152

Vishniac, E. T. 1994, ApJ, 428, 186

Vishniac, E. T., & Ryu, D. 1989, ApJ, 337, 917

Weaver, R., McCray, R., Castor, J., Shapiro, P., & Moore, R. 1977, ApJ, 218, 377 (erratum 220, 742)

Wendker, H. J., Smith, L. F., Israel, F. P., Habing, H. J., & Dickel, H. R. 1975, A&A, 42, 173

Williams, R. J. R. 1999, MNRAS, 310, 789

Wrigge, M. 1999, A&A, 343, 599

Wrigge, M., & Wendker, H. J. 2002, A&A, 391, 287

Wrigge, M., Wendker, H. J., & Wisotzki, L. 1994, A&A, 286, 219

Yang, H., Chu, Y.-H., Skillman, E. D., & Terlevich, R. 1996, AJ, 112, 146

Yorke, H. W. 1986, ARA&A, 24, 49

Yorke, H. W., Bodenheimer, P., Tenorio-Tagle, G., 1982, A&A, 108, 25

Yorke, H. W., & Kaisig, M. 1995, Computer Physics Communications, 89, 29

Yorke, H. W., & Welz, A. 1996, A&A, 315, 555

Abbreviations used for journals:

A&A	Astronomy & Astrophysics
A&AS	Astronomy & Astrophysics Supplement Series
AJ	Astronomical Journal
ApJ	Astrophysical Journal
ApJS	Astrophysical Journal Supplement Series
ARA&A	Annual Review of Astronomy and Astrophysics
MNRAS	Monthly Notices of the Royal Astronomical Society

Acknowledgements

It is a pleasure to thank Gerhard Hensler for his advice and encouragement while I was working on this thesis project.

I also would like to thank Harold Yorke, Sabine Richling, Ralf-Jürgen Dettmar, Don Cox, Mordecai-Mark Mac Low, Pepe Franco, Norbert Langer, and Matthias Wrigge for a lot of helpful comments and interesting discussions on this project over the past years. Thanks also to Matthias Hünsch for a careful reading of the manuscript.

Financial support for this work was provided by the Deutsche Forschungsgemeinschaft (DFG) under grant He 1487/17, by the Graduiertenkolleg GRK 118, and by the Sonderforschungsbereich 191 in Bochum. I also gratefully acknowledge financial support by the German Academic Exchange Service (Doktorandenstipendium HSP II / AUFE).

Additional travel grants enabled me to participate in various conferences and workshops. For this, I am also greatly indebted to the Deutsche Forschungsgemeinschaft, the Astronomische Gesellschaft, the WE-Heraeus-Stiftung, and the Guillermo Haro program. I highly enjoyed the hospitality of the Department of Physics at the University of Wisconsin–Madison during a research visit.

The model computations were performed at the Rechenzentrum der Universität Kiel, the Konrad-Zuse-Zentrum für Informationstechnik in Berlin, and the John von Neumann-Institut für Computing in Jülich. Thanks to the staffs of the computer centers and to Holger Boll and Günter Jonas who take care of our local computer equipment.

Thanks also to all the friends and colleagues in the institute who established this unique working atmosphere. Inge Schmidt and Brigitte Kuhr contributed enormously to it.

I hope that all my team mates enjoyed our soccer matches on Wednesday afternoon like I did. Thanks a lot for your athletic efforts.

Last but not least, a sincere thanks to my family for the continuous support over all the years.

Erklärung

Diese Abhandlung wurde in Form und Inhalt nur unter Zuhilfenahme der angegebenen Hilfsmittel unter Anleitung von Prof. Dr. G. Hensler angefertigt. Sie wurde noch nicht an anderer Stelle ganz oder zum Teil im Rahmen eines Prüfungsverfahrens vorgelegt. Ein Teil der Ergebnisse wurde mit Genehmigung des Dekans vom 16. Oktober 1997 veröffentlicht.

Kiel, den 25. Mai 2005 .....